

Improving the Efficiency of Domestic Ovens

*This thesis is submitted for the degree of
Doctor of Philosophy*

Jamie Davidson
Queens' College

September 2021



UNIVERSITY OF
CAMBRIDGE

Chemical Engineering and
Biotechnology

Preface

This thesis is the result of my own work and includes nothing which is the outcome of work done in collaboration except as declared in the Preface and specified in the text. I further state that no substantial part of my thesis has already been submitted, or, is being concurrently submitted for any such degree, diploma or other qualification at the University of Cambridge or any other University or similar institution except as declared in the Preface and specified in the text. It does not exceed the prescribed word limit for the relevant Degree Committee.

Abstract

Improving the efficiency of domestic ovens, Jamie Davidson

This project aimed to realise and validate a novel design of domestic oven to reduce cooking time and energy consumption compared to a traditional design of domestic oven.

The design concept was developed by Dr Mark Williamson of Cambridge Oven Innovation (COI). Initially computational models were used to predict the efficacy of the design concept. Heat transfer coefficients from literature and a computational fluid dynamics (CFD) simulation were imported into a lumped property model, which predicted that the COI design would reduce both energy consumption and cooking time. Three successive physical prototypes were constructed to develop the concept, successively improve the user experience and progress towards a mass manufacturable design. Comparative food trials were undertaken with the third prototype and a domestic fan oven of traditional design. The COI design was able to reduce energy consumption by 30% and cooking time by 60% across a wide range of thermal masses and Biot numbers.

The CFD simulation was validated using heat flux and velocity measurements taken in the first prototype. The simulation was found to predict velocity, temperature distribution and convective heat flux reasonably accurately, with a mean absolute error in the convective heat flux of 22%. The radiative heat flux was predicted less accurately, with a mean underprediction of 53.2%. This was attributed to an inaccurate prediction of the temperature of the oven walls, due to: (i) neglecting conduction through interior dividing walls of the oven, (ii) an inaccurate estimate of the overall heat transfer coefficient from the inner wall of the oven to the ambient air and, (iii) reliance on empirical wall functions to calculate heat flux on the walls of the cooking chamber.

The CFD simulation was used to investigate the possibility of applying the COI design to a 45 cm high standard kitchen unit, rather than the typical 60 cm height units. The simulation showed that this would increase the heat flux into the food at a given setpoint temperature, and therefore the efficiency and cooking time would be improved. However, the evenness of cooking would be reduced. Potential solutions, namely increasing the number of jet nozzles and changing the size of the jet nozzles, were investigated. This was found to improve evenness at the cost of energy efficiency and cooking time, although they were still less even than the 60 cm design.

Acknowledgements

I would like to express my profound gratitude to my supervisor, Prof. Ian Wilson for his incredible support over the past 4 years, and for the time, energy and attention he has generously spent on my work.

I would also like to thank Dr Mark Williamson of COI for the superlative example he has set for me in problem solving and applying engineering principles and also for the amazing opportunities he has facilitated for me.

The advice and time of Dr Bart Hallmark and Dr Phil Stopford was invaluable in completing the CFD simulations in this project and is much appreciated. I would also like to thank Jon Cowper, Robin Ansell, Peter Benic and Dr Ewa Marek for their patience and prowess in solving the many technical issues that my simulation work presented.

The construction of the various prototype ovens and lab apparatus would not have been possible without the time and skill of the workshop and electronics technicians: Gary Chapman, Andy Hubbard, Lee Pratt, Seb Consnefroy and Mark Scudder. I would like to thank in particular Seb and Gary for their time and patience teaching me new and interesting practical skills and for their good humour.

I would also like to thank my friends in the P4G group for their conversation and camaraderie over the past 5 years. Thank you also to Stuart Fordham for letting me relax and waste his time talking about football, and for supporting a team even worse than mine.

This project would not have been possible without the support, constant encouragement and positivity, going back far beyond the beginning of this project, of my parents, Stephen and Carol Davidson. Thank you for encouraging my curiosity and giving me the self-belief to follow it.

Finally, I would like to thank my partner, Katherine for her incredible support and unwavering belief in me. I have learned far more about myself during the past four years than I have about ovens or engineering, and I owe much of that to Katherine's wisdom, patience and kindness.

Nomenclature

Latin

Symbol	Description	Units
a^2	Anderson-Darling statistic	-
A	Area	m^2
A_{nozzle}	Area of impingement nozzle	m^2
Bi	Biot number	-
C_d	Discharge coefficient	-
C_p	Specific heat capacity	$J\ kg^{-1}K^{-1}$
D	Mass diffusivity	$m^2\ s^{-1}$
D_n	Impingement nozzle diameter	m
f_n	Relative area of impingement nozzles compared to heat transfer target	-
f_x	Probability density function	-
$F_{A \rightarrow B}$	View factor	-
Fo	Fourier number	-
g	Gravity acceleration vector	$m\ s^{-2}$
h	Film heat transfer coefficient	$Wm^{-2}K^{-1}$
h_{measured}	Measured film transfer coefficient	$Wm^{-2}K^{-1}$
h_{oven}	Film heat transfer coefficient from oven air to food	$Wm^{-2}K^{-1}$
H	Enthalpy	$J\ kg^{-1}$
H_n	Distance between impingement nozzle and food	m
H_θ	Fitted energy consumption and cooking time	$kW\ hr, min$
k	Thermal conductivity	$Wm^{-2}K^{-1}$
k_c	Film mass transfer coefficient	$kg\ m^{-2}s^{-1}$
k_{food}	Food thermal conductivity	$Wm^{-2}K^{-1}$
K_r	Radiative heat flux constant	$Wm^{-2}K^{-4}$
L	Length scale	m
L_b	Body thickness	m
L_{el}	Element length scale	m
\dot{m}	Mass flux	$kg\ m^{-2}\ s^{-1}$
\dot{M}	Mass flowrate	$kg\ s^{-1}$
M_w	Molecular weight	$kg\ mol^{-1}$
N_{el}	Number of elements	-
N_{nozzle}	Number of impingement nozzles	-
Nu	Nusselt number	-
P	Pressure	Pa
P_{gauge}	Gauge pressure	Pa
P_{nozzle}	Pressure across impingement jet nozzle	Pa
$P_{w\ air}$	Partial pressure of water in oven air	Pa
$P_{w\ surface}$	Partial pressure of water at food surface	Pa
Pr	Prandtl number	-
q	Heat flux	Wm^{-2}
\bar{q}	Mean heat flux	Wm^{-2}
q_{conv}	Convective heat flux	Wm^{-2}

\bar{q}_{conv}	Mean convective flux	Wm^{-2}
q_{heater}	Heater flux	Wm^{-2}
q_{fitted}	Fitted heat flux	Wm^{-2}
q_{measured}	Measured heat flux	Wm^{-2}
q_{rad}	Radiative heat flux	Wm^{-2}
\bar{q}_{rad}	Mean radiative flux	Wm^{-2}
$\bar{q}_{\text{rad}}^{\text{wall}}$	Mean radiative flux from the heater walls to the sensor	Wm^{-2}
q_{surface}	Heat flux at food surface	Wm^{-2}
q_{wall}	Heat flux through the walls of the heater walls	Wm^{-2}
Q	Rate of heat flow	W
Q_{food}	Rate of heat flow into food	W
$Q_{\text{surroundings}}$	Rate of heat flow into surroundings	W
Q_{wall}	Rate of heat flow through the walls of the heater section	W
r	Radial dimension	m
R	Gas constant	$\text{J kg}^{-1} \text{K}^{-1}$
Re	Reynolds number	-
s_T	External heat added per unit volume	W m^{-3}
t	Time	s
T	Temperature	K
t_{actual}	Actual cooking time	min
t_{ideal}	Cooking time with no heat transfer limitations	min
t_{pen}	Penetration time	s
t_{sim}	Simulation time	s
T_{air}	Oven air temperature	K
T_{ambient}	Ambient air temperature	K
T_{BB}	Blackbody temperature	K
T_{boundary}	Boundary temperature	K
T_{element}	Heat element temperature	K
T_{surface}	Surface temperature	K
T_{wall}	Temperature of the external wall of the heat section	K
u	Velocity perpendicular to the wall	m s^{-1}
u^+	Dimensionless velocity perpendicular to the wall	-
U	Overall heat transfer coefficient	$\text{Wm}^{-2}\text{K}^{-1}$
v	Velocity	m s^{-1}
\mathbf{v}	Velocity vector	m s^{-1}
V	Volume	m^3
w_c	Water mass fraction	-
W_A	Total energy absorbed	J
x_{jet}	Coordinate dimension in LDA experiments	m
y	Cartesian coordinate	m
y^+	Dimensionless distance to the wall	-
y_{jet}	Vertical distance below impingement jet nozzle	m
y_w	Distance to the wall	m
z	Axial dimensions	m
z_{jet}	Coordinate dimension in LDA experiments	m

Greek

Symbol	Description	Units
α	Thermal diffusivity	$\text{m}^2 \text{s}^{-1}$
α_{sf}	Noise constant	-
ϵ	Emissivity	-
η	Thermal efficiency	-
λ	Wavelength	m
λ_I	Peak wavelength	m
μ	Viscosity	Pa s
μ_x	Mean	-
ξ	Uniform probability distribution	-
ρ	Density	kg m^{-3}
ρ_{air}	Density of air	kg m^{-3}
ρ_l	Density of water	kg m^{-3}
ρ_s	Density of dry component	kg m^{-3}
σ	Standard deviation	-
σ_{SB}	Stefan Boltzmann constant	$\text{W m}^{-2} \text{K}^{-4}$
τ_w	Wall shear stress	Pa
θ	Linear model coefficient	-
ψ	Normal probability distribution	-

Abbreviations

CFD	Computational Fluid Dynamics
COI	Cambridge Oven Innovation
HBE	Huxley-Bertram Engineering
LDA	Laser Doppler Anemometry
LEO	Low Emissivity Oven
SST	Shear stress transport

Contents

1: Introduction.....	17
1.1: Description of the Field of Interest	17
1.2: Objectives of the Project	17
1.3: Structure of the Dissertation	18
2: Oven Design.....	20
2.1: Introduction.....	20
2.2: Consumer Expectations	20
2.2.1: Current Domestic Oven Design	20
2.2.2: Additional Features	22
2.2.3: Evolution of the Design.....	23
2.2.4: Food Types	24
2.2.5: Maillard Reactions	27
2.2.6: Physical and Manufacturing Constraints	30
2.3: Existing Technologies	31
2.3.1: Convection	32
2.3.2: Conduction.....	37
2.3.3: Radiation.....	40
2.4: Design Process and Iterations.....	42
2.4.1: Prototype IA	42
2.4.2: Prototype IB.....	45
2.4.3: Prototype II.....	48
2.4.4: Prototype III	51
2.5: Conclusions and Closing Remarks	52
3: Literature Review.....	53
3.1: Previous Studies in Domestic and Catering Oven Efficiency.....	53
3.1.1: Low Emissivity Ovens.....	53
3.1.2: Improved Insulation	56
3.1.3: Improved Control	56
3.1.4: Faster Heat-up	57
3.1.5: Combination of Heating Modes	58
3.1.6: Summary	62
3.2: Computational Modelling	62
3.2.1: Modelling of Food Cooking	63

3.2.2: Flow Modelling (CFD)	70
3.2.3: History and Development of the Field	75
3.2.4: Summary	80
3.3: Conclusions	82
4: Design and Fabrication of the Prototype Ovens	84
4.1: Prototype IA	84
4.1.1: Plenum Assembly	84
4.1.2: Base Heater	86
4.1.3: Fan Motor and Mounting	86
4.1.4: Control Board and Electronics	87
4.1.5: Steam System	89
4.2: Prototype IB	90
4.2.1: Replacement Air Heaters	90
4.2.2: Humidity Generation	91
4.2.3: Fan Speed Sensor	92
4.2.4: Induction Heating:	92
4.2.5: Fan Replacement	93
4.3: Prototype II	95
4.3.1: Electronics Board and Assembly	95
4.3.2: Fan and Plenum Assembly	100
4.3.3: Induction Assembly	103
4.4: Prototype III	105
4.4.1: Electronics Boards and Assembly	106
4.4.2: Ductwork and Infra-Red Lamp Mounting	108
4.4.3: Induction Unit	110
4.4.4: Heat Recovery	111
4.4.5: Humidity Control	114
5: Experimental Materials and Methods	117
5.1: Design and Construction of a 32 Channel Temperature Datalogger	117
5.1.1: Motivation	117
5.1.2: Electronics	117
5.1.3: Mounting and Enclosure	118
5.1.4: Firmware and Driver Software	121
5.1.5: Temperature Calibration and Correction	122
5.2: Design and Construction of the Heat Flux Sensor	125
5.2.1: Overview and Conceptual Design	125

5.2.2: Detailed Design Modelling	126
5.2.3: Construction	138
5.2.4: Experimental Procedure.....	139
5.2.5: Data Processing.....	139
5.2.6: Estimation of the Sensor Uncertainty.....	143
5.3: Laser Doppler Anemometry	145
5.3.1: Measurement Principle	145
5.3.2: Traverse and Probe	147
5.3.3: Seeding Particles and Generator	147
5.3.4: Software	148
5.3.5: LDA Results Processing.....	148
5.3.6: Experimental Procedure.....	153
6: Lumped Property Model	155
6.1: Introduction.....	155
6.2: Model Objects	156
6.2.1: Classes and Governing Equations	157
6.3: Usage.....	159
6.4: Model Architecture.....	161
6.4.1: Common Features.....	161
6.4.2: Traditional Oven Model.....	162
6.4.3: COI Oven Model	162
6.4.4: Parameter Assumptions	163
6.4.5: Timestep Selection	164
6.5: Results.....	165
6.6: Sensitivity Analyses	168
6.6.1: Convection Sensitivity Analysis.....	169
6.6.2: Conduction Sensitivity Analysis	173
6.7: Conclusions.....	175
7: Computational Fluid Dynamics Simulation.....	178
7.1: Software and Computer Specifications.....	178
7.2: Overview and Objectives of the Model.....	180
7.3: Geometry	180
7.3.1: Geometry Bounds	181
7.3.2: Geometry Details	182
7.4: Meshing	186
7.4.1: Mesh Metrics.....	189

7.5: Physics	190
7.5.1: Time step	190
7.5.2: Turbulence and Radiation Model	191
7.5.3: Boundary Conditions.....	191
7.5.4: Initial Conditions.....	196
7.5.5: Material Properties	196
7.5.6: Solver Settings.....	196
7.5.7: Data Export	197
7.6: Validation	198
7.6.1: Iterative Convergence.....	199
7.6.2: Consistency	199
7.6.3: Spatial Convergence.....	199
7.6.4: Temporal Convergence	210
7.6.5: Experimental Comparison.....	212
7.6.6: Model Uncertainties.....	224
7.7: Conclusions.....	225
8: 45 cm Oven Design Study.....	227
8.1: Introduction.....	227
8.2: Simulation Specifications	228
8.2.1: Case 1	229
8.2.2: Case 2	231
8.2.3: Case 3	232
8.3: Results and Discussion.....	234
8.3.1: Conclusions.....	238
9: Comparative Food Trials.....	240
9.1: Introduction.....	240
9.2: Procedure	241
9.2.1: Roast Chicken	241
9.2.2: Bread	242
9.2.3: Pizza	243
9.2.4: Lasagne	243
9.3: Results and Discussion.....	244
9.4: Conclusions.....	258
10: Conclusions	259
10.1: Reflection on Project Aims	259
10.2: Recommendations for Further Work	261
10.2.1: CFD Simulation.....	261

10.2.2: Experimental.....	262
11: Appendix A	264
12: Appendix B.....	267

List of Figures

2.1	Design of a traditional electric fan oven	21
2.2	An Oberlin stove	23
2.3	Overview of the Maillard reaction	29
2.4	Design of an industrial tunnel oven	32
2.5	Common layouts of impingement jets	34
2.6	Layout of a catering oven	37
2.7	Industrial bread baking oven, showing the conveyor	39
2.8	Typical induction heating unit	40
2.9	Layout of prototype IA	45
2.10	Layout of prototype II	50
2.11	Schematic of the design process	52
3.1	Layout of a low emissivity oven	54
3.2	Plot of heating element temperature in a traditional oven during cooking	57
3.3	Timeline of developments in numerical modelling of the cooking of food	65
3.4	Plot of velocity within the boundary layer	74
4.1	Labelled photograph of the interior of prototype I	84
4.2	Labelled photograph of the control board of prototype I	87
4.3	Photographs of the modified air heaters using in prototypes IB and II	89
4.4	Diagram of the fan speed sensor in prototype IB	92
4.5	Photograph of the repairs to the fan impeller in prototype IB	93
4.6	Labelled photographs of prototype II	95
4.7	Labelled photograph of the control board of prototype II	96
4.8	Labelled photographs of the convection system of prototype II	100
4.9	Labelled photographs of the induction system of prototype II	103
4.10	Labelled photographs of prototype III	106
4.11	Labelled photographs of the control board of prototype III	108
4.12	Labelled photographs of the convection system of prototype III	111
4.13	Labelled photographs of the air heaters of prototype III	112
4.14	Labelled photographs of the induction system of prototype III	112
4.15	Labelled photographs of the heat recovery system of prototype III	114
4.16	Labelled photographs of the steam generator of prototype III	115
5.1	Block diagram of the datalogger electronics	118
5.2	Labelled photographs of the datalogger	119

5.3	Diagram of the temperature equalising block	122
5.4	Histogram of the offsets of the datalogger thermocouples from the mean for each multiplexor connection	123
5.5	Deviation of datalogger measured temperatures from the UKAS certified measurements	124
5.6	Details of the heat flux sensor	127
5.7	Temperature profiles within the heat flux sensor, as predicted by the one-dimensional model	129
5.8	Geometry used in the three-dimensional model of the heat flux sensor	131
5.9	Details of the mesh used in the three-dimensional model of the heat flux sensor	131
5.10	Temperature profiles within the heat flux sensor, as predicted by the three-dimensional model	132
5.11	Contours of temperature within the heat flux sensor, as predicted by the three-dimensional model	134
5.12	Film heat transfer coefficient, measured by the simulated heat flux sensor	135
5.13	Example plots of measured and fitted heat flux into the heat flux sensor	141
5.14	Plot of all measured and fitted heat fluxes	142
5.15	Diagram of an LDA probe	144
5.16	Schematic of the LDA apparatus	145
5.17	Example velocity measurements from the LDA apparatus	148
5.18	Example fitted probability density functions, fitted to LDA velocity measurements	151
5.19	Anderson-Darling statistics for probability density functions fitted to LDA velocity measurements	152
5.20	Histogram of LDA velocity measurements from outside the expected range of velocities	152
6.1	Schematic of the lumped property model of a traditional oven	155
6.2	Flowchart of the lumped property model	159
6.3	Schematic of the lumped property model of the COI oven	163
6.4	Effect of timestep length on the accuracy and computation time of the lumped property model	164
6.5	Comparison of energy consumption and temperature profiles predicted by the lumped parameter model and measured in a traditional oven.	166
6.6	Results of the convection sensitivity analysis	171
6.7	Results of the conductive sensitivity analysis	175
7.1	Software packages used for CFD simulations	177
7.2	Overview of the geometry of the CFD simulation	182
7.3	Detail of the geometry of the fan outlet and heater section of the CFD simulation	183
7.4	Detail of the geometry of the cooking chamber of the CFD simulation	184
7.5	Detail of the geometry of the region near the jet nozzles of the CFD simulation	185
7.6	Detail of the mesh used in the CFD simulation in the cooking chamber	186
7.7	Detail of the mesh used in the CFD simulation in the heater section	187
7.8	Detail of the mesh used in the CFD simulation near the jet nozzles	188
7.9	Element skewness of the mesh used in the CFD simulation	189
7.10	Illustration of the boundary conditions used in spatial convergence	199

7.11	Plot of element count against mesh refinement for volume A	201
7.12	Average effect of mesh refinement on jet temperature and velocity	202
7.13	Effect of mesh refinement on individual jet temperature and velocity	203
7.14	Plot of element count against mesh refinement for volume B	206
7.15	Effect of mesh refinement on the mean and standard deviation of heat flux into the food surface	206
7.16	Effect of inflation layer thickness on the mean and standard deviation of heat flux into the food surface	207
7.17	Contours of y^+ on the food boundary	207
7.18	Contours of y^+ on the oven wall boundary	208
7.19	Effect of timestep length on the mean and standard deviation of heat flux into the food surface	210
7.20	Evolution of the mean and standard deviation of heat flux into the food surface	210
7.21	Illustration of the coordinate system used for velocity measurements	212
7.22	Comparison of measured and predicted air velocities beneath an impingement jet nozzle	213
7.23	Contours of measured and predicted air velocities beneath an impingement jet nozzle	214
7.24	Detail of the mesh used by the CFD simulation near the top of the heat flux sensor	217
7.25	Heat flux measurement positions	218
7.26	Simplified schematic of heat transfer through the walls of the heater section	221
7.27	Plot of predicted and measured heat fluxes	222
8.1	Overview of the geometry of the Case 1 simulation	229
8.2	Detail of the geometry of the heater section of the Case 1 geometry	230
8.3	Detail of the geometry of the cooking chamber of the Case 1 geometry	231
8.4	Detail of the geometry of the heater section of the Case 2 geometry	232
8.5	Detail of the geometry of the cooking chamber of the Case 2 geometry	232
8.6	Contours of heat flux into the food boundary for the 4 design cases considered	236
8.7	Illustration of a potential COI oven with angled impingement jet nozzles	238
9.1	Plot of savings in energy consumption in cooking time achieved in the COI oven vs Biot number and thermal mass.	248
9.2	Power and temperature profiles for the roasting of chicken in the COI oven and a traditional oven	249
9.3	Photographic comparison of chickens roasted in the COI oven and a traditional oven	250
9.4	Power and temperature profiles for the baking of bread in the COI oven and a traditional oven	251
9.5	Photographic comparison of bread baked in the COI oven and a traditional oven	252
9.6	Power and temperature profiles for the baking of pizza in the COI oven and a traditional oven	253
9.7	Photographic comparison of pizzas baked in the COI oven and a traditional oven	254
9.8	Power and temperature profiles for the cooking of lasagne in the COI oven and a traditional oven	255

9.9	Photographic comparison of lasagne cooked in the COI oven and a traditional oven	256
-----	--	-----

List of Tables

2.1	Design features and price points for electric fan ovens	22
2.2	Common food type thermal properties and cooking times	25
2.3	Common food types and their approximate geometry	26
2.4	Maillard reaction products and associated flavours	29
2.5	Infra-red penetration depth into various food types for different element temperatures	41
4.1	Power meter connectivity in prototype II	98
4.2	Thermocouple connectivity in prototype II	98
5.1	Physical properties and temperature penetration times for potential heat flux sensor materials	128
5.2	Rates of heat transfer through the faces of the heat flux sensor, predicted by the three-dimensional model	133
5.3	Results of the sensitivity analysis using the three-dimensional model of the heat flux sensor	136
6.1	Physical properties of the food items used in the lumped property model	161
6.2	Geometry and temperature targets for the food items used in the lumped property model	161
6.3	Comparison of energy consumption and cooking time predicted by the lumped property model, and measured in a traditional fan oven	165
6.4	Comparison of predicted energy consumption and cooking time by the lumped property model for the COI oven and a traditional fan oven.	167
6.5	Input parameters for the convection sensitivity analysis	169
6.6	Results of the convection sensitivity analysis	170
6.7	Input parameters for the conduction sensitivity analysis	172
6.8	Results of the conduction sensitivity analysis	174
7.1	Mesh metrics for the mesh used by the CFD simulation	189
7.2	Boundary conditions used for the CFD simulation	190
7.3	Summary of y^+ values for meshes used in the spatial convergence study	208
7.4	Comparison of heat fluxes predicted by the CFD simulation and measured experimentally	219
7.5	Comparison of mean and standard deviation of heat flux into the food surface when using different radiation and turbulence models	223
8.1	Results of the 45 cm oven design study	233
9.1	Summary of food types used in comparative food trials	240
9.2	COI instruction set for roasting chicken	240
9.3	Ingredients list for the bread recipe used in food trials	241
9.4	COI instruction set for baking bread	242
9.5	COI instruction set for baking pizza	242
9.6	Ingredients list for the lasagne recipe used in food trials	243

9.7	COI instruction set for cooking lasagne	243
9.8	Comparison of food cooking metrics for the COI oven and a traditional fan oven	244
9.9	Comparison of lumped parameter model predictions and experimental results for the COI oven	254

1: Introduction

1.1: Description of the Field of Interest

Domestic ovens are a ubiquitous feature of almost every home across the world, with 75% of EU homes containing an oven in 2007¹. Domestic ovens are appliances containing a heated cavity or cooking chamber used for roasting and baking food. Heat is transferred to the food by a combination of convection and radiation. While other forms exist, this work focuses upon electrically heated fan ovens, where the cooking chamber is heated using a variety of resistive electrical elements. A fan is used to distribute heated air throughout the cooking chamber and encourage convective heat transfer. The interior walls of the cooking chamber are typically coated in a black ceramic and are heated by the air within before radiating heat to the food.

Despite their ubiquity, domestic ovens exhibit poor thermal efficiency, with typically only 10-13% of the electrical energy supplied to the appliance absorbed by the food². Additionally, domestic ovens are high power items, typically requiring 16A electrical connections and drawing an average of over 700 W during a cooking cycle. Considering the ongoing climate crisis, finding ways to reduce the power consumption of these items is of increased importance.

For changes to domestic ovens to have a positive impact and reduce energy consumption they must be widely adopted by consumers. Therefore, the design and optimisation of a new oven must meet consumer demands at a price that is still competitive with existing designs, and ideally improve convenience or include new features to encourage uptake.

1.2: Objectives of the Project

Dr Mark Williamson of Cambridge Oven Innovation (COI) developed and supplied a conceptual design of domestic oven that aimed to reduce the energy consumption and cooking time compared to a traditional design. The aims of this project were threefold:

¹ P. Fonseca, A. de Almeida, N. Feilberg, G. Markogiannakis, and C. Kofod, 'Characterization of the Household Electricity Consumption in the EU, Potential Energy Savings and Specific Policy Recommendations', *Energy and Buildings* 43, no. 8 (2011): 1884–94.

² Fonseca, de Almeida, Feilberg, Markogiannakis, and Kofod.

- i) Predict the effectiveness of the design at reducing energy consumption using computational simulations. From this, the viability of further development of the design could be assessed.
- ii) Develop certain aspects of the conceptual design into a practical and manufacturable prototype and compare the performance of this prototype to an existing design of oven for a range of food types. This was required to demonstrate its ability to meet the consumer requirements.
- iii) Produce and validate a framework of simulations able to predict the effect of future design changes. This would allow further development and optimisation of the design to be performed *in silico*, reducing subsequent development time and costs.

1.3: Structure of the Dissertation

This dissertation begins by reviewing current and historic domestic oven design to identify consumer requirements and constraints, thereby defining the design space. Technologies from parallel industries that could be applied to domestic ovens are then surveyed. The most promising are identified and the COI design incorporating these features described. The evolution of the design over the project is then detailed.

Chapter 3 begins by surveying and describing academic literature and patents relating to the COI design and to the goal of increasing domestic oven efficiency. The history and state of the art of oven simulations is reviewed, both the transfer of heat to the food and the processes occurring within the food.

Chapter 4 describes the detailed design and fabrication of the three prototype ovens.

Chapter 5 describes the design and construction of other experimental apparatuses, including a temperature and energy consumption datalogger, a heat flux sensor and the data processing required for LDA measurements.

The modelling portion of the project is detailed in chapters 6, 7 and 8. First, the lumped property model was used to predict the efficacy of the COI design and identify the most important design parameters for future prototypes. Second, the CFD simulation of the first prototype is described, and its predictions of air velocity and heat flux compared to experimental measurements. The

CFD simulation is then used to predict the performance of the COI design in a smaller kitchen unit and recommend design changes.

Chapter 9 describes comparative food trials, in which a range of foods are cooked in a traditional fan oven and in a COI design oven. The energy and time requirements are compared.

Chapter 10 concludes the dissertation, summarizing the scientific and technological advances made. Recommendations for further research building on this work are also presented.

2: Oven Design

2.1: Introduction

This chapter summarises the design process for this project. A comprehensive list of design constraints was created by considering the current state of the art and by conversations with leading oven manufacturers. These constraints must be satisfied in a commercially attractive final design. With the constraints defined, a survey of existing technologies was performed to identify potential features from related applications in parallel industries. Considering the practicalities of domestic oven usage and the fundamental physics, the most attractive were combined into a prototype design which was tested and iterated upon.

2.2: Consumer Expectations

2.2.1: Current Domestic Oven Design

Consumers have an expectation for the performance of a domestic oven which must be met by any new design for it to be commercially viable. This baseline level is given by the current standard domestic appliance, an electric fan oven. Figure 2.1 shows the salient features and typical appearance of one of these devices. The normal operating protocol is to set the heating mode and temperature for cooking, wait for the temperature to reach the set point before putting the food in the oven. The oven air temperature is typically measured by a probe situated at the top of the back wall of the oven. Food is removed after a set time or after a desired degree of surface browning or core temperature has been achieved. The mode and temperature are generally not changed during the cooking cycle. A standard oven unit, outside the USA, has a face size of 600 mm by 600 mm with a maximum depth of 550 mm. These external dimensions are set by the size of standard kitchen unit. The volume of the cooking chamber is typically around 70 litres, with dimensions of 350 mm height, 500 mm width and 400 mm depth.

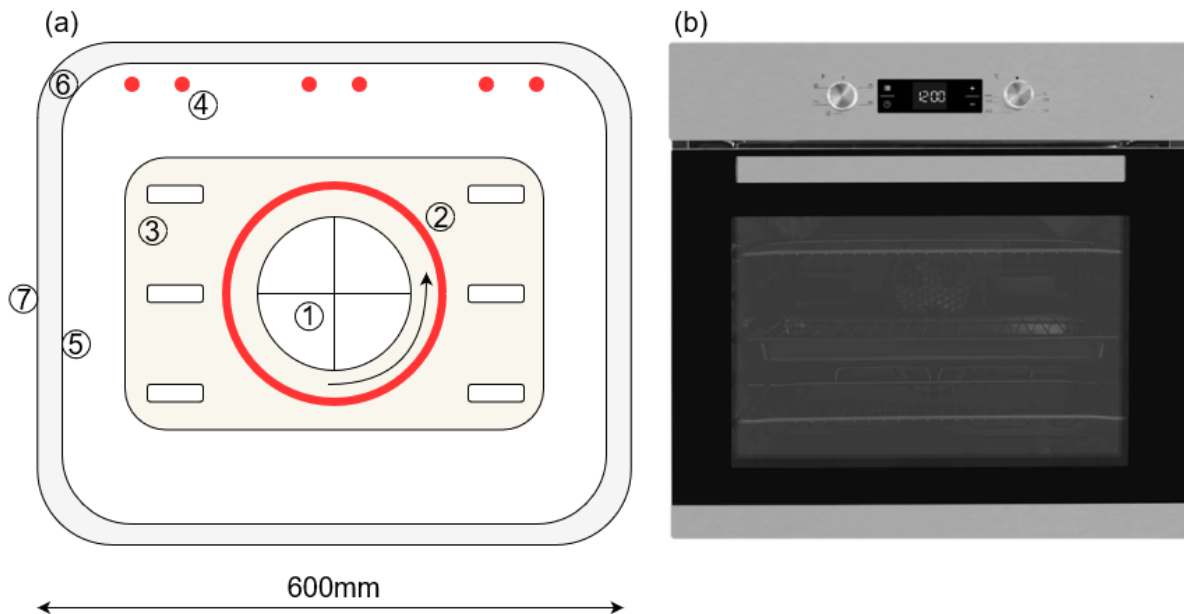


Figure 2.1: Conventional oven design. (a) Shows a cross-section of the oven viewed from the front. 1 - Convection Fan. 2 - Spiral air heater around the fan. 3 - Slotted Back panel, (shown filled). 4 - Radiative elements in the oven roof for grilling. 5 - Stamped, enamelled steel forming the oven chamber. 6 – Ceramic wool insulation around the oven chamber. (b) Photograph, front view.

Most food types are cooked by circulating hot air combined with heat radiating from the hot oven walls which are heated by the circulating hot air. Air is circulated by a fan located at the back of the oven behind a perforated plate that protects it from physical damage and prevents potential injuries to consumers. An electrical resistive heater encircles the fan, heating the oven air as it returns to the cooking chamber through slots around the back plate. Velocities generated by the fan are typically $\lesssim 0.5$ m/s, measured in the centre of the oven cavity³.

An additional element is located in the roof of the oven and provides the grill function. When in this cooking mode the fan is disabled, and the food is cooked mainly by radiative transmission from this heating element. This cooking mode mimics the conditions in a barbeque or broiler and is intended for quick cooking of items where a large amount of surface browning is desirable. In all ovens investigated the grill and convective modes were separate and were not intended to be used in parallel. If both cooking modes are desired to cook an item this is achieved by the consumer switching between modes, in series.

³ J.K. Carson, J. Willix, and M.F. North, 'Measurements of Heat Transfer Coefficients within Convection Ovens', *Journal of Food Engineering* 72, no. 3 (2006): 293–201.

2.2.2: Additional Features

A survey of design features of the ovens manufactured by four European companies; AEG, Beko, Bosch and Miele was conducted. The study was performed by surveying the product catalogues. Every electric oven sold by these manufacturers conformed to the layout shown in Figure 2.1. More expensive models included the following additional features:

- i) Food thermometers that can be inserted directly into food to directly measure the core temperature.
- ii) Steam generation in various forms depending on price point:
 - a. Water dosing: water is added at a fixed rate to the oven, adding uncontrolled humidity to the oven chamber.
 - b. Humidity control: the humidity in the oven is measured using the wet bulb temperature and water is added to maintain the humidity at a set value.
 - c. Steam ovens: The oven chamber can be completely filled with steam.
- iii) Pyrolytic cleaning. Additional insulation allows the oven to be heated to 400°C burning food residues to ash that can then be wiped off.

Table 2.1 summarises the price points at which these additional features were available.

Table 2.1: Summary of domestic electric oven price points and features (2018)

Price Point	Features	Cost
Basic	Fan Grill Timer (control)	£150-£300
Lower Mid-range	Pyrolytic Cleaning	£300-£500
Upper Mid-range	Pyrolytic Cleaning Water Dosing Food Thermometer Microwave-Convection Combination Oven	£500-£1000
High End	Pyrolytic Cleaning Water Dosing Humidity Control / Steam Oven	£1000+

2.2.3: Evolution of the Design

The contemporary oven layout can trace its origins back to the Oberlin stove patented in 1834 and shown in Figure 2.2. This cast iron device ducted the hot exhaust from a wood fire to heat different compartments and hotplates to various temperatures, with the compartments and plates closest to the fire being the hottest. This gave more consistent and convenient cooking than direct heating over a fire, which had been standard practice previously. This was the first cast iron range cooker designed for domestic use that was small and cheap enough to be a commercial success.



Figure 2.2: An Oberlin stove (Credit Sjan McCurry)

With the advent of towns gas in the late 1800's the domestic oven moved from being wood or coal fuelled to gas-fired. The first gas-fired range was patented by Sharps in 1826 in Britain. Gas ranges increased the convenience for the consumer, being able to be turned on and off much more easily and allowing greater degrees of control. Gas stoves saw further improvements in convenience and efficiency in the early part of the 20th century. The enamelled interior was first introduced in 1910, where the inside of the cooking chamber is coated in a thin layer of ceramic which prevents the steel underneath from corroding, as well as being easier to clean. The AGA cooker was patented in 1922, having been developed by the Nobel prize winning chemist Gustaf Delen and providing improvements in consistency and ease of use.

The electrically heated oven was patented in 1882 in Ottawa by Thomas Ahearn, although it took much longer for domestic electricity supplies to be sufficiently widespread for electrical ovens to begin to replace gas ranges. The most common design of electrical oven during the

latter half of the 20th Century was an insulated cooking chamber containing resistive heating elements. Traditionally, British ovens had the elements arrayed down the sides of the cooking chamber while European designs had the elements in the roof and base of the chamber⁴. Buoyancy driven convection currents as well as radiative transfer from the elements and oven walls transferred heat to the food.

In recent years the design in Figure 2.1 has dominated in the domestic oven market. The first patents describing this arrangement were filed in the early 1980s in both the USA and Europe. The forced convection provided by the fan reduced the temperature required compared to natural convection as well as reducing temperature gradients within the oven chamber, leading to more consistent and even cooking.

This development history shows that changes in design of the domestic oven have been driven by consumer preference for more convenient and consistent performance.

2.2.4: Food Types

The consumer expectation of the domestic oven is influenced by the types of food to be cooked. It therefore makes most sense to design an oven that is optimised for the most common food types being prepared. Whilst the dominant domestic oven design has remained essentially unchanged since the 1980s, consumer cooking habits have changed markedly.

In the developed world, people are spending less time cooking. In the USA the mean time spent cooking decreased from 98 minutes per day in 1965 to 55 minutes per day in 2008⁵. In 2016 75% of people spent less than one hour per day cooking food⁶. The food types being prepared are also changing. In the UK the amount of beef consumed per person per week decreased from 215 g/wk to 102 g/wk from 1975 to 2015, while the consumption of vegetables increased by 36% from 2008 to 2017⁷. The value of the chilled ready meal market has increased from £1.01

⁴ C. Scarisbrick, M. Newborough, and S.D. Probert, 'Improving the Thermal Performances of Domestic Electric Ovens', *Applied Energy* 39, no. 4 (1991): 263–300.

⁵ L.P. Smith, S.W. Ng, and B.M. Popkin, 'Trends in US Home Food Preparation and Consumption: Analysis of National Nutrition Surveys and Time Use Studies from 1965-1966 to 2007-2008', *Nutrition Journal* 12, no. 1 (2013): 1–10.

⁶ ReportLinker, 'Insight: American Cooking Habits', 2017.

⁷ ReportLinker, 'Insight: UK Consumer Spending Trending Towards Balanced Diet', 2016.

billion to £1.61 billion over the same time period⁸. Although most ready meals are warmed in a microwave, many still require oven cooking and the trend serves to illustrate the demand for fast and convenient meals at home.

Domestic ovens typically consume around 700 W of power after they have reached setpoint and food has been added to the cooking chamber⁹. Table 2.2 shows several common oven-cooked foods and the cooking time that would be required if this 700 W could be transferred to the food directly, t_{ideal} , compared to how long these foods actually take to cook, t_{actual} . Clearly there is a large discrepancy between this ideal value and practice. This is due to several mechanisms that limit the rate of heat transferring from the element to the food. First, heat must be transferred from the electrical heating element to the air circulating in the oven, and from this circulating air to the surface of the food. The circulating air also convects heat into the oven walls and door, much of which is wasted. There is an additional thermal resistance within the food as heat must be transferred from the surface into the core. This resistance depends on a length scale, L , the mean distance the heat must penetrate, as well as the thermal conductivity of the food, k_{food} .

Table 2.2: Summary of common food type heat capacities and cooking times. Ideal cooking time corresponds to 700 W transferred directly to the food throughout the cooking cycle. All food starts at 4°C and chemical changes and evaporation are ignored. Heat capacities reproduced from Fellows (2009)¹⁰.

Food Type	Approximate mass (kg)	Heat Capacity (Jkg ⁻¹ K ⁻¹)	Final Temp (°C)	t_{ideal} (min)	t_{actual} (min)	$t_{\text{actual}}/t_{\text{ideal}}$
Whole chicken	1.3	3570	75	6.8	90	13.2
Roast joint of beef	2.0	3440	55	7.3	100	13.7
Pasta bake	1.5	3500	100	10.5	60	5.7
Tray of roast vegetables	0.75	3500	100	5.2	45	8.7
Burger / Fishcake	0.5	3440	70	2.3	25	10.9
Pizza	0.4	2800	100	1.7	15	8.8
Cookies	0.4	2800	85	1.8	20	11.1
HIPOR test brick	2.0	4100	60	9.5	60	6.3

The Biot number, Bi , is a ratio of the rate of internal heat transfer by conduction to the external heat transfer to the surface, h_{oven} :

⁸ Statista, 'Spending on Chilled Ready Meals and Main Meal Accompaniments in the United Kingdom', from December 2007 to January 2017 (in Million GBP) Statista Accounts: Access All Statistics', 2017.

⁹ Scarisbrick, Newborough, and Probert, 'Improving the Thermal Performances of Domestic Electric Ovens', 1991.

¹⁰ P.J. Fellows, 'Heat Processing', in *Food Processing Technology (Third Edition)* (Woodhead Publishing, 2009), 339–66.

$$Bi = \frac{h_{\text{oven}}L}{k_{\text{food}}} \quad (2.1)$$

If Bi is large, then heat transfer into the food is limited by internal transfer and increasing the external heat transfer coefficient will have little effect on the cooking time. If Bi is low then the opposite is true and increasing the external heat transfer will have a large effect on cooking time. A conventional electric fan oven gives external heat transfer coefficients of approximately $15 \text{ W m}^{-2} \text{ K}^{-1}$ ¹¹. Comparing this value with the k_{food}/L values in Table 2.3 shows that $Bi < 1$ for all food groups, and $Bi < 0.25$, for pizza, burgers and cookies. This indicates that improving the external heat transfer coefficient of the domestic oven will improve cooking times for all these common food types. Combining the cooking trend data and Table 2.3 shows that the food cooked in ovens is moving from high Bi food types like roast meat, towards low Bi food like fish cakes and pizza for which the impact of increasing the external heat transfer will be greater.

Table 2.3: Summary of approximate surface area (SA) to volume (V) ratios and internal heat transfer parameters for common oven cooked foods.

Food Type	SA/V (m^{-1})	Shape	k_{food} ($\text{W m}^{-1} \text{K}^{-1}$)	k_{food}/L ($\text{W m}^{-2} \text{K}^{-1}$)
Whole Chicken	30	Sphere	0.4 ¹²	12
Roast joint of beef	50	Cylinder	0.4 ¹³	20
Pasta bake	60	Slab	0.6 ¹⁴	36
Tray of roast vegetables	100	Slab	0.5 ¹⁵	60
Burger / Fishcake	175	Slab	0.4 ¹⁶	70
Pizza	200	Slab	0.25 ¹⁷	70
Cookies	400	Slab	0.4 ¹⁸	160
HIPOR test brick	60	Cuboid	0.4	24

¹¹ Carson, Willix, and North, 'Measurements of Heat Transfer Coefficients within Convection Ovens', 2006.

¹² H. Chen, B.P. Marks, and R.Y. Murphy, 'Modeling Coupled Heat and Mass Transfer for Convection Cooking of Chicken Patties', *Journal of Food Engineering* 15, no. 11 (1999): 823–33; V. Sweat, C.G. Haugh, and W.J. Stadelman, 'Thermal Conductivity of Chicken Meat at Temperatures between -75 and 20°C', *Journal of Food Science* 38, no. 1 (1973): 158–60.

¹³ M.S. Baghe-Khandan and M.R. Okos, 'Effect of Cooking on the Thermal Conductivity of Whole and Ground Lean Beef', *Journal of Food Science* 46, no. 5 (September 1981): 1302–5.

¹⁴ M. Mattea, M.J. Urbicain, and E. Rotstein, 'Prediction of Thermal Conductivity of Vegetable Foods by the Effective Medium Theory', *Journal of Food Science* 51, no. 1 (January 1986): 113–15.

¹⁵ Mattea, Urbicain, and Rotstein.

¹⁶ Baghe-Khandan and Okos, 'Effect of Cooking on the Thermal Conductivity of Whole and Ground Lean Beef'.

¹⁷ C. Rask, 'Thermal Properties of Dough and Bakery Products: A Review of Published Data', *Journal of Food Engineering* 9, no. 3 (January 1989): 167–93.

¹⁸ Rask.

The HIPOR test brick is the test load in the European Committee for Electrotechnical Standardization (CENELEC) test for oven efficiency.

In the above discussion it was assumed that cooking only involves heating these items from fridge temperature to a desired final temperature. This is rarely the case: other processes affect food quality and the time taken to reach the desired cooked state. These include chemical changes, browning and evaporation.

2.2.5: Maillard Reactions

The Maillard reaction is a complex set of reactions between reducing sugars and amino acids, first discovered by Louis Maillard in 1916¹⁹. Figure 2.3 shows an overview of the reaction scheme. The first to report such a reaction schematic was Hodge in 1953²⁰. The reaction is primarily dependent on time, temperature, pH and water content in addition to the food's composition²¹. The reaction is often called the “browning reaction” due to the dark brown colour of many of the reaction products. Not only does this give a more visually appealing product but many of reaction products are important to the flavour profile of the cooked food, a selection of which are shown in Table 2.4. Providing the required temperatures and time for these reactions to progress is another reason that the cooking times in Table 2.3 are much longer than the theoretical heating time. The food may be heated to the target temperature but require longer to reach the required level of browning and flavour development.

Controlling these reactions is important to producing appealing food. Too little of the reaction's products will give pale and unappealing food lacking in flavour, while too much of the reaction products or the wrong ratio of reaction products can give “off” tasting food²². This gives additional performance requirements for a new oven design. The new oven must be able to generate the conditions necessary for these reactions at least as well as a standard electric fan oven. For meat and bread a food surface temperature between 100°C and 150°C must be

¹⁹ G.P. Ellis, ‘The Maillard Reaction’, ed. M.L. Wolfrom, vol. 14, *Advances in Carbohydrate Chemistry* (Academic Press, 1959), 63–134.

²⁰ J.E. Hodge, ‘Dehydrated Foods, Chemistry of Browning Reactions in Model Systems’, *Journal of Agricultural and Food Chemistry* 1, no. 15 (October 1953): 928–43.

²¹ J.M. Ames, ‘Control of the Maillard Reaction in Food Systems’, *Trends in Food Science & Technology* 1 (1 July 1990): 150–54.

²² Ames.

achieved²³: below this the rate of the reactions will be too low, while higher temperatures cause the food surface to burn. Surface temperature can be controlled both by the heat flux into the food and the mass flux of water from the food. The oven can increase the heat flux and therefore the surface temperature by increasing h or by increasing the air temperature.

Another way to impact the temperature of the food surface is by controlling the water content of the food. Maintaining a higher water fraction at the food surface will limit the temperature there to closer to the boiling point of water at 100°C, while evaporating more water and reducing the water fraction will do the opposite. This rate of evaporation can be controlled by increasing the mass transfer coefficient, k_c , or by increasing the water content of the oven air and thereby reducing the concentration gradient driving mass transfer. As k_c and h are interrelated²⁴, varying the humidity is a convenient and independent control on the rate of evaporation.

²³ J. Liu, M. Liu, C. He, H. Song, and F. Chen, 'Effect of Thermal Treatment on the Flavor Generation from Maillard Reaction of Xylose and Chicken Peptide', *LWT - Food Science and Technology* 64, no. 1 (November 2015): 316–25; F. Rabeler, J.L. Skytte, and A.H. Feyissa, 'Prediction of Thermal Induced Color Changes of Chicken Breast Meat during Convective Roasting: A Combined Mechanistic and Kinetic Modelling Approach', *Food Control* 104 (October 2019): 42–49; A. Kondjoyan et al., 'Towards Models for the Prediction of Beef Meat Quality during Cooking', *Meat Science* 97, no. 3 (July 2014): 323–31; M. Nakamura, W. Mao, M. Fukuoka, and N. Sakai, 'Analysis of the Color Change in Fish during the Grilling Process', *Food Science and Technology Research* 17, no. 6 (2011): 471–78.

²⁴ T.H. Chilton and A.P. Colburn, 'Mass Transfer (Absorption) Coefficients Prediction from Data on Heat Transfer and Fluid Friction', *Industrial & Engineering Chemistry* 26, no. 11 (November 1934): 1183–87.

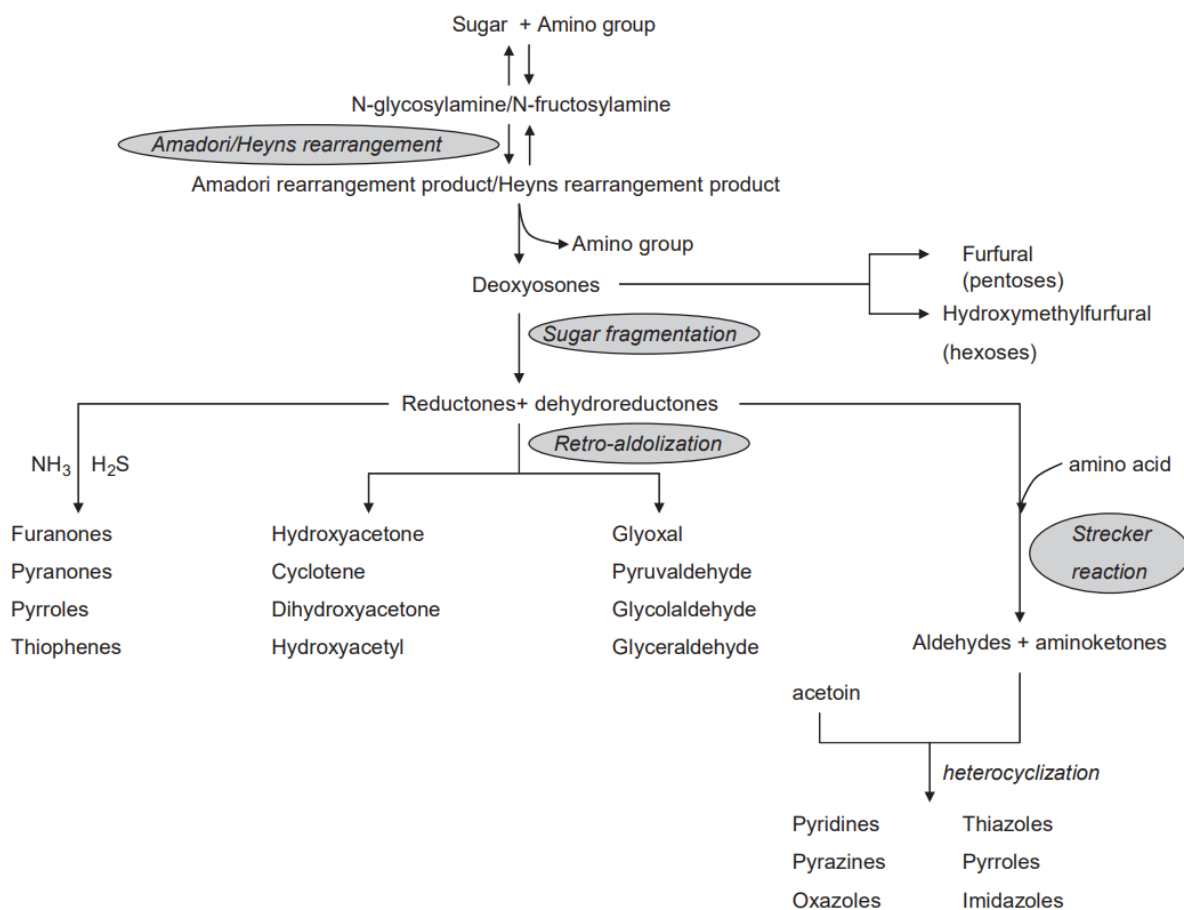


Figure 2.3: General overview of the Maillard reaction showing important flavour compounds as end products. (Reproduced from van Boekel 2006)

Table 2.4: Some classes of flavour compounds from the Maillard reaction that occur in oven cooked foods²⁵

Compound Class	Associated Flavour	Food Examples
Pyrazines	Cooked, roasted, toasted, baked cereals	Heated foods in general
Acylpyridines	Cracker-like	Cereal products
Pyrroles	Cereal-like	Cereals, coffee
Furans, furanones, pyranones	Sweet, burnt, pungent, caramel-like	Heated foods in general
Oxazoles	Green, nutty, sweet	Cocoa, coffee, meat
Thiophenes	Meaty	Heated meat

²⁵ M.A.J.S. van Boekel, 'Formation of Flavour Compounds in the Maillard Reaction', *Biotechnology Advances* 24, no. 2 (March 2006): 230–33.

This analysis of the electric fan oven suggests a list of constraints that consumer will expect any new design to meet, as well as giving insight into areas that the oven can improve over contemporary designs.

- i) Consumer cooking habits have shifted to faster cooking and smaller food items. Domestic oven design has not evolved to meet this change in consumer demand. A novel design that targets this aspect will therefore have an advantage. In addition, the change to food that cooks in a shorter amount of time indicates that there is demand for more convenient and less time-consuming cooking methods.
- ii) Consumers will expect a new design to be as easy, or easier, to use than a traditional one. The design must therefore work with no oversight, with one setting inputted at the start of the cooking process and produce high-quality food.
- iii) The oven must give consistent cooking results across different forms of cookware and within the range of normal use. For example, orienting the food in different ways should not give very different results.
- iv) Conversations with manufacturers have also given some aesthetic constraints.
 - a) The interior of the oven must be black enamelled. This is due to consumer requirements of being both easy to clean and not appearing dirty. Black enamelling has a high emissivity (≈ 0.9) which makes the oven walls absorb and emit infra-red radiation very readily. This will likely reduce efficiency as it will increase the amount of heat absorbed by the walls from the chamber air compared to a low emissivity finish.
 - b) The oven must have a windowed door. This will also reduce efficiency as a glazed door has a higher heat transfer coefficient across it than an equivalent thickness of ceramic wool insulation.

2.2.6: Physical and Manufacturing Constraints

In addition to constraints and parameters derived from consumer usage and expectations, there are a number of constraints related to manufacturing and installing the oven.

- i) The power supply to the oven must be the same as a standard built in oven, 230 V and either 16 or 13 A single phase AC, depending on the availability of a dedicated socket. This gives a total maximum power draw of 3700 or 3000 W, respectively.

- ii) A majority of ovens are delivered with multiyear warranties. Any design must be robust and reliable, and not require any in-situ recalibration or maintenance. One manufacturer stated that the appliance is expected to last 12 years with no repair or servicing.
- iii) Domestic appliance prices are extremely competitive and the oven must be as cheap to build as possible. Manufacturers have stated that any increase in manufacturing cost results a $6\times$ greater increase in sale price. To be competitive the oven must sell for less than £800 and therefore must be able to be produced for less than £135.

2.3: Existing Technologies

An obvious parallel line of development in oven technology is the design of ovens for non-domestic applications. One of these is the tunnel oven, used to cook food on an industrial scale.

Figure 2.4 shows the standard design of an industrial tunnel oven. A typical oven may bake between 1000 and 3000 loaves of bread per hour²⁶. Cooking times in industrial ovens are much shorter than in domestic ovens due to much higher heat fluxes. 7000 Wm^{-2} is regularly achieved²⁷, compared to 1000 Wm^{-2} in domestic ovens²⁸. This high heat flux is achieved through all three heat transfer modes. Examining technologies relating to all three transfer modes was therefore a promising avenue for maximising both the efficiency and speed of the oven, as well as control over the cooking process.

²⁶ Z. Khatir, 'Computational Fluid Dynamics (CFD) Investigation of Air Flow and Temperature Distribution in a Small Scale Bread-Baking Oven', *Applied Energy*, 2012, 8.

²⁷ O.D. Baik, S. Grabowski, M. Trigui, M. Marcotte, and F. Castaigne, 'Heat Transfer Coefficients on Cakes Baked in a Tunnel Type Industrial Oven', *Journal of Food Science* 64, no. 4 (1999): 688–94.

²⁸ Carson, Willix, and North, 'Measurements of Heat Transfer Coefficients within Convection Ovens', 2006.

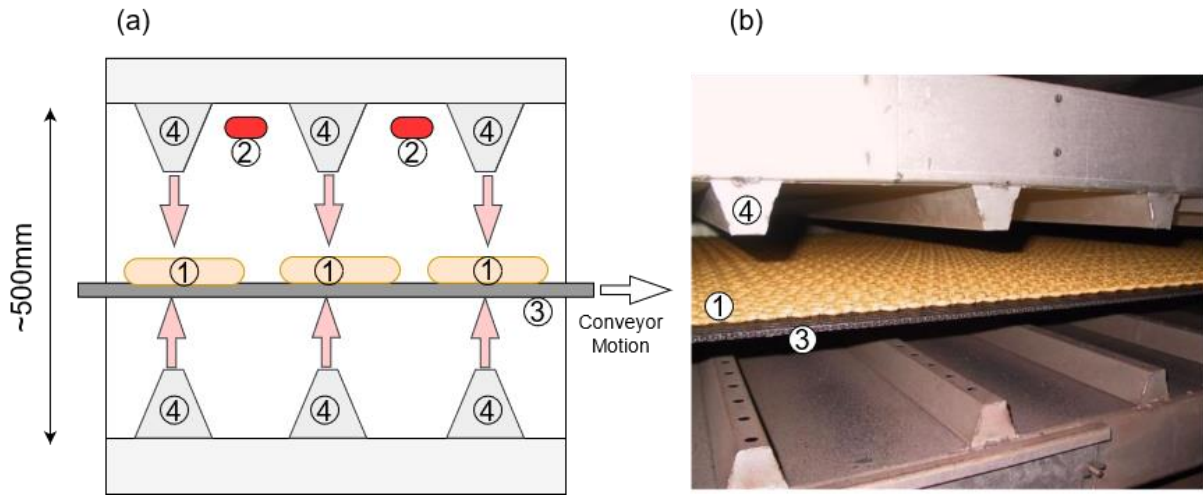


Figure 2.4: Features of industrial tunnel ovens. (a) Schematic of one section of the oven. (b) Photograph, side view. 1 – Food being cooked, 2 – infra-red lamps, 3 – conveyor, 4 – hot air impingement jets.

2.3.1: Convection

Convective heat transfer is the result of bulk movement of fluid molecules. In an oven convection arises when air moves, gains energy from a heat source, travels through the chamber to the food before transferring a portion of that thermal energy to the food as a result of a difference in temperature. In an oven both natural and forced convection can occur. Natural convection occurs due to heated air having a lower density than unheated air, resulting in a buoyancy-driven flow of air around the chamber. Forced convection results from a fan or blower driving a flow around the cooking chamber, carrying heat with it. The rate of heat transfer from the air to the food per unit of surface area in both cases is given by:

$$q_{\text{conv}} = h (T_{\text{air}} - T_{\text{surface}}) \quad (2.2)$$

where q_{conv} is the convective heat flux, h is the film heat transfer coefficient and T_{air} and T_{surface} are the temperatures of the air and food surface, respectively.

Analytical or theoretical results for the heat transfer coefficient, h , are not available for the turbulent flow patterns found in domestic ovens and h is estimated using empirical correlations,

numerical methods, or a combination of the two. A commonly used correlation²⁹ for calculating h for forced convection is:

$$Nu = \frac{h L}{k} = 0.0266 Re^{0.805} Pr^{0.333} \quad (2.3)$$

where:

$$Re = \frac{\rho v L}{\mu} \quad (2.4)$$

$$Pr = \frac{C_p \mu}{k} \quad (2.5)$$

where Nu is the Nusselt number, k is the thermal conductivity, Re is the Reynolds number, Pr is the Prandtl number, ρ is the density, v is the flow velocity, μ is the viscosity and C_p is the specific heat capacity.

Expanding equation 2.3 shows that h depends on the flow velocity raised to 0.805, as well as physical properties and a length scale. Increasing the flow velocity is therefore one route for increasing the heat transfer coefficient. Applying equation 2.3 with a typical flow velocity within domestic ovens ($v = 0.5 \text{ m s}^{-1}$) gives a heat transfer coefficient between the air and food of $15 \text{ W m}^{-2} \text{ K}^{-1}$, in agreement with measured values in literature³⁰.

An additional consideration if altering the heat transfer coefficient from the air to the food is that this will also alter the mass transfer coefficient, k_c between the two bodies, altering the mass flux of water, \dot{m} , from the food:

$$\dot{m} = \frac{M_w P}{RT} k_c \ln \left(\frac{P - P_{w \text{ air}}}{P - P_{w \text{ surface}}} \right) \quad (2.6)$$

²⁹ E. Obuz, T.H. Powell, and M.E. Dikeman, 'Simulation of Cooking Cylindrical Beef Roasts', *LWT - Food Science and Technology* 35, no. 8 (December 2002): 637–44.

³⁰ Carson, Willix, and North, 'Measurements of Heat Transfer Coefficients within Convection Ovens', 2006.

where M_w is then molecular weight, R is the gas constant, T is the air temperature, P is the total pressure of the system and $P_{w\text{ air}}$ and $P_{w\text{ surface}}$ are the partial pressure of water in the oven air and at the food surface, respectively³¹.

This is important in cooking as evaporation and the water content of the food throughout the cooking process affects the food quality, both in how moist the food is as well as its flavour, as previously discussed. Controlling the value of $P_{w\text{ air}}$ will control the concentration gradient driving evaporation and therefore \dot{m} . Over time this determines the water content of the food.

Impinging Jets

Impinging jets are an established technology in the food industry. They consist of a pressurised header of hot air that blows the heated air down onto the top of food pieces. The three arrangements in common use are shown in Figure 2.4(b) and Figure 2.5.

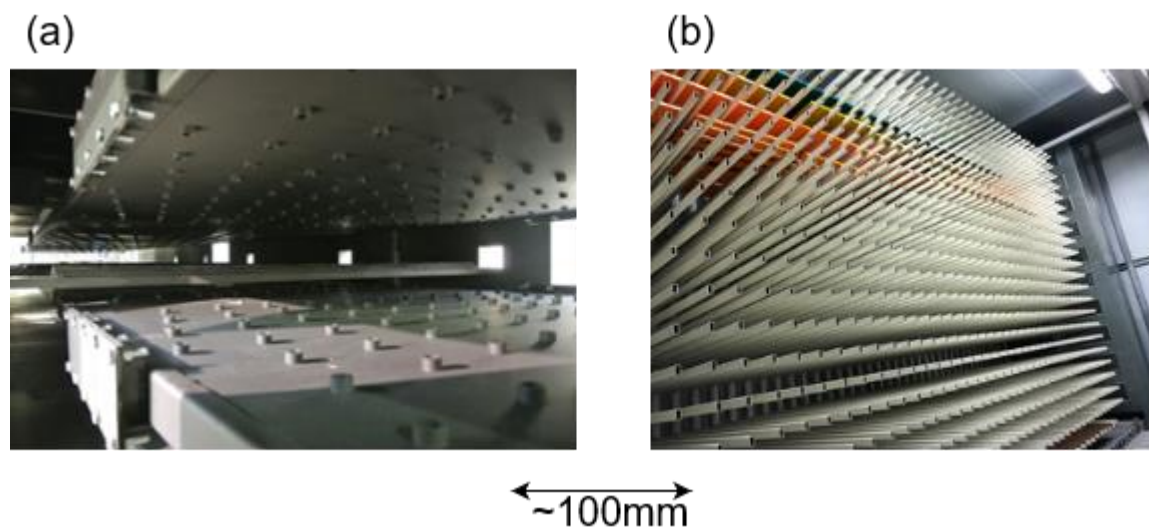


Figure 2.5: Common impingement jet configurations in industrial ovens. (a) Swaged plate, (b) high velocity piped jets.

Empirical relationships for estimating the heat transfer coefficient from the air to the food in an impingement jet system have been reported by Martin³², depending on Re , Pr , as well as the

³¹ B. Hallström, 'Mass Transport of Water in Foods — A Consideration of the Engineering Aspects', *Journal of Food Engineering* 12, no. 1 (January 1990): 45–52.

³² H. Martin, 'Heat and Mass Transfer between Impinging Gas Jets and Solid Surfaces', ed. J.P. Hartnett and T.F. Irvine, vol. 13, *Advances in Heat Transfer* (Elsevier, 1977), 1–60.

distance between the nozzle and the food, H_n , the diameter of the nozzle, D_n and f_n , the relative area of the nozzles compared to that of the target.

$$Nu = F(Re) G(H_n, D_n, f_n) K(H_n, D_n, f_n) Pr^{0.42} \quad (2.7)$$

where:

$$F = 2 Re^{0.5} (1 + 0.005 Re^{0.55})^{0.5} \quad (2.8)$$

$$G = 2 \sqrt{f_n} \frac{1 - 2.2\sqrt{f_n}}{1 + 0.2 \left(\frac{H_n}{D_n} - 6 \right) \sqrt{f_n}} \quad (2.9)$$

$$K = \left(\frac{H_n/D_n}{0.6/\sqrt{f_n}} \right)^{-0.3} \quad (2.10)$$

Although more complex than equation 2.3, equation 2.7 also shows that the heat transfer coefficient increases with flow velocity. The geometry terms now depend on several length scales. One dependency is on the ratio of the distance between the jet and the food and the nozzle diameter, H_n/D_n ; bringing the food closer to the jets increases the heat transfer coefficient. A shorter distance between the nozzle and the food reduces the mixing between the jet and the ambient air, giving a greater impact velocity and a higher impact temperature for the jet, both of which increase the heat flux into the food. The second geometrical parameter, f_n , is the ratio of the area of the flow of the jets to the total area of the food. Increasing the density of jets while keeping all other parameters constant gives a higher average heat transfer coefficient.

Where very high heat transfer rates are desired, piped jets (Figure 2.5(b)) are used: heat transfer coefficients of $225 \text{ Wm}^{-2}\text{K}^{-1}$ are achievable with this arrangement. The nozzle of the pipe is positioned close to the food surface to minimise H_n/D_n , while the spaces between the nozzles allow spent air to dissipate into the oven, minimising back pressure and allowing a high value of f_n to be possible. This design is often paired with high jet velocities.

In the header arrangement in Figure 2.4(b), the gaps between the headers gives space for spent cooking air to be exhausted and in some cases provides a location where radiative heating elements can be situated. The swaged plate in 2.5(a) is the simplest design. Cooking air is ducted into a chamber above the cooking chamber and flows through the holes in the plate onto the top of the food. This technology is used in both industrial baking ovens as well as in high-speed catering ovens such as the Turbochef®. Impingement jets are often installed in both the roof and the floor of industrial tunnel ovens (e.g. Figure 2.5(b)) to cook both the top and bottom of the food.

An advantage of impinging air systems is that the velocity of the air is higher when the jet impacts the food than the circulation flow path in the rest of the oven. This means the heat transfer coefficient to the food is larger than that to the oven fittings, allowing more energy to be transferred to the food without increasing the amount of energy lost to the walls of the oven.

Forced Convection

As discussed in section 2.2.1, modern domestic ovens utilise a fan in the back of the oven to induce air currents stronger than would occur by natural convection, approximately 0.5 m s^{-1} , giving $h = 15 \text{ Wm}^{-2}\text{K}^{-1}$ ³³. In commercial ovens used for cooking large amounts of meals, for example in restaurants, schools and hospitals, a similar design is implemented. In this case, however, multiple fans with much greater power than in a domestic setting are used. This gives higher velocities within the oven chamber and commensurably higher heat transfer coefficients of approximately $30 \text{ Wm}^{-2}\text{K}^{-1}$ which corresponds to an air velocity of 1 m s^{-1} . More complicated ducting of the air is also employed to ensure even cooking across multiple trays of food. Air from the fan is ducted through the side walls of the oven before flowing through holes in the walls of the cooking chamber and returning to the eye of the circulation fan, as shown in Figure 2.6(b). It is important to note that by increasing the velocity of air in this way the heat transfer coefficient from the air to the oven walls and fittings is also increased.

³³ Carson, Willix, and North, 'Measurements of Heat Transfer Coefficients within Convection Ovens', 2006.

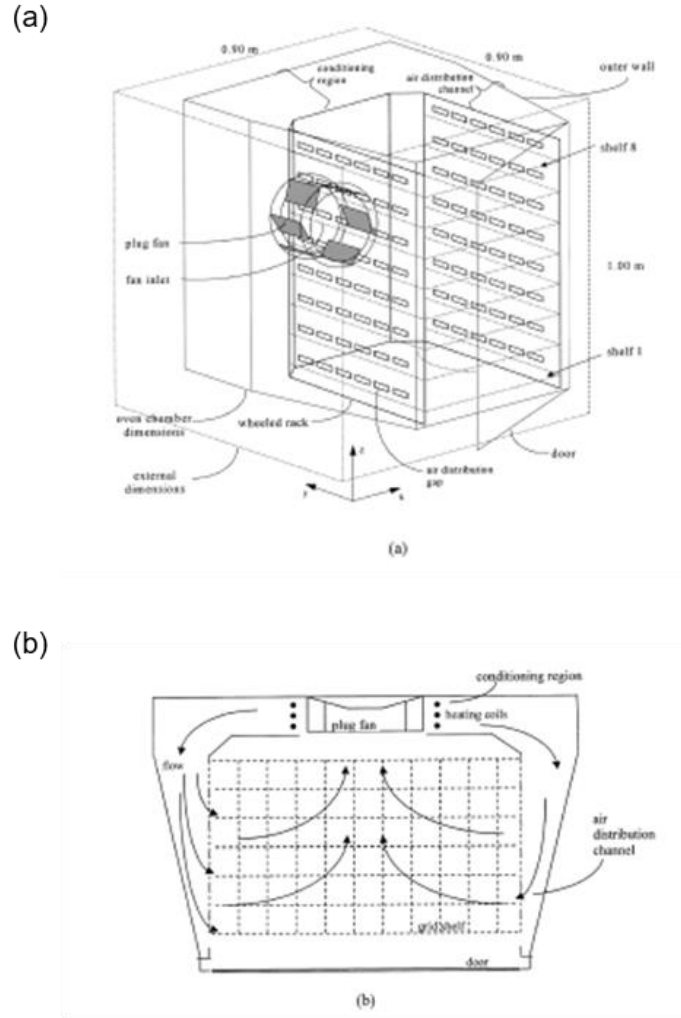


Figure 2.6: Geometry of a typical catering oven design, (a) 3D view, b) plan view at fan plane. Reproduced from Verboven *et al.*, 2000³⁴.

2.3.2: Conduction

Conducting heat directly from a heating element to the food is the most energy efficient cooking method: efficiencies of 80% are achievable for stovetop cooking³⁵. This is due to the arrangement of elements preferentially transferring heat to the food rather than to the surroundings. Consider the top surface of a hot pan upon which food is cooking, the efficiency of the system, η , is given by the ratio of heat usefully transferred to the food, Q_{food} , versus the heat that is wasted and convected to the surroundings, $Q_{\text{surroundings}}$:

³⁴ P. Verboven, N. Scheerlinck, J.D. Baerdemaeker, and B.M. Nicola, 'Computational Fluid Dynamics Modelling and Validation of the Isothermal Air Flow in a Forced Convection Oven', *Journal of Food Engineering*, 2000, 13.

³⁵ L. Koller and B. Novák, 'Improving the Energy Efficiency of Induction Cooking', *Electrical Engineering* 91, no. 3 (November 2009): 153–60.

$$\eta = \frac{Q_{\text{food}}}{Q_{\text{food}} + Q_{\text{surroundings}}} \quad (2.11)$$

These rates of heat transfer are dependent on three terms: the heat transfer coefficient, the contact area over which heat transfer occurs and the temperature driving force. Considering these three terms shows why cooking by conduction can achieve such high efficiencies. The convective heat transfer from the top surface of the pan to the surroundings will be relatively low, even within a forced convection oven, with h of the order of $30 \text{ Wm}^{-2}\text{K}^{-1}$. Conductive heat transfer coefficients between cooking surfaces and food are greater³⁶, typically over $200 \text{ Wm}^{-2}\text{K}^{-1}$, and as high as $800 \text{ Wm}^{-2}\text{K}^{-1}$. Within an oven the food surface temperature will be lower than the air temperature, giving an additional temperature driving force to transfer heat to the food rather than the surroundings. Combining these with a similar transfer area means the pan transfers a higher proportion of its energy to the food than to the surroundings, leading to the high measured efficiency.

In industrial ovens conduction is achieved using preheated containers or conveyors. These remain within the oven and food is continuously added to them, as shown in Figure 2.7. This arrangement is possible as these ovens run continuously so the time to heat up the conveyor or containers via convection is not of concern when the oven is only restarted daily or weekly. In a domestic oven that must start from ambient for every cooking event a more direct heating method will be required.

³⁶ Z. Pan and R.P. Singh, 'Heating Surface Temperature and Contact-Heat Transfer Coefficient of a Clam-Shell Grill', *LWT - Food Science and Technology* 35, no. 4 (June 2002): 348–54.

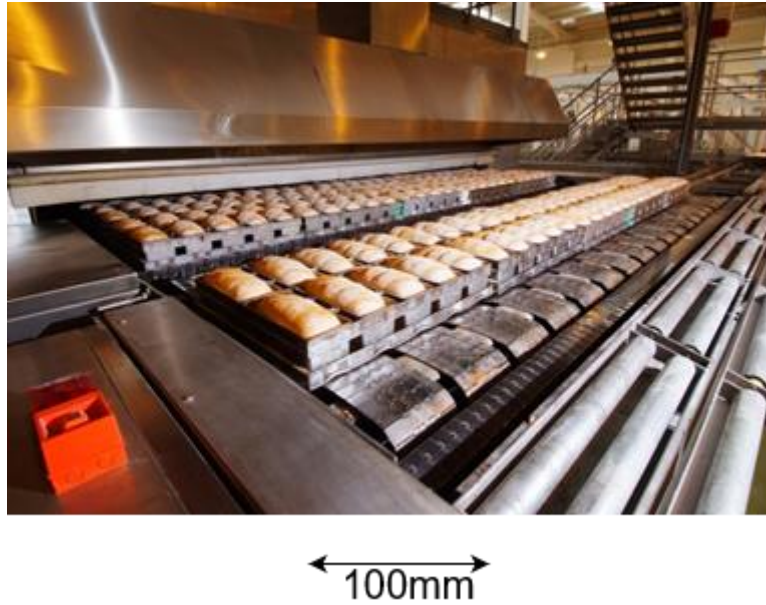


Figure 2.7: Industrial bread baking oven, showing the preheated metal containers in which the bread is baked.

Inductive Cooking

Amongst domestic cooking tops, induction has been shown to be the most efficient³⁷, compared to gas burners and electrical resistive heaters. Induction hobs contain a large copper coil through which a high frequency alternating current is passed. This induces eddy currents in the cookware above, the dissipation of which heats the cookware. The advantage of this transfer method is that only the cookware is heated, reducing the fraction of heat convecting or conducting away from the food as well as allowing very fast temperature changes in the cookware. Figure 2.8 shows the typical arrangement of components within an induction cooker. The zero volts switching (ZVS) is a highly efficient circuit used to generate the high frequency and high current signal required in the coil.

³⁷ Koller and Novák, 'Improving the Energy Efficiency of Induction Cooking'.

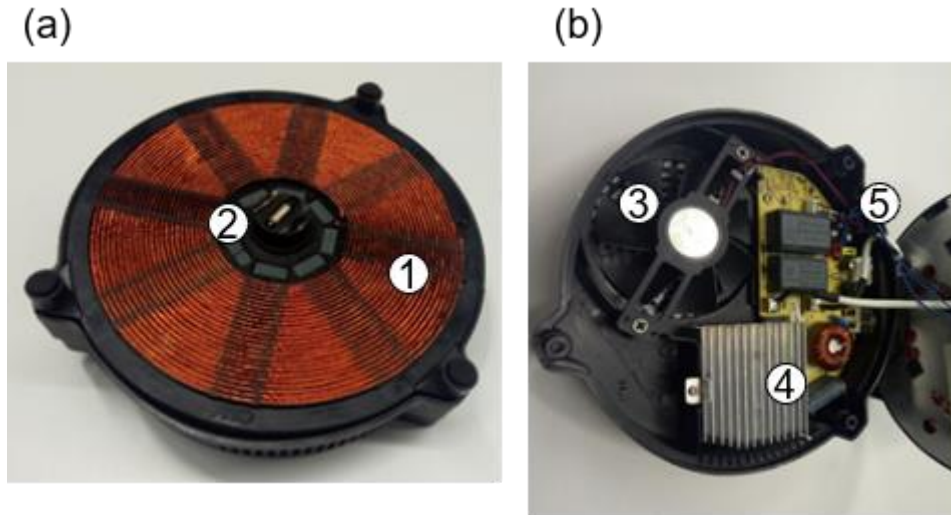


Figure 2.8: (a) Typical enclosed induction heating unit. (b) Internal view of the device.
 1 – Copper coil, 2 – high temperature trip, 3 – cooling fan, 4 – heat sink for transistors,
 5 – control electronics and ZVS circuit.

2.3.3: Radiation

Food will exchange heat with the walls of the oven by radiative heat transfer. The rate changes as both bodies heat up over the course of a cooking cycle, even one using a convective cooking mode. Radiative heat transfer can also be promoted by a number of other means, with the effects on the food depending on the distribution of wavelength used.

The convective heat flux in an oven operating at 180°C will more than halve as the temperature of the food surface rises from 4°C (standard fridge temperature) to 100°C, after which evaporation of water may limit further temperature rise. In comparison, the radiative flux, q_{rad} , will change very little:

$$q_{\text{rad}} = K_{\text{R}}(T_{\text{element}}^4 - T_{\text{surface}}^4) \quad (2.12)$$

where T_{element} is the temperature of the heater element and K_{R} is a constant depending on the geometry of the system and the emissivity of the surfaces.

For a rise in T_{surface} from 4°C to 100°C, q_{rad} will decrease by only 1% for an element operating at 800°C and by 0.002% for an element operating at 2500°C. Infra-red radiative heat transfer can

therefore be advantageous for maintaining high heat fluxes into food after the surface has warmed.

Infra-red radiation, with a peak wavelength (λ_{peak}) of approximately $3\text{ }\mu\text{m}$ is used to transfer heat in the grill of a domestic oven. This gives a short penetration depth into the food and a high surface temperature. Near infra-red, with a peak wavelength of approximately $1\text{ }\mu\text{m}$, can be generated using lamps with elements operating at higher temperatures, approximately 3000 K. This high element temperature necessitates the element being enclosed in a quartz tube to prevent the element material burning. The shorter wavelength penetrates an order of magnitude further into the food, as summarised in Table 2.5.

This greater penetration has a large impact on how the infra-red cooks the food. For a constant radiative flux through the food surface, a greater penetration depth will spread the energy absorbed by the food over a larger volume. This reduces the surface temperature giving less surface browning by giving less favourable conditions and less activation energy for Maillard reactions to proceed. However, short wavelength cooking can also give uneven results. In areas that absorb more thermal radiation, either due to a higher local emissivity or a shorter distance to the heating element, Maillard reactions will occur more rapidly. This in turn will darken the surface of the food in these areas further increasing their emissivity and ability to absorb thermal radiation, creating a feedback loop.

Table 2.5: Measured penetration depths into food from infra-red radiation emitted by heater elements at 2500 K and 1000 K³⁸

Filament Temperature (K)	λ_{peak} (μm)	Penetration Depth (mm)		
		Potato	Pork	White Bread
2500	1.16	4.8	2.38	6.25
1000	2.90	0.33	0.28	1.52

Food can also be cooked using other types of electromagnetic (EM) radiation. Domestic microwave appliances use radiation at 2.45 GHz to cook food. The EM waves are generated by a magnetron which emits into the chamber. The all-metal interior wall reflects waves back into the

³⁸ Dagerskog and Osterström, 'Infra-Red Radiation for Food Processing I. A Study of the Fundamental Properties of Infra-Red Radiation', *Lebensmittel - Wissenschaft + Technologie. Food Science + Technology* 12, no. 4 (1979): 237–42.

interior, allowing only the food to absorb them. 2.45 GHz is strongly absorbed by the water present, penetrating around 1 cm into the food. Microwaves cook food very quickly and efficiently but the low ambient temperatures within the cooking chamber reduce the surface temperature of the food, inhibiting Maillard reactions and crisping³⁹. Additionally, microwave cooking gives less desirable structure in many baking applications⁴⁰. Recently, microwave ovens have been combined with convection oven features to overcome these issues.

2.4: Design Process and Iterations

This section discusses the design philosophies for each of the three prototype ovens constructed during this project and the technologies applied. Specifics of the oven construction, detailed design and control information are given in chapter 4.

2.4.1: Prototype IA

Prototype IA was designed and built in eight weeks so that it could be exhibited at the 2017 Internationale Funkausstellung (IFA) trade fair in Berlin. Due to the limited time scale, speed and ease of construction were additional constraints to those discussed in section 2.2.6. To this end a domestic oven was modified instead of a new unit constructed, and as many parts as possible were retained.

Technology Selection

To maximise convection, impinging jets were used. These were chosen over the catering oven style convection (Figure 2.6) for the following reasons;

- i) The convective heat transfer coefficient achievable using jets is higher than that using circulating air, meaning that food will cook more quickly and potentially at a lower air temperature, reducing energy consumption. Additionally, as the food will be under the jets it will have a higher heat transfer coefficient to it from the air than from the air to the walls or oven door, meaning the air will preferentially heat the food over the body of the

³⁹ G. Sumnu, 'A Review on Microwave Baking of Foods', *International Journal of Food Science & Technology* 36, no. 2 (February 2001): 117–27.

⁴⁰ G. Sumnu, S. Sahin, and M. Sevimli, 'Microwave, Infrared and Infrared-Microwave Combination Baking of Cakes', *Journal of Food Engineering*, 2005, 6.

oven, again increasing efficiency. This contrasts with the catering oven configuration where the air velocity is highest when flowing close to the walls of the oven, giving the reverse effect. The catering oven arrangement gives the most even cooking in an oven filled with multiple trays of food, but this is not common in domestic ovens which are usually cooking one food type at a time.

- ii) The catering oven arrangement requires large amounts of space between the cooking chamber and outer wall of the oven for the air to flow from the fan. Incorporating this into a domestic oven would greatly reduce the cooking volume, violating one of the consumer constraints. In comparison, impingement jets can be built into an existing dead space above the cooking chamber, reducing the impact on cooking volume. Additionally, the second layer of metal between the outer wall of the exterior and the cooking chamber would add a significant thermal mass to the oven, increasing the heat up time. This is not a major concern in a catering environment where the oven will run for many hours, but is important in a domestic setting where cooking times are shorter.

The type of impingement system chosen was the header arrangement shown in Figure 2.4(b). Although the impingement pipes shown in Figure 2.5(b) give the highest heat transfer coefficient and therefore the highest potential efficiency, they are impractical for a domestic oven. Firstly, they intrude into the cooking chamber and would reduce the usable volume. Secondly, they are designed to be positioned close to the food, which is impractical in a domestic oven expected to cook food items of varying shape and sizes.

The header arrangement was preferred to the swaged plate (Figure 2.5(a)) initially as it allowed space between the headers to be used for infra-red lamps and reduced the amount of metal work in the roof of the oven, reducing the thermal mass of the oven. The increased pressure required for impinging jets was generated by replacing the existing 20 W motor with a 225 W model.

Infra-red lamps with an element temperature of 3000 K were chosen for the radiative component of cooking. This component and segment of the EM spectrum was deemed to best fulfil the needs of the oven.

The grill elements used in a standard domestic oven were not used since they typically require 2-3 minutes to reach operating temperature, limiting their use in a cooking cycle combining all three heat transfer modes. Microwaves were not employed as including microwaves in

convection ovens is an existing technology which has had limited success and impact. Microwaves are unable to generate sufficiently high temperatures in the food for Maillard reactions to occur⁴¹, a key driver in food quality. Microwaves have also been shown to give poor crumb structure in baking. 3000 K elements were chosen over 800 K elements due to the greater penetration depth into food. As discussed above, one advantage of cooking food radiatively over convectively is that the flux is not diminished as the food heats up. A shorter wavelength lamp can be used for longer at the end of the cooking cycle before giving a burnt food surface and can therefore take greater advantage of this effect.

Finally, heat was conducted into the food through a steel plate heated by a resistive element. The design was chosen primarily due to time constraints. An induction system would have been preferred due to its increased efficiency and rapid temperature and power changes. However, this would have been more difficult to accommodate spatially in the oven, as the electronics unit must be kept cool whilst sufficiently close to the oven chamber to heat the cookware and food. Additionally, inductive units are typically self-contained with some form of serial control required to link them to the central oven controller. Designing and testing the software for this purpose was deemed too time consuming with a high risk of failure at the 2017 event.

The humidity of the air circulating in the oven was measured by a proprietary COI sensor and steam could be supplied to the cooking chamber from an external steam generator.

Summary

A layout of prototype IA including the above-mentioned technologies, is shown in Figure 2.9. Three rows of fifteen jets blew heated air down onto the food surface. Two short wavelength infra-red lamps were located between these headers. The base heater was a self-contained unit in the bottom of the oven.

⁴¹ S. Geedipalli, A.K. Datta, and V. Rakesh, 'Heat Transfer in a Combination Microwave–Jet Impingement Oven', *Food and Bioproducts Processing* 86, no. 1 (March 2008): 53–63.

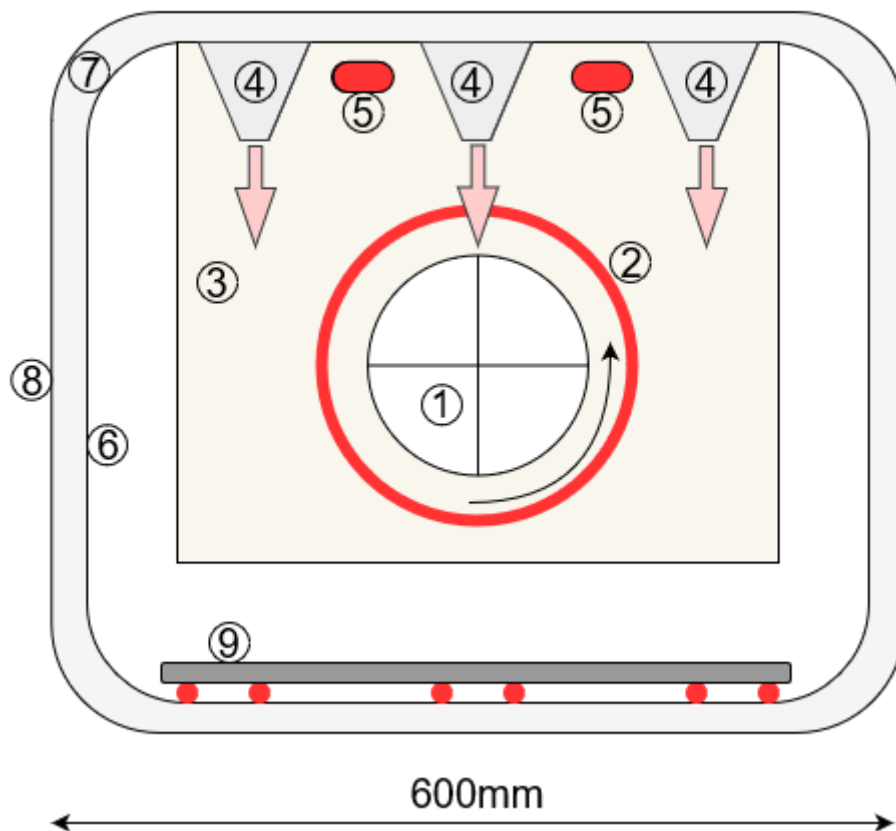


Figure 2.9: Design of prototype IA, schematic elevation looking into the front of the oven.
 1 -Convection fan (run at a higher speed than in a standard design). 2 - Spiral air heater around the fan. 3 - Back panel, 4 - Impingement air jets blowing hot air onto the food.
 5 – Infra-red lamps. 6 - Stamped, enamelled steel forming the oven chamber.
 7 – Ceramic wool insulation around the oven chamber. 8 – Outer skin of the oven,
 9 - Steel plate directly heated by a resistive element below.

The oven was controlled using three setpoints; (i) the air temperature within the cavity, (ii) the temperature of the base heater, and (iii) a duty cycle for the infra-red lamps. All set points had to be set manually.

2.4.2: Prototype IB

Despite being able to cook some food types very quickly, prototype IA was not a viable design as it had a very long heat up time, taking 40 minutes to reach a point at which food could be cooked. This resulted in poor convenience for the consumer as well as a low energy efficiency as the heaters were run for a long time during which no food was cooked. Further modifications aimed to eliminate the heat up time of the oven entirely and allow it to cook consistently from a

cold start. This involved reducing the thermal mass of the oven and by making the transfer of heat from the elements to food as direct as possible, meaning the oven could cook food without it attaining thermal steady state.

Air Heater Modifications

In prototype IA, the layout of the air heating system resulted in a long heat-up time for the air jets. Air from the oven cavity was drawn into the fan and discharged over a spiral heater wrapped around the impeller, generating hot, high velocity air. This air was then directed into the three rows of nozzles in the roof of the oven and blown down onto the food surface. This design presented a problem as the air was hottest and at its highest velocity (and therefore the highest heating potential) as it left the fan. As it passed to the nozzles it heated the oven back and the metal ductwork around the nozzles. This meant that the metal ductwork and oven back had to reach steady state for the air jets to reach their set point, wasting energy and increasing the heat-up time significantly.

The solution identified was to heat the air as close to the food as possible, so it did not transfer energy to the walls or ductwork before it contacted the food. The original air heater was removed and replaced with three custom heaters, designed by COI, which sat inside the jet nozzles. These heated the air immediately before it passed through the nozzles, and onto the food. The heaters were made from laser cut mica with kanthal ribbon wrapped around it, described in detail in section 4.2.1.

Inductive Base Heater

The original bottom heater had a number of problems and was replaced by an inductive heating system, as follows:

- i) The heated surface on which the food was cooked was a solid piece of steel. This meant any steam evolved from the base of the food could not escape, potentially resulting in a soggy base. Also, it was not possible to change the base piece if a different cooking utensil was required. The replacement aluminium plate had holes drilled in it to allow steam to escape. Any ferromagnetic utensil could be used in the oven without modification.

- ii) The power draw of the resistive heater was too high to be run simultaneously with the air heater, meaning that “on” time was split between the two, further increasing the heat-up time. In an induction system, the power transferred to the pan from the coil was dependent on their separation, as this determines the inductive coupling between them. By setting the separation it was possible to limit the maximum power draw so that the base heater and air heater could be run simultaneously.
- iii) The original heater weighed over 7 kg, most of which was steel, which gave a thermal mass of approximately 3500 JK^{-1} , meaning that it required 700 kJ to reach its set point of 220°C from a starting temperature of 20°C . With a heater power of 1.4 kW, a heat up time of 500 s was required. This is not an improvement on the heat up time of an unmodified oven. The replacement aluminium plate had a mass of 1.5 kg, a thermal mass of 1360 JK^{-1} and a heat up time of 195 s, representing a significant reduction in heat up time over a traditional design. Additionally, the induction heater device was located outside the oven chamber so was not heated above ambient.

Control and Cooking Sequence

Typically, domestic ovens are connected to a 230 V and 16 or 13 A electrical supply, which gives a maximum power draw of 3700 or 3000 W, respectively. When cooking using the convection oven mode, an unmodified oven will draw 2000 W during the preheat stage and draw an average of 700 W once this is complete and food has been added to the oven. This control scheme is undesirable for three reasons:

- i) The preheat takes ten minutes during which no food can be cooked, wasting energy and increasing the time taken to prepare food. It is also inconvenient for the consumer.
- ii) The oven metalwork and insulation must be heated to steady state before food can be cooked, wasting energy.
- iii) The oven uses a maximum of 53% of the total available power as it cannot transfer energy to the food any quicker.

These issues were also present in prototype IA as only one of the heaters could be active at a time. This meant that before cooking could commence the air heater had to heat the circulating air and metal frame of the oven to setpoint. Only after this was the base heater able to begin heating the baseplate ready for cooking.

Prototype IB aimed to cook food as quickly as possible, both for consumer convenience and also so that food could be cooked before the fabric of the oven reached steady state, thereby saving energy. Balancing the power draw of the radiative, convective and conductive heating elements would allow the oven to draw the full 3700 W available to cook the food quickly. The air heater power was maintained at 2400 W using the original resistive element, giving 1300 W available for the conductive element. The power of the lamps was also set to 2400 W as radiative and convection elements are unlikely to be required in parallel, with convection being more effective at the beginning of the cooking cycle and radiation being more effective at the end. This is because the food surface temperature is limited to the air temperature when cooking using convection while radiative cooking is able to achieve higher food surface temperatures.

Steam Generation

The humidity control in prototype IA was not optimal. The steam generator had to be manually powered on and off, making control at a given set point very difficult. The steam generator also required a separate 240 V and 13 A power supply which would not be viable in a commercial implementation.

Prototype IB replaced the external generator with a tank and pump that when activated, dripped water onto the circulation fan. The spinning fan atomised the water which would evaporate and increase the humidity within the cooking chamber. The humidity sensor and pump were connected to the oven controller. A feedback control loop could then regulate the humidity in the oven.

2.4.3: Prototype II

A second prototype oven was constructed that aimed to improve on prototype I in three ways, maintaining the philosophy of minimising heat up time and maximising the heat transfer coefficient into the food. The design features were:

- i) Incorporate the replacement air heaters described in section 2.4.2 from the beginning of the design process.
- ii) Incorporate induction heating for the base heater from the start. This includes making the induction unit and cooling solution fit within the standard oven footprint and

integrating the induction heater into the oven control system, rather than a separate manual control panel.

- iii) Aim for a more production-ready design that is easier to manufacture and easier for a consumer to use.

Convection System

Figure 2.10 shows a schematic diagram of prototype II. The convection system was arranged in a similar way to in prototype I. The fan in the back of the oven drives the convection mode. Air was drawn in through a grill at the bottom of the base of the oven into the eye of the fan. From the fan it was ducted into the “heater box” positioned in the roof of the oven. Positive pressure drove the air through three mica heaters identical to those described in section 2.4.2. The base of the mica heaters contained the jet nozzles which directed the heated air onto the food surface.

A new inlet was designed to accomplish two things: (i) to include a grease catching mesh to prevent atomized fat arising from cooked food reaching the heating systems, and (ii) the air outlet from the cooking chamber was moved to the base of the oven rather than the middle. The CFD model of prototype I showed that the negative pressure of the fan inlet drew some of the impinging air directly into the fan, rather than allowing it to impact the food. By moving the inlet to the base of the oven this effect was reduced.

The change in heater housing from three separate metal structures to a single box aimed to simplify construction by reducing the number of welds and folds required. Additionally, the box was designed to fit in the recessed portion of the oven roof, increasing the usable cooking volume of the oven. The box section was also more easily removed compared to the metal work in prototype I, enabling easier maintenance and potential for further modifications.

To accommodate the new box section the infra-red lamps were moved to the sides of the oven roof. They were angled so that the centre of the beam was directed to the centre of the cooking area.

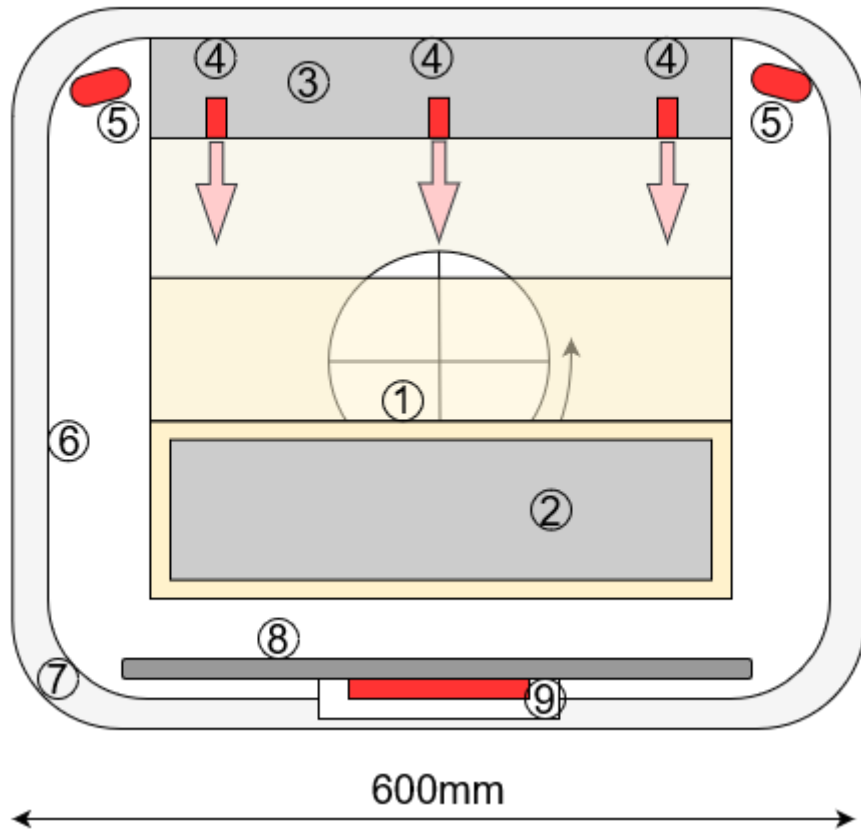


Figure 2.10: Schematic of prototype 2, front view. 1 - Convection fan. 2 -Fan inlet grill. 3 - Heater box. 4 - Heater units, as shown in Figure 7. 5 – Infra-red lamps. 6 - Stamped, enamelled steel forming the oven chamber. 7 – Ceramic wool insulation around the oven chamber. 8 - Glass base. 9 - Induction unit with coil on the top surface in red.

Humidity System

The humidity sensor was the same as that in prototypes IA and IB. Humidity in the oven could be increased by pumping water from an external reservoir into a tray within the heater box. The hot circulating air would then evaporate water from the tray and increase the humidity within the oven.

Induction Heater

The base heater was replaced with an inductive heating system, shown in Figure 2.8. The induction unit was self-contained, containing the signal generation circuit and heating coil as well

as a fan to cool the switching transistors and capacitors. The unit was sited in the base of the oven as shown in Figure 2.10. The metal base of the oven was cut away above the unit and replaced with a ceramic glass plate that was penetrable by the inductive field. A sheet of Microtherm™ insulation below the glass both reduced heat loss through the base of the oven and isolated the induction unit from the temperature of the cooking chamber. The induction heater was controlled on an average power basis. The oven microcontroller sent power instructions to the induction unit which then switched on and off in a duty cycle to deliver the requested average power. A thermal fuse cut power if the temperature below the Microtherm™ rose above 200°C.

Control and Electronics

Control in prototype I was entirely manual, with setpoints having to be changed in real time to follow a recipe. The control system in prototype II aimed to make this more convenient for a potential consumer and make cooking more consistent. To allow this the software included a recipe system. The recipe system could follow multistep programs of different setpoints, moving between cooking steps depending on either the time since the start of the cook or on the basis of temperature measurements from an internal food probe. Recipes could be defined using a 10 cm touchscreen display on the front panel. Setpoints could also be changed manually during cooking using the touchscreen.

2.4.4: Prototype III

Prototype III had few physical differences from prototype II, the aim being the evolution to a more production-ready design, maximising the use of punched and folded metal parts and reducing the amount of expensive machined components. The control electronics was provided by a custom printed circuit board (PCB) rather than a hand-soldered and Arduino-based board as used on prototypes I and II.

The one alteration to the oven layout was to move the infra-red lamps from the corners as in prototype II to inside the heater box, this was for two reasons. One was to give the lamps greater protection by siting them within the box, behind a quartz glass panel. The second was to prevent the lamps overheating by moving them to an area of high air flow rather than the top of the oven where the air was almost stagnant. Another advantage of this was that waste heat from the lamps transferred directly into the air impinging on the food, marginally increasing efficiency.

The humidity control system was also updated. The custom humidity sensor was replaced with a new system that used the behaviour of the circulation fan to infer the humidity of the circulating air. A tank located above the cooking chamber could be filled with water and contained a cartridge heater. This heater could be powered on to create steam that was ducted into the oven chamber to increase the humidity within.

2.5: Conclusions and Closing Remarks

An investigation of the history of the domestic oven showed that convenience and consistency were key drivers for new developments. Considering the physics of the cooking process within a domestic oven, combined with market data on the types of food being cooked in homes showed that an oven with higher heat transfer could improve efficiency and convenience. Several technologies from parallel industries were identified for increasing the heat transfer coefficient in domestic ovens and combined in a series of prototypes. These technologies were impinging jets, infra-red lamps and induction heating. This process is summarised in Figure 2.11.

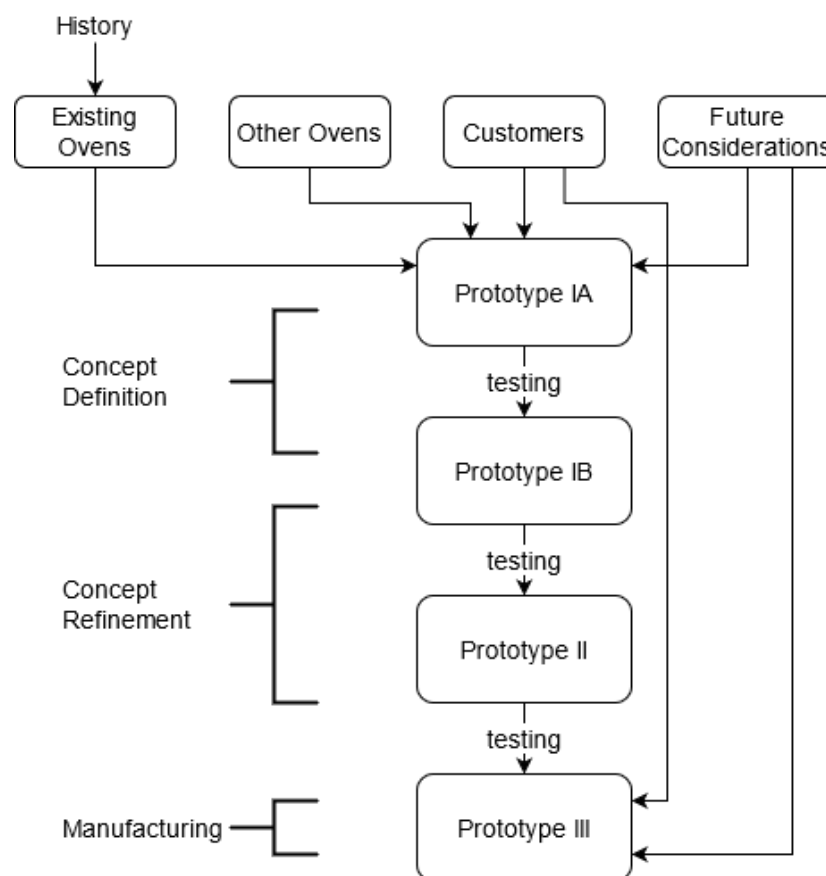


Figure 2.11: Schematic of the design process

3: Literature Review

3.1: Previous Studies in Domestic and Catering Oven Efficiency

The majority of the research on improving domestic and catering oven efficiency occurs within corporate R&D departments and is therefore largely unpublished. This section gives an overview of published work relating to designs that aim to improve oven efficiency, both from journal articles and a search of relevant patents. The patent search was performed in December 2020 and covered the following areas:

- i) Catering or domestic ovens that claimed to improve cooking speed or reduce the heat-up time before cooking starts.
- ii) Catering or domestic ovens that claimed to reduce energy consumption.
- iii) Catering or domestic ovens that combine and control multiple heat transfer modes, for example, controlling both conductive and convective heat transfer into the food.
- iv) Catering or domestic ovens that include induction heating.

It is important to note that patent literature is based solely on the claims of the applicant and often does not contain any quantitative information about the invention, nor is it peer reviewed. The aim of the patent search is therefore only to assess the state of the art and existing designs.

3.1.1: Low Emissivity Ovens

In low emissivity ovens (LEOs) a high fraction ($\approx 80\%$) of the total heat transferred during a cooking cycle is by radiative exchange. Figure 3.1 shows a section of a typical LEO design. The device consists of an insulated cooking chamber with exposed heating elements and reflective walls. The walls have an emissivity of <0.1 , compared to >0.8 for the black enamel coatings employed in a traditional design. The oven is operated by supplying the heating elements with electrical power. The elements become hot and emit infra-red radiation. The low emissivity and absorptivity of the oven walls means the majority the radiation is reflected rather than absorbed.

In comparison, the higher emissivity of the food makes it more likely to absorb the radiation. The rate of heat transferred to the food can be controlled by varying the voltage across, and therefore power delivered to, the electrical elements.

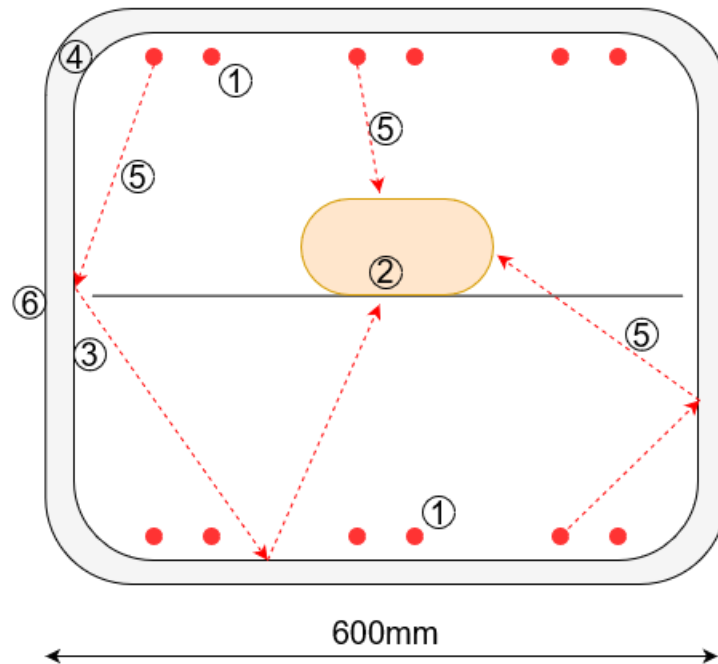


Figure 3.1: Section of a low-emissivity oven, front view. 1- Radiant heaters. 2 – Food on tray/shelf. 3 – Reflective walls. 4 - Insulation. 5 – Example infra-red beam paths. 6 – Oven outer wall.

Numerous prototype LEO's have been built and tested. Studies on a 2.4 kW rated prototype at Cranfield University have demonstrated energy savings of 35%, as well as significantly reduced times for the European Committee for Electrotechnical Standardisation (CENELEC) test compared to a traditional design⁴². A prototype with a maximum power of 1 kW and built by the Oak Ridge National Laboratory in the USA was used to cook various food types. The energy consumption and food quality were compared to results from a traditional design. Reductions in energy consumption for a cooking cycle of between 57 and 73% were reported⁴³. Another study

⁴² B.M. Shaughnessy and M. Newborough, 'Energy Performance of a Low-Emissivity Electrically Heated Oven', *Applied Thermal Engineering* 20, no. 9 (June 2000): 813–30.

⁴³ D.P. DeWitt and M.V. Peart, 'Bi-Radiant Oven: A Low-Energy Oven System. Volume I. Development and Assessment', 1980.

at the University of Manchester investigated ovens using predominantly radiative heat transfer and achieved energy savings of 25%⁴⁴.

Despite the reported improvements in efficiency and speed, LEOs have not been commercialised as they have a number of characteristics that are not compatible with the consumer constraints in section 2.2.

- i) The interior walls of the oven must be made from a low-emissivity material, such as polished stainless steel. Oven manufacturers have indicated to COI that this is undesirable due to the consumer reaction to the discoloration that will occur over time. This is caused by oxidation of the metal surface at high temperatures and the deposition of fat and cooking residues from food.
- ii) The low emissivity of the walls is only maintained if they are clean. If grease and fats are allowed to build up on the walls the heat transferred to the food is reduced, not only decreasing efficiency but also increasing cooking time. This introduces inconsistency to the cooking results and gives rise to a need for regular cleaning.
- iii) The type of cookware has a large effect on the cooking time as the emissivity of the food container determines the amount of energy absorbed. DeWitt and Peart observed that the cooking time of cake could change from 19 minutes to 25 minutes depending on the utensil used⁴⁵, again increasing the inconsistency of cooking in this design of oven.
- iv) When cooking multiple items within the oven on different levels each item shades the others, reducing the radiation incident upon them and introducing further inconsistency to the cooking⁴⁶.
- v) Cooking exclusively with radiation reduced food quality in some cases. In such instances, excessive surface drying and browning was encountered⁴⁷. This may be attributed to the long wavelength infra-red radiation used, which has a short penetration depth⁴⁸.

Attempts have been made to mitigate (v) by using shorter wavelengths of infra-red that penetrates further into the food⁴⁹. A separate patent⁵⁰ presented an oven using a mixture of

⁴⁴ D. Amienyo, 'Sustainable Manufacturing of Consumer Appliances: Reducing Life Cycle Environmental Impacts and Costs of Domestic Ovens', *Sustainable Production and Consumption*, 2016, 10.

⁴⁵ DeWitt and Peart, 'Bi-Radiant Oven: A Low-Energy Oven System. Volume I. Development and Assessment'.

⁴⁶ Shaughnessy and Newborough, 'Energy Performance of a Low-Emissivity Electrically Heated Oven'.

⁴⁷ DeWitt and Peart, 'Bi-Radiant Oven: A Low-Energy Oven System. Volume I. Development and Assessment'.

⁴⁸ L. Dagerskog and M. Osterstrom, 'Infrared Radiation for Food Processing.', *Libensm Technol.* 12, no. 4 (1979): 237–42.

⁴⁹ L. Cavada, Multi-Purpose Oven Using Infrared Heating for Reduced Cooking Time, USPTO 7323663 (USA, issued 2008).

⁵⁰ L. Bergendal and S. Lidingo, Domestic Infra-Red Radiation Oven, USPTO 4575616, issued 1986.

elements with different element temperatures that could be switched on and off to vary and control the wavelength depending on the desired effect on the food.

3.1.2: Improved Insulation

A simple way to reduce losses from the oven and increase thermal efficiency is to either increase the thickness of insulation around the oven cavity or use insulation with a lower thermal conductivity. A number of studies investigating thicker insulation have been conducted. Penšek and Hole found that adding an additional 30 mm of standard insulation around the cooking chamber reduced energy consumption by 7%⁵¹. A similar study by the US Department of Energy reported a saving of 5%⁵². However, the increase in insulation thickness also increases the cost to the consumer as well as reducing oven cavity volume and, therefore, utility to the consumer.

Scarbrick *et al.*⁵³ investigated the use of improved insulation by replacing the typical ceramic wool insulation with a thermal conductivity, $k = 0.045 \text{ Wm}^{-1}\text{K}^{-1}$ with MicrothermTM, an alumina based insulation with $k = 0.03 \text{ Wm}^{-1}\text{K}^{-1}$. The change increased the thermal efficiency from 14.2% to 15.9% for an hour-long cook. Scarbrick *et al.*⁵⁴ reported, however, that this effect was reversed for shorter cooking times. MicrothermTM has a larger heat capacity than ceramic wool, at $\sim 320 \text{ kJ m}^{-3}$ compared to $\sim 130 \text{ kJ m}^{-3}$, thereby increasing its thermal diffusivity and thus the energy and time requirements to bring the oven to steady state in preparation for cooking. The authors did not provide energy consumption and cooking times for these shorter cooking events.

3.1.3: Improved Control

Scarbrick *et al.*⁵⁵ and Penšek and Hole⁵⁶ investigated improved control methods in ovens. Typically, the oven heater is controlled in an on/off manner by a thermostat, giving swings in element and oven temperature (Figure 3.2). Scarbrick *et al.* investigated the use of a proportional, integral, derivative (PID) control loop, using pulse width modulation (PWM) to

⁵¹ M. Penšek and N. Hole, 'Energy Consumption Analysis of Domestic Oven', *Journal of Mechanical Engineering*, 2005, 6.

⁵² Lawrence Berkeley National Laboratory, 'Technical Support Document For Residential Cooking Products', 1993.

⁵³ C. Scarbrick, M. Newborough, and S.D. Probert, 'Improving the Thermal Performances of Domestic Electric Ovens', *Applied Energy* 39, no. 4 (January 1991): 263–300.

⁵⁴ Scarbrick, Newborough, and Probert.

⁵⁵ Scarbrick, Newborough, and Probert.

⁵⁶ Penšek and Hole, 'Energy Consumption Analysis of Domestic Oven'.

give analogue rather than digital control of the air heater power. Penšek and Hole kept the on/off control but reduced the magnitude of the temperature oscillations by altering the control software. Both studies showed that reducing temperature oscillations improved thermal efficiency, with total consumption reduced by 10% and 19% by Scarisbrick *et al.* and Penšek and Hole, respectively.

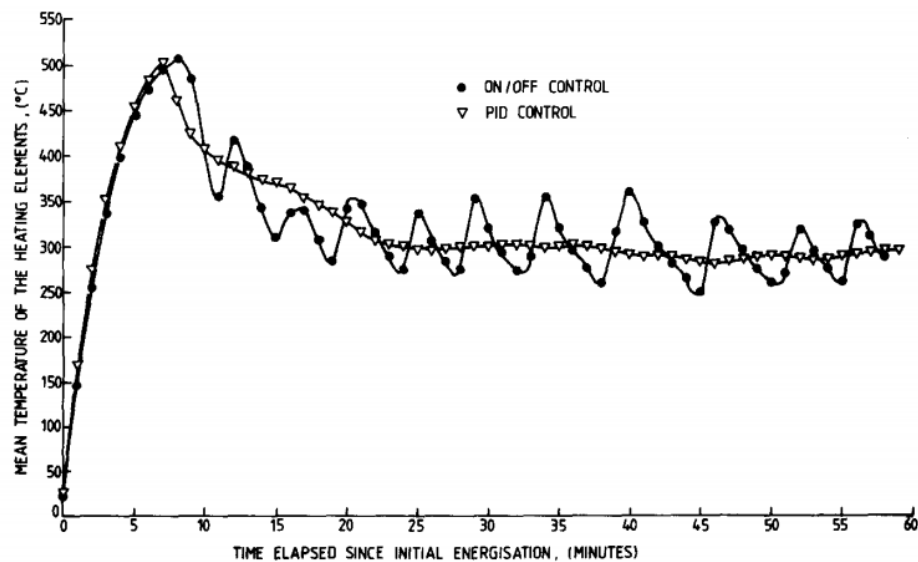


Figure 3.2: Plot of mean heating element temperature vs time in an electrical domestic oven for conventional on/off control and PID control using PWM. (Reproduced from Scarisbrick *et al.*, 1991)

3.1.4: Faster Heat-up

A key feature of the COI prototype oven is the ability to cook food with short heat-up times. Fast heat-up is claimed or covered by few patents or pieces of academic literature. Those that do lie in two areas:

- i) Using a heater element with greater power during the pre-heat phase in order to reach steady state more quickly. A patent granted to the Maytag corporation⁵⁷ uses both the convection element and grill element in the top of the cooking chamber

⁵⁷ K. Sauter and J. Mcfarland, Convection Cooking Appliance with Rapid Preheat System, USPTO 26388235, issued 2002.

during preheat. Park *et al.*⁵⁸ similarly found that using the more powerful grill element during the preheat phase reduced both preheating time as well as overall power consumption. The reduction in power consumption was attributed to the greater amount of insulation in the roof combined with a lower air velocity in the section of the cooking chamber closest to the oven roof. The local heat transfer coefficient in the roof was therefore lower than in the back of the oven around the fan. Park also found that excessive use of the grill element during preheat led to reduced food quality, as the residual heat from the element could burn the top of the food even when it was turned off after the pre-heat was completed. The use of the grill element also created a temperature gradient within the oven, meaning food on lower trays cooked more slowly than those nearer the top of the cooking chamber.

- ii) Another set of patents uses additional heater elements within the oven walls to heat the walls and insulation of the oven directly during the preheat phase and therefore bring them to steady state more quickly. Such a system, applied to a standard electrical fan oven, was patented in 2003 by Samsung⁵⁹. LG made a patent application in 2003 where the walls of the oven were heated using induction heating⁶⁰. Whirlpool made a similar application in 2009, omitting a circulation fan from the design⁶¹. While all these inventions will likely reduce the length of the heat-up phase their effect on energy efficiency is hard to ascertain without testing, as heating the oven walls will not contribute directly to heating the food.

3.1.5: Combination of Heating Modes

The second key feature of the COI oven is independently controlling, and where appropriate, maximising all three heat transfer modes into the food. To the best of the author's knowledge this methodology has not been applied to domestic ovens before⁶². Several patents have been granted for controlling two of the three modes.

⁵⁸ D.H. Park, E.R. Seo, M.K. Kwon, and Y.J. Park, 'The Study on the Heater Usage for Better Energy Efficiency of Domestic Convection Oven', *Journal of Mechanical Science and Technology* 32, no. 2 (February 2018): 907–14.

⁵⁹ T.-S. Kim, Y. Cho, and K.-H. Hahm, Electric Oven and Method of Controlling the Same, USPTO 7038179, issued 2006.

⁶⁰ W. Kim, Y. Kim, and Y. Lee, Electric Oven, USPTO 20040144773, issued 2005.

⁶¹ F. Farachi, R. Galli, D. Gerola, and F. Dughiero, Electric Induction Oven, USPTO, issued 2009.

⁶² M.E. Williamson, Oven, method of controlling oven, and sensors, IPO GB2566401, issued 2018.

Convection and Radiation

A series of patents covers the TurboChef® and MerryChef® series of ovens designed for the rapid heating of convenience food in cafes and shops. A maximum power draw of approximately 3 kW allows them to be plugged into a standard wall socket. These use impingement jets from above and below combined with microwaves to heat and crisp the food. They are designed for foods such as pizzas, toasted sandwiches or breakfast muffins and use a recipe system that automatically changes air temperature, microwave power and cooking time depending on the food type being prepared. The microwaves heat the interior of the food quickly and efficiently while the impingement jets heat and crisp its exterior by generating high heat and mass transfer coefficients.

The earliest patent combining microwave and convection heating was granted to Hirst Microwave Heating Inc. in 1968⁶³. This applies the forced convection scheme used in the electric fan oven (Figure 2.1) alongside a microwave emitter. The patent claimed that the convection aspect of the cooking gave superior food quality compared to ovens using microwaves alone, while being more efficient and faster cooking than a purely convection oven. General Electric were granted a similar patent in 1982⁶⁴ in which a heated airflow scheme similar to that of a commercial convection oven (Figure 2.6) was combined with microwaves. The patent specifically covered countertop devices, similar in size and shape to a typical microwave oven.

In 1973, Donald Smith⁶⁵ patented a commercial oven that combined impingement air and microwaves, again claiming to combine the efficiency and speed of microwave cooking with improved food quality. The design included a mechanisms for moving the food and the jet plenum within the oven to improve the even-ness of cooking and prevent areas of food directly beneath the jets from burning.

The TurboChef® rapid oven was developed between 1995 and 2000 based on a number of patents. The first patent in 1995⁶⁶ details a countertop oven using impingement jets, suitable for

⁶³ K. Hilton and R. Constable, Combined Microwave and Hot Air, USPTO 3514576, issued 1968.

⁶⁴ R. Dills, Food Browning System Incorporating a Combined Microwave and Hot Air Oven, USPTO 4480164, issued 1982.

⁶⁵ D. Smith, Cooking Apparatus, USPTO 3884213, issued 1973.

⁶⁶ P. McKee and E. Winkelmann, Quick-Cooking Oven, USPTO 5558793, issued 1996.

use in cafes or convenience stores. The design differs from previous impingement ovens in two ways:

- i) The heating elements are located within the plenum to allow for more rapid changes in impingement air temperature, similar to those described in the COI oven (Figure 4.3).
- ii) The oven includes a recipe system that maximises consistency of cooking for the same food type, regardless of which food has been prepared in the oven previously and the temperature within the oven at the start of the cooking cycle. This allows one oven to be used to prepare many food types. Control is achieved by adapting the recipe in real time when the temperature within the oven is higher or lower than desired. If the temperature is too low the cooking time is extended according to a formula, if the temperature is too high the fan speed is reduced according to a different formula. The aim of this approach is to keep the energy absorbed by the food during the cooking cycle the same despite differences in air temperature within the oven.

A second patent, granted in 1998⁶⁷, added microwaves to the power calculation and an altered convection scheme. In this scheme air exhausted from the cooking chamber to the fan through holes in the base. A third patent from 2000⁶⁸ added radiative elements to the system and a catalytic converter for cleaning the vent gases. The catalytic converter for the oven was described in a 1999 patent, also awarded to TurboChef®⁶⁹. The purpose of the catalytic converter was to oxidise oils and materials emitted by the food as it cooks, preventing them from coating the interior of the oven and being released into the kitchen. This reduced the amount of cleaning required and also meant that the oven did not require a dedicated vent, reducing the capital and running costs of the unit.

Another design of oven applying radiation and convection is described in patents assigned to JennAir⁷⁰ in 1979 and UltraVection⁷¹ in 1995. This design is similar to an LEO but also includes

⁶⁷ P. McKee, E. Winkelmann, and J. Pool, Compact Quick-Cooking Convectional Oven, USPTO 6060701, issued 1998.

⁶⁸ D. Mcfadden, J. Pool, E. Winkelmann, and J. Gidner, Compact Quick-Cooking Oven, USPTO 6376817, issued 2000.

⁶⁹ P. McKee and E. Winkelmann, Recycling Cooking Oven with Catalytic Converter, USPTO 5927265, issued 1997.

⁷⁰ L. Jenn and J. Cerola, Convertible Radiant Convection Oven, USPTO 4071739, issued 1977.

⁷¹ D. Wassman and G. Loveless, Convectively-Enhanced Radiant Heat Oven, USPTO 5676870, issued 1995.

a convection fan to provide forced convection. The power of the grill elements controls the air temperature and therefore the rate of convective heat transfer as well as the rate of radiative heat transfer. The speed of the fan can be changed to give a degree of independent control of the convective heat transfer.

Convection and Conduction

A number of patents cover heating the shelves within a standard electric fan catering or domestic oven to increase the rate of conductive heat transfer into food. A 1992 patent by Samsung⁷² describes an oven shelf containing a heating element. When the shelf is inserted into the oven it connects to a plug in the back of the oven chamber through which it can be powered and controlled. In 2014 General Electric patented a similar system⁷³ except using an induction heater below the cooking chamber to heat the shelf. McGraw-Edison were granted a patent in 1965⁷⁴ for a catering oven in which heated air for the fan was ducted through the shelves of the oven to heat them. A similar design but with removable shelves was patented in 2014 by Alto-Shaam⁷⁵.

Radiation and Conduction

Oven designs focussing on the control of radiative and conductive heat transfer are typically “finishing ovens” designed to generate high heat fluxes and surface temperatures in the food, both drying the surface and promoting Maillard reactions. Examples of these include a Garland Group patent⁷⁶ and Taco Bell patent⁷⁷, granted in 1999. The Garland Group design used an electrically heated griddle on the base to conduct heat into the food. In the roof of the cooking chamber radiant elements transmitted heat onto the top surface of the food. Low emissivity walls reflected heat emitted by the elements on to the food, as in an LEO. The TacoBell design used inductively heated metal elements embedded in the base and roof of the cooking chamber to provide conductive and radiative heat transfer respectively.

⁷² W. Ryu, Food Support Shelf Comprising Metal Grill with Heater, USPTO 5272317, issued 1992.

⁷³ E. Watson and P. Cadima, Inductively Heated Divider for an Oven Appliance, USPTO 9695538, issued 2014.

⁷⁴ S. Beasley, Oven Supplied with Hot Air Through Foraminous Duct-Shelves, USPTO 3221729, issued 1965.

⁷⁵ P. McKee, T. Vanlanen, and T. Coleman, Cooking Oven, USPTO 9879865, issued 2016.

⁷⁶ M. Reay, Griddle Plate with Infrared Heating Element, USPTO 6614007, issued 1999.

⁷⁷ J. Sowerby, Domed induction oven, USPTO 5872351, issued 1997.

3.1.6: Summary

A review of academic literature and patents showed that the COI oven design is novel in two ways:

- i) It is specifically designed to cook food before steady state is reached.
- ii) Optimisation and control of all three heat transfer modes.

Some features of the COI design exist in the surveyed literature, primarily the use of impingement jets and infra-red lamps to maximise convective and radiative heat transfer to the food. Other patents covered the control and optimisation of two of the three heat transfer modes. The majority of academic literature covers designs that do not meet the constraints detailed in section 2.2. Scarisbrick *et al.*⁷⁸ and Penšek and Hole⁷⁹ showed that improving temperature control by reducing oscillations in temperature as the heaters power on and off can reduce energy consumption considerably. 'The prototype ovens' control software was therefore designed to minimise temperature oscillations.

3.2: Computational Modelling

The COI design was tested and changes to it explored using computational models, reducing the number of prototype stages required. The modelling of food cooking in ovens can be split into two parts:

- i) Fluid and heat flow within the oven and how energy is transferred from the heating elements to the surface of the food.
- ii) Processes occurring within the food: how the energy delivered to the surface of the food changes the food from an uncooked to a cooked state.

⁷⁸ Scarisbrick, Newborough, and Probert, 'Improving the Thermal Performances of Domestic Electric Ovens', January 1991.

⁷⁹ Penšek and Hole, 'Energy Consumption Analysis of Domestic Oven'.

The following sections summarise and discuss previous studies in these two areas and how they can be applied to the modelling and testing of the COI oven.

3.2.1: Modelling of Food Cooking

Delivery of thermal energy to the surface of the food is only one part of the cooking process, how the food responds to this thermal energy and how the food changes from an uncooked to cooked state is another. This is primarily a heat transfer problem, governed by the heat equation:

$$\frac{\partial}{\partial t}(H) = (\nabla(k\nabla T)) \quad (3.1)$$

where H is the enthalpy of the food.

However, there are a number of complicating factors that must also be considered to produce a model that accurately describes the cooking process, for example:

- i) Complexities in H , such as phase changes and chemical reactions.
- ii) Spatially and temperature varying thermophysical properties.
- iii) Food of irregular shapes, requiring 3 dimensional meshes.
- iv) Food that changes shape or size during cooking, such as bread rising or meat shrinking.
- v) Complex boundary conditions: surface flux is often non-uniform and varies with time.

A timeline of the major developments in modelling these processes is shown in Figure 3.3. Developments in the field correspond to both advances in the understanding of the fundamental processes occurring within the food and the increase in available computing power, allowing more complex sets of equations and geometries to be considered.

Early work on modelling the heating or cooking of food focussed on sterilisation⁸⁰. Pflug and Kopelman⁸¹ presented analytical solutions of the transient heat equation in one dimensional geometries, namely an infinite slab, infinite cylinder and a sphere. They modelled the internal temperature profile of these objects, initially at a constant temperature, after being submerged in a heating or cooling fluid. The boundary condition on the surface of the solid included an external film heat transfer coefficient. Part of the work was a method to simplify the thermophysical properties of the solid into a single ‘temperature response parameter’ and an experimental method to obtain its value.

In 1977 Baerdemaeker *et al.*⁸² presented an early use of finite element numerical methods to model heat transfer within axisymmetric food pieces, numerically solving a dynamic heat balance across a regular grid of points in cylindrical coordinates:

$$\frac{\partial}{\partial r} \left(r k \frac{\partial T}{\partial r} \right) + \frac{\partial}{\partial z} \left(r k \frac{\partial T}{\partial z} \right) = r \rho C_p \frac{\partial T}{\partial t} \quad (3.2)$$

where r is the radial dimension and z is the axial dimension.

Axisymmetric representations of food cans, pears and chicken legs were modelled. Only heat transfer within the food was considered, with the surface temperature fixed. Reasonable agreement with experiment was reported for the heating of canned food and the chilling of pears and chicken legs. Naveh and Kopelman in 1983⁸³ described work in modelling the heating of canned and jarred food using a similar finite element model but including external film heat transfer from a fluid with a fixed bulk temperature and heat transfer coefficient. When modelling the jar they also included different physical properties for the glass container and the food contained within.

⁸⁰ C.O. Ball and F.C.W. Olson, *Sterilization in Food Technology. Theory, Practice, and Calculations*. (New York: Toronto : London : McGraw-Hill Book Company, Inc, 1957).

⁸¹ I.J. Pflug and I.J. Kopelman, ‘Correlating and Predicting Transient Heat Transfer Rates in Food Products.’, *Food Technology* 22 (1968): 799–804.

⁸² J. Baerdemaeker, R.P. Singh, and L.J. Segerlind, ‘Modelling Heat Transfer in Foods Using the Finite-Element Method’, *Journal of Food Process Engineering* 1, no. 1 (January 1977): 37–50.

⁸³ D. Naveh, I.J. Kopelman, and I.J. Pflug, ‘The Finite Element Method in Thermal Processing of Foods’, *Journal of Food Science* 48, no. 4 (July 1983): 1086–93.

Year	Developments	Example Papers
1950 1960	Analytical Solutions to Simplified Heat Equation	<i>Pflug and Kopelman (1968)</i>
1970	Numerical Solution to the Heat Equation (Axisymmetric)	<i>Baerdemaeker et al (1977)</i>
1980	● Evaporation at food surface	
	Coupled Heat and Mass Transport	<i>Balaban and Pigott (1988)</i>
1990	● 3D geometries	<i>Chang et al. (1998)</i>
	● Material Properties a Function of Temperature and Water Content	
2000	Porous Models	<i>Ni and Datta. (1999)</i>
2010	● Internal Pressure Gradient from Internal Evaporation	<i>Zhang and Datta. (2008)</i>
	● Internal Pressure from Protein Denaturation and Chemical Changes	
	● Dynamic Meshes (Changing Geometry)	
	● Calculation of food quality metrics from temperature and water content history	<i>Rabeler and Feyissa (2019)</i>

Figure 3.3: Timeline showing the development of the numerical modelling of oven cooking of food.

Singh *et al.*⁸⁴ in 1984 included a more complex boundary condition at the outer surface of the food, including the latent heat of water evaporating at the food surface.

$$q_{\text{surface}} = \underbrace{h(T_{\text{air}} - T_{\text{surface}})}_{\text{convection}} - \underbrace{\Delta H k_c (P_{w \text{ surface}} - P_{w \text{ air}})}_{\text{evaporation}} \quad (3.3)$$

where q_{surface} is the heat flux into the food from the oven and ΔH is the enthalpy of vaporisation for water. $P_{w \text{ surface}}$ is a function of T_{surface} and T_{air} and $P_{w \text{ air}}$ vary with time.

They modelled the roasting of an axisymmetric beef joint in a convection oven. Good agreement with experimental results was reported for the temperature profile but the model over-predicted the moisture loss from the beef.

Chang *et al.* in 1998⁸⁵ further expanded this type of model by applying it to a fully 3D geometry. They modelled the cooking of an unstuffed turkey by convection. The model gave reasonable agreement with experiment. Obuz *et al.*⁸⁶ present similar work, on irregular shaped beef roasts: as with Singh *et al.*, the model accurately predicted the development of the temperature profile within the meat but over-predicted moisture loss as it did not consider internal mass transfer.

Balaban and Pigott⁸⁷ presented a simultaneous heat and mass transfer model in 1988. Their model solved both the heat and mass balances in 1-D, accounting for internal resistance to mass transfer in modelling moisture loss. The heat and mass transfer models were not fully coupled, as they did not include the energy associated with the movement of liquid within the food. The mass and heat balance equations were:

⁸⁴ N. Singh, R.G. Akins, and L.E. Erickson, 'Modelling Heat and Mass Transfer during the Oven Roasting of Meat', *Journal of Food Process Engineering* 7, no. 3 (July 1984): 205–20.

⁸⁵ H.C. Chang, J.A. Carpenter, and R.T. Toledo, 'Modeling Heat Transfer during Oven Roasting of Unstuffed Turkeys', *Journal of Food Science* 63, no. 2 (28 June 2008): 257–61.

⁸⁶ Obuz, Powell, and Dikeman, 'Simulation of Cooking Cylindrical Beef Roasts'.

⁸⁷ M. Balaban and G.M. Pigott, 'Mathematical Model of Simultaneous Heat and Mass Transfer in Food with Dimensional Changes and Variable Transport Parameters', *Journal of Food Science* 53, no. 3 (May 1988): 935–39.

$$\text{mass} \quad \rho_l \frac{\partial w_c}{\partial t} = \frac{\partial}{\partial x} \left(D \rho_l \frac{\partial w_c}{\partial x} \right) \quad (3.4)$$

$$\text{sensible heat} \quad \rho_s C_p \frac{\partial T}{\partial t} = \frac{\partial}{\partial x} \left(k \frac{\partial T}{\partial x} \right) \quad (3.5)$$

where w_c is the fraction of water in the food, D is the effective mass diffusivity of water within the food, x is the depth into the food and ρ_l and ρ_s are the densities of water and the dry components of the food, respectively.

The boundary conditions were similar to those used by Singh *et al.*. Balaban and Pigott also accounted for changing physical properties during drying, with k , C_p and D all expressed as functions of T and w_c . They modelled the drying of perch fish in an air-drying oven where the fish was treated as a semi-infinite slab. The model predicted the temperature profile in the fish and mass loss in good agreement with experiments.

Huang and Mittal⁸⁸ used the same simultaneous heat and mass transfer equations to model the cooking of spherical meatballs. Three cases were considered: cooking in boiling water; in a natural convection oven; and in a fan driven, forced convection oven. These cases were represented by manipulating the boundary conditions. Both k and D were treated as fitting parameters and differed between cooking methods. Good agreement with experiment was observed for the temperature profile within the meatballs and the moisture loss. The fitted parameters lay within the range of uncertainty in those measured experimentally by Ngadi *et al.* in 2006⁸⁹.

Chen *et al.*⁹⁰ applied the simultaneous heat and mass transfer equations (equations 3.4 and 3.5), combined with thermal and water diffusivities from Huang and Mittal to model the convection cooking of cylindrical chicken patties. The average error in the temperature profile was reported as 3.8-5.7 K for a core temperature of approximately 345 K when modelling both heat and mass transfer. The average error was 5.9-12.9 K when only heat transfer was considered, showing the

⁸⁸ E. Huang and G.S. Mittal, 'Meatball Cooking — Modeling and Simulation', *Journal of Food Engineering* 24, no. 1 (January 1995): 87–100.

⁸⁹ M. Ngadi, K. Dirani, and S. Oluka, 'Mass Transfer Characteristics of Chicken Nuggets', *International Journal of Food Engineering* 2, no. 3 (2006).

⁹⁰ Chen, Marks, and Murphy, 'Modeling Coupled Heat and Mass Transfer for Convection Cooking of Chicken Patties'.

importance of surface evaporation. A standard error of 1.2% was reported for the model predictions of patty mass after cooking.

Ni and Datta presented a more detailed model of cooking food in 1999 that captured three additional physical processes ignored in previous studies.

- i) The heat balance contained a term accounting for energy transferred by mass transport within the food, fully coupling the heat and mass transport equations.
- ii) The model included the evaporation of water within the food, rather than exclusively at the surface. The model therefore considered the mass transport of water and steam throughout the food. The heat transport equation (equation 3.5) was expanded to consider conduction, the heat convected by both water and steam and the latent heat of the vaporisation of water within the food.
- iii) The mass transport equation in models discussed previously (equation 3.4) only considered diffusion. Ni and Datta considered both diffusion and pressure driven flow through the food, treating the food as a porous medium. Internal pressure could be generated by internal evaporation or from changes in the food microstructure.

In three papers published in 1999 they applied this model to different cases: convection drying of a slab of potato⁹¹; deep frying of potato⁹²; and microwave heating of vegetables⁹³. All three foods were modelled as semi-infinite slabs to reduce the computational complexity. In all cases the models gave reasonable agreement for temperature and moisture loss compared to experimental results.

Their model also gave insights into the behaviour of food during cooking. Datta's group demonstrated that the internal evaporation caused by microwave heating results in an increased pressure within the food. This drives moisture to the surface faster than it can be evaporated by the relatively cool air within the microwave oven, resulting in a soggy product. A subsequent investigation in 2008⁹⁴ combined this microwave model with infra-red heating and impingement

⁹¹ H. Ni and A.K. Datta, 'Heat and Moisture Transfer in Baking of Potato Slabs', *Drying Technology* 17, no. 10 (November 1999): 2069–92.

⁹² H. Ni and A.K. Datta, 'Moisture, Oil and Energy Transport during Deep-Fat Frying of Food Materials', *Food and Bioproducts Processing* 77, no. 3 (September 1999): 194–204.

⁹³ H. Ni, A. k. Datta, and K. e. Torrance, 'Moisture Transport in Intensive Microwave Heating of Biomaterials: A Multiphase Porous Media Model', *International Journal of Heat and Mass Transfer* 42, no. 8 (April 1999): 1501–12.

⁹⁴ Geedipalli, Datta, and Rakesh, 'Heat Transfer in a Combination Microwave–Jet Impingement Oven'.

jets to determine their relative effectiveness in removing water from the surface and increasing food quality.

Zhang and Datta modelled the baking of bread in 2006⁹⁵ using a more complex porous medium model and fitting it to experimental data. The internal pressure generated by the thermal expansion of gas and internal evaporation of water was calculated. This was then used to determine both the mass transfer within the porous structure of the bread and how the bread rises in the oven. The dough was treated as a viscoelastic fluid and a dynamic mesh was used to model its change in shape with time. Additionally, the temperature history of the bread surface was used to predict the amount of surface browning achieved. Good agreement was achieved for volume change, temperature rise, moisture loss and degree of browning although mass diffusivities were treated as fitted variables in the analysis.

In meat products, internal pressure driving mass transfer can arise from the denaturation of proteins as well as internal evaporation. Van der Sman⁹⁶ developed an empirical model for this effect in 2007, deriving the “water holding capacity” of the protein component of the meat as a function of temperature and fitting it to experiment. This could then be used to find the pressure gradient driving flow from the centre of the cooking meat to the surface. This technique could then be included in porous media models, similar to those developed by Datta and co-workers. Goni and Salvadori⁹⁷ applied this method to the roasting of beef in 2010, and measured both the mass of water evaporated from the beef and the “dripping mass” of water squeezed from the meat by denaturing proteins during cooking. Their model gave a 4% error in cooking time and an 8% error in weight loss. A 20% error in weight loss was observed when dripping mass was ignored. Van der Sman⁹⁸ and Feyissa *et al.*⁹⁹ modelled the cooking of chicken in a tunnel oven and the pan cooking of steak using a similar method.

⁹⁵ J. Zhang and A.K. Datta, ‘Mathematical Modeling of Bread Baking Process’, *Journal of Food Engineering* 75, no. 1 (July 2006): 78–89.

⁹⁶ R.G.M. van der Sman, ‘Moisture Transport during Cooking of Meat: An Analysis Based on Flory–Rehner Theory’, *Meat Science* 76, no. 4 (August 2007): 730–38.

⁹⁷ S.M. Goñi and V.O. Salvadori, ‘Prediction of Cooking Times and Weight Losses during Meat Roasting’, *Journal of Food Engineering* 100, no. 1 (September 2010): 1–11.

⁹⁸ R.G.M. van der Sman, ‘Modeling Cooking of Chicken Meat in Industrial Tunnel Ovens with the Flory–Rehner Theory’, *Meat Science* 95, no. 4 (December 2013): 940–57.

⁹⁹ A.H. Feyissa, K.V. Gernaey, S. Ashokkumar, and J. Adler-Nissen, ‘Modelling of Coupled Heat and Mass Transfer during a Contact Baking Process’, *Journal of Food Engineering* 106, no. 3 (October 2011): 228–35.

Rabeler and Feyissa developed this methodology further by using the temperature and moisture content within the food to calculate food quality metrics relating to texture¹⁰⁰: gumminess, hardness, chewiness, and colour¹⁰¹, both internal and surface browning. Good agreement with experiment was achieved for all metrics while using experimentally derived, rather than fitted, physical property values. The temperature of the cooking air and the heat transfer coefficient were varied, both in the model and in experiments. Increasing the heat transfer coefficient reduced cooking time but had no effect on final food texture. A further study by Feyissa and Rabeler¹⁰² used a Monte-Carlo analysis to rank the importance of oven conditions and chicken meat properties on texture and their development over time.

The modelling of heat and mass transfer within food is not considered further in this work. External heat transfer determines the temperature profile within the food, and the temperature history of the food then drives the development of texture and flavour. As such, any modelling undertaken will focus on the transfer of thermal energy from the heating elements within the oven to the surface of the food. Modelling the processes within the food is not only computationally expensive but requires a coupled and transient CFD model of the oven, which is also computationally very expensive. Moreover, each different food type would require its own specific model and parameters.

3.2.2: Flow Modelling (CFD)

Governing Equations

CFD involves the numerical solution of three conservation equations across discrete spatial volumes¹⁰³. These spatial volumes combine to give the geometry of interest, while the boundary conditions specified give the operating conditions. A complete description and derivation of the relevant equations is given by Anderson¹⁰⁴:

¹⁰⁰ F. Rabeler and A.H. Feyissa, 'Modelling the Transport Phenomena and Texture Changes of Chicken Breast Meat during the Roasting in a Convective Oven', *Journal of Food Engineering* 237 (November 2018): 60–68.

¹⁰¹ Rabeler, Skytte, and Feyissa, 'Prediction of Thermal Induced Color Changes of Chicken Breast Meat during Convective Roasting'.

¹⁰² F. Rabeler and A.H. Feyissa, 'Modelling of Food Processes under Uncertainty: Mechanistic 3D Model of Chicken Meat Roasting', *Journal of Food Engineering* 262 (December 2019): 49–59.

¹⁰³ T. Norton and D.-W. Sun, 'Computational Fluid Dynamics (CFD) – an Effective and Efficient Design and Analysis Tool for the Food Industry: A Review', *Trends in Food Science & Technology* 17, no. 11 (November 2006): 600–620.

¹⁰⁴ J.D. Anderson, 'The Governing Equations of Fluid Dynamics', in *Computational Fluid Dynamics: The Basics with Applications* (McGraw Hill, 1995), 37–93.

- i) The conservation of mass, or continuity, which states that the mass flows entering a fluid element must balance with those leaving.
- ii) The conservation of momentum, which states that the sum of external forces acting on a fluid particle is equal to its rate of change of linear momentum. This principle gives rise to one equation per coordinate dimension.
- iii) The conservation of energy, which states the rate of change of energy of an element of fluid is equal to the heat addition and the work done on the element.

Combining continuity and conservation of momentum gives the Navier Stokes equations (NSEs), which for an incompressible fluid are:

$$\rho \left[\frac{\partial \mathbf{v}}{\partial t} + \mathbf{v} \cdot \nabla \mathbf{v} \right] = \rho \mathbf{g} - \nabla P + \mu \nabla^2 \mathbf{v} \quad (3.6)$$

$$\nabla \cdot \mathbf{v} = 0 \quad (3.7)$$

where \mathbf{v} is the velocity vector and \mathbf{g} is the gravitational acceleration vector.

The energy equation is:

$$\rho C_p \left(\frac{\partial T}{\partial t} + \mathbf{v} \cdot \nabla T \right) = k \nabla^2 T + s_T \quad (3.8)$$

where s_T is external heat added or removed to the element per unit volume.

Most CFD solvers can be run in two modes, steady-state or transient. In steady-state mode the solver will try and find a time-invariant or time-averaged solution. In transient mode the solver will solve for individual timesteps, capturing any variation in the solution with time. Steady-state solutions are generally less computationally expensive as only one solution is reached, but the model may not converge for systems with transient fluctuations where there is not a single steady state for the solver to find.

Turbulence

In a convection oven the Reynolds numbers are well above the laminar-turbulent transition indicating the flow is turbulent. The vortices and flow patterns that constitute turbulence exist on the microscale. Direct numerical simulation (DNS) modelling of these phenomena therefore requires extremely fine spatial and temporal discretisation. For the size and complex shape of an

oven geometry DNS is therefore not practical. One alternative approach is given by the Reynolds averaged Navier Stokes equations (RANS) which do not directly model the vortices but instead average their effect on the fluid flow over a period of turbulent fluctuations. These equations result in 6 additional unknown variables, known as the Reynolds stresses. Various models have been proposed and used to calculate Reynold stresses from known parameters and thus solve the flow field within the system. Three common two-equation approaches are the k - ε , k - ω and shear stress transport (SST) models. Their governing equations can be found in Wilcox¹⁰⁵.

- i) The k - ε is the most widely used and applied turbulence model¹⁰⁶. It is a two-equation model, meaning that two additional quantities must be found by the model. These are k , the turbulent kinetic energy and ε the dissipation of this energy. A weakness of the model is that it cannot resolve flow in the viscous sub-layer or the buffer layer close to the wall (see Figure 3.4).
- ii) The k - ω model was the first two equation model, proposed by Kolmogorov in 1942¹⁰⁷. The two quantities calculated are the turbulent kinetic energy, k and dissipation per unit turbulent energy, ω . Unlike the k - ε model it is applicable close to the wall.
- iii) The SST model is a combination of the k - ω and k - ε models, using k - ω in the boundary layers close to the wall, then switching to k - ε in the turbulent core of the flow.

Other methods have been developed to close the RANS equations and model turbulence, such as the large eddy simulation summarised by Marchioli¹⁰⁸, Reynolds stress models summarised by Thakur and Shyy¹⁰⁹, and detached eddy simulation, summarised by Spalart¹¹⁰. These methods can be more accurate than the two-equation models but are more computationally expensive.

¹⁰⁵ D. Wilcox, 'One-Equation and Two-Equation Models', in *Turbulence Models for CFD*, 3rd ed. (DCW industries, 1998), 107–230.

¹⁰⁶ Wilcox; Norton and Sun, 'Computational Fluid Dynamics (CFD) – an Effective and Efficient Design and Analysis Tool for the Food Industry'.

¹⁰⁷ Wilcox, 'One-Equation and Two-Equation Models'.

¹⁰⁸ C. Marchioli, 'Large-Eddy Simulation of Turbulent Dispersed Flows: A Review of Modelling Approaches', *Acta Mechanica* 228, no. 3 (March 2017): 741–71.

¹⁰⁹ S. Thakur and W. Shyy, 'Reynolds Stress Models for Flows in Complex Geometries - Review and Application', in *30th Fluid Dynamics Conference* (30th Fluid Dynamics Conference, Norfolk, VA, U.S.A.: American Institute of Aeronautics and Astronautics, 1999).

¹¹⁰ P.R. Spalart, 'Detached-Eddy Simulation', *Annual Review of Fluid Mechanics* 41 (2008): 181–202.

Many CFD packages also include wall functions. These are empirical functions that describe fluid behaviour close to walls¹¹¹. The advantage of these is that a relatively coarse mesh, where the viscous boundary layer and transition layer, shown in Figure 3.4, is contained entirely within one mesh element, can still impose suitable edge conditions on the core of the flow¹¹². These functions are calculated in terms of y^+ and u^+ , which are dimensionless forms of distance from the wall and velocity, respectively:

$$y^+ = \frac{y_w \rho}{\mu} \times \sqrt{\frac{\tau_w}{\rho}} \quad (3.9)$$

$$u^+ = u \times \sqrt{\frac{\rho}{\tau_w}} \quad (3.10)$$

$$\tau_w = \mu \left(\frac{\partial u}{\partial y_w} \right)_{y=0} \quad (3.11)$$

where y_w is the distance from the wall, u is the flow velocity parallel to the wall and τ_w is the wall shear stress. These values are updated with each iteration of the solver

The disadvantage of this approach is that the behaviour close to the wall is not being modelled, only approximated. This can be an issue in cases where the behaviour very close to the wall is of interest, such as heat transfer applications. Many solvers, such as ANSYS CFX, are able to change between wall treatments depending on the element size. Zuckerman and Lior (2006) recommend the first node is placed at $2 < y^+ < 5$ for accurate modelling of heat transfer using the SST model¹¹³.

¹¹¹ N. Zuckerman and N. Lior, 'Jet Impingement Heat Transfer: Physics, Correlations, and Numerical Modeling', in *Advances in Heat Transfer*, vol. 39 (Elsevier, 2006), 565–631.

¹¹² . ANSYS Inc., 'Modelling Flow near a Wall', in *ANSYS CFX, Release 18.2, Help System*, 2021.

¹¹³ Zuckerman and Lior, 'Jet Impingement Heat Transfer'.

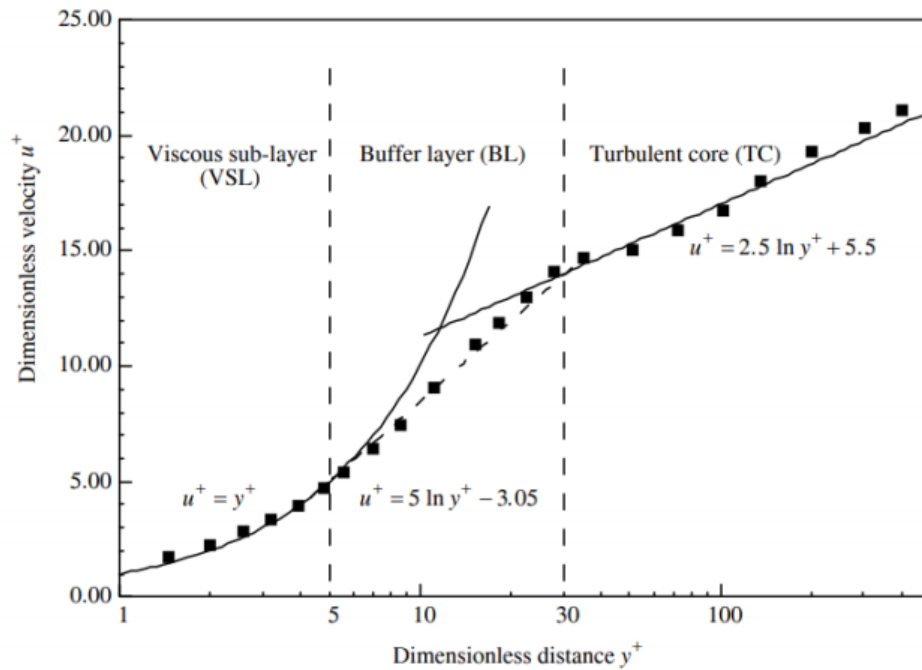


Figure 3.4. Plot of dimensionless fluid velocity profile close to a wall. Solid lines indicate the ideal profiles in the various zones while points indicate the actual behaviour. (credit to Prof. S. Cardoso)

Radiative Heat Transfer

The solution to equations 3.6 and 3.8 determines the convective heat flux, however, radiative exchange must be calculated separately. Radiation modelling in CFD generally runs in parallel to the flow equations discussed above. It seeks to calculate the heat energy transferred via radiation, this is incorporated into the heat fluxes at the walls of the simulation and in the s_T term of the energy equation (equation 3.8). Numerous models exist to approximate radiation within a simulation. The discrete ordinate, Monte-Carlo and discrete transfer models are widely available models for transfer involving transparent or near-transparent fluid domains in commercial CFD packages.

- i) The discrete ordinate (DO) model solves the radiation transfer equation over a discrete number of angles from the surface emitting radiation, with the size of the discretisation increasing the accuracy and computational cost. The DO model is attractive due to relatively low computational cost but has a number of drawbacks¹¹⁴.

¹¹⁴ 'Impact of Radiation Models in CFD Simulations of Steam Cracking Furnaces', *Computers and Chemical Engineering*, 2007, 18.

It does not ensure conservation of energy and can lead to unphysical numerical artifacts known as false scattering and ray effects, discussed by Chai *et al.*¹¹⁵.

- ii) The Monte-Carlo model involves releasing a statistically large number of photons from sources within the model. The photons are tracked around the model with their absorbance, scattering and reflections and the effect of these interactions recorded. The Monte-Carlo model can give good accuracy but is computationally expensive¹¹⁶.
- iii) The discrete transfer model was first described by Lockwood and Shah in 1981¹¹⁷. It is similar to the Monte-Carlo model, tracing rays of thermal radiation around the model. The path of these rays is then discretised, and the energy transfer solved numerically. The advantage over the Monte-Carlo model is that photon tracing only needs to be completed once per run, rather than every iteration, reducing computational effort¹¹⁸.

These models can be simplified in the case of non-participating media, or when the fluid within the simulation does not absorb or scatter infra-red radiation strongly. In this case a surface-to-surface (S2S) model can be applied where only exchange between solid boundaries are considered.

3.2.3: History and Development of the Application of CFD to Oven Modelling

The availability of commercial finite element CFD software resulted in a number of modelling studies of industrial and commercial catering ovens in the early 2000's. These early studies tested and demonstrated the ability of CFD to simulate various oven arrangements and geometries, as well as exploring different model parameters.

¹¹⁵ J.C. Chai, H.S. Lee, and S.V. Patankar, 'Ray Effect and False Scattering in the Discrete Ordinates Method', *Numerical Heat Transfer, Part B: Fundamentals* 24, no. 4 (1993): 18.

¹¹⁶ . ANSYS Inc., 'The Monte-Carlo Model', in *ANSYS CFX, Release 18.2, Help System*, 2021.

¹¹⁷ F.C. Lockwood and N.G. Shah, 'A New Radiation Solution Method for Incorporation in General Combustion Prediction Procedures', *Symposium (International) on Combustion* 18, no. 1 (1981): 1405–14.

¹¹⁸ . ANSYS Inc., 'The Discrete Transfer Model', in *ANSYS CFX, Release 18.2, Help System*, 2021.

Verboven *et al.* modelled a commercial catering oven at first isothermally¹¹⁹ before including the energy equation¹²⁰. Both studies used ANSYS CFX 4.1 and the k - ε turbulence model. The mesh contained 56,000 elements and radiation was neglected. The circulation fan was modelled as a pressure increase given by an experimentally-derived fan curve, the heaters were modelled as volume sources. The model was steady state, but heat flux data were extracted and inputted into a lumped parameter model which was used to model the heating up phase of the oven in a transient manner.

The model results were experimentally validated using hot film anemometry for the velocity field and thermocouples for the temperature field. Additionally, PVC cubes were placed within the oven and the rate of temperature rise used to calculate the heat flux into the cube. The local heat transfer coefficient was calculated using the local air temperature and cube surface temperature. The model had a mean velocity error of 22% and captured the temperature field accurately, with the model prediction within the measurement error range in most cases. The model nevertheless underestimated the heat transfer coefficient and flux by approximately 50% in all cases. This was attributed to the neglect of radiation as well as the limitations of the k - ε turbulence model.

Therdthai *et al.*¹²¹ and Mirade *et al.*¹²² both presented early CFD studies of industrial tunnel ovens, baking bread and biscuits, respectively. Therdthai *et al.* applied CFDDACE+ to a 21,800 element 2D mesh. Neither the turbulence nor radiation models used were reported. Mirade *et al.* used a fully 3D geometry and mesh, capturing the full length and width of the oven. The mesh contained 1.3 million elements and was solved in steady state using Fluent V6. The k - ε turbulence model was used but the radiation model was not reported. The temperature field predicted by the model was compared to experimental measurements. In the centre of the oven the average error was 10%, however towards the ends errors of up to 70% were found. This error was attributed to difficulty in describing the open air boundary at the openings of the tunnel leading to the model being unable to capture the swirl of ambient air being entrained.

¹¹⁹ Verboven, Scheerlinck, Baerdemaeker, and Nicola, 'Computational Fluid Dynamics Modelling and Validation of the Isothermal Air Flow in a Forced Convection Oven'.

¹²⁰ P. Verboven, N. Scheerlinck, J.D. Baerdemaeker, and B.M. Nicola, 'Computational Fluid Dynamics Modelling and Validation of the Temperature Distribution in a Forced Convection Oven', *Journal of Food Engineering*, 2000, 13.

¹²¹ N. Therdthai, W. Zhou, and T. Adamczak, 'Two-Dimensional CFD Modelling and Simulation of an Industrial Continuous Bread Baking Oven', *Journal of Food Engineering* 60, no. 2 (November 2003): 211–17.

¹²² P.S. Mirade, J.D. Daudin, F. Ducept, G. Trystram, and J. Clément, 'Characterization and CFD Modelling of Air Temperature and Velocity Profiles in an Industrial Biscuit Baking Tunnel Oven', *Food Research International* 37, no. 10 (January 2004): 1031–39.

Mirade *et al.* modelled the oven with and without including the interior metalwork in the simulation and found no difference in the velocity or temperature fields between the two cases.

CFD models have been reported for many more oven geometries and designs, with additional physics added to the models such as the transient modelling of food within the oven and inclusion of the oven walls. Mistry *et al.* used ANSYS Fluent to model an electrically powered domestic oven without forced convection in 2006¹²³ and a gas-fired domestic oven in 2011¹²⁴. These models were validated using measurements of the temperature field and the heat flux into an aluminium rod, respectively. Wong *et al.* expanded previous modelling of bread baking ovens by including the loaves in the model and using a transient model with a dynamic mesh to capture the heating of the bread as it travelled along the tunnel. The 30 minute bake took 7 days to run on an IBM p690 supercomputer, demonstrating the computational cost of transient modelling. The k - ϵ turbulence model and discrete ordinate (DO) radiation models were applied to a 2 dimensional mesh with 160,000 elements. The model was validated by comparing experimental bread surface and internal temperature profiles with those predicted by the model. The model accurately predicted bread surface temperature but simplifications to the chemical and physical changes within the bread meant the internal temperature profile was not predicted accurately. Boulet *et al.*¹²⁵, Pinelli and Suman¹²⁶, Chhanwal *et al.*¹²⁷ and Tank *et al.*¹²⁸ also presented models of catering style ovens.

With the ability of CFD to model various oven geometries and arrangements established, the method could then be applied to design studies and design optimisation. Williamson and Wilson¹²⁹ presented a study using ANSYS CFX to model a novel radiant gas burner for use in industrial tunnel ovens. Monte-Carlo radiation modelling and the SST turbulence model were

¹²³ H. Mistry, Ganapathi-subbu, S. Dey, P. Bishnoi, and J.L. Castillo, 'Modeling of Transient Natural Convection Heat Transfer in Electric Ovens', *Applied Thermal Engineering* 26, no. 17–18 (December 2006): 2448–56.

¹²⁴ H. Mistry, S. Ganapathisubbu, S. Dey, P. Bishnoi, and J.L. Castillo, 'A Methodology to Model Flow-Thermals inside a Domestic Gas Oven', *Applied Thermal Engineering* 31, no. 1 (January 2011): 103–11.

¹²⁵ M. Boulet, B. Marcos, M. Dostie, and C. Moresoli, 'CFD Modeling of Heat Transfer and Flow Field in a Bakery Pilot Oven', *Journal of Food Engineering* 97, no. 3 (April 2010): 393–402.

¹²⁶ M. Pinelli and A. Suman, 'Thermal and Fluid Dynamic Analysis of an Air-Forced Convection Rotary Bread-Baking Oven by Means of an Experimental and Numerical Approach', *Applied Thermal Engineering* 117 (May 2017): 330–42.

¹²⁷ N. Chhanwal, D. Indrani, K.S.M.S. Raghavarao, and C. Anandharamakrishnan, 'Computational Fluid Dynamics Modeling of Bread Baking Process', *Food Research International* 44, no. 4 (May 2011): 978–83.

¹²⁸ A. Tank, N. Chhanwal, D. Indrani, and C. Anandharamakrishnan, 'Computational Fluid Dynamics Modeling of Bun Baking Process under Different Oven Load Conditions', *Journal of Food Science and Technology* 51, no. 9 (September 2014): 2030–37.

¹²⁹ M.E. Williamson and D.I. Wilson, 'Development of an Improved Heating System for Industrial Tunnel Baking Ovens', *Journal of Food Engineering* 91, no. 1 (March 2009): 64–71.

employed in the steady-state type model. The model was validated by comparing heat flux values with those from a full-scale prototype. An average error of 10% was observed. Potential design changes were tested in-silico with the aim of minimising the variation of radiative flux along the longitudinal axis. Changes in geometry and operating conditions were inputted manually into the model and the impact quantified and used to inform the final design.

Smolka *et al.* presented two design studies on two types of laboratory heating ovens. A 2010 paper¹³⁰ examined a forced convection design, similar in arrangement to a commercial catering oven. As with Williamson and Wilsons's study, design parameters were altered manually with a "grid" of designs inputted and tested using the model. ANSYS Fluent was used with the DO and $k-\epsilon$ models for radiation and turbulence. The circulation fan was modelled directly using a moving mesh. The model was validated using the temperature field, with an average error of 2.1 K when operating at a 100°C temperature setpoint. Six design configurations were evaluated in the model, each with different baffles surrounding the circulation fan and a different shape of air heater. As with Williamson and Wilsons's study the aim was to reduce variation in heat flux within the oven. This was quantified by how much the temperature at various points within the oven differed from the setpoint. The largest difference was used as the metric to be minimised. The best design configuration as predicted by the model was then constructed and tested. The model of the new configuration had an average temperature error of 2.6 K when operating at 100°C, showing the ability of CFD to make small extrapolations while maintaining accuracy.

A second design study by Smolka *et al.* was published in 2013 across two papers, relating to optimising the heater design in a natural convection laboratory drying oven. The first paper¹³¹ reported the creation of a 11.2 million element model using the $k-\epsilon$ and DO models and its validation, with a maximum temperature error of 14.1% in the model compared to experiment. Smolka *et al.* were also able to use particle image velocimetry (PIV) to measure the velocity field within the oven by cutting a hole in the wall of the oven and replacing it with a glass panel. The second paper used a genetic algorithm to automatically alter the shape of the heating elements in the model such that they gave the most even temperature distribution. A simplified 50,000

¹³⁰ J. Smolka, A.J. Nowak, and D. Rybarz, 'Improved 3-D Temperature Uniformity in a Laboratory Drying Oven Based on Experimentally Validated CFD Computations', *Journal of Food Engineering* 97, no. 3 (April 2010): 373–83.

¹³¹ J. Smolka, Z. Bulinski, and A.J. Nowak, 'The Experimental Validation of a CFD Model for a Heating Oven with Natural Air Circulation', *Applied Thermal Engineering* 54, no. 2 (May 2013): 387–98.

element model was applied to minimise computational cost, with the final design tested in the full size model.

A design study using CFD for a domestic fan oven of standard size and 2.4 kW heater power was presented by Rek *et al.* in 2012¹³². A transient CFD simulation was used to model the effect of internal geometry changes on how uniformly a layer of biscuits would bake within the oven, with 10 configurations tested and the best chosen qualitatively. Geometry changes considered were the positions of the outlet slots in the back plate of the oven (Figure 2.1) and the angle of these outlet slots. The model had 1.5 million elements and used the RANS and DO turbulence and radiation models. The model was validated by comparing the internal temperature of the biscuit during cooking with experiment. The selected design was then built as a prototype and agreement between experiment on this design and the model was found to be good. The design was put into production by Gorenje.

Khatir *et al.* developed a series of CFD models of industrial baking ovens between 2010 and 2014. A 2D model was developed and validated using temperature measurements, with a 5% average temperature difference between the model and experiment¹³³. A section of this geometry containing only 3 impingement jets was then used for optimisation¹³⁴. The model was transient and contained a loaf of bread being baked in the oven: the transport parameters of the bread were functions of temperature, but the model did not consider moisture transport or changes in loaf dimensions. The size, height and velocity of the impinging jets were varied in a parameter sweep and the time to bake and standard deviation of the bread surface temperature used to compare the speed and evenness of cooking.

¹³² Z. Rek, M. Rudolf, and I. Zun, 'Application of CFD Simulation in the Development of a New Generation Heating Oven', *Strojniški Vestnik – Journal of Mechanical Engineering* 58, no. 2 (15 February 2012): 134–44.

¹³³ Khatir, 'Computational Fluid Dynamics (CFD) Investigation of Air Flow and Temperature Distribution in a Small Scale Bread-Baking Oven'.

¹³⁴ Z. Khatir, H. Thompson, N. Kapur, V. Toropov, and J. Paton, 'Multi-Objective Computational Fluid Dynamics (CFD) Design Optimisation in Commercial Bread-Baking', *Applied Thermal Engineering* 60, no. 1–2 (October 2013): 480–86.

3.2.4: Summary

Reviews of the development of CFD methods and their application can be found in Anderson¹³⁵, Shang¹³⁶, Xia and Sun¹³⁷ and Norton and Sun¹³⁸. The development of CFD was driven during the 1980's and 1970's by the demands of the aerospace industry, who had a clear need for CFD as a tool to reduce expensive prototyping and testing and increase safety as well as the resources to run their code on high-end computers. By the 1990's the cost of the computing power required was reduced, making CFD available to workers in a wider range of industries. This was combined with increased availability of CFD programs with more user-friendly and graphical user interfaces, such as CFX, COMSOL and Fluent, giving non-specialists the ability to apply CFD to their areas of study. The literature discussed above shows the ability of this commercial CFD software to accurately model processes within both domestic oven geometries and industrial ovens utilising impinging jets. Building on this, several studies have demonstrated the ability of these models to test geometry and operational changes to optimise for evenness and speed of cooking.

Turbulence Models

A majority of CFD studies on ovens use the k - ϵ turbulence model due to its relative ease of convergence¹³⁹, however a number of experimental and numerical studies of impinging jet systems have illustrated its inaccuracy when predicting heat transfer fluxes¹⁴⁰ due to its inaccuracy close to solid walls. In these cases, the SST model has been shown to offer a good combination of accuracy and computational complexity when suitable meshes are employed¹⁴¹.

¹³⁵ J.D. Anderson, 'Philosophy of Computational Fluid Dynamics', in *Computational Fluid Dynamics: The Basics with Applications* (McGraw Hill, 1995), 37–93.

¹³⁶ J.S. Shang, 'Three Decades of Accomplishments in Computational Fluid Dynamics', *Progress in Aerospace Sciences* 40, no. 3 (April 2004): 173–97.

¹³⁷ B. Xia and D.-W. Sun, 'Applications of Computational FLuid Dynamics (CFD) in the Food Industry: A Review', *Computers and Electronics in Agriculture*, 2002, 20.

¹³⁸ Norton and Sun, 'Computational Fluid Dynamics (CFD) – an Effective and Efficient Design and Analysis Tool for the Food Industry'.

¹³⁹ Boulet, Marcos, Dostie, and Moresoli, 'CFD Modeling of Heat Transfer and Flow Field in a Bakery Pilot Oven'.

¹⁴⁰ Verboven, Scheerlinck, Baerdemaeker, and Nicola, 'Computational Fluid Dynamics Modelling and Validation of the Temperature Distribution in a Forced Convection Oven'; Y. Xing, S. Spring, and B. Weigand, 'Experimental and Numerical Investigation of Heat Transfer Characteristics of Inline and Staggered Arrays of Impinging Jets', *Journal of Heat Transfer* 132, no. 9 (1 September 2010): 092201; S. Spring, B. Weigand, W. Krebs, and M. Hase, 'CFD Heat Transfer Predictions of a Single Circular Jet Impinging with Crossflow', in *9th ALAA/ASME Joint Thermophysics and Heat Transfer Conference* (9th AIAA/ASME Joint Thermophysics and Heat Transfer Conference, San Francisco, California: American Institute of Aeronautics and Astronautics, 2006); Zuckerman and Lior, 'Jet Impingement Heat Transfer'.

¹⁴¹ Zuckerman and Lior, 'Jet Impingement Heat Transfer'.

Radiation Models

Four approaches to radiation modelling are found in the literature: ignoring radiative transfer, discrete ordinate model, discrete ordinate only considering surface-to-surface transfer and the Monte-Carlo model. Many papers run the complete CFD model using all three approaches to decide if the additional accuracy is worth the increased computational complexity. For example, Mistry¹⁴² found only a 2% difference in radiative flux when applying discrete ordinate with participating media and the surface-to-surface discrete ordinate model, and thus used the surface-to-surface model in subsequent calculations.

Experimental Validation Methods

Experimental validation is the comparison of model predictions to experimental measurements. Four physical quantities have been used for this in oven modelling literature: air temperature, air pressure, heat flux and food temperature. The purpose of an oven is to heat food, therefore it could be said that the most important characteristic of a model of an oven is how well it predicts the heating of food. However, as discussed in section 3.2.1 the modelling of food is complex. It is possible to have an accurate model of the transfer of heat from the heating elements to the food surface but an inaccurate or incomplete model of the food's behaviour, making it difficult to separate these two aspects of the model and evaluate its performance. Additionally, modelling the cooking of food is computationally expensive and requires a transient model of the oven over the full timescale of cooking. This is likely to make the approach impractical and expensive.

The cooking of food within the oven is dependent on the convective and radiative heat flux incident up on it, and the convective mass transfer from the food to the oven air. These define the boundary condition in the numerical models of food discussed in section 3.2.1. Heat flux can be extracted from steady-state or transient models over shorter timescales than a full cooking cycle. It is therefore a useful quantity for validation as it directly describes the fundamental purpose of the oven while being simpler to measure and extract from the model than food temperature.

Air temperature, velocity or pressure are also straightforward to find experimentally and extract from a CFD model. While in reality the heat flux is determined by the velocity and temperatures

¹⁴² Mistry, Ganapathi-subbu, Dey, Bishnoi, and Castillo, 'Modeling of Transient Natural Convection Heat Transfer in Electric Ovens'.

within the oven, accurate prediction of these quantities by the model does not guarantee an accurate prediction of heat flux. This can be due to a number of factors such as empirical wall functions being applied due to the mesh being too coarse to capture near wall behaviour¹⁴³, turbulence models that are invalid within the boundary layer or an inaccurate treatment of radiative heat transfer¹⁴⁴.

3.3: Conclusions

There has been little academic research into more energy efficient or faster cooking domestic ovens. What has been published focuses on designs that compromise the design constraints laid out in section 2.2, making them unattractive to consumers and manufacturers. A patent search showed the same for corporate research; few patents claim to reduce energy consumption. The work reported in this thesis therefore addresses a clear need for a novel design of domestic oven that reduces energy consumption whilst also meeting consumer needs. The two core principles of the design; being able to cook without the oven reaching steady state and being able to maximise and control all three transfer modes is also novel. Existing designs only focus on two of the three transfer modes. Rapid heat-up in literature is achieved by increasing the heater power to reach steady state in the oven more quickly, not by altering the design such that steady state is not required.

There is a large body of work documenting predictive and explanatory numerical modelling of food cooking. The field has progressed from 2 dimensional models of heat transfer in food, to simultaneous heat and mass transfer modelling and finally, fully coupled heat and mass transfer equations in 3 dimensional geometries. Models can include empirical equations for how physical properties change with time and temperature, and also relate these parameters to flavour, colour and texture. This allows the models to predict food quality depending on cooking time and conditions. These models are however, complicated and tailored to individual food types. While they can be coupled to CFD simulations of ovens it is complex and computationally expensive to do so.

¹⁴³ Xing, Spring, and Weigand, 'Experimental and Numerical Investigation of Heat Transfer Characteristics of Inline and Staggered Arrays of Impinging Jets'; Zuckerman and Lior, 'Jet Impingement Heat Transfer'; Verboven, Scheerlinck, Baerdemaeker, and Nicola, 'Computational Fluid Dynamics Modelling and Validation of the Temperature Distribution in a Forced Convection Oven'.

¹⁴⁴ Verboven, Scheerlinck, Baerdemaeker, and Nicola, 'Computational Fluid Dynamics Modelling and Validation of the Temperature Distribution in a Forced Convection Oven'.

From the early 2000s commercial CFD software has been shown to be able to model various oven geometries and arrangements accurately, from natural convection type ovens to impingement jet industrial ovens. The use of CFD in design has also been documented. It has been used to test different design configurations and used to optimise designs for efficiency and evenness of heating, both manually and automatically. The use of CFD for oven modelling and optimisation is therefore well established, the novelty of the work presented here is the application of CFD to an entirely new design.

4: Design and Fabrication of the Prototype Ovens

4.1: Prototype IA

The various constraints on the construction and design of the prototype IA oven were described in section 2.2. The overall design strategy was outlined in section 2.4. The starting point for the prototype IA oven was a Beko fan oven with an EU efficiency rating of A and an electrical rating of 16 A and 230 V (Model number: BXIM25300XP, Arcelik, Istanbul, TK). Figure 2.9 shows a labelled cross section of prototype IA. As discussed in section 2.4 the aim of the design was to maximise the heat transferred to the food by all three heat transfer modes; convection, radiation and conduction. Prototype IA was constructed over the summer of 2017 to be exhibited at the IFA industrial fair. It was built over a short time scale of eight weeks with a corresponding limited scope for detailed design work.

Four assemblies were added to the oven, described in greater detail in following sections:

- i) A new electronics control board was designed and constructed that allowed customised control firmware to be installed. This was mounted on the roof of the oven.
- ii) The fan motor was replaced by a larger and more powerful unit.
- iii) A plenum assembly was constructed and fitted to the oven roof, to provide the impinging air jets and mount the short-wave infra-red lamps.
- iv) A directly heated steel plate was mounted in the base of the oven to provide the high temperature surface for conducting heat into the food.

4.1.1: Plenum Assembly

The plenum assembly is shown in Figure 4.1 and performed two functions. First, it acted as a duct to take air from the centrifugal fan in the back of the oven to the three rows of jets in the roof of the oven. Second, it acted as a mount for the two infra-red lamps. The plenum was made from folded and welded aluminium sheet with a thickness of 2 mm. The surface was cleaned before installation in a blast cleaning booth. The assembly was secured in the oven by runners

which slot into the existing tray racks and self-tapping screws. The back of the plenum assembly was sealed against the internal frame of the oven using high temperature silicone.

The distance between the internal frame of the oven and the plenum panel that shrouds the fan impeller was 35 mm and was determined by the dimensions of the fan impeller.

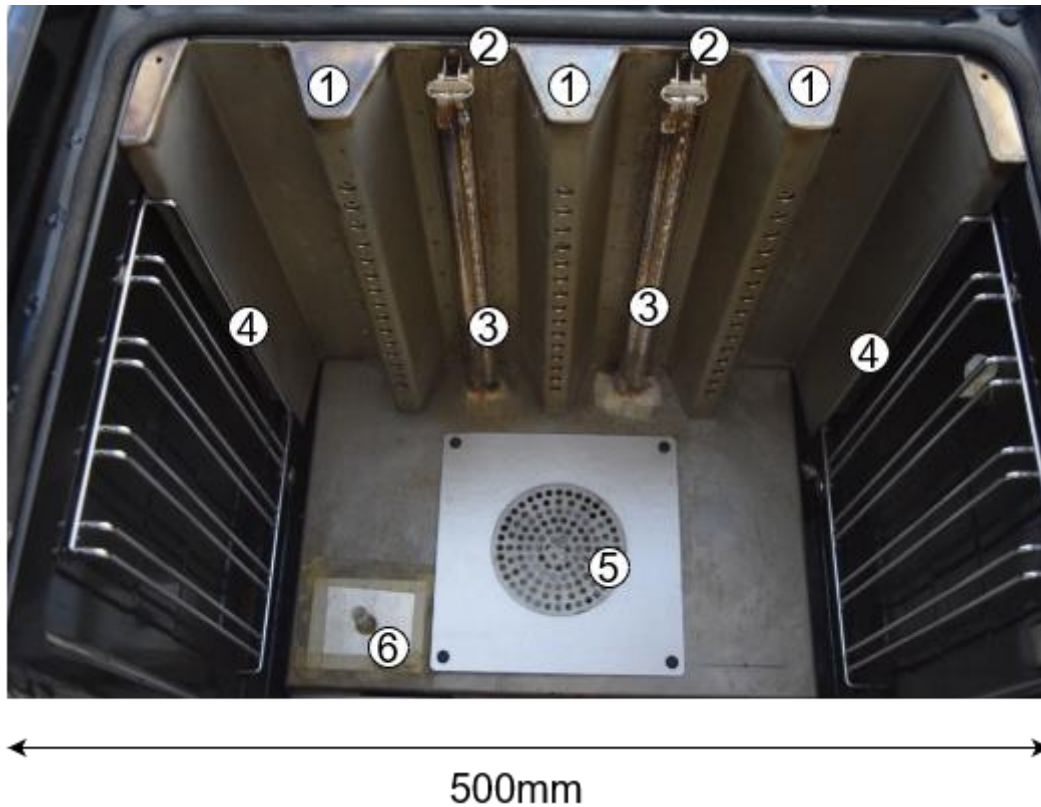


Figure 4.1: Labelled photograph of the plenum assembly in prototypes IA and IB, front view.
1 – Row of air jets, 2 – lamp mount, 3 – infra-red lamp, 4 – mounting point using existing oven rack system, 5 – fan inlet, 6 – steam inlet.

The infra-red labs were provided by Heraeus-Noblelight (Cambridge, UK). Both lamps were rated at 650 W with filament temperatures of 2000°C, giving a peak wavelength of 1.16 μm . This wavelength was chosen for its greater penetration into the food (section 2.3.3). The lamps were secured in the oven by two clips, which were in turn attached to the plenum assembly by self-tapping screws. The lamps were fitted through holes drilled in the back of the oven. The lamps were sealed against the oven walls using high temperature silicone (Loctite SI 5399, Loctite Dusseldorf, DE) and glass fibre tape.

Nozzle and Distributor Sizing

The arrangement of the nozzles in 3 rows was chosen for its ease of construction and fitting as well as to give space for the 2 infra-red lamps. The size and spacings were chosen to give a pressure drop across the nozzles of 100 Pa, measured by a manometer. This measurement and sizing process was performed by COI and aimed to make the nozzle performance comparable to that of a tunnel baking oven. The final arrangement chosen was 3 rows of 15 jets, each with a diameter of 5 mm. At 100 Pa this gave a jet velocity between 10 and 15 m/s at an air temperature of 180°C for a range of discharge coefficients (C_d) of 0.65-0.95. These values were comparable to the data for industrial ovens described in section 2.3.1.

4.1.2: Base Heater

The base heater assembly consisted of a low carbon steel plate with dimensions of $406 \times 206 \times 10$ mm resting on top of a 2.4 kW resistive element. The latter was originally the oven's grill element. The base of the oven was protected from the heat of the element by a 7 mm thick layer of silica insulating sheet (RS, Corby, UK). A 1 mm thick sheet of aluminium was located between the heating element and silica insulation and supported the weight of the baking steel and element, preventing damage to the insulating sheet. These components were enclosed within a folded aluminium casing. The temperature of the baking steel was measured by a 1 mm diameter steel clad K-type thermocouple (RS, Corby, UK) located in a 1 mm diameter thermowell drilled into the centre of the steel block.

4.1.3: Fan Motor and Mounting

The additional ductwork and air impingement jets required a much higher pressure drop than the original oven layout, thus requiring a more powerful motor. The AC shaded pole motor was replaced with a DC motor (Cat. No. 225-9591, RS, Corby, UK). The DC motor supplied significantly more power and higher rotational speed than the AC motor, 221 W and 3,200 rpm compared to 65 W and 1400 rpm. It also allowed the power and speed of the fan to be changed by altering the supplied voltage, thus enabling different impingement jet velocities to be investigated.

The DC motor had a larger mass (3 kg) and radius than the original motor (0.5 kg). A new mounting was constructed that maintained the rigidity of the back panel of the oven and

prevented the fan shaft from vibrating or processing. The fan shaft bushing was replaced with a high temperature ball bearing from FAG (Schaeffler, Herzogenaurach, De) which can be seen in Figure 4.4(b).

4.1.4: Control Board and Electronics

In a traditional fan oven only one heating element is used during a cooking cycle; either the grill element in the roof of the oven which is used for broiling, or the spiral heating element around the fan which is used to heat air for baking and roasting. In the COI prototype oven, all three heating elements and heat transfer modes can be used during a single cooking cycle. A new electronic control board was therefore designed and built. This also allowed different control schemes and algorithms to be tested and evaluated. Figure 4.2 shows a labelled photograph of the completed control board.

An Arduino UNO Rev3 microcontroller (Somerville, MA, USA) was chosen to control the system owing to its low price, ease of programming and reprogramming, and convenient input and output hardware and firmware. The mains voltage heating elements were switched on and off by 6 PF240D25 solid state relays (Schneider Electric, Rueil-Malmaison, FR) with the switching voltage and current supplied by the Arduino. Temperatures were measured by K-type thermocouples connected to 2 PVN012 multiplexors (International Rectifier, El Segundo, CA, USA), via 2 AD595CQ (Analog Devices, Norwood, MA, USA) thermocouple amplifiers with cold junction compensation. These gave a signal voltage of 0-5 V for a measured temperature range of 0-500°C. The signal voltage was read by the Arduino. Power for the fan was provided by a 24 V power supply (Mean Well LRS-200-24 model, Mean Well, Taiwan). The voltage and power delivered to the fan motor was controlled using a pulse width modulation (PWM) pin on the Arduino, via an MJH6284 power transistor (ON Semiconductors, Denver, CO, USA). Isolation between the power and control electronics was provided by an HCPL 3120 optocoupler (Broadcom, San Jose, CA, USA).

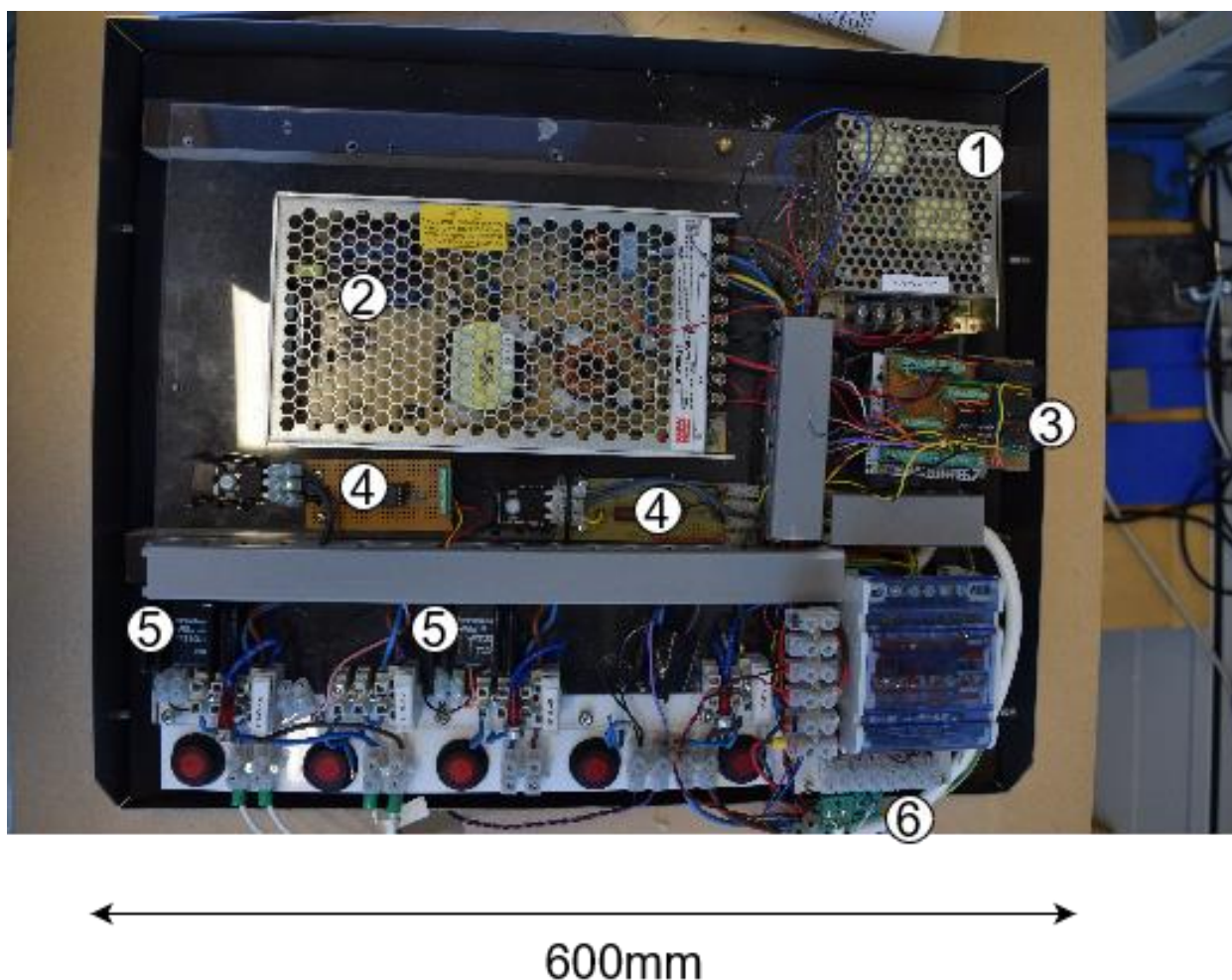


Figure 4.2: Prototype 1A control board, plan view. 1 – Arduino power supply, 2 – motor power supply, 3 – multiplexors and thermocouple amplifiers, with Arduino microcontroller beneath. 4 – Motor control boards, 5 – solid state relays for heater control, 6 – thermocouple plugs.

Humidity within the oven was measured using a proprietary sensor provided by COI. This supplied a 0-5 V signal to the Arduino, corresponding to 0-100% humidity within the oven. The humidity sensor was connected to the oven via a short piece of silicone tubing. The short length was intended to reduce condensation in the tube which would affect the reading. The mount for the sensor was 3D printed in a Form2 stereolithographic printer (FormLabs, MA, USA) using High Temperature Resin v2.0. This material was chosen as it could withstand direct contact with the inner wall of the oven while having a poor thermal conductivity. This ensured a large temperature gradient within the mount which protected the sensor from overheating.

The oven control software switched the air and base heating elements on and off to maintain the air and base temperature set points. The firmware compared the temperature measured in the

oven cavity and in the base plate and if the measured temperature is lower than the set point, power was supplied to the respective heating element, if the measured temperature was higher than the set point then power to the heater element was cut off.

The infra-red lamps were controlled over a 10 s duty cycle. The set point was a percentage power and the control software turned the lamps on for that percentage of each 10 s interval. For example, if the set point was 40%, the controller powered the lamps for the first 4 s of the 10 s interval, then left them unpowered for the remaining 6 s.

As the total rating of the 3 heating elements was greater than the 3800 W that can be supplied by a 16 A single phase AC supply, the firmware included an interlock that prevented the base heater being activated when the air heater is powered. A second interlock prevented the air heaters being powered unless the fan speed set point was above 30%. Set points were supplied to the oven via a serial connection to a laptop computer. Temperature measurements were sent to the laptop for data logging every 5 s over the same serial connection. Logging functionality was provided by the same software used for the data logger described in section 5.1

4.1.5: Steam System

A steam source supplied steam to the oven cavity and to allow the effect of humidity on cooking to be investigated. This consisted of a domestic wallpaper stripper (Ealex SS125 2000 W) with the outlet connected by silicon tubing to the plenum chamber of the oven. This could fill the oven with steam in approximately 3 minutes. Power to the steam source was separate from the control electronics of the oven and was controlled manually.

4.2: Prototype IB

Prototype IB was constructed by modifying prototype IA. The aim of the modifications was to reduce the heat-up time of the oven.

4.2.1: Replacement Air Heaters

The resistive spiral heater from the original oven, that was used as the air heater in prototype IA, was removed and replaced with three bespoke designed and constructed air heaters located within the impingement jet headers. Photographs of these heaters are shown in Figure 4.3.

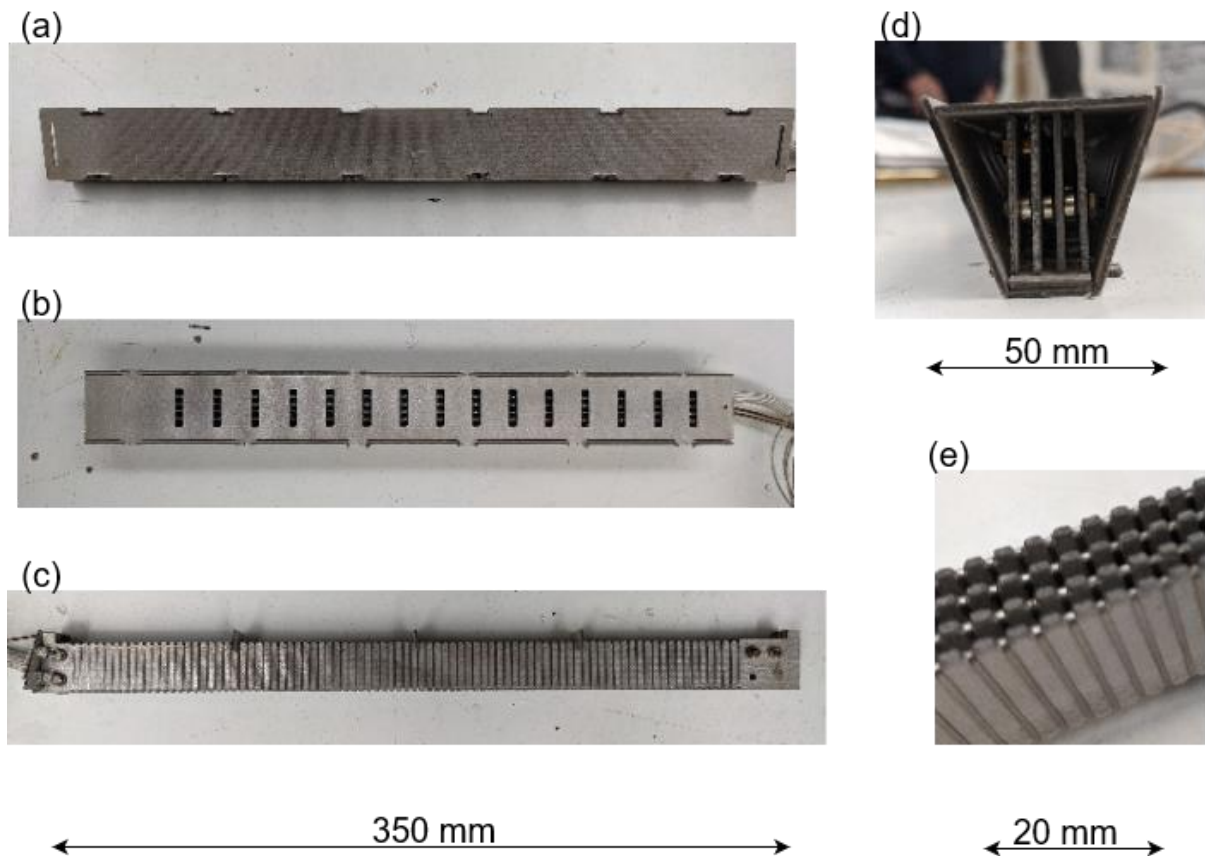


Figure 4.3: Replacement air heaters used in prototypes IB and II. (a) Completed assembly, side view. (b) Completed assembly, top view. (c) Heating elements side view. (d) End view of completed assembly with end piece removed, showing heating elements within. (e) Detail of heating element, showing resistive wire on mica support.

The heaters were constructed from 1 mm thick mica sheet. Kanthal resistive wire was wrapped around 4 notched mica beams to form the heating element. These elements are shown in Figure

4.3(c) and (e). The heating element assembly was surrounded by a mica box that prevented contact between the live heating wire and the frame of the oven as well as ducting air from the fan through the heater and to the jets. The top sheet of mica, in which holes were cut, also acted to shield the roof of the oven from thermal radiation from the heating elements.

The mica pieces were cut out using a HPC laser cutter (HPC Laser Ltd, Elland, UK). The laser cutter was unable to cut through the mica sheet completely, leaving the heater parts connected to the original mica sheet by embrittled and burned mica. This waste material was removed by blast cleaning the sheet. Once the burned material was removed the heater parts could be removed from the sheet and the heaters constructed. The external assembly was secured by wrapping with additional kanthal wire, while the heating elements were held together by four M2.5 bolts. The heaters were connected to the mains supply with copper wire electrically insulated by ceramic beads (Omega Engineering, Manchester, UK) and glass fibre sleeves. These wires were fed out of the oven with the infra-red lamp supply then sealed with silicone and connected to the control board.

4.2.2: Humidity Generation

The use of a wallpaper stripper to provide steam to the oven proved unsatisfactory as it required a separate 13 A power supply and was manually controlled. A small DC pump with a supply voltage of 9 V rated at 9.5 W (GoSo AB11, GoSo Technology, Guandong, CN) with a 1 litre water reservoir was added. The outlet of the pump was connected by 3 mm I.D. silicone tube to an opening positioned within the oven, vertically above the fan. This configuration gave a flowrate of 60 ml/min. The proposed concept was to drip water onto the spinning fan causing the water to be atomised and evaporate in the hot recirculating air. The pump was controlled by a circuit identical to that used for controlling the fan motor speed. An interlock prevented the pump from running when the recirculating air temperature was below 100°C. The pump was switched on and off by the Arduino in a control scheme identical to that used for the base plate and air temperature controllers, using the humidity as the measured variable.

This altered steam delivery system was unable to provide as great a supply of steam to the oven chamber as the original system. To allow the oven to fill with steam the rate at which steam could leak from the oven had to be reduced. The following measures were taken to seal the oven:

- i) High temperature silicone (Loctite SI 5399) sealed the oven vent in the roof of the oven.
- ii) A 2 mm hole was cut in the glass fibre insulation around the heater power cables and high temperature silicone (Loctite SI 5399) injected into the sleeve.
- iii) A 20 mm diameter hole was drilled through the side of the oven for thermocouple wire to be fed into the oven. Previously, thermocouple wire was fed through the door seal which prevented the door from sealing properly when closed. A 0.5" plumbing fitting was fitted in this hole and the gap between the thermocouples sealed using polyimide tape.

4.2.3: Fan Speed Sensor

A Hall-effect speed sensor was fitted to the fan motor in order to investigate the effect of humidity on fan behaviour. The resistance across the sensor decreases in the presence of a magnetic field which can be detected and counted by a separate integrated circuit. A magnet attached to a spinning fan shaft with the Hall-Effect sensor mounted nearby therefore allows the rotation of the fan to be measured.

The completed assembly is shown in Figure 4.4. A neodymium magnet was held in a 3D printed ring fitted around the fan shaft and held in place with grub screws. A Hall-effect sensor (Omdhon CHE-12 10NB, Omdhon, CN) is mounted next to the fan shaft in another 3D printed part shown in Figure 4.4. The sensor was supplied with an integrated device that converted the pulses received from the sensor into an RPM measurement displayed on an LCD display.

4.2.4: Induction Heating:

The base heater described in section 4.1.2 was replaced with an induction heating system. A self-contained, kitchen countertop induction cooker was selected. A 300×300 mm square hole was cut in the metal base of the oven using a plasma torch, with both the inner frame of the oven and outer skin being removed. This was required to remove any ferrous metal from between the inductive coil and the cookware. Aluminium section bolted to the outer shell of the oven supported the induction heating unit. The control panel of the induction unit was left exposed at the back of the test oven to allow the power delivered to be controlled. The spacing between the induction heater and the cookware was set at 10 mm which gave a maximum power delivered by

the heater of 1.4 kW. This gave the combined power of the air and base heaters as 3.8 kW, allowing them to be run simultaneously from a 16 A, 240 V connection.

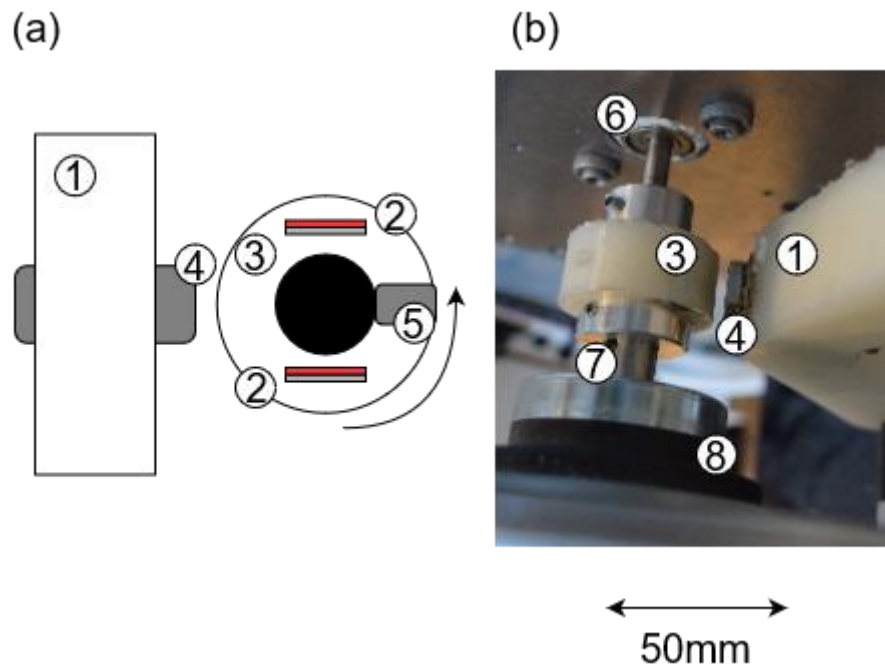


Figure 4.4: (a) schematic of the fan speed sensing system, view from the back. (b) Photograph of the system, side view. 1 - sensor mount, 2 - neodymium magnet, 3 - magnet holder, 4 - hall effect sensor, 5 - set screw, 6 - fan bearing, 7 - fan shaft, 8 - motor.

4.2.5: Fan Replacement

The fan rotor supplied with the oven was used in prototypes IA and IB. The rotor was constructed from thin sheet steel with the rotational force from the fan shaft transferred to the rotor via a flat key as shown in Figure 4.5(a). The increased speed and force supplied by the larger replacement motor caused it to distort, eventually preventing the fan shaft from gripping the rotor and causing the motor and fan shaft to spin, while the rotor remained motionless. The impeller was repaired by drilling out the eye and fitting a left-hand thread clinch nut that screwed directly onto the fan shaft, as shown in Figure 4.5(b). The clinch nut was further secured with high temperature silicone.

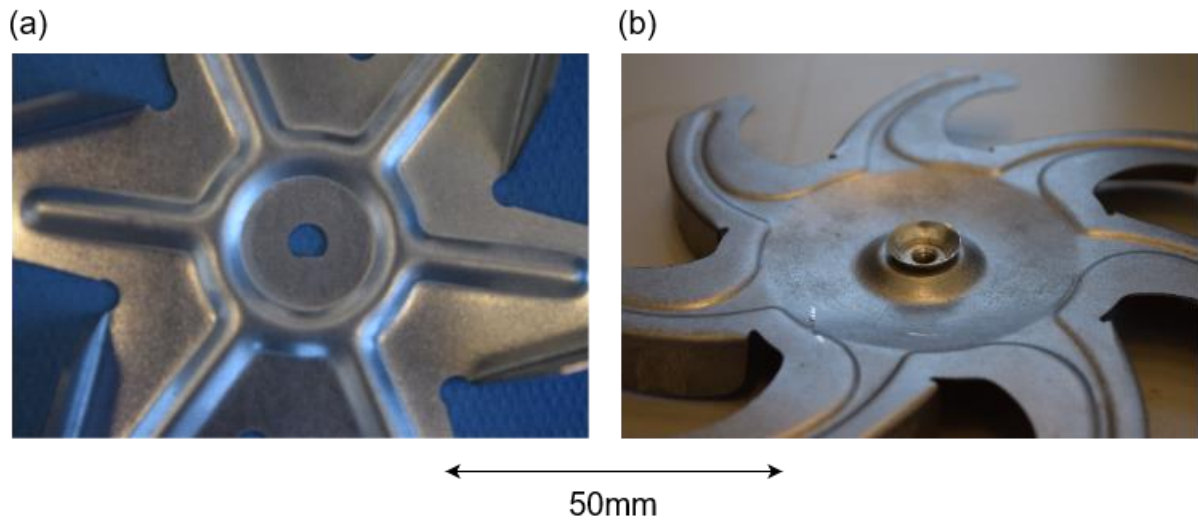


Figure 4.5: (a) Original fan impellor, (b) fan impellor with replacement connection to the fan shaft.

4.3: Prototype II

COI were engaged in talks with Chinese OEM manufacturer Quingdao XingBang (Shangdong CN) as a manufacturing partner for the completed design. An oven supplied by this company was therefore used as the basis for the prototype II oven.

The XingBang oven was stripped of the following components and assemblies:

- i) The control panel and electronics board.
- ii) All heating elements were removed; the spiral air heater around the fan, the grill element in the roof of the oven and heater element in the base of the oven.
- iii) The fan and fan motor.
- iv) The fan shroud at the back of the cooking chamber

Three assemblies were designed, constructed, and fitted to the stripped-out oven shell:

- i) An electronics assembly was fitted above the oven cavity but within the oven shell. This included a microcontroller, relays to control all the heating elements and fans, a touchscreen for reporting and user control, and power consumption and temperature logging functionality.
- ii) Ductwork on the back and roof of the oven interior. This contained the oven fan, air heaters and jets and the infra-red lamps. This was split into two assemblies: (i) a backplate assembly that contained the fan and associated ductwork, and (ii) the heater box assembly that contained the heater units and impinging jets.
- iii) An induction heating assembly in the base of the oven.

These assemblies are shown in Figure 4.6 and are described in the following sections.

4.3.1: Electronics Board and Assembly

Overview and Changes from Prototype I

The electronics board in prototype II aimed to improve on prototype I by allowing easier control for consumers and to include power consumption data logging within the oven, rather than relying on an external datalogger. Figure 4.7 is a labelled photograph of board using prototype II.

Maxim MAX31855 (Maxim Integrated, San Jose, CA, USA) thermocouple amplifiers were used. These reported the temperature using serial communications, rather than a voltage. This was more accurate than relying on the Arduino's inbuilt analogue to digital converters. The DC motor was replaced with a shaded pole AC motor (Guangdong Shunde Electric Motor, Guangdong, CN). The motor was chosen to give similar RPM to that generated by the DC motor while being significantly cheaper and without requiring a separate DC supply. The disadvantage was a lack of analogue fan speed control. The induction unit was integrated into the central oven control and power supply rather than the independent control and supply in prototype I. This necessitated additional software in the Arduino and additional hardware on the control board.

Microcontroller

An Arduino MEGA microcontroller (Somerville, MA, USA) was chosen to control the oven. The Arduino family of microcontrollers was chosen due to experience using the UNO model in prototype I. The more powerful MEGA unit was selected as the user interface (UI) for prototype II required a greater amount of onboard memory, while the built-in logging of power consumption gave increased demand for digital output and input pins. Two dedicated serial communication chips were also required for separate control of a touchscreen and induction heating unit.

Touchscreen

A 107 mm (4.2") resistive touchscreen was used for displaying the oven status and inputting and amending oven setpoints. The 4D GEN4-ULCD-43DT (4D systems, Minchinbury, AU) unit was selected due to availability and inclusion of an Arduino library that allowed simplified communication between the microcontroller and touchscreen. A SparkFun 3.3 V to 5 V level switcher (SparkFun electronics, Niwott, CO, USA) converted the 5 V serial communication on the Arduino side to the 3.3 V switching required by the touchscreen unit.

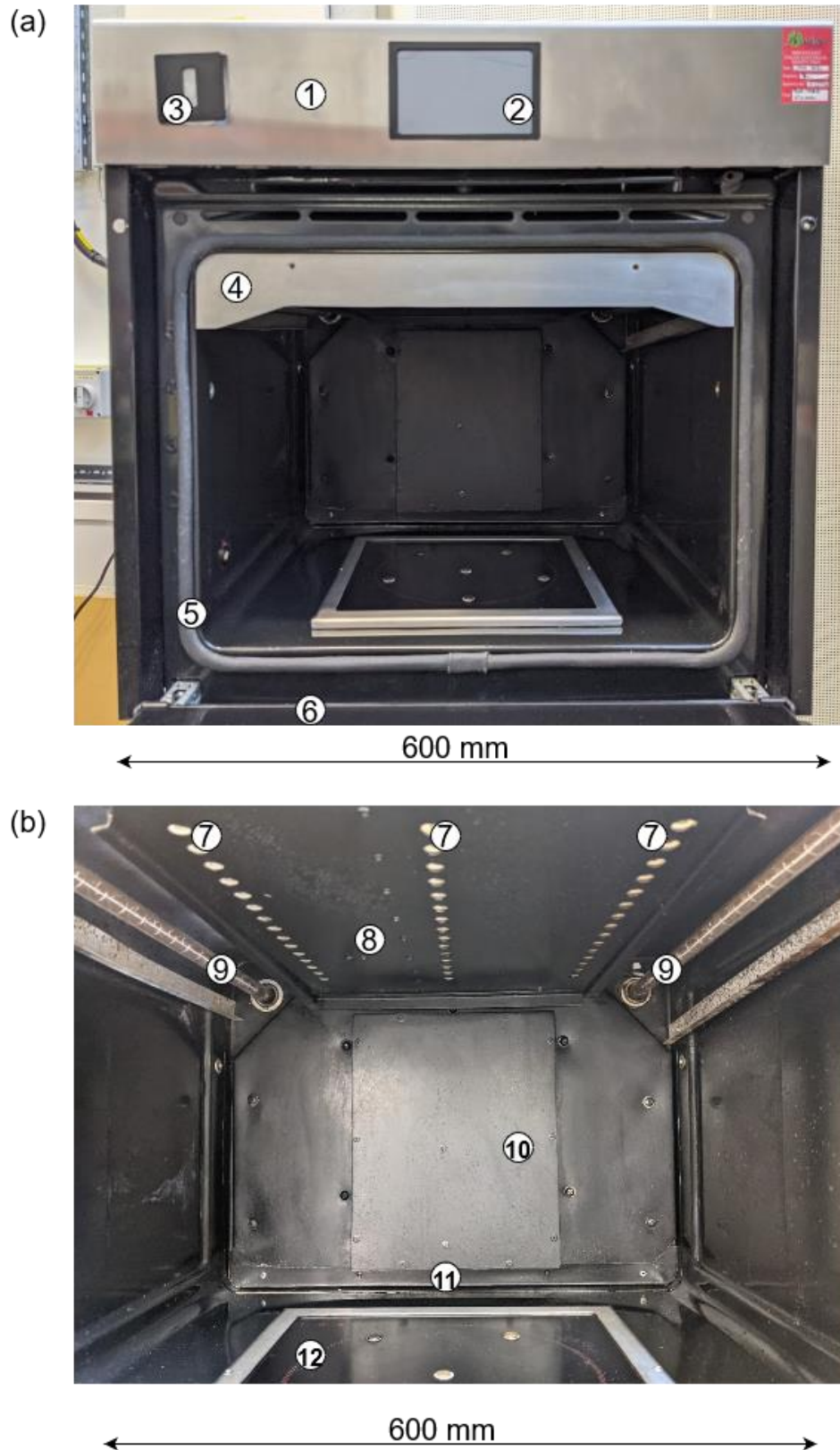


Figure 4.6: Labelled photographs of prototype II, front view. (a) External view, (b) Interior of cooking chamber. 1 – Fascia plate, 2 – resistive touchscreen, 3 – water reservoir, 4 – fascia covering heater box assembly, 5 – door seal, 6 – door (open position). 7 – Impingement jets, 8 – heater box assembly, 9 – infra-red lamps, 10 – back plate assembly, 11 – fan inlet duct, 12 – induction heating plate.



← 350 mm →

Figure 4.7: Labelled photograph of the control board for prototype II. 1 – Resistive touch screen, 2 – isolation chip for connection to the induction unit, 3 – optocoupler board connecting the power meters to the Arduino, 4 – Arduino MEGA microcontroller, 5 – power meters, 6 – thermocouple connections, 7 – multiplexors and thermocouple amplifiers, 8 – solid state relays for heater control, 9 – solid state relays for fan control.

Induction Control

The microcontroller communicated status and power setpoints to the induction unit using inter-integrated circuit (I2C) serial communication. Both the Arduino and induction board use 0-5 V switching. However, the ground on the induction board was floating at 120 V AC, due to the design of its internal DC supply preventing a direct connection between the Arduino, grounded at 0 V and the induction unit. A MikroElectronica M-1878 (Belgrade, SRB) board separated the Arduino and induction unit and isolated the two sides of the serial communication, allowing either side to drive the digital signal while providing complete voltage isolation between the two sides. The induction unit could be controlled in two ways, either (i) power could be set directly (0-100%) or (ii) used to control the pan temperature with an on/off control method, similar to that used for the air heaters.

Heater, Fan and Humidity Control

The air heaters and infra-red lamps and fans were switched on and off using PF240D25 solid state relays (Schneider Electric, Rueil-Malmaison, FR) in an identical arrangement to that used for heater control in prototype I. The control algorithms used were also identical to those used in prototype I. Humidity was measured by a proprietary COI humidity sensor. This reported humidity as a 0-5 V reading that the Arduino scales to 0-100% volume percentage water vapour in the oven air. Humidity could be increased by pumping water into the oven chamber. A GoSo AB11 DC peristaltic pump (Guangdong Zhongshan Gaoshuo Electronics Company, Guangdong, CN) was used, controlled by a simple on/off control loop. The evaporator part of the humidity control was enclosed with the convection system, described in section 4.3.2.

Power Meters

Five Grässlin Taxo E45 power meters (Grässlin GmbH, St. Georgen im Schwarzwald, DE) were used to record the power consumed by different parts of the oven. Table 4.1 presents the metering arrangement. Power consumption was automatically reported by each power meter by a pulse after each 0.001 kWhr (3.6 kJ) of electricity consumed. This pulse was generated by supplying 12 V across the pulse terminals on the power meters. The current allowed by the power meter increased from ~ 0 mA to 27 mA for 90 ms during each pulse. Lite-On, LTV-847 optocouplers (Lite-On, Cramlington, UK) connected in series with the pulse terminals gave a 0-5 V pulse that was detected and recorded by the Arduino.

Table 4.1: Oven electricity consumers and associated power meter in prototype II

Power meter channel	Consumers Connected
P0	Total oven consumption
P1	Air heaters
P2	Infra-red lamps
P3	Induction unit
P4	Fan motor

Thermocouple Connections

As in prototype I, K-type thermocouples were used to measure temperatures within prototype II. Table 4.2 presents the allocation of the 8 thermocouple channels on the electronics board.

Two CD4052BE (Texas Instruments, Dallas, TX, USA) 4 channel multiplexors connected the 8 thermocouple channels to the two thermocouple amplifiers.

Table 4.2: Thermocouple numbering and location within prototype II

Thermocouple channel	Location
T0	Induction pan
T1	Fan outlet
T2	Air heater outlet
T3	Infra-red lamp 1
T4	Infra-red lamp 2
T5	Control board temperature
T6	Spare 1
T7	Spare 2

Oven Firmware:

The Arduino firmware and screen user interface was developed by Milford's software engineering (Cambridge, UK). Setpoints for air temperature, infra-red lamp duty cycle, plate temperature or power and humidity could be changed using the touchscreen display. The touchscreen reported the measured temperatures. The Arduino recorded temperature and power consumption data in .csv files for each cooking cycle that could be accessed via the USB connection for further analysis.

4.3.2: Fan and Plenum Assembly

As with prototype I, the fan and plenum assembly acted to duct air into the circulation fan and duct the outlet from the fan to 45 4 mm diameter impingement nozzles in the roof of the oven. The plenum also housed the infra-red lamps and air heaters of the same design described in section 4.2.1 and shown in Figure 4.3.

The changes in plenum design between prototypes I and II were made to simplify construction alteration and repair.

Figure 4.8 shows that the plenum was formed of 2 assemblies both fabricated from folded 2 mm thick aluminium sheet. The backplate assembly was formed from two parts, the fan scroll which was rivetted to the frame of the oven, and the outer plate which bolted over the top of the fan scroll and was attached to the oven frame via a set of clinch nuts. The backplate assembly is

shown with the outer plate removed in Figure 4.8(a) and with the outer plate in place in Figure 4.6. Air was drawn from the cooking chamber through a slot in the base of this assembly and into the eye of the impeller which then fed the air into the second assembly, the heater box.

The heater box is shown *in-situ* in Figure 4.6 and removed and opened in Figure 4.8(b). Air from the backplate assembly was fed into the assembly via an opening in the back. The positive pressure drove air down through the top of the heater units and out through the impingement jets onto the food. The heater box was formed from two folded aluminium trays that were screwed together to form the box and sealed with polyimide tape. Power and thermocouple wires were fed into the box via a gland in the top tray. The heater box was fixed within the oven by a mount that connected to the top of the backplate assembly and by a pair of M5 bolts at the front of the oven.

An extruded aluminium section was fixed within the heater box as a part of the steam generation system. Water from the pump described in section 4.3.1 flowed into the tray and was evaporated by the hot and fast-flowing air within the heater box, thereby increasing humidity within the oven. A drain in the heater box ducted any excess water that spilled from the tray out of the heater box and into the cooking chamber. This was to prevent standing water within the heater box causing an electrical fault.

The infra-red lamps were located on either side of the plenum in the oven roof and rested on folded aluminium brackets rivetted to the sides of the plenum as shown in Figure 4.6. Different lamps were selected to those in prototype I. A Chinese manufacturer (O-Yate Lighting Electrical Company, Lianyungang, CN) was selected due to a much lower cost per unit which made them a more realistic choice for a production version of the oven. Additionally, a larger power draw of 1200 W per lamp was selected to investigate the efficacy of doubling the amount of infra-red power that could be supplied. This was specified by COI.

The fan motor was replaced by a shaded pole motor as discussed in section 4.3.1, this fitted into the mount for the fan supplied with the oven. A Hall effect rotation sensor (Honeywell, Charlotte, NC, USA) was fitted, similar to prototype I. The magnet was fixed by milling a slot on the end of the fan shaft then fixing the magnet using epoxy. The sensor was fitted to the back of the motor in a 3D printed ring.

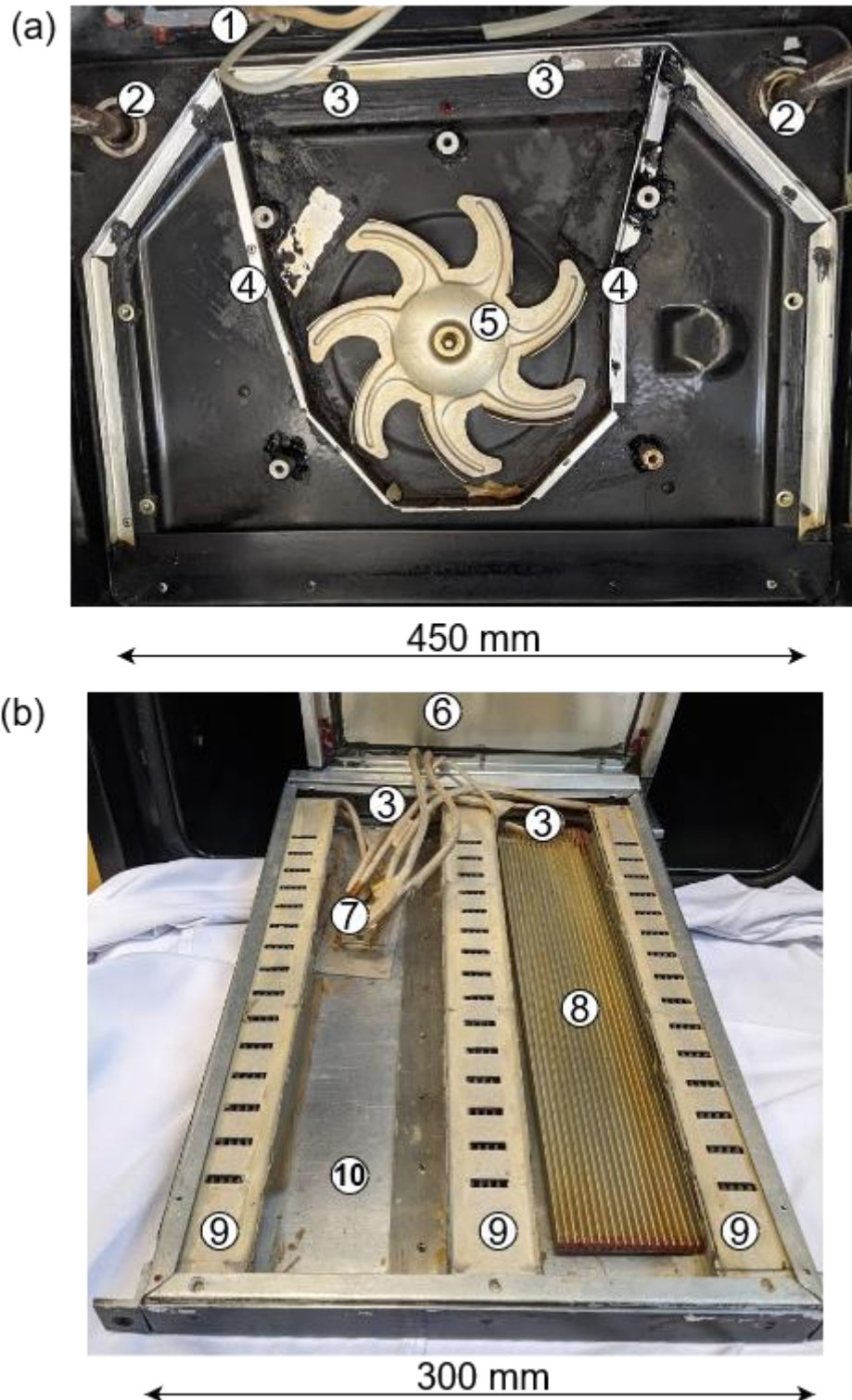


Figure 4.8: Photographs of the convection system in prototype II. (a) Back plate assembly with fan cover removed - front view. (b) Heater box with top cover removed – top view. 1 – Gland for power and thermocouple wires to enter the oven. 2 – Infra-red lamp, 3 – duct for air to flow from the back plate assembly into the heater box. 4 – Fan scroll, 5 – fan impeller, 6 – heater box top tray, 7 – junction box for connecting heaters to mains supply. 8 – Tray for steam generation, 9 – Heater units, 10 – Heater box bottom tray.

4.3.3: Induction Assembly

Induction heating was provided by a self-contained unit, provided by CHK Corp (Shenzhen, CN). This unit is shown in Figure 2.8. The unit required a 240 V AC power supply and communicated with the control board over I2C serial communication, receiving power set point information and transmitting status updates.

A circular hole of diameter 200 mm was cut in the centre of the base of the oven using a plasma torch. A sheet of ceramic glass with dimensions 300×300×5 mm was then positioned over the hole for cookware to rest on. The ceramic glass was secured in place by a folded aluminium frame which bolted to the base of the oven. A laser cut piece of mica and a ring of high temperature silicone (Loctite SI 5399) acted as a seal and were pinched between the oven base and the aluminium frame. This completed glass and frame assembly is shown in Figure 4.9.

The cookware rested on six brass pins machined from M8 brass bolts. These were sited in 8 mm holes drilled through the ceramic glass, as shown in Figure 4.9(a). The holes were made using a diamond tipped drill and secured using PTFE nuts. PTFE was chosen as its softness prevented overtightening from cracking the glass. A K-type thermocouple was sited within one of the brass pins and used to give a contact measurement of the cookware temperature that could be used to control the induction plate's power. The thermocouple junction was electrically insulated using polyimide tape to prevent the electrical currents generated by the induction coil influencing the reading.

Four pieces of 20×3 mm aluminium L-section were rivetted to the underside of the base of the oven chamber. As supplied, the base of the oven chamber was dished and the aluminium section acted to pull the sheet steel flat, in turn allowing the ceramic glass and mica gasket to sit flush against oven base. This was required to seal the base, as well as preventing any point loads on the ceramic glass which could cause it to crack.

The induction heating unit was pressed against the underside of the ceramic glass by two aluminium strips which bolted to the aluminium section. The induction unit included a cooling fan which required air flow in order to cool the power transistors and capacitors within. To allow the cooling fan to draw in air a 100 mm diameter hole was cut in the outer skin of the oven, shown in Figure 4.9(c).

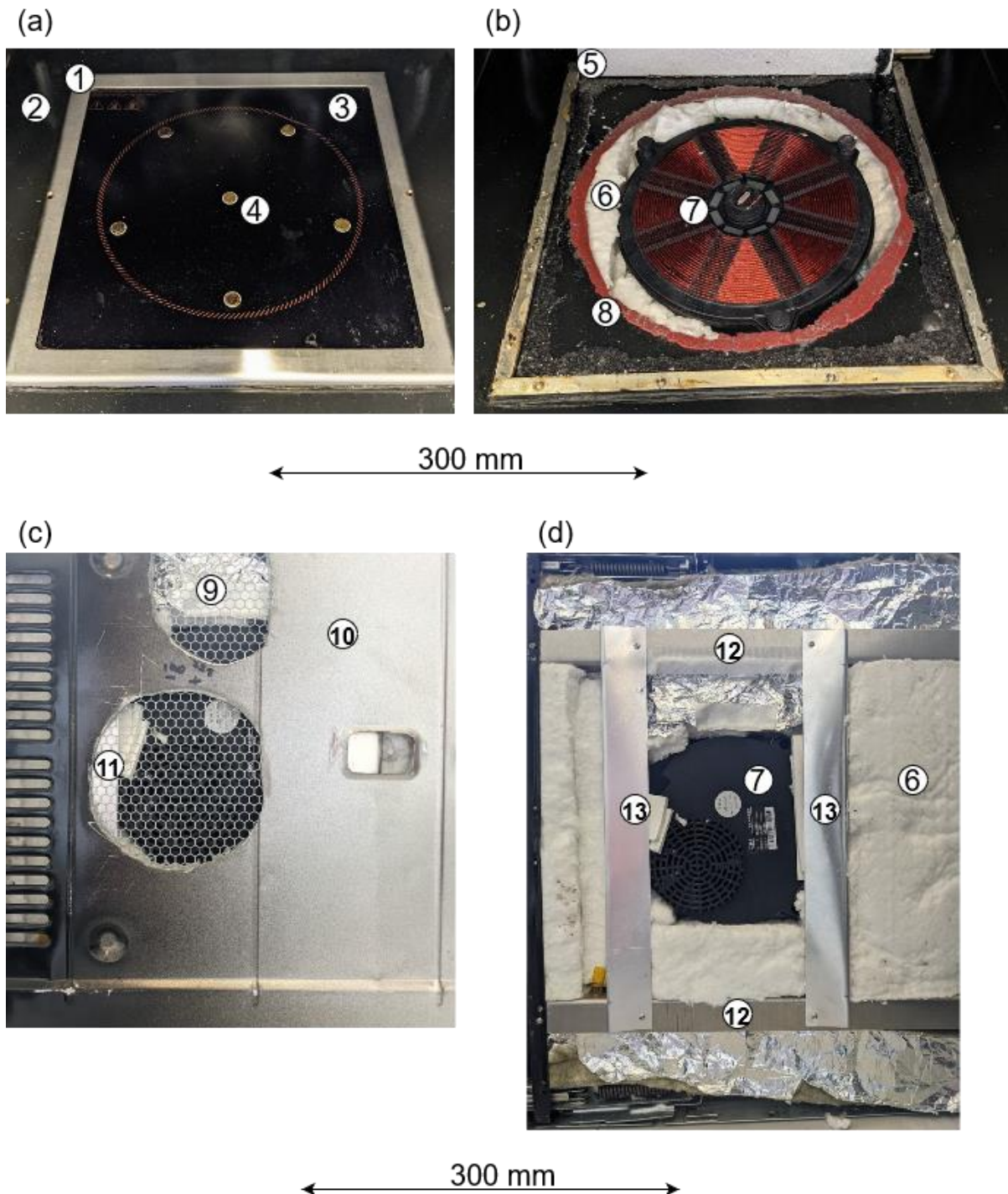


Figure 4.9: Induction unit, top view. (a) With glass plate in place, (b) with glass plate removed. Bottom view (c) with oven base sheet in place, (d) with oven base sheet removed.
 1 – Metal frame, 2 – base of the oven, 3 – glass plate, 4 – brass pin for temperature measurement. 5 – Underside of glass plate, 6 – ceramic wool insulation beneath cooking chamber. 7 – Induction unit, 8 – seal formed from high temperature silicone (Loctite SI 5399). 9 – Exhaust port, 10 – oven base sheet, 11 – cooling fan inlet port, 12 – aluminium section for pulling base of cooking chamber flat. 13 – Aluminium section holding induction unit in place.

4.4: Prototype III

Prototype III was a final pre-production prototype incorporating all the learnings from the construction and testing of prototypes I and II. It was also designed to be as close as possible to a mass-manufacture design. As much as was practical of the frame was formed from stamped and press folded aluminium sheet. The electronic components were all machine made rather than hand soldered and built. Mechanical design was performed by Huxley Bertram Engineering Limited (Cottenham, UK) (HBE) and COI; electronic design was completed by COI while firmware was created by Milford Software Engineering. Sheet metal stamping and folding was performed by RnJ Fabrications (Huntingdon UK), machined parts were produced by R&D Precision (St. Ives Cambridgeshire, UK). Assembly and conceptual design was performed by the author and Dr Mark Williamson of COI.

The oven frame was supplied by XingBang appliances (Shangdong, CN) who were able to supply oven carcasses without the components not required in the COI design. The oven carcass supplied from China consisted of the following parts:

- i) A black enamelled inner frame that forms the cooking chamber of the oven.
- ii) 20 mm of ceramic wool insulation around the internal frame.
- iii) A quadruple glazed oven door sealed with glass fibre rope.
- iv) A centrifugal fan and duct sited at the top of the oven drew air from the rear of the oven and from the space between the panes of glass and blew it out of the unit, preventing the electronics from overheating and reducing the temperature of the external surfaces.
- v) An external sheet steel skin that covered the ceramic wool insulation and provided a solid structure to support the inner oven frame, oven door, circulation fan and electronics.

In previous prototypes all the control electronics, heating elements and oven circulation fan motor had to be removed and disposed of which was both wasteful of materials and time consuming.

Labelled photographs, showing the salient features of prototype III are shown in Figure 4.10. As with earlier prototypes various assemblies were added to the oven carcass to provide the required functionality:

- i) A custom pair of Printed Circuit Boards (PCB) including a resistive touchscreen provided control of the various heating elements and fans. A user interface was included for changing set points and inputting recipes. The boards also logged power consumption and the readings from 8 K-type thermocouples sited around the oven.
- ii) An induction heating unit identical to that used in prototype II. The assembly containing this unit was also similar to that described in section 4.3.3.
- iii) A ducting system in the back and roof of the oven that drew air from the back of the oven, heated it and fed the impingement jets that blew down on to the top of the food. This assembly also contained the infra-red lamps.
- iv) An additional assembly mounted above the oven chamber was used to evaluate the plausibility of recovering heat from gases venting from the oven chamber and using it to heat water, with the intention of using the heated water for domestic chores. This assembly also contained the water reservoir for the steam generator which used a cartridge heater to heat water and generate steam to fill the oven cavity.

4.4.1: Electronics Boards and Assembly

Figure 4.11 shows the two custom printed circuit boards which were provided by COI. One board (Figure 4.11(a)) housed the mains power components: relays used to switch the power to the heating elements and fans on and off and the 12 V DC power supply for the control board and touchscreen. The second board (Figure 4.11(b)) provided the processing, memory, USB and WiFi connectivity. Instructions and updated setpoints could be sent to the oven over WiFi while power and temperature data could be downloaded to a computer over the USB connection for processing and analysis. As with earlier prototypes, temperatures within the oven were measured using K-type thermocouples. An additional thermistor was housed within a stainless-steel probe to measure the internal temperature of food within the oven, particularly meat joints.

Electromechanical relays were used for power switching, as these were significantly cheaper than the solid-state relays used on prototypes I and II. The infra-red lamps were switched with a solid-state relay to deal with the in-rush current into the lamps.

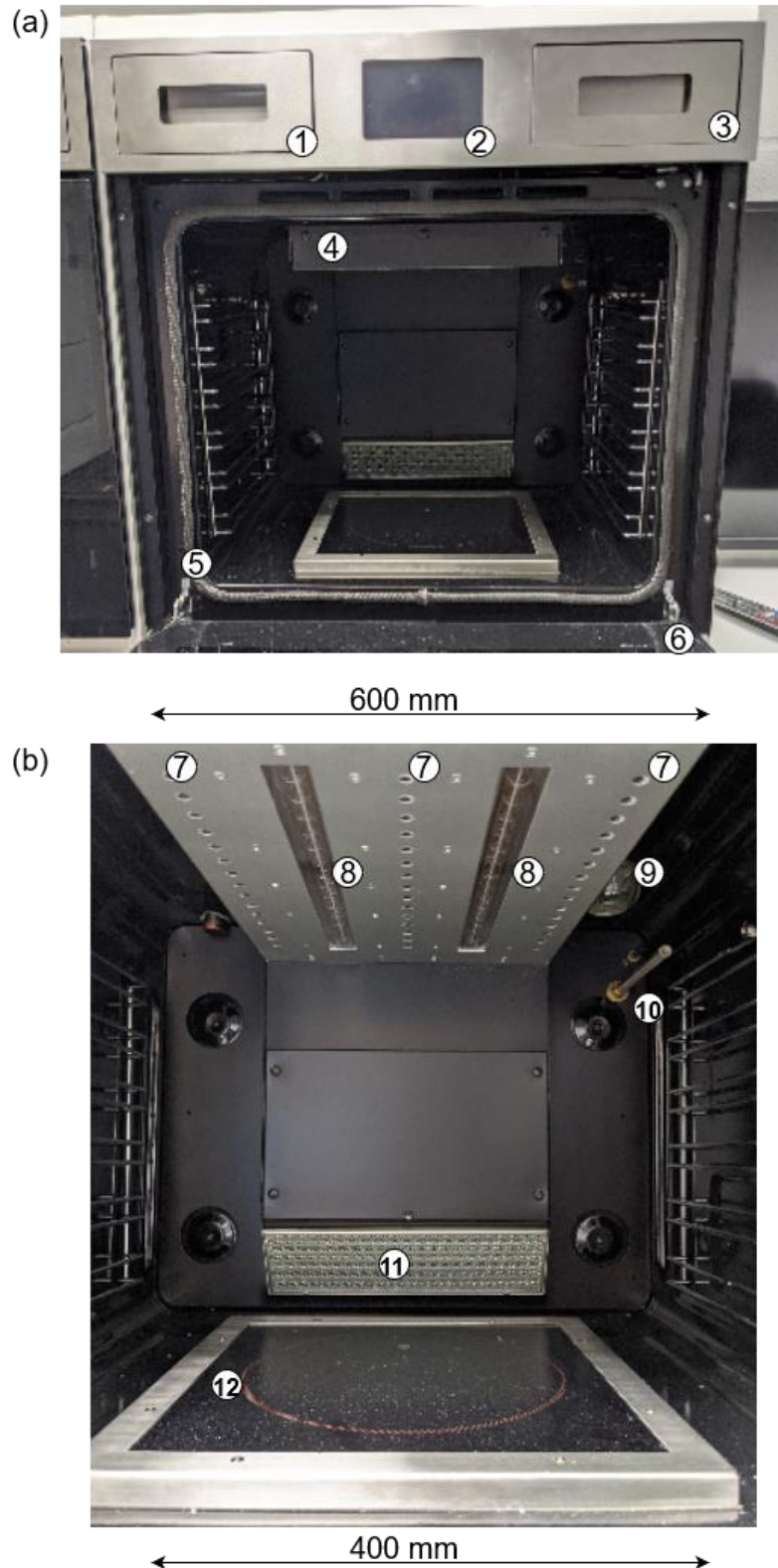


Figure 4.10: Labeled photograph of prototype III, front view. (a) External view, (b) cooking chamber. 1 - Heat recovery tray, 2 – resistive touchscreen for control, 3 – water tray for humidity generator, 4 – heater box, 5 – glass fibre door seal, 6 – quadruple glazed door (open position). 7 – Impingement jets, 8 – infra-red lamps, 9 – oven light, 10 – cartridge heater for steam generation, with water tray removed. 11 – Fan inlet with grease catcher. 12 – Induction plate.

Firmware for the oven was written by Milford's Software Engineering, who also provided software for prototype II. Oven setpoints could be inputted in two ways. One was to manually alter the oven settings on the display during the cooking process as with a traditional oven and prototypes I and II. Given the more complex nature of the various heating elements compared to a traditional oven, a recipe system was also included. Each recipe consisted of multiple intervals for which the oven temperature setpoints, humidity setpoint and infra-red duty cycle could be set individually. The oven would progress from one interval to the next based either on the time elapsed or when the temperature measured by the food probe reached a specific value. Air heater, induction plate and infra-red lamp control was identical to that described in section 4.3.1 for prototype II. The humidity system used a cartridge heater to boil water, generate steam and increase humidity within the oven. The oven could also reduce humidity by opening a valve to allow fresh air into the cooking chamber and displace humid air. The humidity was controlled to the nearest 10% to prevent the controller rapidly changing between the two control actions.

4.4.2: Ductwork and Infra-Red Lamp Mounting

The overall design for the convection assembly was very similar to prototype II and is shown in Figure 4.12. The number of parts compared to the assembly in prototype II was reduced by the application of CNC stamping and folding machines by RnJ fabrications, which allowed larger sheets of metal to be cut and folded. The convection assembly was formed from two parts: (i) the heater box, a folded aluminium section built outside the oven that contained the air heaters and infra-red lamps. This was then inserted into the second part, (ii) a mount that had been riveted to the oven interior and contained the circulation fan and scroll. The heater box was then secured using self-tapping screws.

The heater units were altered from the those used in prototypes IB and II and are shown in Figure 4.13. The kanthal wire wrapped mica sheets were replaced with a finned cartridge heater with the same power rating, to reduce cost.

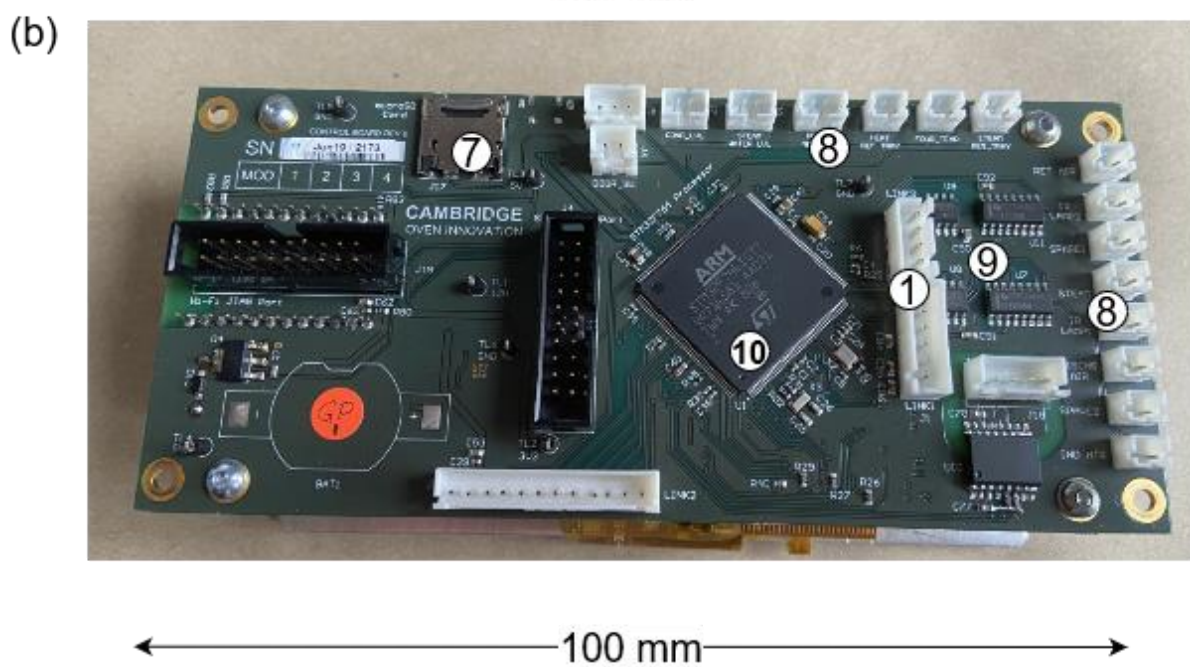
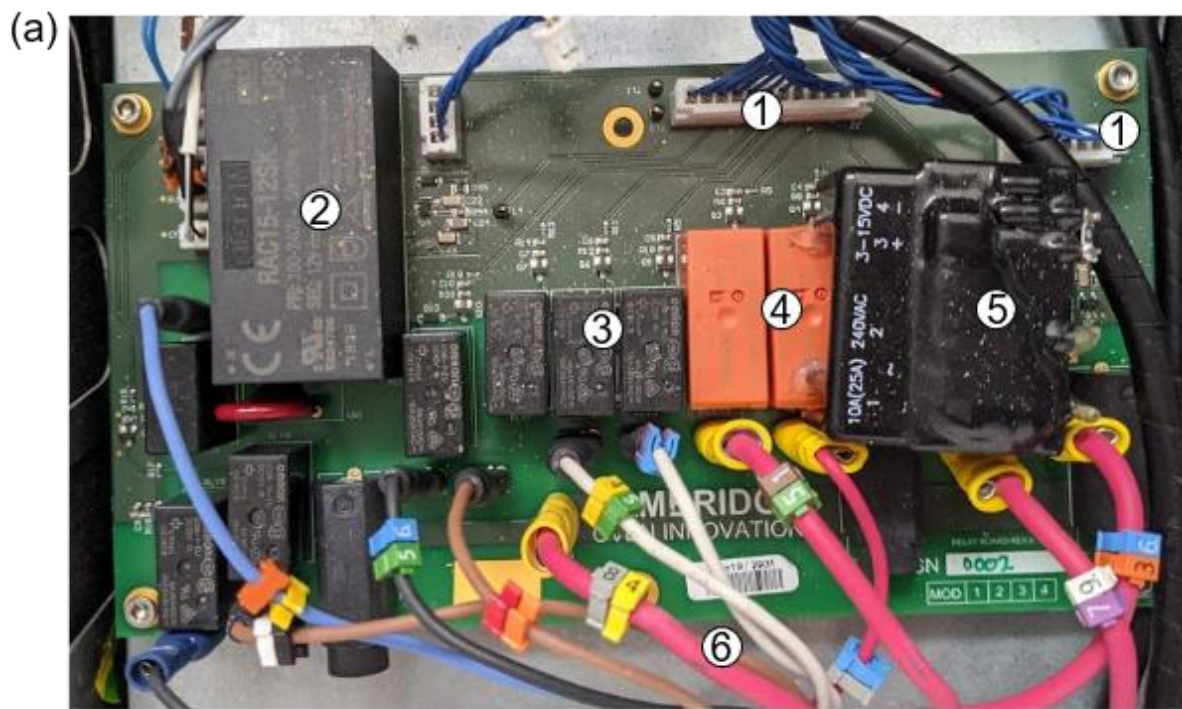


Figure 4.11: Labelled photographs of prototype III electronics, top view. (a) High voltage board, (b) low voltage board. 1 – Control link between boards, 2 – 12 V DC power supply for low voltage board, 3 – motor control relays, 4 – heater control relays, 5 – infra-red lamp control relay, 6 – heater power supply wires, 7 – SD card slot, 8 – thermocouple connections, 9 – thermocouple amplifiers, 10 – ARM microcontroller.

The position of the infra-red lamps was also changed from prototype II. The lamps were moved into the heater box and located behind quartz glass panels. The purpose of this change was: (i) give the lamps greater protection from mechanical damage by completely enclosing them. (ii) protect the lamps from overheating. The position of the lamps in prototype II in the top corners of the oven proved problematic as the air in this region was stagnant, causing the lamps to exceed their design temperature of 500°C and damage the reflective coating. The air within the heater box is at a higher velocity and as it has yet to pass through the air heaters, it is also relatively colder and therefore more able to cool the lamps.

Another advantage of this configuration was that the thermal energy lost by the lamps to the air in the heater box is not wasted as it heats the air passing out of the impingement jets and onto the top of the food, giving a small increase in thermal efficiency.

4.4.3: Induction Unit

The induction unit was of a similar design to that trialled in prototype II but a more production ready design, with fewer individual parts. It is shown in Figure 4.14. The assembly consisted of three subassemblies:

- i) Electronics and heater unit
- ii) A cover and cooking surface within the cooking chamber
- iii) A frame external to the cooking chamber for mounting the heating unit and ensuring the base of the oven remained flat.

A 200 mm circular hole was cut in the centre of the bottom of the cooking chamber. The induction heating unit was identical to the CHK unit used in prototype II and described in section 4.3.3. The sole change was the addition of a cooling duct, allowing cool air to be drawn from under the oven by the unit's inbuilt cooling fan and discharged down a fluorinated ethylene propylene (FEP) duct leading to the back of the oven.

The cooking surface within the cooking chamber consisted of a piece of ceramic glass upon which cookware could be placed. Underneath the ceramic glass a tile of MicrothermTM insulation reduced heat losses and protected the induction heater electronics from the heat of the oven. This was included as the oven was designed to clean pyrolytically which requires air temperatures

of 400°C. The insulation and ceramic glass were held in place by a brushed stainless-steel frame. An 8 mm diameter counter bored hole was cut in the glass using a diamond drill. Into this an aluminium plug was inserted that contained a thermocouple and could be used to measure the temperature of the cookware. Temperature measurements were only taken by the firmware while the induction unit was temporarily unpowered to prevent interference from the coil affecting the readings. The unit was sealed against the frame of the oven chamber by a laser cut mica gasket which was pinched between the brushed stainless-steel frame and the oven frame.

External to the cooking chamber, another stainless-steel frame was mounted between the cooking chamber and the outside of the oven unit. This frame was riveted to the skin of the cooking chamber and served to pull the base of the oven flat. As supplied, the metal of the oven was very uneven and this would prevent the induction unit sealing against the oven skin and could cause the ceramic glass to shatter or crack.

4.4.4: Heat Recovery

A concept trialled in prototype III was to recover heat from the oven vent gases and use this to heat water that could be used elsewhere. The system also condensed grease and water from the vent gases that would otherwise deposit on surfaces within the kitchen and reduce the load on air conditioning systems if applicable. The reservoir was removable, allowing easy filling and emptying of water and condensate. The pressure gradient to drive flow through the system was provided by connecting the outlet from the heat exchanger to the inlet of the cooling fan which is at negative pressure. The heat recovery tray and its connection to the oven is shown in Figure 4.15.

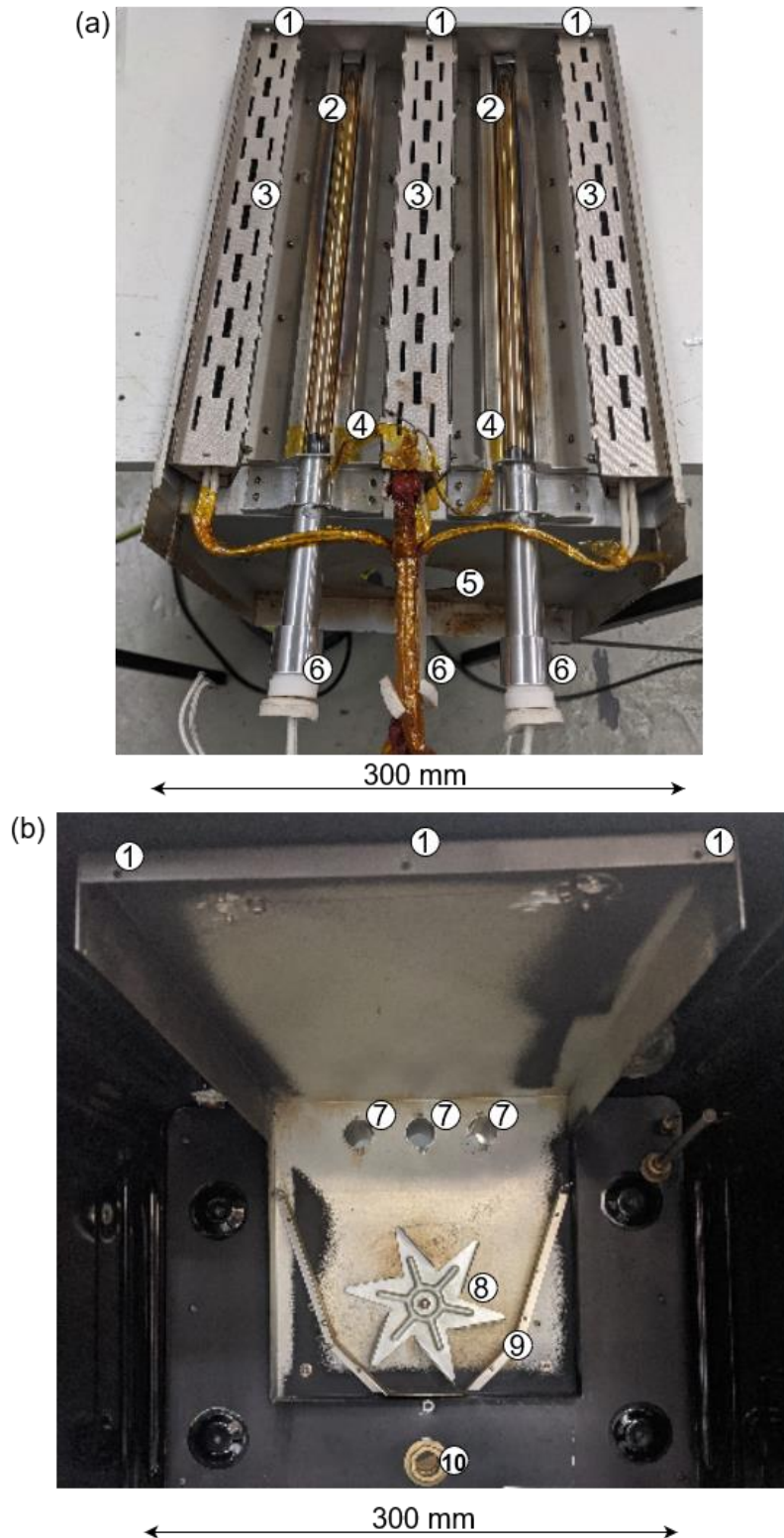


Figure 4.12: Labeled photograph of the convection system in prototype III. (a) Internals of the heater box assembly, top view. (b) Inside of the cooking chamber with the heater box assembly removed, front view. 1 – Screw holes for securing the heater box assembly. 2 – Infra-red lamps with reflecting panels. 3 – Air heaters, 4 – thermocouples for measuring the lamp temperature. 5 – Fan inlet, 6. foamed silicone seals, 7 – ports for infra-red lamps, power cables and thermocouple wire to enter the oven. 8 – Fan impeller, 9 – fan scroll, 10 – fresh air inlet.

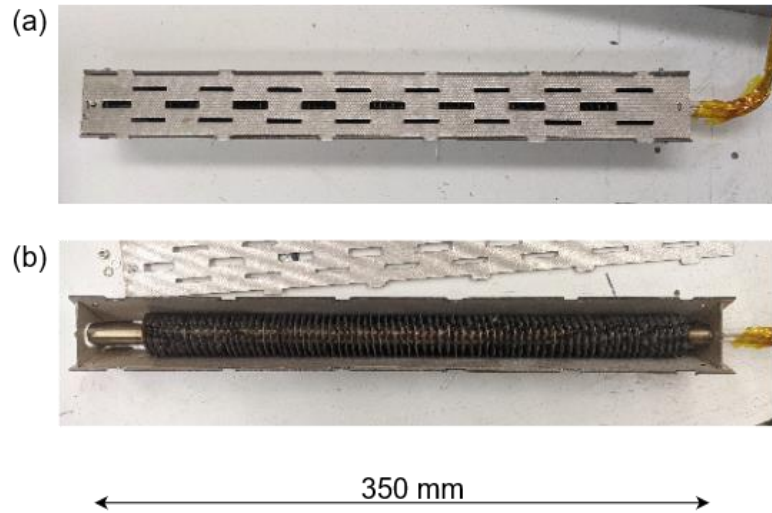


Figure 4.13: Photographs of the heater units within prototype III, top view. (a) Completed assembly. (b) Completed assembly with the top panel removed, showing the finned heater within.

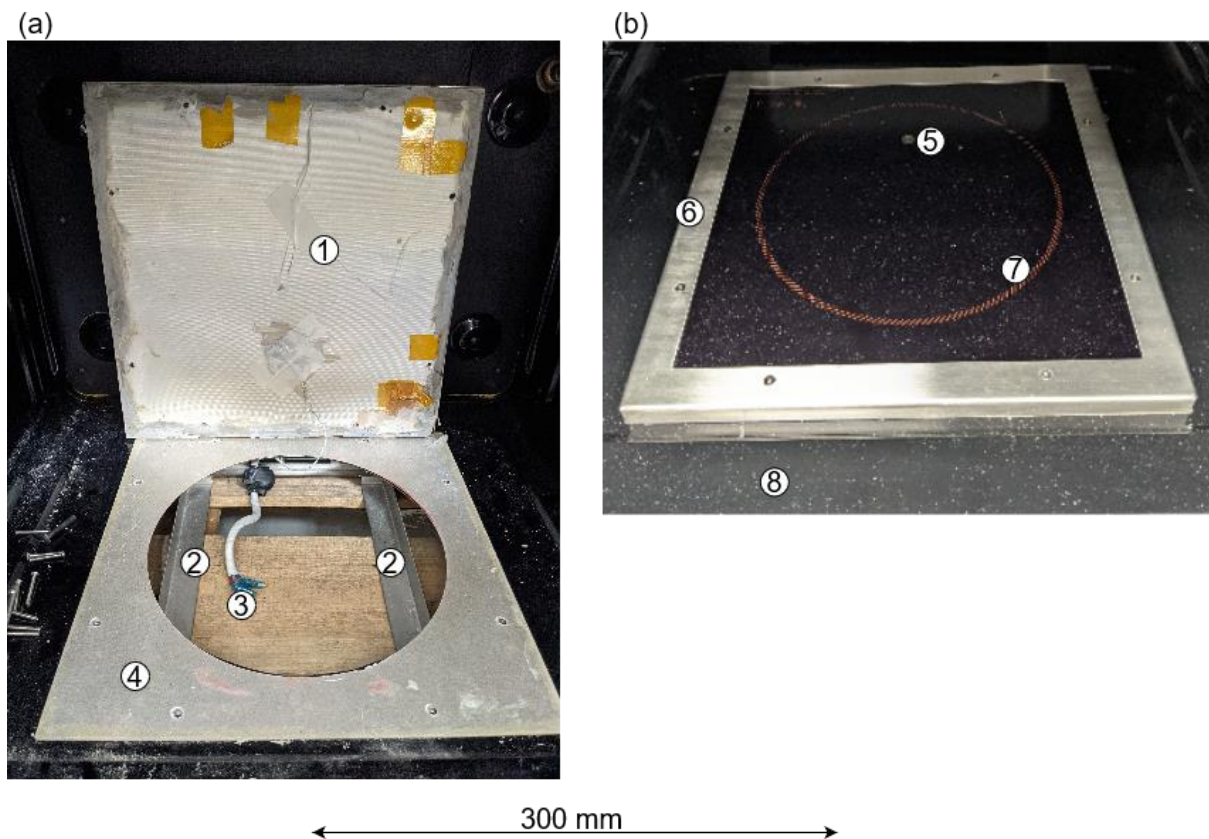


Figure 4.14: Photographs of the prototype III induction system, front/top view. (a) With the glass panel raised. (b) Completed system. 1 – Microtherm™ insulation panel, 2 – induction heater mount, 3 – induction heater power supply and control cables. 4 – Mica “gasket”, 5 – cookware contact temperature measurement pin. 6 – Aluminium frame, 7 – glass plate, 8 – base of the cooking chamber.

4.4.5: Humidity Control

Tests in prototypes I and II showed that hot oven air evaporating standing or atomised water to generate steam was not able to fill the cooking chamber with steam early in the cooking cycle. Additionally, it was found that removing steam from the oven was a consideration in the later stages of cooking. Thus, a new system was designed to be able to increase humidity quickly early in the cooking cycle while also being able reduce humidity if required by the recipe.

Steam was generated in a small tray that slid over an 800 W cartridge heater protruding into the cooking chamber from the back. The tray was formed from folded and welded stainless steel with two drilled support brackets within it that fixed it in place over the cartridge heater. Water was prevented from leaking out around the heater tube by a sheet of silicone foam. An undersized hole was punched in the silicone to ensure a tight fit. The completed assembly is shown in Figure 4.16(a)

The tray was made removable to allow the tray and cartridge heater to be more easily cleaned and descaled. The cartridge heater included a thermocouple within it which was monitored by the firmware: a heater temperature above 150°C indicated that all the water in the tray had evaporated. The firmware would then power the pump to transfer water from the reservoir above the cooking chamber to the evaporation tray via the water supply tube.

The second part of the humidity system was to reduce the humidity within the oven. The only way to do this was to vent the humid air within the oven and replace it with dry air from outside. A tube of internal diameter 25 mm was inserted through the cooking chamber wall in the fan inlet section. A solenoid valve was then attached to the external end of the tube and could be opened by the oven control software to allow fresh air into the oven. The inlet of the fan is at negative pressure, providing the pressure drop to draw fresh air into the oven and vent humid air through the oven vent system discussed in the previous section.

Humidity was measured using a proprietary COI sensor.

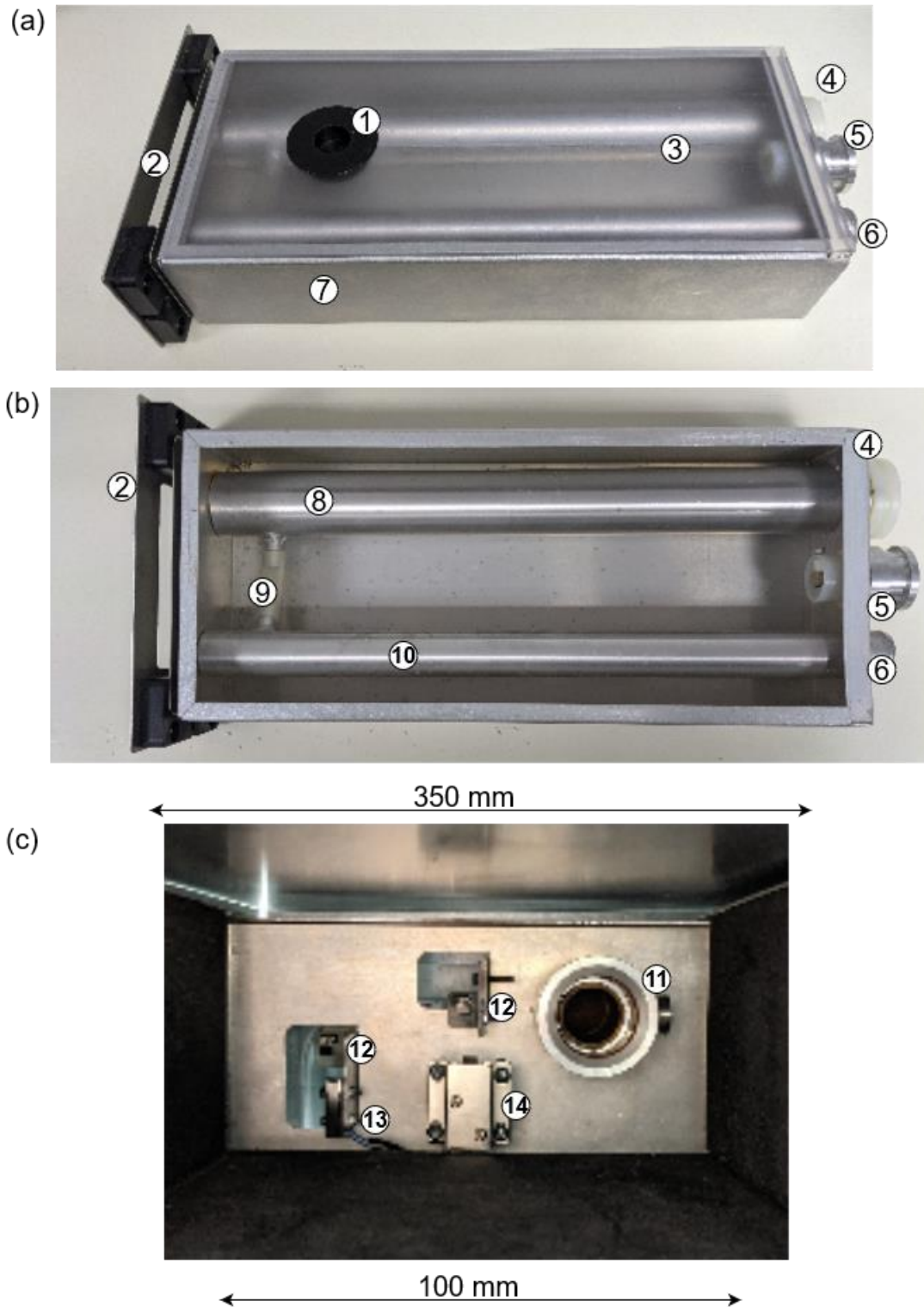


Figure 4.15: Labeled photographs of the heat recover system. (a) Complete heat recovery tray, side view. (b) Heat recovery tray internals, top view. (c) Connection point of the oven and the heat recovery tray, front view. 1 – Water fill point, 2 – handle and front fascia, 3 – top cover, 4 – condensate level switch and emptying port, 5 – water level switch and catch for the latch, 6 – oven vent gas entry and exit point, 7 – heat recovery tray wall, 8 – condensate reservoir, 9 – condenser drain, 10 – condenser body, 11 – oven vent gas entry and exit connection, 12 – level switch hall effect sensors, 13 – push switch, 14 – latch.

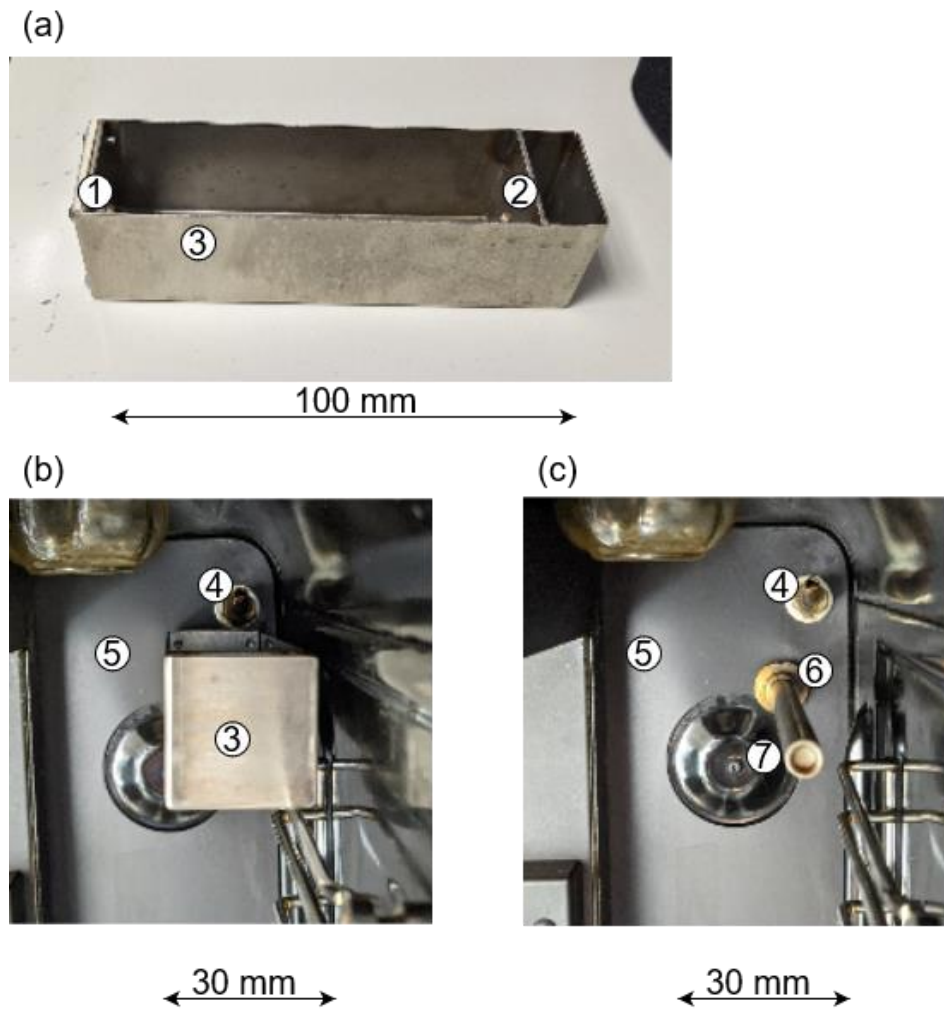


Figure 4.16: Photographs of the steam generation system in prototype III. (a) Water tray, removed from the oven. (b) Steam generation system within the cooking chamber. (c) Steam generation system with the water tray removed. 1 – Silicone seal, 2 – support bracket, 3 – water tray walls, 4 – water supply tube, 5 – back wall of the cooking chamber, 6 – cartridge heater mount with internal thermocouple, 7 – cartridge heater.

5: Experimental Materials and Methods

5.1: Design and Construction of a 32 Channel Temperature Datalogger

5.1.1: Motivation

A 32 thermocouple channel datalogger was constructed to record temperature data required for model validation experiments and food trials. A further 4 power meter channels were added subsequently to measure the power consumption of the first prototype oven. Later prototype ovens included power consumption logging internally. A custom datalogger was constructed due to the large number of thermocouple channels required for model validation experiments and the lack of commercial temperature dataloggers with this capability.

5.1.2: Electronics

The datalogger was controlled using an Arduino Micro (Somerville, MA, USA) microcontroller. This provided the serial communications with an attached PC, interpreted the temperature data from the thermocouple amplifiers and switched the multiplexors in sequence. A block diagram of the datalogger electronics is shown in Figure 5.1.

A multiplexor is a chip that selects between several input signals and forwards the selected input to a single output line. The selection is directed by a separate set of digital inputs known as select lines. Ten AD409, four-into-one multiplexors (Analog Devices, Norwood, MA, USA) were arranged in two layers to allow any two of the thirty-two thermocouple signals to be connected to the two thermocouple amplifiers and read.

The first layer of multiplexing consisted of eight multiplexors, giving eight outputs from thirty-two inputs. The second layer of two multiplexors took this output and further condensed it to only two outputs which connected to the thermocouple amplifiers. Eight select lines from the microcontroller switched the multiplexors to connect a specific pair of thermocouples to the amplifiers. Sequentially switching allowed each thermocouple to be read every 1.6 s.

The Maxim MAX31855 thermocouple amplifiers (Maxim Integrated, San Jose, CA, USA) converted the voltage signal from the thermocouple to a temperature reading. This was transmitted to the microcontroller using serial communication. The amplifiers also included cold junction compensation, which allows accurate temperature measurements when the “cold” side of the thermocouple is not at the reference temperature.

Power consumption was measured by three Grasslin Taxo 80-1 (Grässlin GmbH, St. Georgen im Schwarzwald, DE) power meters. Each power meter was connected to one of the heating elements; the air heaters, infra-red lamps and base heater. The power meters communicated with the data logger using a pulldown transistor, reducing the resistance across a pair of terminals for 50 ms for every 0.001 kWhr (3.6 kJ) measured by the meter. A DC supply held 18 V across these terminals, which were connected in series with PC827 optocouplers (Lite-On, Cramlington, UK) and a 1 k Ω resistor. When the power meter pulsed, current flowed through the optocoupler and dropped the voltage at the connected Arduino pin to 0 V. In this way the Arduino recorded the oven power consumption.

31 of the 32 thermocouples connected to the datalogger were made from the same roll of PFA insulated thermocouple wire (Radio Spares, Corby, UK) to ensure consistency. The final thermocouple was glass fibre insulated and was used as its higher maximum operating temperature would give greater flexibility.

5.1.3: Mounting and Enclosure

The datalogger electronics were mounted on 3 circuit boards, with one housing the Arduino, thermocouple amplifiers and optocouplers. The other two boards contained the multiplexors and screw terminals for connecting the thermocouples. The three boards were mounted in 3D printed shelves, as shown in Figure 5.2(b), to prevent electrical contact between the boards while allowing access to the thermocouple screw terminals. The assembly was then housed in an aluminium box with holes cut for thermocouple wires and the USB connection to the computer. The aluminium box served two purposes: one was to maintain a similar temperature for all three boards as temperature differences would influence the thermocouple readings. The second was to reduce electrical interference, the aluminium box could be grounded and act as a Faraday cage, preventing electrical noise from the prototype ovens influencing the temperature readings.

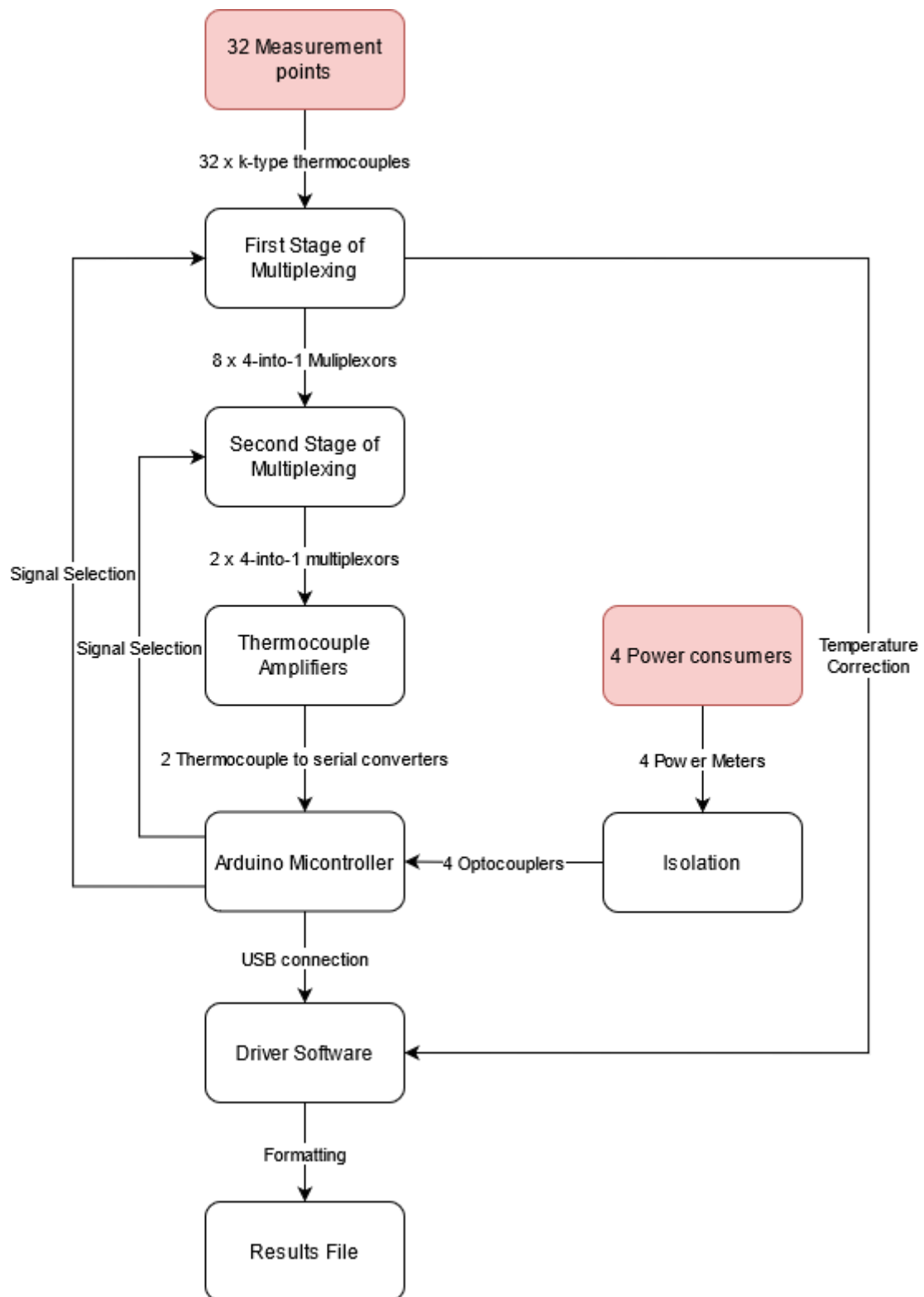


Figure 5.1: Block diagram showing the flow of information through the datalogger components.

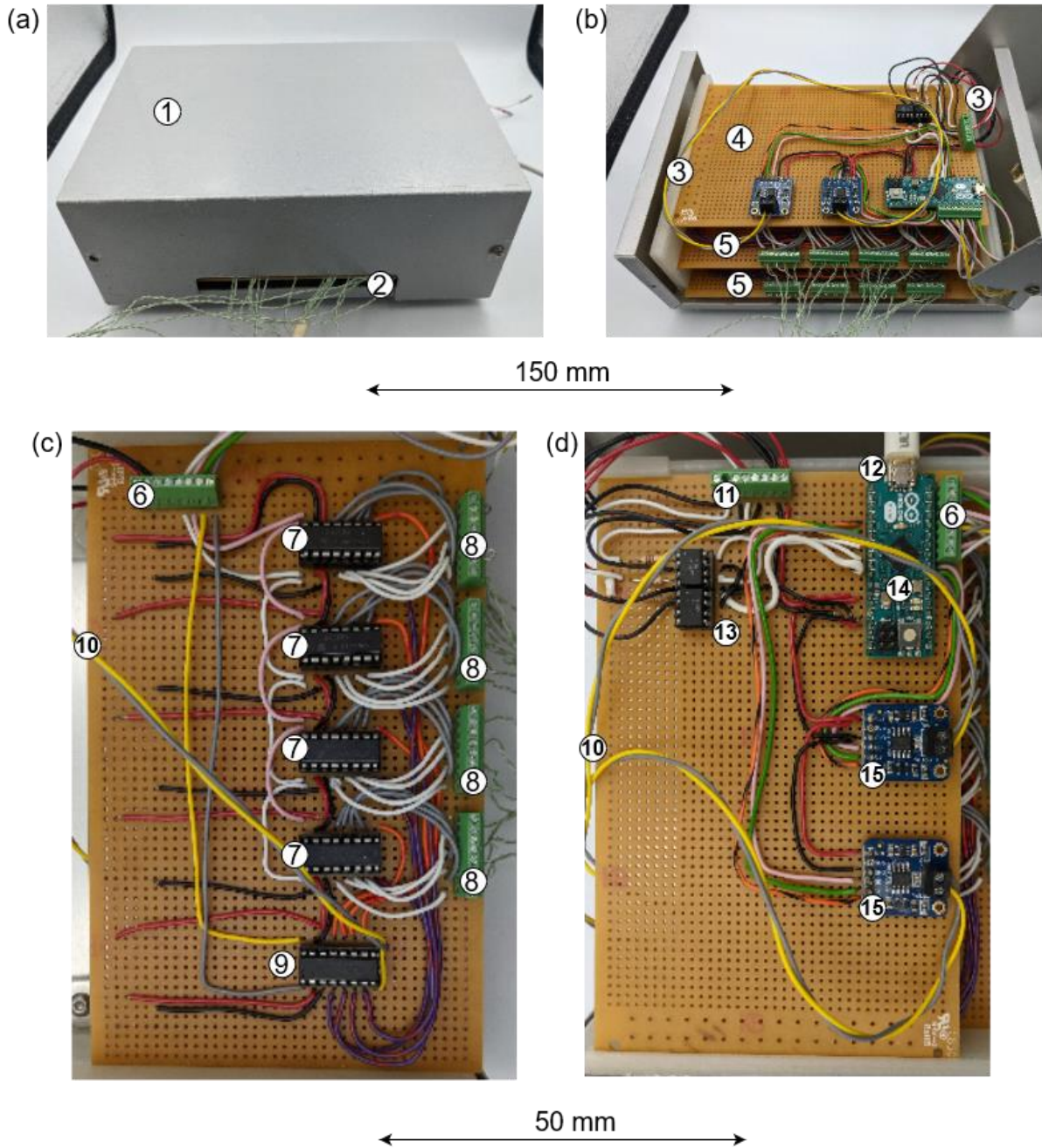


Figure 5.2: Labeled photographs of the finished datalogger. (a) External enclosure, front view. (b) External enclosure with lid removed, front view. (c) Multiplexing board, top view (d) control board, top view. 1-Aluminium enclosure, 2-port for thermocouple cables, 3-3D-printed mount for the circuit boards. 4-Control board, 5-multiplexing boards, 6-selection pins for controlling the multiplexors. 7-First stage of multiplexing, 8-thermocouple terminals, 9-second stage of multiplexing, 10-connection from multiplexors to thermocouple amplifier. 11-Connection to powermeters, 12-USB connection to PC, 13-optocouplers, 14-Arduino Micro microcontroller, 15-thermocouple amplifiers.

5.1.4: Firmware and Driver Software

The firmware on the datalogger performed four functions.

- i) Switch the multiplexors in sequence.
- ii) Query the thermocouple amplifiers and decode the results.
- iii) Detect power meter pulses.
- iv) Package the temperature and power data and transmit it to a computer via the USB connection.

The multiplexors ran on a 100 ms sequence. The selection pins were switched to connect a specific pair of thermocouples to the amplifiers before being allowed to settle for 50 ms to reduce noise. The temperatures were then read and reported by the amplifiers over the remaining 50 ms. The two amplifiers and multiplexing boards ran in antiphase with one another with one switching and settling while the other read. The thermocouple amplifiers were queried using serial communication, with the temperature transmitted as a 32-bit float value.

As described in section 5.1.2, the power meters were connected via an optocoupler to digital pins on the Arduino. The Arduino checked the voltage on the pins every repeat through its main code loop, approximately every 1 ms. If the pin was at 0V that implied that the power meter is pulsing. When the next update was sent to the computer it would include that the Arduino had registered a pulse from that power meter. It then ignored that pin for 1 s to prevent “debounce” and double reading.

Information was transmitted to the attached computer over a USB connection which also provided the power required to run the datalogger. Data packets were sent every 50 ms consisting of a string of ASCII characters with three parts. The first part was a tag describing the value being sent, for example “T0” describes the first thermocouple reading. The second part was the numerical value, reported to 2 decimal places. The third part was information from the power meters. If a power meter pulse was registered by the Arduino during the 50 ms since the previous data packet was transmitted, this information was included here. An example packet would therefore be “T0, 25.75, P2”. This indicates that T0 was read and gave a temperature of 25.75°C and that power meter P2 registered a pulse.

Driver software written in Python decoded the strings of ASCII characters and stored the temperature and power data in a .csv file. The computer time at which the data packet was received was also recorded. The driver software also allowed real-time plotting of temperatures, power consumption and cumulative power consumption, this functionality was controlled using a command line interface.

5.1.5: Temperature Calibration and Correction

The datalogger was calibrated against a UKAS standard. Two UKAS calibrated and certified thermocouples and a RS-51 (Radio Spares, Corby, UK) two channel reader with the same certification were purchased. Together these gave a quoted accuracy of $\pm 0.3\%$, or $\pm 1^\circ\text{C}$, whichever was larger.

To calibrate the data logger and thermocouples a temperature equalising block was constructed from aluminium. The design of the block is based on work by Bojkowski *et al.*¹⁴⁵ on modelling and optimising temperature equalising blocks. The geometry is shown in Figure 5.3. The central cavity contained a 50 W, 24 V cartridge heater (Elmatic LTD, Cardiff, UK), the power to which was controlled using a bench top power supply. The six surrounding wells held thermocouples. The entire block was encased in ceramic wool insulation and aluminium foil. The power to the cartridge heater was adjusted to give a steady temperature in the thermocouple wells. The UKAS certified thermocouples were inserted into diametrically opposite wells to check for errors. The remaining four wells were occupied by thermocouples connected to the data logger for comparison with the standard.

¹⁴⁵ J. Bojkowski, J. Drnovšek, and I. Pušnik, 'Analysis of Equalising Blocks in Calibration of Thermometers', *Measurement* 23, no. 3 (April 1998): 145–50.

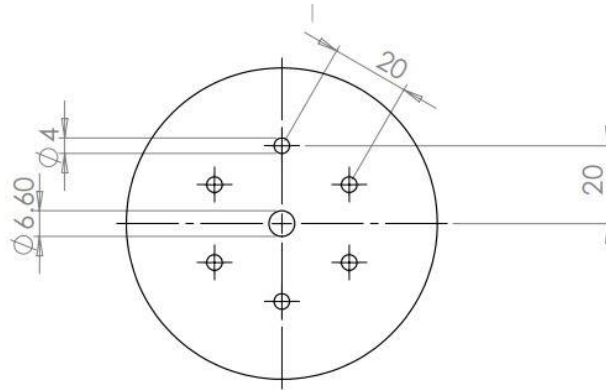


Figure 5.3: Plan view of the aluminium temperature equalising block. The depth of the block was 55 mm, the depth of the wells was 35 mm. All dimensions in mm.

The consistency of the temperature equalising block was checked using the two UKAS calibrated thermocouples. Each thermocouple well was checked against the others at ambient temperature, 100°C, and 200°C. The temperatures were found to lie within the 0.1°C precision of the thermocouple reader at all three temperatures.

As all the thermocouples were made from the same batch of wire, any error in the junction itself would be consistent across them all. The error in the reading made at the amplifier would therefore be due to the multiplexors, solder junctions and the amplifiers themselves. It was therefore hypothesised that the error would be equal for each set of four thermocouples connected to one multiplexor as all the junctions would be common between them. This hypothesis was tested by comparing every thermocouple to the UKAS thermocouples at ambient and at 200°C in the temperature equalising block.

The mean reading for the four thermocouples attached to each multiplexor was calculated for each unit. This “multiplexor mean” was then compared to the individual readings from its four associated thermocouples. The difference between the multiplexor mean and the thermocouple reading is plotted in Figure 5.4. All but one of the thermocouples gave signals within 0.4°C of its multiplexor mean. The outlier was the reading from the glass fibre insulated thermocouple. Excluding this value, the mean difference between a thermocouple reading and its multiplexor mean was 0.025°C. This indicated that any correction factor could be common between each set of 4 thermocouples attached to a multiplexor, except for the glass fibre insulated thermocouple, which was given its own individual correction factor.

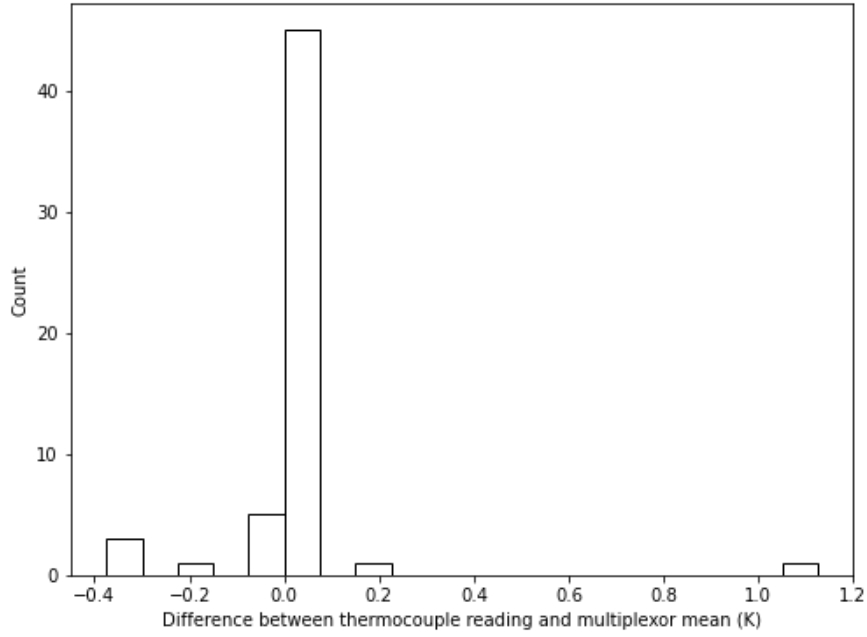


Figure 5.4: Histogram showing the distribution of offsets from the mean temperature reading for each multiplexor. Readings taken at 20°C and 200°C. Number of measurements = 64.

The correction factor was found by comparing one thermocouple from each multiplexor and the glass fibre thermocouple to the UKAS thermocouples at 20, 60, 80, 120, 140, 160, 180 and 200°C. The difference between the temperatures and the datalogger and the UKAS values was computed and fitted to a second order polynomial using the SciPy python library. The experimental results and fitted function are shown for one of the multiplexors in Figure 5.5. This polynomial fit was added to the datalogger driver code and used to correct the temperature readings reported by the datalogger between 20 and 200°C: outside this range no correction was performed. The R^2 value for all fits was greater than 0.999, indicating a good fit.

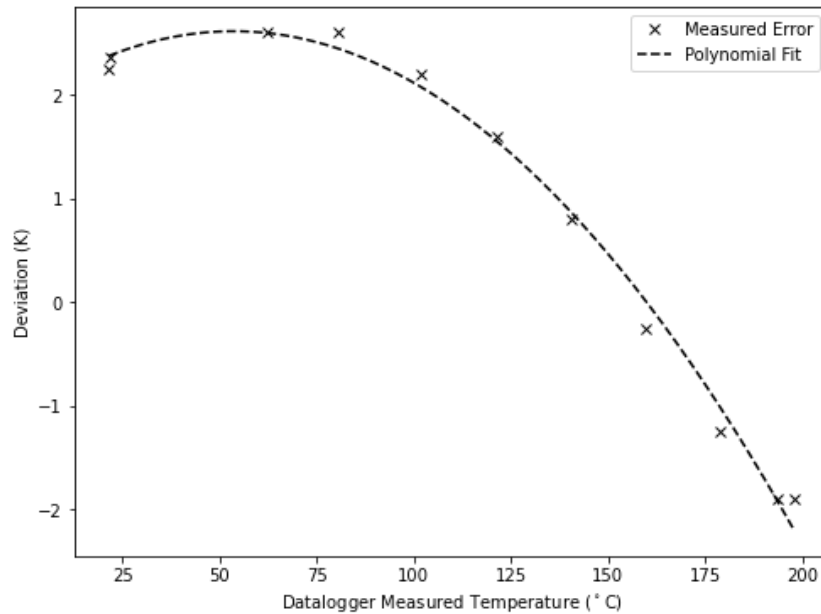


Figure 5.5: Deviation of datalogger measured temperatures from the UKAS certified measurements at different temperatures.

5.2: Design and Construction of the Heat Flux Sensor

5.2.1: Overview and Conceptual Design

A sensor was developed and built to record radiative and convective heat fluxes within the oven. The use of water cooled blocks was considered, where water is pumped through a cuboidal copper block within the oven and the temperature rise of the water flowing through the block is measured and used to calculate the heat flow into the block. The advantage of this system is that the block can remain within the oven indefinitely and measure the flux over the whole cooking cycle. The disadvantage is the need to pipe water into and out of the oven at a precise flowrate. An alternative was therefore considered that was easier to install and move around within the oven.

The alternative was to use some form of reservoir within the oven that can dynamically absorb heat while making the measurement, the approach used by Carson *et al.*¹⁴⁶ and Verboven *et al.*¹⁴⁷. The reservoir could then be cooled to ambient between experiments. The rate at which

¹⁴⁶ J.K. Carson, J. Willix, and M.F. North, 'Measurements of Heat Transfer Coefficients within Convection Ovens', *Journal of Food Engineering* 72, no. 3 (1 February 2006): 293–301.

¹⁴⁷ Verboven, Scheerlinck, Baerdemaeker, and Nicola, 'Computational Fluid Dynamics Modelling and Validation of the Temperature Distribution in a Forced Convection Oven'.

temperature rises within the reservoir whilst in the oven is used to calculate the flow of thermal energy into the sensor. The advantage of this design is that the sensor only needs thermocouple wires to be run from the sensor to a datalogger. These thin wires can be easily routed round the oven door.

The challenges with this design are:

- i) How to exclusively measure heat flux from above, isolating the sensor from heat fluxes from the base and sides. It is also important to prevent heat leakage out of the reservoir as this will introduce a systematic error in the measurement.
- ii) Have sufficient capacity for the sensor to remain in the oven for long enough to ensure a reliable measurement.
- iii) Be small enough that it can be moved around the oven and record flux variations within the oven with sufficient granularity. A maximum thickness of 50 mm and a maximum top surface of 100×100 mm was desired.
- iv) The temperature of the reservoir will change during the test in turn changing the heat flux. This needs to be accounted for.
- v) The emissivity of the top surface must be able to be varied between experiments to distinguish the convective and radiative fluxes.

A labelled schematic of the final design is shown in Figure 5.6(b). The design consisted of an aluminium top plate that could be removed and reattached to the Perspex reservoir. A matt black top plate and a polished aluminium top plate allowed the emissivity to be varied. The sides and base of the reservoir were insulated using ceramic wool to prevent heat flow to the sides and base of the reservoir impacting the measurement. Ceramic wool was preferred to Microtherm® due to greater ease of cutting and shaping. Two numerical models were created to assess the accuracy of the sensor and select the materials of construction.

5.2.2: Detailed Design Modelling

Design Calculations

Two conditions limited the measurement time for the sensor:

- i) The maximum operating temperature for the sensor materials - approximately 120°C for Perspex, >200°C for titanium or aluminium.

- ii) The temperature at the base of the reservoir rising above its value at the start of the test. Calculation of the heat flux by this reservoir method assumed all the heat absorbed by the top surface of the sensor is stored within the reservoir and the aluminium top plate. A temperature rise at the base of the reservoir indicates that heat is being transferred between the insulation and the reservoir, and that this assumption no longer holds.

The “penetration time”, t_{pen} , for the heat wave to reach the base of the reservoir from the aluminium top plate or through the insulation can be estimated using the Fourier number, Fo :

$$Fo = \frac{\alpha t}{L^2} \quad (5.1)$$

where L is the thickness of the reservoir and α is the thermal diffusivity;

$$\alpha = \frac{k}{\rho C_p} \quad (5.2)$$

Treating the reservoir as an infinite slab, heat reaches a depth x into the slab when $Fo = 0.0625^{148}$, giving t_{pen} as:

$$t_{\text{pen}} = \frac{L^2}{16\alpha} \quad (5.3)$$

Applying this result to a reservoir of thickness 25 mm for aluminium, titanium and Perspex gave the values in Table 5.1. Ceramic wool is included to estimate the effectiveness of 25 mm of insulation at the sides and base of the reservoir.

¹⁴⁸ J.C. Jaeger, *Conduction of Heat in Solids*, 1st ed. (Oxford University Press, 1959).

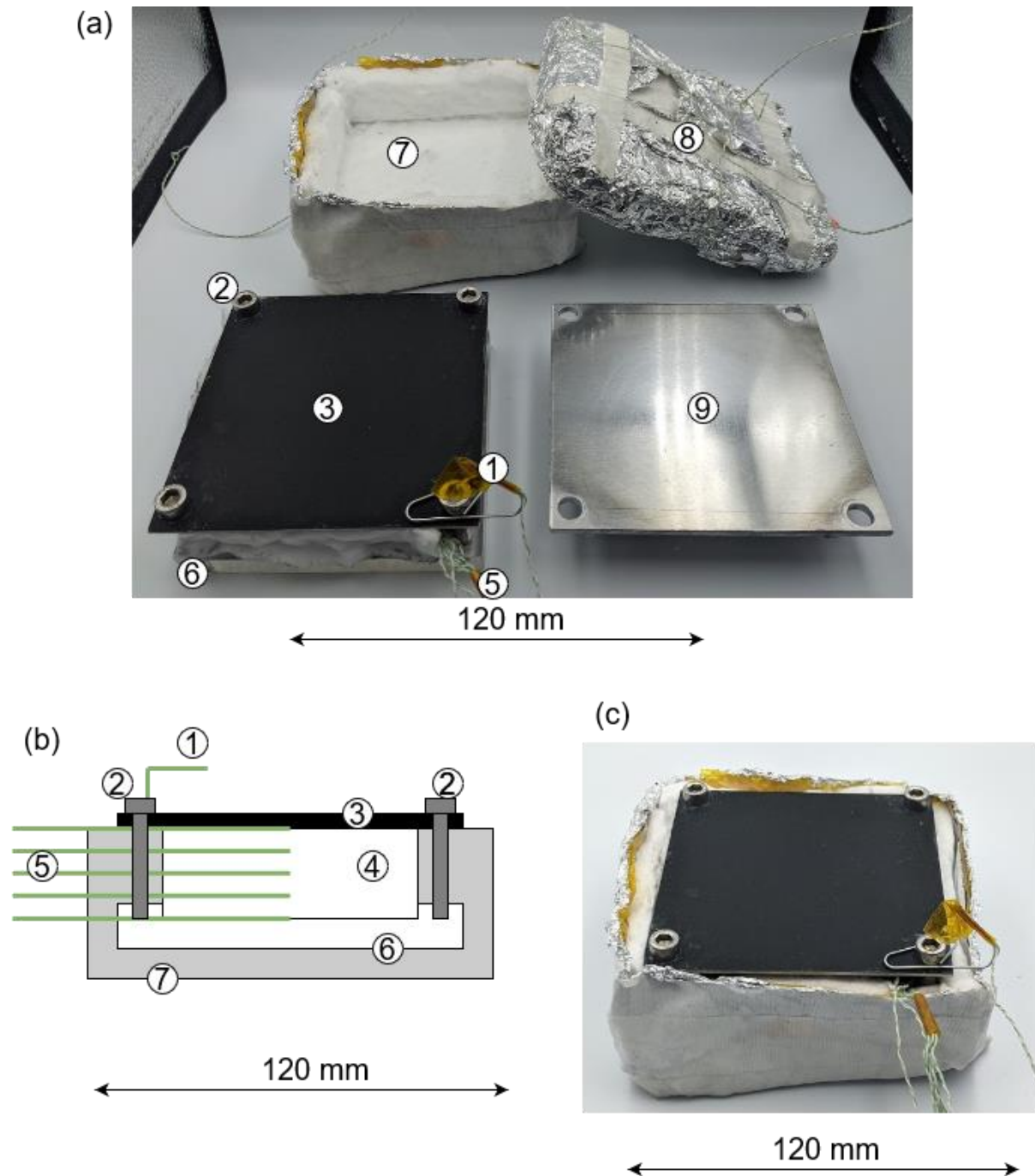


Figure 5.6: Detail of the finished heat flux sensor. (a) Photograph of the main parts of the sensor. (b) Schematic diagram, side view. (c) Photograph of the assembled sensor. 1-Air temperature thermocouple, 2-bolt securing the top plate. 3-Matte black aluminium top plate, 4-perspex reservoir, 5-thermocouple leads, 6-perspex base plate, 7-ceramic wool insulation, 8-insulated, removable lid, 9-low emissivity, polished aluminium top plate.

Table 5.1: Physical properties and calculated t_{pen} for a 25 mm deep reservoir.

Material	k (Wm ⁻¹ K ⁻¹)	ρ (kgm ⁻³)	C_p (Jkg ⁻¹ K ⁻¹)	α (m ² s ⁻¹)	t_{pen} (s)
Aluminium	205	2700	920	8.25×10^{-5}	0.473
Titanium	7	4500	524	2.96×10^{-6}	13.2
Perspex	0.2	1190	1466	1.15×10^{-7}	339
Ceramic wool	0.04	250	500	3.2×10^{-7}	112

Although the high maximum operating temperature of a metal reservoir is attractive, the results in Table 5.1 show that the high values of k and α give a sensor with a metal reservoir a short measurement period and that a polymer reservoir may be more practical.

One Dimensional Model

A one-dimensional mathematical model of the design was created using Wolfram MathematicaTM. The model numerically solved the heat equation in one dimension:

$$C_p(x)\rho(x)\frac{dT}{dt} = k(x)\frac{d^2T}{dx^2} \quad (5.4)$$

where x is the depth into the sensor from the top surface. The material properties were made piecewise functions of x to represent sensor designs formed from multiple materials. A constant heat flux of 4000 Wm⁻² was set as the top surface boundary condition. The base of the sensor was set as 100°C to approximate the sensor being placed on the hot base of the oven.

The temperature profile for a 25 mm deep reservoir was calculated for three different reservoir materials: Perspex, aluminium and titanium. A 2 mm thick aluminium top plate was added between the oven air and the reservoir material. 20 mm of ceramic wool insulated the reservoir from the oven base.

Figure 5.7 shows the evolution of the temperature at the top and bottom of the reservoir, for the three different reservoir materials. Figure 5.7(a) reflects the t_{pen} values in Table 5.1: the temperature at the base of the metal reservoirs begins to rise almost immediately, compared to after approximately 300 s with Perspex. Plot (b) shows that the top of the Perspex device heats up more quickly than the others, both due to the lower volumetric heat capacity and the lower thermal conductivity that hinders the thermal energy conducting away from the top of the

reservoir. The model predicts that the Perspex will overheat in approximately 300 s, which was deemed to be an acceptable measurement window.

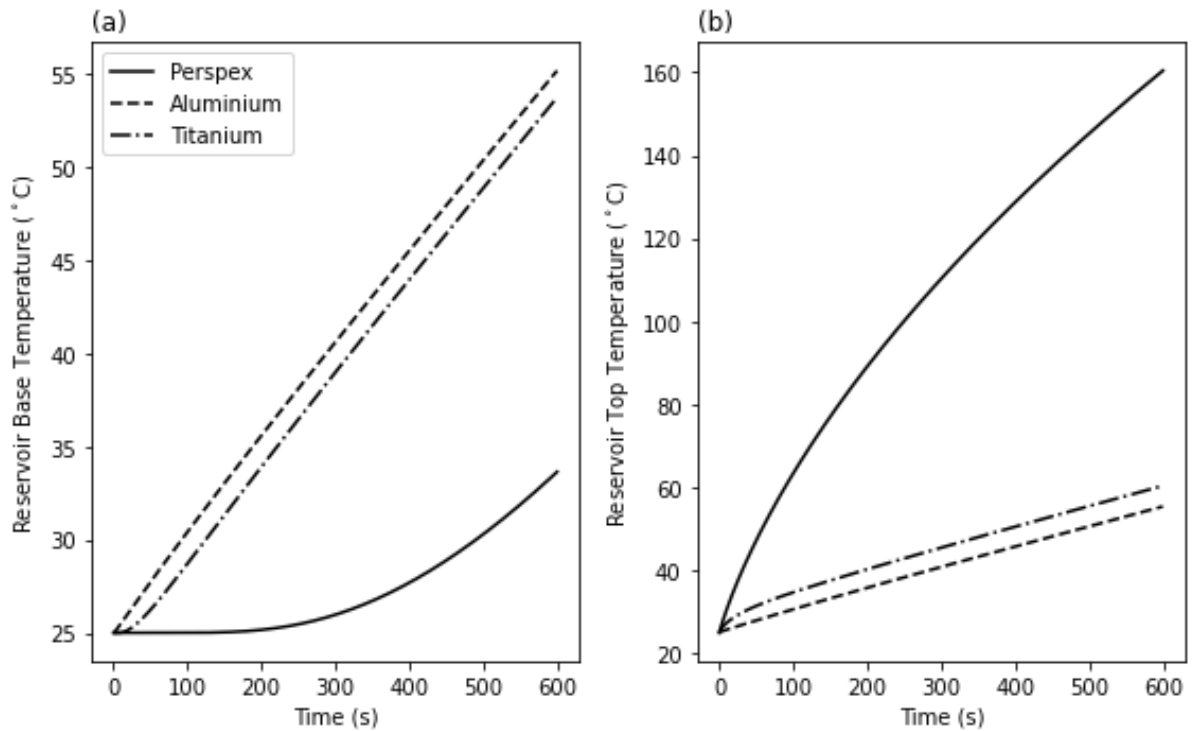


Figure 5.7: Temperature profiles calculated by the one-dimensional model for the reservoir common legend. (a) Base, (b) top surface.

Three-Dimensional Model

The design was also investigated using a 3-dimensional transient model in ANSYS CFX. This model was designed as a final test of the sensor design and data processing method. The geometry tested is shown in Figure 5.8. The Perspex baseplate was added for two reasons:

- i) The Perspex had a lower thermal diffusivity than the ceramic wool. In combination with the insulation it would further slow the conduction from the base of the sensor to the reservoir.
- ii) A Perspex baseplate could be drilled and tapped to bolt the top plate to the reservoir to ensure good contact. Drilling and tapping the reservoir would be possible, but metal bolts would form a thermal bridge through the reservoir and affect the reading.

The aim of the three-dimensional model was to investigate the accuracy of the sensor design while making fewer assumptions than in the one-dimensional model and using more realistic

boundary conditions. Extracting temperature data from the model also enabled the data processing code to be tested and the accuracy of the sensor to be estimated. A sensitivity analysis was performed to quantify the impact of material properties and oven conditions on the sensor's accuracy.

A fine mesh was used to model the sensor. Only the energy equation was solved, giving a relatively quick solution time even with a large number of mesh elements. A tetrahedral mesh with 4.15 million elements was selected and is shown in Figure 5.9. The boundary conditions for the top and sides of the sensor were dependent on the difference between the oven air temperature, fixed at 200°C, and the surface temperature, T_{surface} :

$$q = h(200 - T_{\text{surface}}) \quad (5.5)$$

where h is the film heat transfer coefficient, set to 35 Wm⁻²K⁻¹ for the top surface and 15 Wm⁻²K⁻¹ for the sides of the sensor. The lower heat transfer coefficient on the sides of the sensor was due to the air from the jets not impinging on this surface. A fixed temperature of 100°C was applied to the base of the sensor. Material properties are listed in Table 5.1. The sensor was initially at 25°C and was modelled for 300 s with 1 s timesteps.

The temperature profiles at the top and the base of the Perspex reservoir are plotted in Figure 5.10, alongside the results from the one-dimensional model for comparison. The profiles are similar, and confirm that the Perspex sensor will have a measurement time of the order of 300 s. It is important to note that the one-dimensional and three-dimensional models used different boundary conditions on the top surface: the discrepancy between the results will therefore arise from a combination of the additional dimensions and the change in boundary condition. The temperature at the base of the sensor after 300 s rose by 4.5°C in the three-dimensional case. This is small compared to the temperature rise elsewhere in the reservoir, giving a commensurably small error. The temperature at the top of the reservoir is 106°C after 300 s, which is below the operating limit.

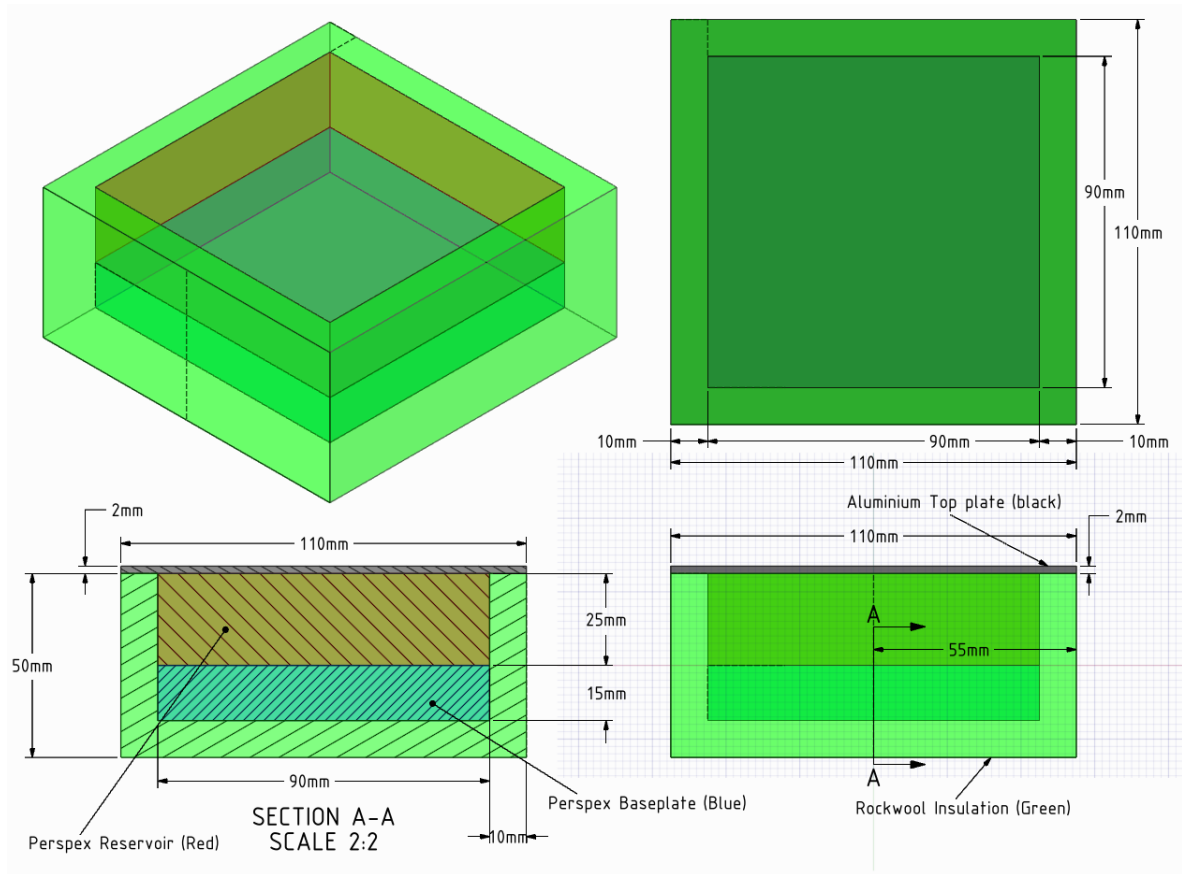


Figure 5.8: Schematic of the geometry used in the three-dimensional model of the heat flux sensor, third angle projection. All dimensions in mm.

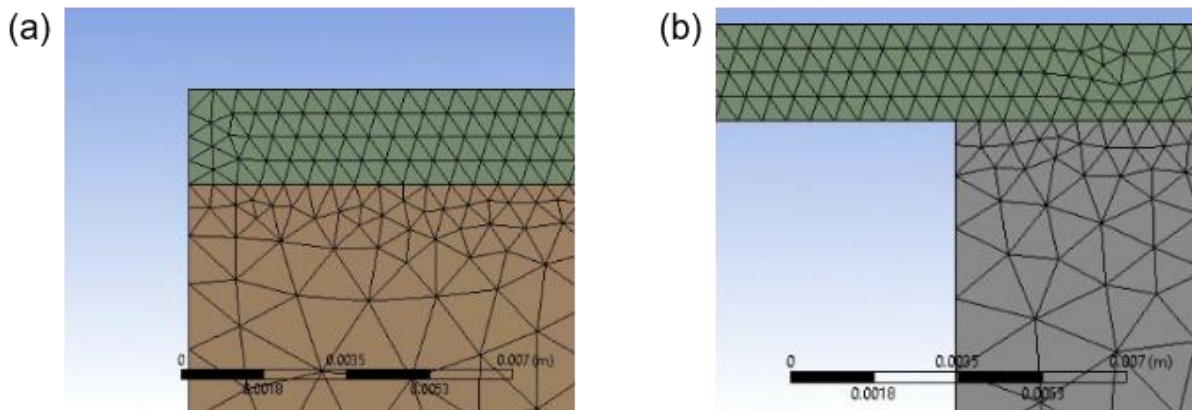


Figure 5.9: Screen captures showing detail of the mesh used in the three-dimensional model, side views. (a) Aluminium top plate (top) and the transition to the insulation. (b) Aluminium top plate (top) and the transition to the reservoir.

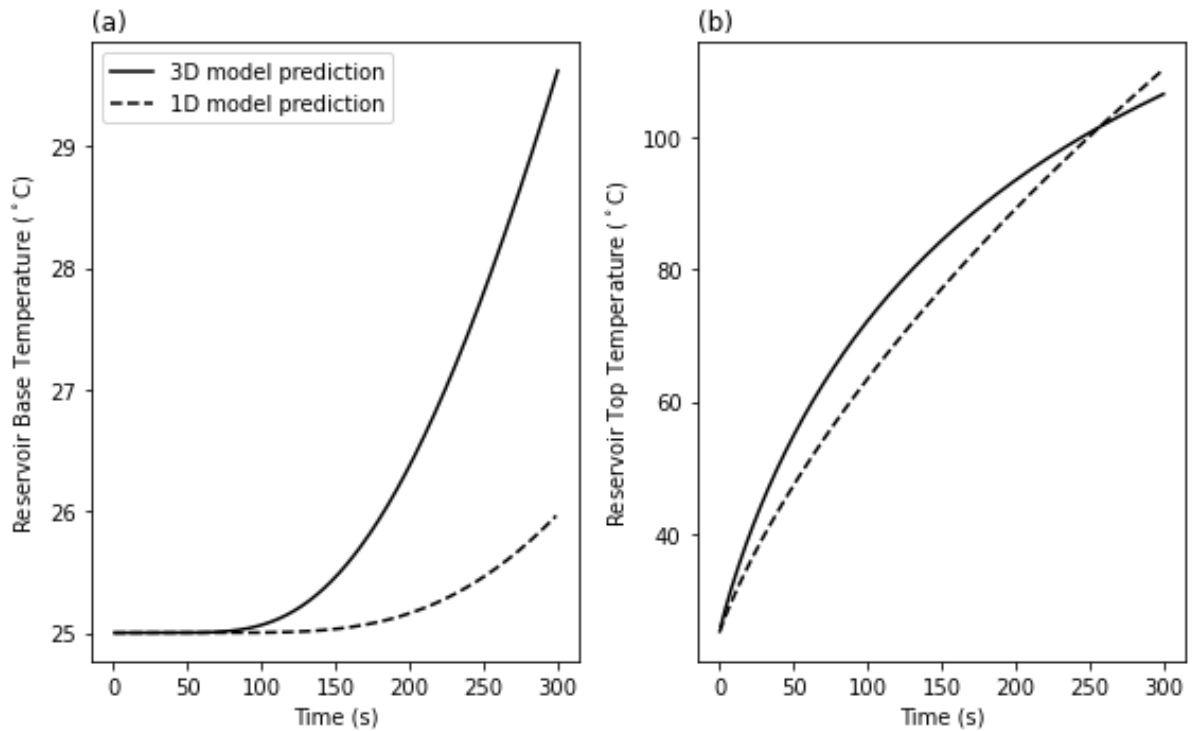


Figure 5.10: Evolution of the (a) temperature at the base of the reservoir, (b) temperature on the top surface of the reservoir. Calculated by the three and one-dimensional models, common legend.

The calculation method, described in section 5.2.5, that converts the temperature profile within the reservoir to a heat flux and heat transfer coefficient measurement, assumes:

- i) The heat flow within the sensor is one dimensional, from the top plate through the Perspex reservoir.
- ii) The temperature in the aluminium top plate is homogenous.

The validity of these assumptions was tested using the three-dimensional model.

Examining the temperature profiles within the sensor after 300 s, the maximum temperature within the aluminium is 112.0°C, and the minimum is 110.0°C, giving a range of 2.0 K. The same analysis after 30 s gives 46.8°C, 44.4°C, and 2.4 K, respectively. This low range indicates that the temperature in the aluminium top plate is close to homogenous and that assumption (ii) is valid.

Figure 5.10 shows a contour plot of temperature across the sensor and reservoir after 300 s.

Figure 5.10(a) shows that the temperature difference across the insulation layers, at the vertical

edges of the sensor, is large indicating that the insulation is effective at reducing heat flux into the sides and base of the sensor. In Figure 5.10(b), which shows the temperatures within the reservoir only, straight horizontal contour lines would be expected if the heat transfer is one dimensional. This is not the case, as the contours curve towards the walls of the reservoir, indicating some heat is flowing into the reservoir through the sides. However, towards the midline of the reservoir, where the temperature measurements are taken, the contours are very close to horizontal, indicating that the rate of heat transfer into the sides of the sensor is magnitudes smaller than the heat transfer from the top. This indicates that assumption (i) is also valid.

The magnitudes of the heat transfer rates in the vertical and horizontal directions can be quantified by integrating the heat flux over the top, bottom and sides of the reservoir. The results of this calculation are presented in Table 5.2 and show that the amount of heat flowing into the reservoir from the sides and base is relatively small compared to the top plate, again indicating that assumption (i) is valid.

Table 5.2: Total thermal energy flowing into the top, bottom and sides of the reservoir in the three-dimensional model near the start and end of the simulation.

Time (s)	Heat flow from top (W)	Heat flow through sides		Heat flow through base	
		Total (W)	% of flow from top	Total (W)	% of flow from top
30	52.7	0.72	1.4	-9×10^{-4}	-1.7×10^{-3}
300	51.8	3.48	6.7	-1.04	-2.10

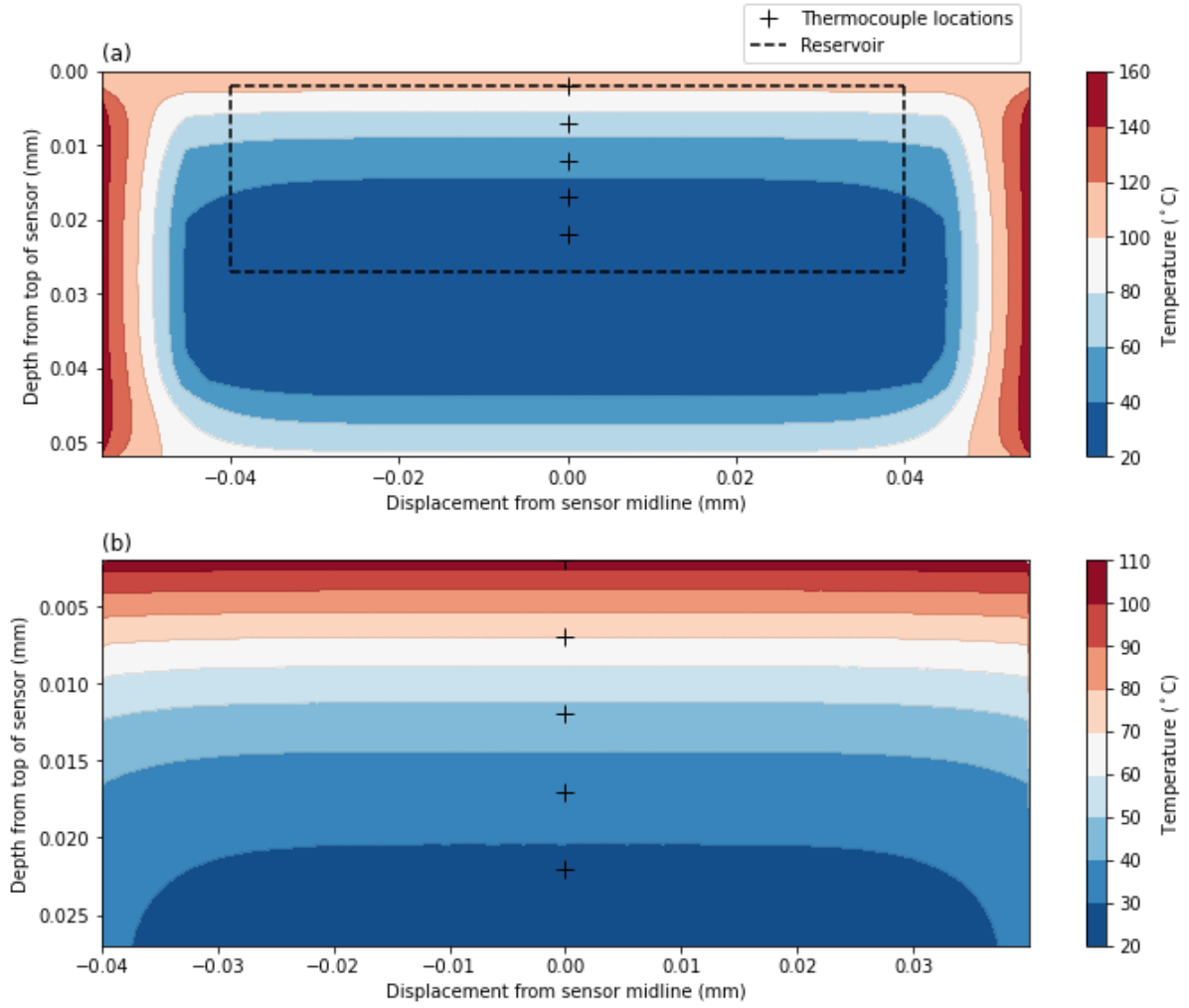


Figure 5.11: Predicted temperature distribution from the centre line of the sensor, shown as section A in Figure 5.8. Results from the three-dimensional model after 300 s. (a) Shows the whole sensor, (b) shows the reservoir alone.

To test the data processing method, temperatures were sampled at the locations of the thermocouple junctions in the preliminary design, these are shown in Figure 5.11. The data were fed into the data processing script described in section 5.2.5 and used to calculate heat flux into the sensor, $q_{\text{measured}}(t)$, and the heat transfer coefficient h_{measured} :

$$h_{\text{measured}}(t) = \frac{q_{\text{measured}}(t)}{200 - T_{\text{surface}}} \quad (5.6)$$

T_{surface} is assumed to be equal to the temperature at the top of the reservoir, immediately below the aluminium top plate. h_{measured} is plotted against time in Figure 5.12. The first 30 s of the simulations were discarded due to transients giving rise to anomalous readings of h_{measured} . The

mean value between 30 and 300 s is $39.1 \text{ Wm}^{-2}\text{K}^{-1}$, compared to the value of $35 \text{ Wm}^{-2}\text{K}^{-1}$ specified in the simulation, representing an error of 11.7%.

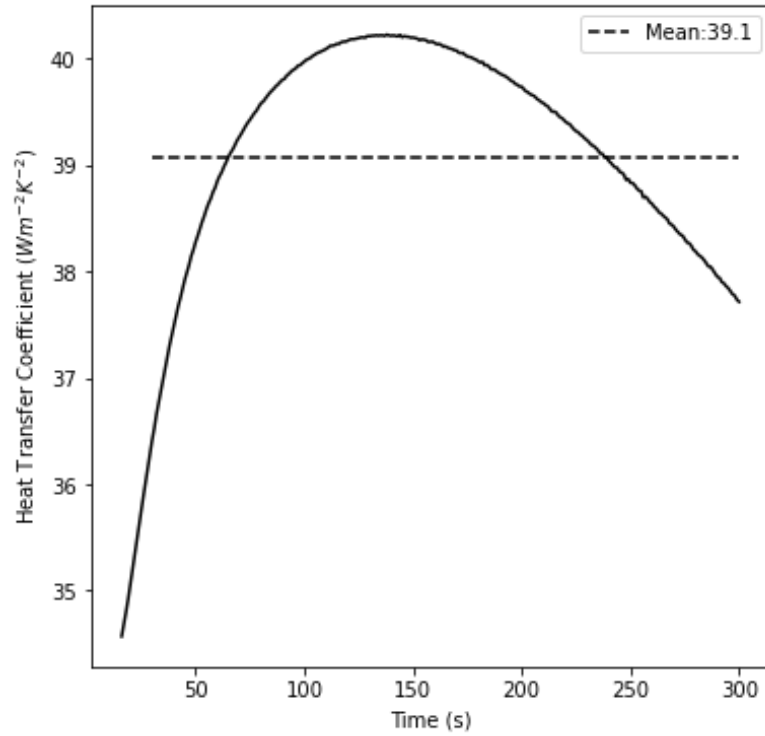


Figure 5.12: Plot of calculated heat transfer coefficient using temperature data from the three-dimensional model and the data processing method described in section 5.2.5.
Horizontal dashed line – mean value

Sensitivity Analysis

Two variables were considered in the sensitivity analysis, the heat transfer coefficient between the sides of the sensor and the oven air, and the volumetric heat capacity of the reservoir material. Results from the analyses and from the base case are shown in Table 5.3. The evolution of h_{measured} showed the same trend as Figure 5.11 in all four cases.

The heat transfer coefficient between the sides of the sensor and the oven air was increased from 15 to $35 \text{ Wm}^{-2}\text{K}^{-1}$. The latter value is the same as the heat transfer coefficient on the top surface, associated with jet impingement: this represents a worst case. The simulation was rerun with otherwise unchanged settings. The results in Table 5.3 shows the mean calculated heat transfer coefficient increased from $39.1 \text{ Wm}^{-2}\text{K}^{-1}$ in the base case to $39.3 \text{ Wm}^{-2}\text{K}^{-1}$. The error compared to the true value of $35 \text{ Wm}^{-2}\text{K}^{-1}$ therefore increased from 11.7% to 12.3%. This was considered a

small change and showed the sensor design was able to give reasonably accurate readings even in this worst-case scenario.

The value of h_{measured} in Table 5.3 for Cases 0 and 1 was calculated when the physical properties in the model and in the data processing script were identical. In practice, the physical properties of the reservoir may not exactly match those in the script and will also vary with temperature. To investigate the impact of inaccurate estimates of physical properties on the accuracy of the sensor, the volumetric heat capacity of the reservoir material and aluminium top plate was varied by $\pm 10\%$ in the model. The properties used by the data processing script when calculating the heat transfer coefficient were not changed. The equations used by the data processing script to calculate heat flux (equations 5.7 and 5.8) are linearly dependent on heat capacity and it was therefore expected that a 10% change in heat capacity in the model would result in approximately a 10% error in the measured heat flux.

Table 5.3 shows that reducing heat capacity in the model by 10% increased h_{measured} from 39.1 $\text{Wm}^{-2}\text{K}^{-1}$ to 42.3 $\text{Wm}^{-2}\text{K}^{-1}$, an increase of 8.0%. Increasing heat capacity in the model by 10% reduced the measured heat transfer coefficient by 8.6% to 36.1 $\text{Wm}^{-2}\text{K}^{-1}$. This confirms the hypothesis that the error in the calculated heat flux will be approximately linearly dependent on any error in the volumetric heat capacity value used in data processing.

Table 5.3: Results from sensitivity analysis using the three-dimensional model

Case	Description	Mean h_{measured} ($\text{Wm}^{-2}\text{K}^{-1}$)	Error in h_{measured} (%)	Change from base case (%)
0	Base case	39.1	+11.7	-
1	Increased h at the sides of the sensor	39.3	+12.3	+0.6
2	10% reduction in α	42.3	+20.8	+8.0
3	10% increase in α	36.1	+3.1	-8.6

Conclusions

The one-dimensional and three-dimensional models of the heat flux sensor demonstrated that the design is able to measure heat flux within the oven for approximately 300 s. The data processing method was shown to be reasonably accurate, with a 12% error compared to the model inputs. The sensor design was not affected significantly by changes to the heat transfer

rate through the sides. The error in the heat flux value calculated by the sensor and data processing stage is linearly dependent on the accuracy of the material properties. Aluminium and Perspex are therefore suitable materials of construction, with the advantage of being well characterised.

5.2.3: Construction

The sensor was formed from 4 parts as shown in Figure 5.6.

The aluminium top cover was cut using a cropping tool then machined to size using a mill. To make the matt black cover, the top surface was blast cleaned and spray painted black using an air brush and Vallejo black polyurethane primer (AcrylicosVallejo, Barcelona, ES). The low emissivity surface was produced by successive polishing with increasing grades of emery paper, and finally, polishing compound. The surface was repolished using compound between every experiment to ensure a consistent emissivity.

The Perspex reservoir was roughly cut from a 25mm thick Perspex sheet using a circular saw. It was then cut to size accurately using a manual milling machine. Thermowells were drilled using a 1.5 mm bit on the same milling machine. The thermocouple channels on the base and top surfaces were milled to a depth of 1 mm using a 2 mm diameter ball-nosed cutter.

The Perspex base plate was similarly cut from a sheet using a circular saw before being milled to the required dimensions.

The insulation layers were made from ceramic wool (Radio Spares, Corby, UK) and cut to the correct dimensions using scissors before being wrapped in aluminium foil and secured using glass fibre tape.

The base of the thermowells were filled with a silicone-based heat transfer compound with $k = 5 \text{ Wm}^{-2}\text{K}^{-1}$ (RS-Pro, Corby, England) which was also used between the aluminium top plate and the Perspex block, to reduce contact resistances.

The Perspex parts and aluminium top plate could be removed from the insulation to cool down more quickly between experiments.

An insulating, removable lid was constructed with a ceramic wool core, wrapped in aluminium foil and secured with glass fibre tape. When the sensor was inserted into the oven to begin a measurement, the insulating lid was initially placed on top of the sensor. The oven door needed to be opened and closed to insert the sensor, and the oven required 2 minutes to re-equilibrate and reach steady state after the door was closed. The lid acted to delay the start of the measurement by insulating the sensor from the oven air. Once the oven had reattained steady state the lid could be removed by pulling on the attached wire, and the measurement begun. The lid therefore prevented part of the sensor's limited measurement window being wasted during this equilibration time.

5.2.4: Experimental Procedure

Heat flux measurements were made for oven setpoints of 150°C and 200°C. The measured variable was the temperature of the air returning to the air heaters. Measurements were made for surface emissivities of 1 and 0.05 for the matt black and polished top surfaces, respectively. Measurements were taken at 5 positions around the base of the oven, shown in Figure 7.25. The positions were marked with permanent marker on the base of the oven to ensure consistent placement between repeats. Two repeats were made for each combination of position, emissivity, and oven setpoint.

Before taking a measurement, the oven setpoint was set and the oven was left for 90 minutes to reach steady state. The sensor was located at the marked position with the insulated lid in place. The sensor was left to record either until the temperature at the top of the Perspex reached 110°C, or the base reached 30°C: this was typically longer than the 300 s measurement period predicted by the models. Recording was then stopped and the sensor removed from the oven, removed from its insulated basket (labelled no. 7 in Figure 5.12) and left to cool. Once all the thermocouples within the reservoir read less than 25°C the next test could begin.

5.2.5: Data Processing

Temperature measurements from the heat flux sensor were processed using a Python script to calculate the heat flux. First, the temperature data for the 5 thermocouples in the Perspex block were smoothed using a Butterworth low pass filter to remove any noise caused by electronic interference within the oven chamber. An interpolating surface was then fitted to the data using

a Clough-Tocher interpolator: this fitted a smooth function to the temperature, T , in terms of the time, t , and the depth into the sensor, y . The total energy absorbed by the sensor per unit area, $W_A(t)$ was then calculated using equation 5.7. The temperature of the aluminium top plate was measured by the topmost thermocouple which was connected to the aluminium by a thin layer of heat transfer compound.

$$W_A(t) = \underbrace{c_p^{\text{Al}} \rho^{\text{Al}} L^{\text{Al}} (T(0, t) - T(0, 0))}_{\text{Al slab}} + \underbrace{c_p^{\text{Px}} \rho^{\text{Px}} \int_0^{L^{\text{Px}}} T(y, t) - T(y, 0) dy}_{\text{Perspex reservoir}} \quad (5.7)$$

where L is the total thickness of material, and superscripts indicate the material

The heat flux into the top plate of the sensor, q_{measured} , was calculated by differentiating W_A with respect to time:

$$q_{\text{measured}}(t) = \frac{d}{dt}(W_A(t)) \quad (5.8)$$

The heat flux varied over the course of an experiment, as T_{surface} rises the flux decreases. To compare the experiment to model predictions, the heat flux had to be converted to parameters independent of the sensor temperature. These were the film heat transfer coefficient, h_{measured} , and the blackbody temperature, T_{BB} , describing convective and radiative heat transfer, respectively.

$$q_{\text{fitted}}(t) = \underbrace{h(T_{\text{boundary}}(t) - T_{\text{surface}}(t))}_{q_{\text{conv}}} + \underbrace{\epsilon \sigma_{\text{SB}}(T_{\text{BB}}^4 - T_{\text{surface}}^4(t))}_{q_{\text{rad}}} \quad (5.9)$$

here σ_{SB} is the Stefan-Boltzmann constant and T_{boundary} is the air temperature measured above the sensor by the thermocouple labelled 1 in Figure 5.12. The convective and radiative fluxes are denoted by q_{conv} and q_{rad} , respectively.

The values of h and T_{BB} were established for each experiment by fitting $q_{\text{fitted}}(t)$ to the $q_{\text{measured}}(t)$ data reported by the heat flux sensor. The value of h was assumed to be constant

for a given position in the oven, while T_{BB} was also constant for each position and oven setpoint combination.

Figure 5.13 shows four example measured heat flux profiles and fitted fluxes for position 2. All profiles show the flux decreases as the experiment progresses and T_{surface} rises. The fitted flux function matches the measured values well in all cases. Figure 5.14 presents every measured flux value against the fitted flux at the same time. The majority of the data lie on or close to the line of equality, indicating a good fit. The outlier values typically correspond to the start or end of experiments, when transient effects can introduce noise and incorrect readings. The R^2 for all the fits is 0.960, indicating q_{fitted} matched q_{measured} well.

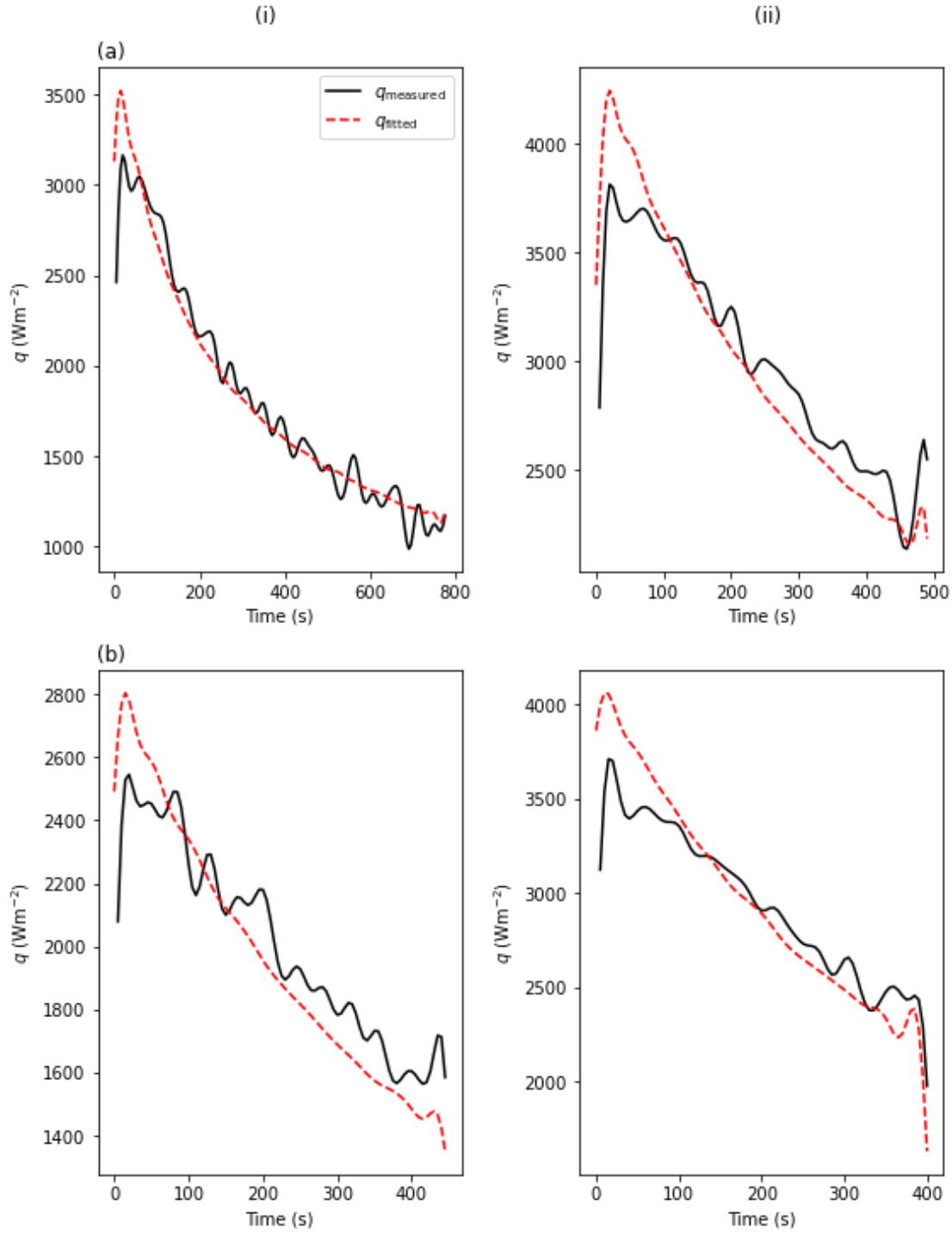


Figure 5.13: Example plots of q_{measured} and q_{fitted} , for position 2 in the oven, with $h = 34.6 \text{ Wm}^{-2}\text{K}^{-1}$ (a) oven setpoint 150°C, $T_{\text{BB}} = 120^\circ\text{C}$ (b) oven setpoint 200°C, $T_{\text{BB}} = 172^\circ\text{C}$. (i) $\epsilon = 0.05$, (ii) $\epsilon = 1$. Note different axis scales, legend in (a,i) common to all.

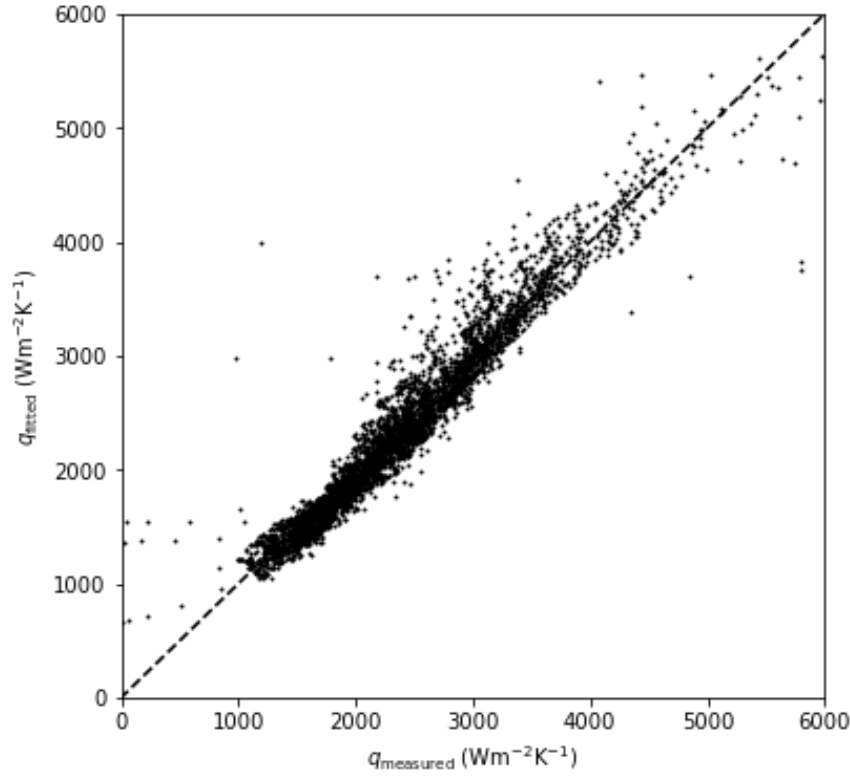


Figure 5.14: Plot of all measured heat fluxes vs the fitted values at the same timestep. Dashed line shows line of equality.

5.2.6: Estimation of the Sensor Uncertainty

Determination of the uncertainties in q_{fitted} , q_{rad} and q_{conv} was challenging as substantial calculation was required to find the heat fluxes from the thermocouple readings, including a low pass filter, two fitted functions and an integration and differentiation step. Therefore, the uncertainty in these measurements was estimated by identifying the primary sources of error and estimating their total effect.

The three-dimensional simulation of the sensor indicated that q_{measured} could be overpredicted by 20%, but was unlikely to be underpredicted. This systematic error was due to the Clough-Tocher surface fitted to the thermocouple measurements not exactly matching the temperature profile within the reservoir and uncertainty in the physical property parameters in the data processing script. Neither of these factors will change between tests and therefore the fractional error in q_{measured} will be constant. The uncertainty in q_{fitted} is linearly dependent on that of q_{measured} and therefore between 0 and +20%.

The largest source of uncertainty in q_{rad} lay with the value of ϵ used. The matt black top plate was assumed to have $\epsilon=1$ and the polished aluminium top plate emissivity was taken as 0.05¹⁴⁹. When fitting q_{fitted} to q_{measured} , q_{rad} can be found from the difference in q_{measured} between the high and low emissivity experiments by assuming that q_{conv} remains the same:

$$q_{\text{rad}} = \frac{q_{\text{measured}}(\epsilon_{\text{high}}) - q_{\text{measured}}(\epsilon_{\text{low}})}{\epsilon_{\text{high}} - \epsilon_{\text{low}}} \quad (5.10)$$

where ϵ_{high} and ϵ_{low} indicate emissivities for the matt black and polished top plates, respectively and $q_{\text{measured}}(\epsilon_{\text{high}})$ and $q_{\text{measured}}(\epsilon_{\text{low}})$ indicate the corresponding measured heat fluxes.

The percentage uncertainty in q_{rad} can therefore be estimated as the sum of the percentage uncertainties in q_{measured} and in $\epsilon_{\text{high}} - \epsilon_{\text{low}}$. The absolute uncertainty in ϵ was ± 0.1 , giving a minimum $\epsilon_{\text{high}} - \epsilon_{\text{low}} = 0.75$ and a maximum of 1, compared to the value of 0.95 used in the data processing script. This indicated that the uncertainty in ϵ contributed a percentage uncertainty in q_{rad} of +20% and -5%. The percentage uncertainty in $q_{\text{measured}}(\epsilon_{\text{high}}) - q_{\text{measured}}(\epsilon_{\text{low}})$ was between +20% and 0%, which gave a total percentage uncertainty in q_{rad} of between +28% and -5%, taking the square root of the sum of squares.

The uncertainty in q_{conv} could then be estimated. Using the logic applied in equation 5.10:

$$q_{\text{conv}} = q_{\text{measured}} - q_{\text{rad}} \quad (5.11)$$

The absolute uncertainty in q_{conv} is therefore the square root of the sum of squares of the absolute uncertainties in q_{measured} and q_{rad} .

¹⁴⁹ Fluke Process Instruments, 'Emissivity Values for Metals', in *Fluke Knowledge Centre*, 2018.

5.3: Laser Doppler Anemometry

5.3.1: Measurement Principle

Velocity measurements within the prototype I oven were made using a Dantec Flowlite 1D (Dantec Dynamics, Skovlunde, DK) laser doppler anemometry (LDA) system. LDA was invented by Yeh and Cummins in 1964 and a full description of its measurement principles can be found in Russo (2011)¹⁵⁰. LDA was good for measuring the velocity distribution due to its non-intrusive measurement and high spatial resolution.

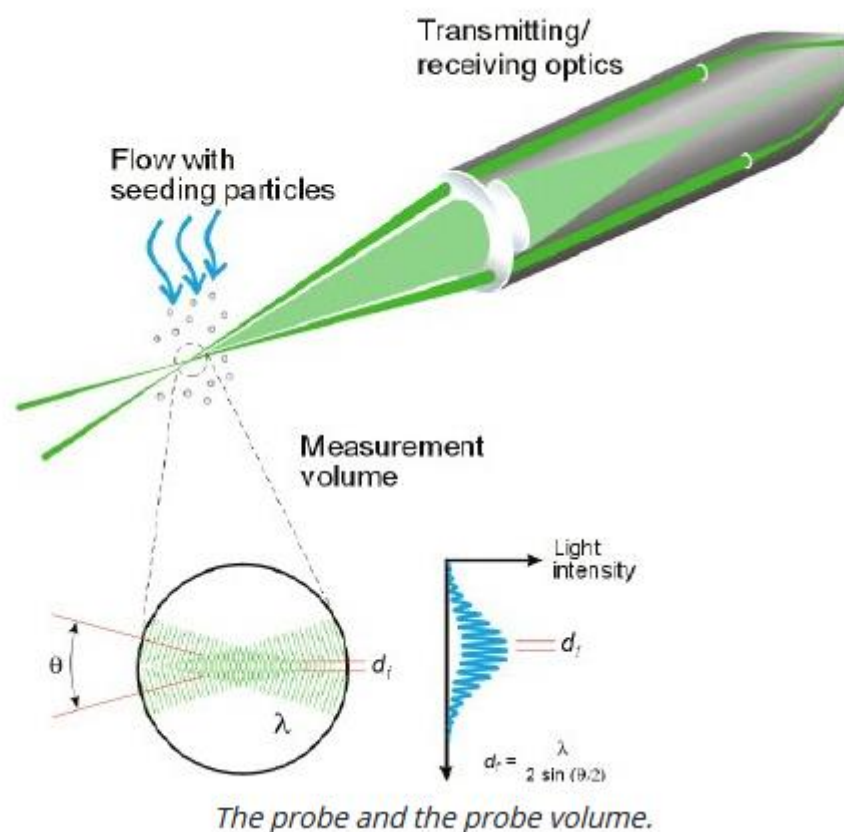


Figure 5.15: Diagram of the probe part of an LDA apparatus, source:¹⁵¹

Figure 5.15 illustrates the LDA operating method. The device functions by splitting a laser source into two beams that converge at point a fixed distance from the emitters: this is the point at which the velocity of the flow is measured. Seeding particles within the flow reflect light back into a lens on the LDA probe. The shift in frequency of this light compared to that emitted by

¹⁵⁰ G.P. Russo, 'Laser Anemometry', in *Aerodynamic Measurements* (Elsevier, 2011), 99–142.

¹⁵¹ Dantec Dynamics, 'Measurement Principles of LDA', 2021.

the laser is used to calculate the velocity of the seeding particles, and therefore the velocity of the fluid flow. The velocity component in the same direction as the vector between the two laser emitters is measured. Additional velocity components can be measured using additional laser probes with different wavelengths.

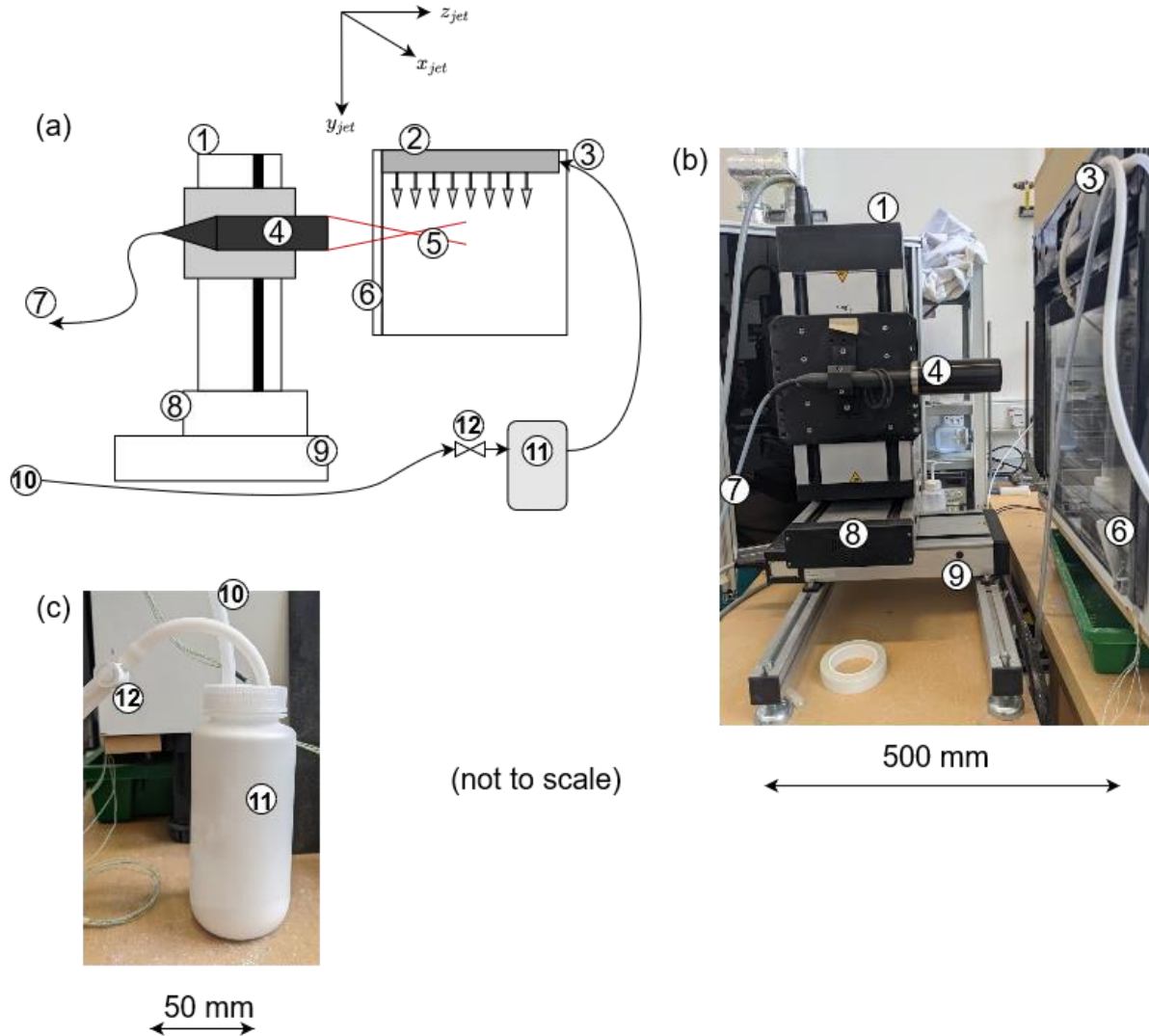


Figure 5.16: (a) Schematic of the LDA apparatus, side view. (b) Photograph of the LDA apparatus, side view. (c) Seeding particle generator, side view. 1 – y-axis traverse, 2 – impingement jets within the oven, 3 – seeding particle entry into the oven, 4 – LDA probe, 5 – measurement point for the LDA, 6 – replacement Perspex oven door, 7 – fibre optic connection to the laser and signal processing equipment, 8 – x-axis traverse, 9 – z-axis traverse, 10 – instrument air supply, 11 – seed particle generator, 12 – seed particle control valve.

5.3.2: Traverse and Probe

The LDA apparatus and the prototype I oven are shown in Figure 5.16. The Dantec assembly was supplied with a 3-axis traverse system that allowed 3 dimensional surveys of the velocity within the oven to be performed. The probe and signal processing allow velocities between -37 and 37 m/s to be measured. The velocity is measured 10 cm from the lens. The voxel over which the velocity is measured is approximately $2 \times 2 \times 2$ mm.

The traverse was placed on a table with a fixed position relative to the oven to maintain spatial consistency between measurements. The position of the z -axis was set such that the lens touched the Perspex door when at its most forward position. The y -axis was set such that the confluence of the laser was 20 mm below the jet openings at the highest setting. This was the closest approach to the nozzles possible without the metalwork blocking the upper laser emitter. The x -axis was set such that at zero the measurement position was parallel to the left side of the jet holes.

The double-glazed oven door was removed and replaced with a piece of laser cut Perspex, thickness 5 mm. This increased optical clarity, increasing the reliability of LDA measurements and allowed holes to be drilled for the seeding particle line to be fed into the oven. The Perspex door was removed and cleaned using anti-static cleaning fluid between each survey to prevent alumina particles sticking to the inside and interfering with measurements.

5.3.3: Seeding Particles and Generator

Dantec¹⁵² recommended alumina particles with diameter $< 8 \mu\text{m}$ as seeding particles. $1 \mu\text{m}$ alumina particles obtained from MetPrep (Coventry, UK) were used. These were fluidised within a seeding particle generator (shown in Figure 5.16(c)) by instrument air, the pressure of which could be varied by opening and closing a valve on the air supply line. The seeding particle generator was based on a 500 ml bottle that could be filled with alumina particles. Two holes were drilled through the lid for the air supply tube and connection to the oven. The air supply tube was cut such that air left the supply tube at the base of the flask. Conversely, the tube leading to the oven was cut with 1 cm protruding into the flask. This was to promote a flow of

¹⁵² Dantec Dynamics, *BSA Flow Software*, 8th ed., vol. 3, 2004.

air from the base of the flask to the top, carrying a controlled amount of alumina particles up and into the oven.

Fluidised alumina was carried into the oven through 3 mm i.d. silicone tubing. The tube was fed through a hole drilled in the front of the central impingement jet header. The length of tube within the oven was 30 cm, chosen such that seeding particles would enter the air flow within the oven at the point where air from the fan enters the row of impingement jets, thus ensuring particles were emitted from every impingement jet in the header.

5.3.4: Software

The traverse and signal processing module were controlled using Dantec BSA flow software, version 3 running on a Dell Dimension 5000 computer. As stated above, the software and traverse allow the LDA to measure the velocity at multiple coordinate points and move between them automatically. Once the traverse has moved the probe to the measuring point the signal processor reports measured velocities either for a set time period or until a set number of samples has been collected. The software does not report a single velocity measurement at each point: instead it reports a list of all the readings taken over the sampling period. An example of these readings is shown in Figure 5.17.

5.3.5: LDA Results Processing

The velocity results from the LDA were affected by noise. Only velocities between 0 and -15 m/s were expected within the oven but the LDA reported velocities across the device's entire measurement range, well outside the expected values. This led to difficulties in interpreting the results. A modal value of approximately -6 m/s is evident in Figure 5.17, which is within the range of expected values. However, the sample mean, shown in red, does not match this modal value and is greatly affected by the noise.

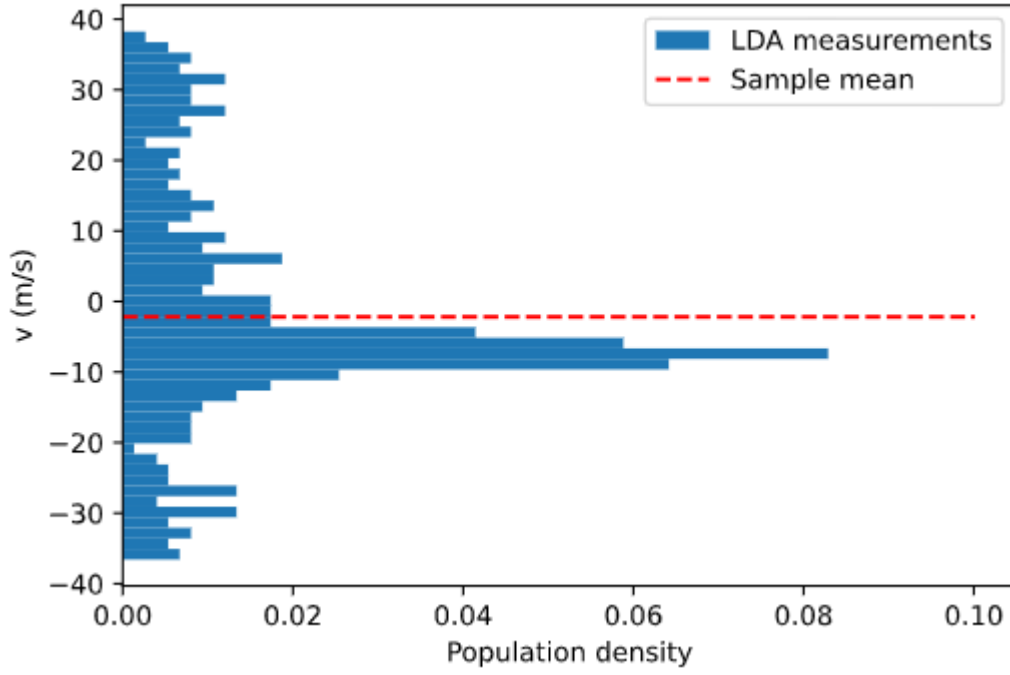


Figure 5.17: Histogram of an example of an LDA point measurement. Horizontal dashed line indicates the sample mean. (Number of samples=1000)

To separate the signal of velocities measured by the Dantec from the background noise readings a number of assumptions were made:

- i) Individual velocity readings from the LDA fall into two exclusive categories that can be described independently, either they are measurements of the velocity of seeding particles, the “signal”, or they are artefacts from the signal processor and are “noise”. The fraction of the total number of readings that are signal is given by α_{sf} .
- ii) Artefacts from the signal processing or “noise” readings are uniformly distributed across the measurement range.
- iii) Readings of the velocity of the seeding particle, or the “signal” are normally distributed around the mean velocity of the flow.

These assumptions mean that the distribution of readings across the measurement range can be described by the sum of a uniform and normal distribution:

$$f_X(v) = \alpha_{sf} \times \psi(v) + (1 - \alpha_{sf}) \xi(v) \quad (5.12)$$

where $f_X(v)$ is the probability density function of the velocity, α_{sf} is the fraction of the LDA measurements that are “signal”, and $\psi(v)$ and $\xi(v)$ are the normal and uniform probability density functions of v , respectively. Given by:

$$\psi(v) = \frac{1}{\sigma\sqrt{2\pi}} e^{-\frac{1}{2}\left(\frac{v-\mu_x}{\sigma}\right)^2} \quad (5.13)$$

$$\xi(v) = \begin{cases} 0, & v < v_{LDAmin}, v > v_{LDAmax} \\ \frac{1}{v_{LDAmin} - v_{LDAmax}}, & v_{LDAmin} \leq v \leq v_{LDAmax} \end{cases} \quad (5.14)$$

where σ is the standard deviation, μ_x is the mean and v_{LDAmin} and v_{LDAmax} are the minimum and maximum of the LDA measurement range, -37.9 and 37.9 m/s respectively.

Values of the fitting parameters, μ_x , σ and α_{sf} were altered to fit f_X to the LDA measurements by maximising the log likelihood function:

$$\log \text{likelihood} = \sum_{i=1}^n \ln [f_X(v_i)] \quad (5.15)$$

A basin hopping numerical optimiser was used from the Scipy python library. Basin hopping aims to find the global maximum by finding local maxima by gradient ascent before applying random perturbations of a given size and beginning gradient ascent again. A number of iterations of this process are run and the largest local maximum reported. The random perturbations aim to prevent the algorithm becoming “stuck” at local maxima in rugged functions.

An example of a fitted distribution is shown in Figure 5.18(a), superimposed upon the same LDA measurements plotted in Figure 5.17. The uniform “noise” and normal “signal” distributions have been labelled separately and the mean of the “signal” distribution, μ_x , is shown in red.

The fitted distribution fits the data well for this example. The peak in the data is matched by the fitted distribution with the mean of the “signal” distribution matching this peak. The background “noise” readings across the measurement range are accounted for by the uniform part of the

distribution. Truncated normal and normal distributions fitted to the same data set are shown in Figure 5.18(b). Neither of these was able to differentiate the sharp peak from the background noise.

The goodness of fits for different distributions to data can be compared using the Anderson-Darling statistic, a^2 . Details of this test are given in the paper introducing the method¹⁵³: lower values of a^2 indicate a better fit. The value of a^2 was computed for the normal, truncated normal and combined uniform normal distributions for all the measurements made using the LDA. This was performed using the Scipy python library, using the dask library for parallelisation to reduce the computation time. The histogram of the a^2 values in Figure 5.19 demonstrates that the combined uniform and normal distribution is consistently able to fit the data from the LDA. The mean value of a^2 for the combined uniform and normal distribution was 2.04, compared to 15.5 and 16.7 for the normal and truncated normal distributions, confirming the superior fit to the data for the former.

The assumption that the “noise” LDA measurements are uniformly distributed could be checked by examining the distribution of readings outside the range of velocities expected within the oven. Velocities reported by the LDA outside this range must be “noise” readings and therefore if the assumption is valid, their distribution should not depend on v . Figure 5.20 shows a histogram of LDA measurements with the values between 5 and -15 m/s removed. The plot shows that the distribution does not have a clear dependence on v , so the assumption of a uniform distribution is valid. The mean of the data is 1.1 m/s, the standard deviation is 24.6 m/s.

¹⁵³ T.W. Anderson and D.A. Darling, ‘Asymptotic Theory of Certain “Goodness of Fit” Criteria Based on Stochastic Processes’, *The Annals of Mathematical Statistics* 23, no. 2 (June 1952): 193–212.

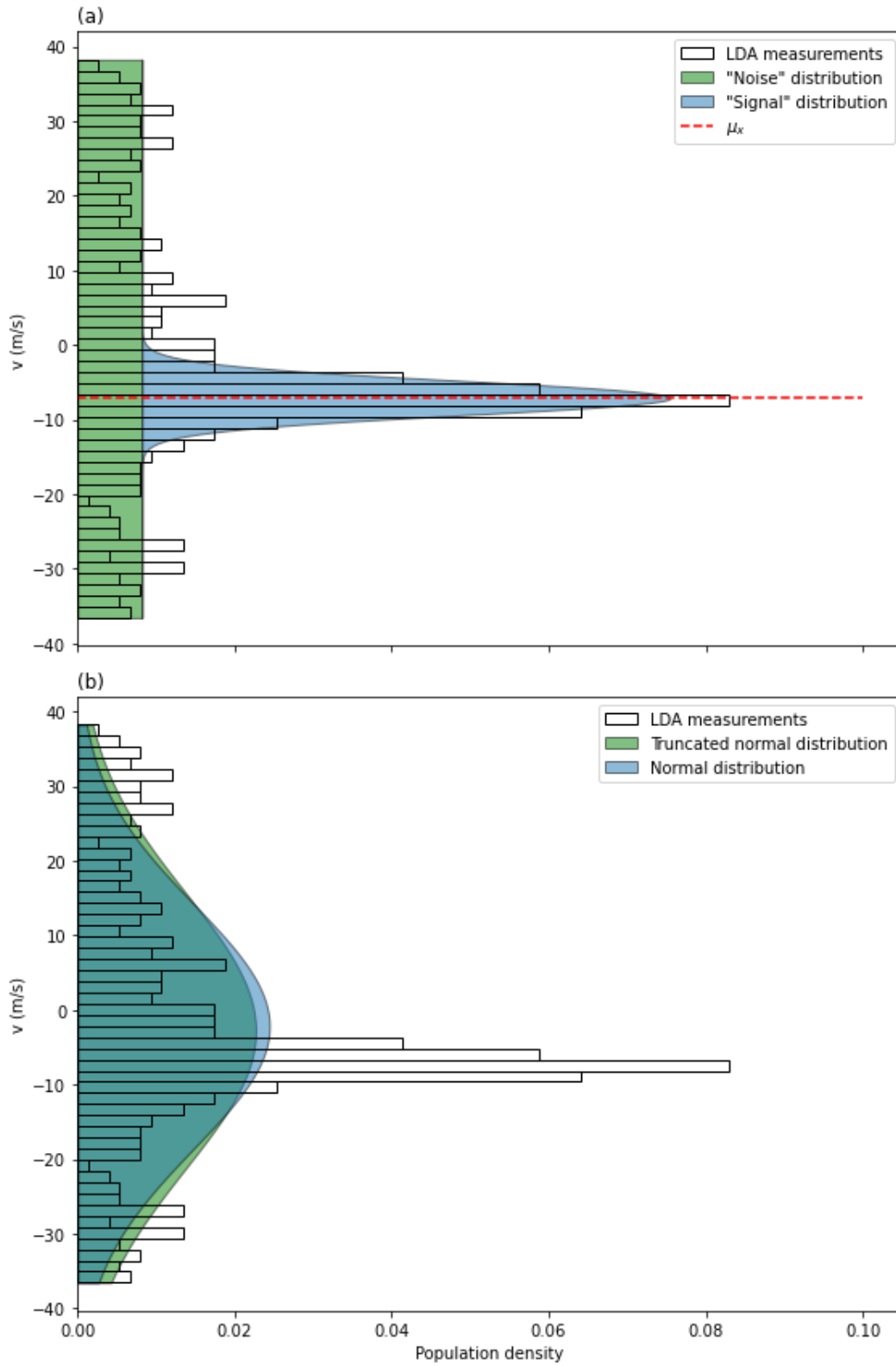


Figure 5.18: Histogram of velocity sampled at a single point by the LDA apparatus with fitted probability distributions superimposed. (a) Normal + Uniform distribution, (b) truncated normal and normal distributions (Number of samples = 1000.)

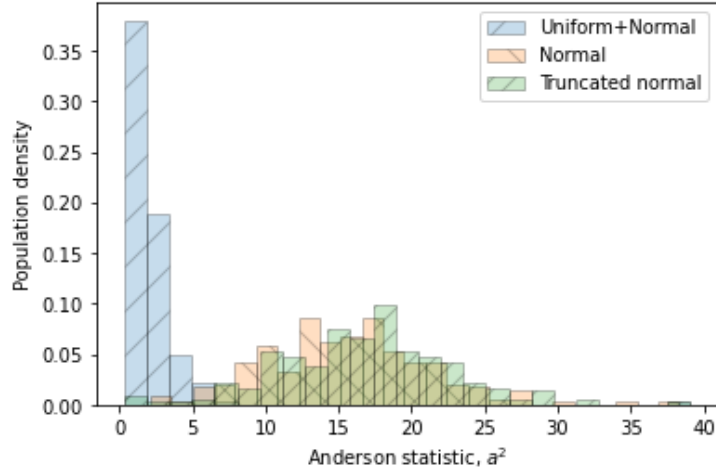


Figure 5.19: Histogram of a^2 values computed for three distributions fitted to the velocities recorded at each LDA measurement point. (Number of samples=245)

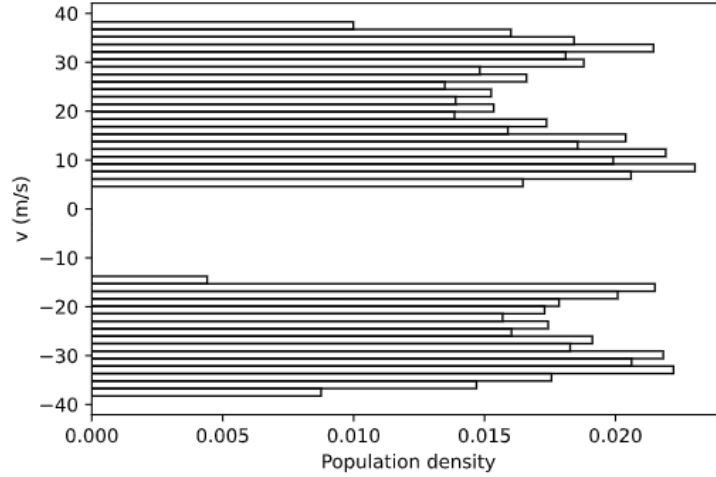


Figure 5.20: Histogram of LDA measurements for all measurement points that are outside the expected velocity range. (Number of samples=61600)

5.3.6: Experimental Procedure

The coordinate system used for the LDA measurements is shown in Figure 5.16 and 7.21. LDA measurements were taken in surveys of a 20×40 mm area in x_{jet} and z_{jet} respectively.

Measurements were spaced at 5 mm intervals, giving a grid of 5×9 points. These surveys were undertaken at $y_{jet} = 20, 40, 60$ and 80 mm. The LDA traverse proved to be defective and did not return to the same zero position when commanded to between surveys, giving inconsistent

x_{jet} and z_{jet} values. Instead, the coordinates were zeroed by taking $x_{\text{jet}} = z_{\text{jet}} = 0$ at the point with the highest velocity in each survey. The y_{jet} axis was set using a ruler and manually moved to the correct position for each survey.

The signal processor was set with the maximum voltage and input gain, 1000 V and 32 dB. The system was configured to record 1000 sample velocities at each measurement point before moving to the next coordinate.

Before a survey was begun, the interior of the oven was cleaned using a vacuum cleaner and anti-static cleaning solution to prevent seeding particles sticking to the interior surfaces. The oven fan was run at full speed and left for 60 s to equilibrate. The seed particle generator was filled with alumina powder, the air supply turned on, and the survey begun. The number of samples recorded by the LDA signal processor per second was monitored during the survey. When this value dropped below 100 s^{-1} it indicated the number of seeding particles in the jet had dropped due to the powder in the generator settling. The seeding particle generator was then shaken to redistribute the powder and increase the rate of seeding particle flow.

6: Lumped Property Model

6.1: Introduction

Lumped property models of the COI oven and a traditional oven were created to predict the performance of the COI design and identify the parameters most important to its performance. A lumped property model is created by treating each body within a system as homogenous. These homogenous bodies can then exchange energy and mass according to defined equations. The fluxes calculated are then used to find how the bodies' temperatures change with time. The arrangement of these bodies used to model a traditional oven design is shown in Figure 6.1. The model featured many simplifications:

- i) Only convective and conductive heat exchange is considered.
- ii) Material properties are constant.
- iii) No chemical changes occur in the food.
- iv) Food is considered cooked once the core reaches a target temperature, neglecting factors such as browning.
- v) The temperature of a solid body has no spatial variation.
- vi) Heat transfer into a solid is approximated by considering the transfer between the surface and a point halfway to its centre.

Due to these simplifications the model was not expected to be quantitatively accurate. The model had two aims: first, it was a simple and quick method to evaluate the effectiveness of the COI design compared to a traditional fan oven. Secondly, the short computation time of the model meant the impact of changing design parameters could be assessed over a wide range. The results of this analysis were used to investigate the sensitivity of the design to various factors, informing future design iterations.

Key:

Shape	Meaning	Line	Meaning
Red	Heater	Dashed	Control signal
Blue	Gaseous Body	Red	Heat exchange
White	Solid Body	Blue	Mass exchange
Yellow	Food		

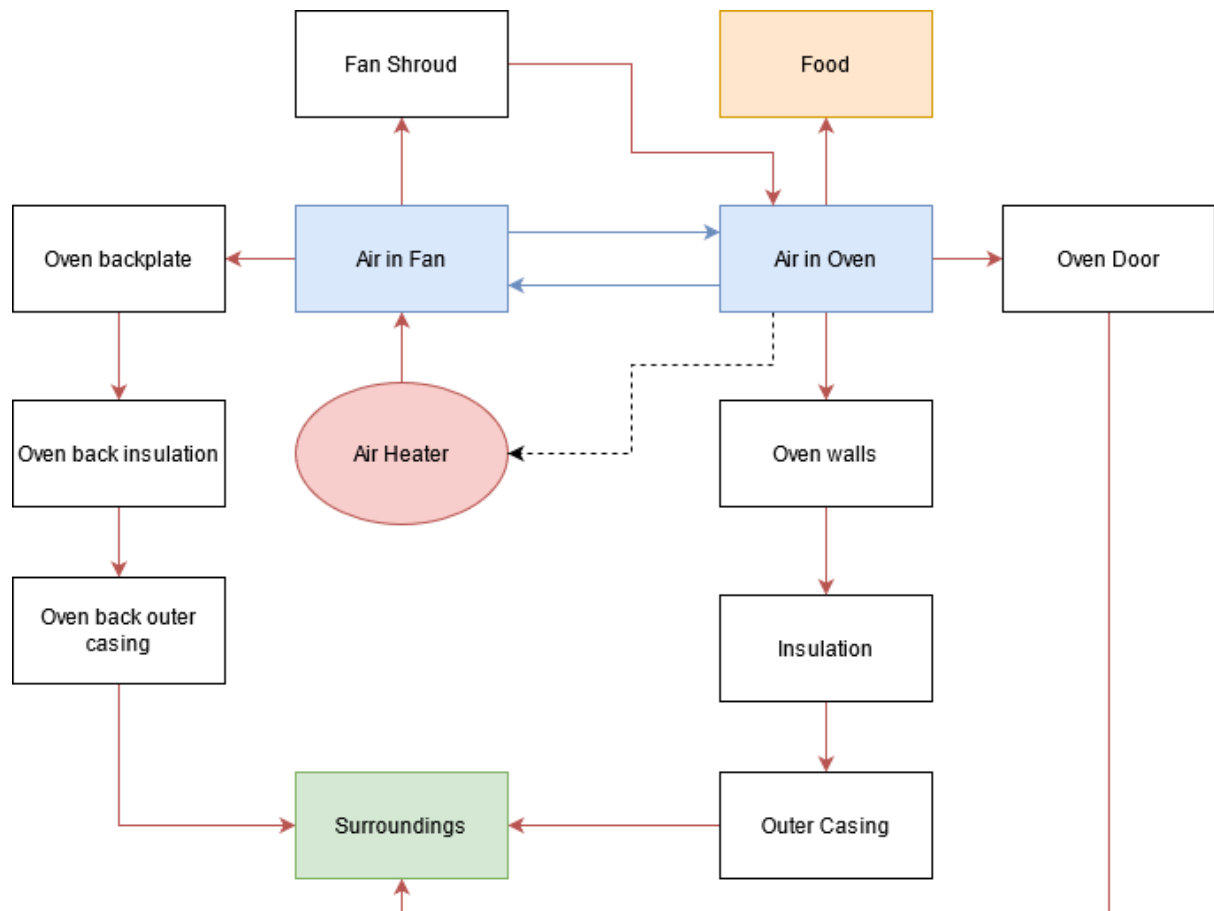


Figure 6.1: Schematic of the traditional oven lumped parameter model

6.2: Model Objects

A new python library was written for quick creation of lumped property models. This section gives an overview of the library's classes and methods, how the transfer of heat is calculated and how the temperature changes with time are found.

6.2.1: Classes and Governing Equations

The library contains three classes that are used to define the system.

i) **Material:**

This class stores thermophysical properties that can be accessed by the other classes: density, specific heat capacity and thermal conductivity.

ii) **Body:**

The body class is used to model one body within the system. Each body has the following attributes; volume, material, temperature and a fixed heat transfer coefficient that is calculated based on the type of body. At each time step energy can be added or removed from each body using the *add_heat* method. Three different forms are used to capture the behaviour of different parts of the model:

- a) Solid body: Used to model the food and walls of the oven. Requires a thickness parameter that is used to calculate the heat transfer coefficient into the solid. The heat transfer coefficient is calculated from:

$$h = k \times \frac{2}{L_b} \quad (6.1)$$

where L_b is the total thickness of the body

- b) Gaseous body: Used to model air volumes within the oven. The heat transfer coefficient for the body must be defined by the user, taken from literature, experiment or a CFD model.
- c) Surroundings: Used to model the surroundings of the system. As with the gaseous body class, the heat transfer coefficient for this class must be defined by the user. The surroundings class differs in that the temperature is constant, independent of the heat flow into it.

The temperature of a gaseous or solid body is calculated for each timestep in the *time_step* method:

$$T_i(t + \Delta t) = T_i(t) + \Delta t \left(\frac{1}{V_i \rho_i C_{p,i}} \sum Q_e \right) \quad (6.2)$$

where the i subscript denotes a property of body i , $T_i(t)$ is the temperature at time t , V is the volume of the body, Δt is the length of one timestep and ΣQ_e is the sum of all the rates of heat flow into the body, calculated by the exchanger classes described in the next section.

iii) **Exchanger:**

The exchanger class manages the exchange of energy between bodies in the system. All exchangers take two bodies as arguments and during each timestep the rate of heat transfer between the two bodies is calculated using the *calc_transfer* method. The rate of heat flow calculated is added to the two bodies using the aforementioned *add_heat* method. Three types of exchanger can be defined:

- a) Heat exchanger: Used to define heat flux between two solids or a solid and a gas. Exchanger area A must be given as well as an optional film resistance argument, $1/h_{\text{film}}$. The overall heat transfer coefficient between the two bodies, U_e , can then be calculated:

$$U_e = \left(\frac{1}{h_1} + \frac{1}{h_2} + \frac{1}{h_{\text{film}}} \right)^{-1} \quad (6.3)$$

where h_1 and h_2 represent the heat transfer coefficients for the 2 bodies.

Equation 6.4 then gives the heat transferred per second for the exchanger, Q_e :

$$Q_e = U_e A (T_1 - T_2) \quad (6.4)$$

The *add_heat* method for bodies 1 and 2 is then called with $(-Q_e)$ and $(+Q_e)$ as the arguments respectively.

- b) Mass exchanger: Used to define the exchange of energy between two gaseous bodies where gas is flowing between them. The energy transferred from body 1 to body 2 of the exchanger is equal to the enthalpy of the gas flow, as calculated by equation 6.5:

$$Q_e = \dot{M} C_{p1} T_1 \quad (6.5)$$

where \dot{M} is the mass flow of gas which is defined by the user.

As with the heat exchanger class the *add_heat* method is then called for both bodies, with the argument $(-Q_e)$ for body 1 and $(+Q_e)$ for body 2. Care must be taken to ensure the mass flows sum to zero for each body.

- c) Heaters: Heaters are modelled by calling the *add_heat* method with Q_e equal to the power rating of the heating element. Oven control can be incorporated by

only calling *add_heat* when certain conditions are met. For example, $Q_e = 0$ when the oven air temperature is equal to or higher than a set point value.

6.3: Usage

A flowchart of the model process is shown in Figure 6.2. The model was constructed using the above classes as building blocks. First, materials were defined and used to create the bodies. The heat transfer coefficient for the solid bodies was calculated at this time using equation 6.1. The bodies were then connected using the exchanger classes. The model simulated the cooking process by calculating the fluxes and temperature changes for discrete timesteps; for each timestep it iterated over every exchanger running the *calc_transfer* function. This step calculated the heat flux into and out of all bodies in the model using equations 6.3, 6.4 and 6.5. The model then iterated over all the bodies in the model, calculating the change in temperature that resulted from the summed fluxes in the timestep, using equation 6.2. The body temperatures were then updated and the calculation for the next timestep begun. This continued until the food reached a target temperature. The model recorded the total time taken to cook, the energy consumption and the temperature profiles for each body.

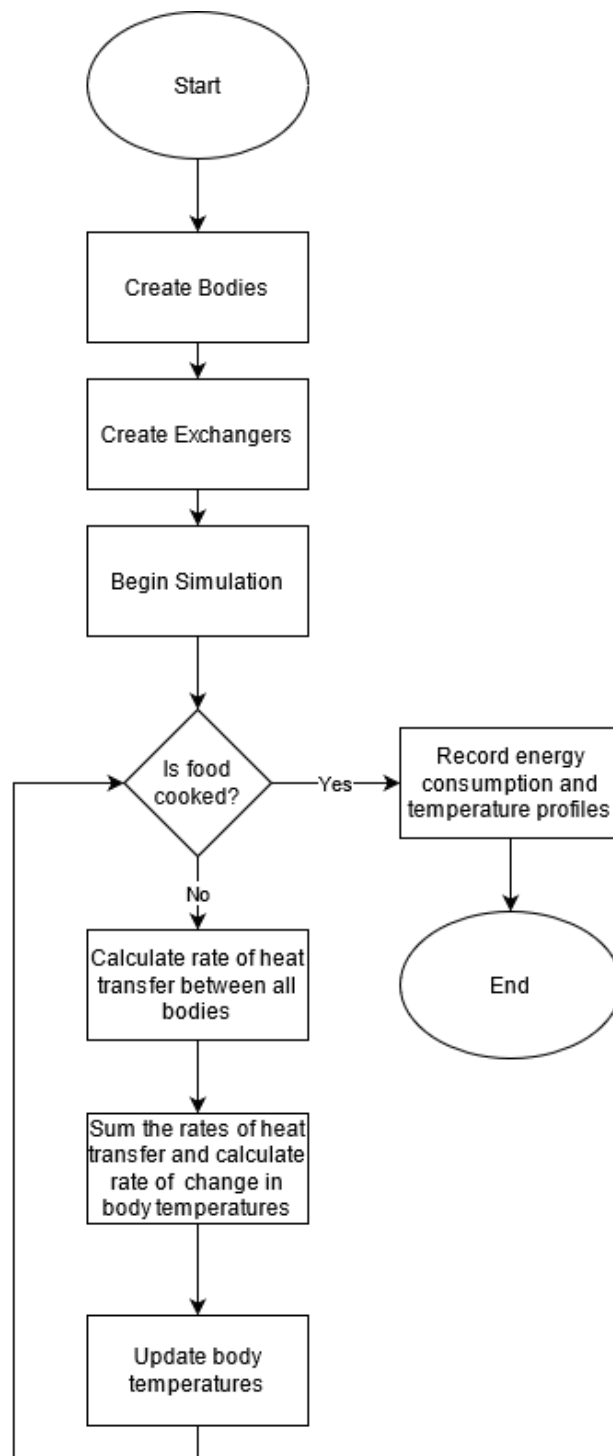


Figure 6.2: Flowchart for the lumped property model python library

6.4: Model Architecture

This section describes the specific arrangements of bodies and exchangers used to model the COI and traditional fan ovens.

6.4.1: Common Features

The COI oven was built from the frame of a standard fan oven. As such, there are a number of exchangers and volumes that are common to both oven models. These are summarised in this section. Areas of the heat exchangers and volumes were measured on a standard Beko fan oven (Model number: BXIM25300XP, Arcelik, Istanbul, TK). Volumes were separated into multiple bodies within the model where significant differences in heat transfer coefficient or temperature were thought to exist, for example, between the heater section in the back of the oven and cooking chamber. The oven door was treated as one body with a heat transfer coefficient taken from Aydin and Orhan¹⁵⁴, which for a double-glazed window of thickness 3 cm gave an overall heat transfer coefficient of $12 \text{ W m}^{-2} \text{ K}^{-1}$. The heat capacity and density of the door was a weighted average of the glass and air contained within it, namely, 750 kg m^{-3} and $1500 \text{ J kg}^{-1} \text{ K}^{-1}$.

Chicken and pizza were modelled to assess the performance of the COI design when cooking food with a high and low Biot number. The properties used in the model are given in Table 6.1. The geometries of the food items are given in Table 6.2. Chicken properties were taken from Chen *et al.*¹⁵⁵. Pizza properties were taken from a review of bread properties by Rask¹⁵⁶. The chicken's volume was assumed to be 0.002 m^3 which gave a mass of approximately 2 kg. The meat parts of the chicken (breast and thighs) were assumed to be 6 cm thick: the area of 0.13 m^2 was derived from assuming the chicken to be a sphere with radius 10 cm. The pizza was assumed to be a disc of radius 15 cm and height 2 cm. The target temperature for chicken of 75°C was the USDA recommendation for poultry: the target for pizza was assumed to be 100°C .

¹⁵⁴ O. Aydin, 'Conjugate Heat Transfer Analysis of Double Pane Windows', *Building and Environment*, 2006, 8.

¹⁵⁵ Chen, Marks, and Murphy, 'Modeling Coupled Heat and Mass Transfer for Convection Cooking of Chicken Patties'.

¹⁵⁶ Rask, 'Thermal Properties of Dough and Bakery Products'.

Table 6.1: Physical properties assumed for pizza and chicken in the lumped parameter model

Food	ρ (kg m ⁻³)	C_p (J kg ⁻¹ K ⁻¹)	k (Wm ⁻¹ K ⁻¹)
Pizza	500	2200	0.25
Chicken	1100	3570	0.412

Table 6.2: Geometry and temperature parameters used for the pizza and chicken bodies, Bi is calculated for $h = 35 \text{ Wm}^{-2}\text{K}^{-1}$

Food	Starting Temperature (°C)	Target Temperature (°C)	Volume (m ³)	Thickness (m)	Area (m ²)	Bi
Chicken	4	75	0.0012	0.06	0.13	2.8
Pizza	4	100	0.00075	0.02	0.14	0.7

6.4.2: Traditional Oven Model

The traditional oven model was formed from 13 bodies and 16 exchangers (see Figure 6.1).

Power was supplied to the system by the air heater in the back of the oven. On/off control was used, using the temperature of the air within the cooking chamber as the measured variable.

Parameters defining the bodies and exchangers are given in Appendix B. The convective heat transfer coefficient within the oven chamber was taken as $15 \text{ Wm}^{-2}\text{K}^{-1}$, as measured by Carson *et al*¹⁵⁷.

6.4.3: COI Oven Model

A schematic of the COI oven model is shown in Figure 6.3. While the model of the oven shell remained the same as the traditional oven, several additional bodies, exchangers and heaters were required to describe the air flow and heating arrangement of the design.

The air cycle within the oven is described by 4 gaseous bodies. Air initially enters the heater section and energy is transferred to it by the air heaters. This air then flows out from the jets in the roof of the oven and impinges onto the top of the food. The volume of air between the jets and the food surface is called the “impingement air”. All the air leaving the jets enters this body.

¹⁵⁷ Carson, Willix, and North, ‘Measurements of Heat Transfer Coefficients within Convection Ovens’, 1 February 2006.

Additionally, the jets entrain an amount of air from the surrounding bulk air within the cooking chamber. The mass ratio of entrained air from the cooking chamber to air flowing from the jets can be controlled using the mixing ratio parameter in the model. After impinging on the food, all the impingement air flows into the bulk air within the cooking chamber. This bulk air in the cooking chamber is finally drawn into the back of the oven, through the fan and ductwork and back to the heater section, completing the loop.

The base heater is modelled by supplying heat directly to a solid metal plate. The temperature of this metal plate is used to control the power supplied using on/off control. A heat exchanger object calculates the energy transfer between the metal plate and the food. The contact area for heat transfer and film resistance can be varied.

6.4.4: Parameter Assumptions

The heat transfer coefficient for the impingement air was $35 \text{ Wm}^{-2}\text{K}^{-1}$, taken from an early iteration of the CFD model (chapter 7). This was also the heat transfer coefficient assigned to the air in the heater section and ductwork due to the similarly high velocity. A reduced coefficient of $15 \text{ Wm}^{-2}\text{K}^{-1}$ was used for the bulk air within the cooking chamber, assuming that it behaved similarly to the air within a traditional convection oven. The power of the air heater was set at 2400 W to be consistent with the traditional oven. The base heater was therefore limited to 1200 W so that the oven could not draw more than the maximum 13 A. The heat transfer coefficient between the pan and the food was set at $100 \text{ Wm}^{-2}\text{K}^{-1}$. Pan and Singh measured heat transfer coefficients as high as $800 \text{ Wm}^{-2}\text{K}^{-1}$ ¹⁵⁸ when cooking burger patties on a smooth heating surface. The lower value used in the model accounts for the fact that foodstuffs will often not be as flat as a burger patty and will therefore not form as good a contact with the pan surface.

¹⁵⁸ Pan and Singh, 'Heating Surface Temperature and Contact-Heat Transfer Coefficient of a Clam-Shell Grill'.

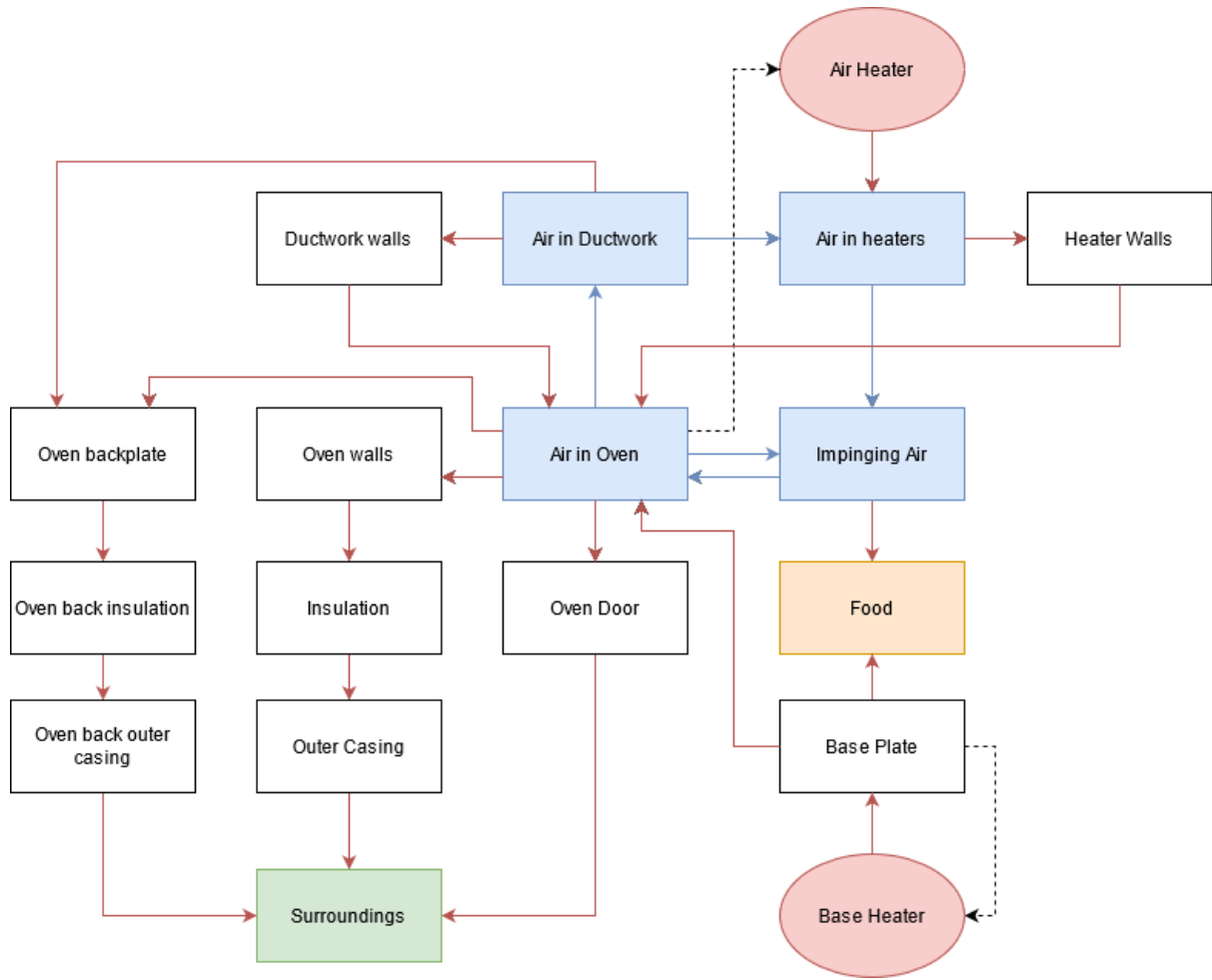


Figure 6.3: Schematic of the COI oven lumped parameter model, key can be found in Figure 6.1.

6.4.5: Timestep Selection

To select an appropriate timestep the traditional and COI oven models were run with chicken as the food. The timestep was varied and both the total power consumption and cooking time recorded. These values were then compared to the model results with a timestep of 1 ms, the smallest timestep tested, to calculate the fractional error. These are plotted in Figure 6.4(a). Timesteps greater than 0.3 s led to unstable behaviour, likely due to the low thermal mass of the “air in heaters” body where thermal energy is delivered into the model by the heater.

The effect of timestep length on the time taken to run the model of the COI oven cooking a chicken is plotted in Figure 6.4(b). This shows the computation time decreased approximately linearly as timestep length increased, until the onset of instability at timesteps > 0.1 s.

A timestep of 10 ms was chosen for subsequent models as the error in both power and energy was less than 1% and the computation time of 20 s was convenient. As the model runs in a single process, multiple models can be run in parallel with no effect on solution speed.

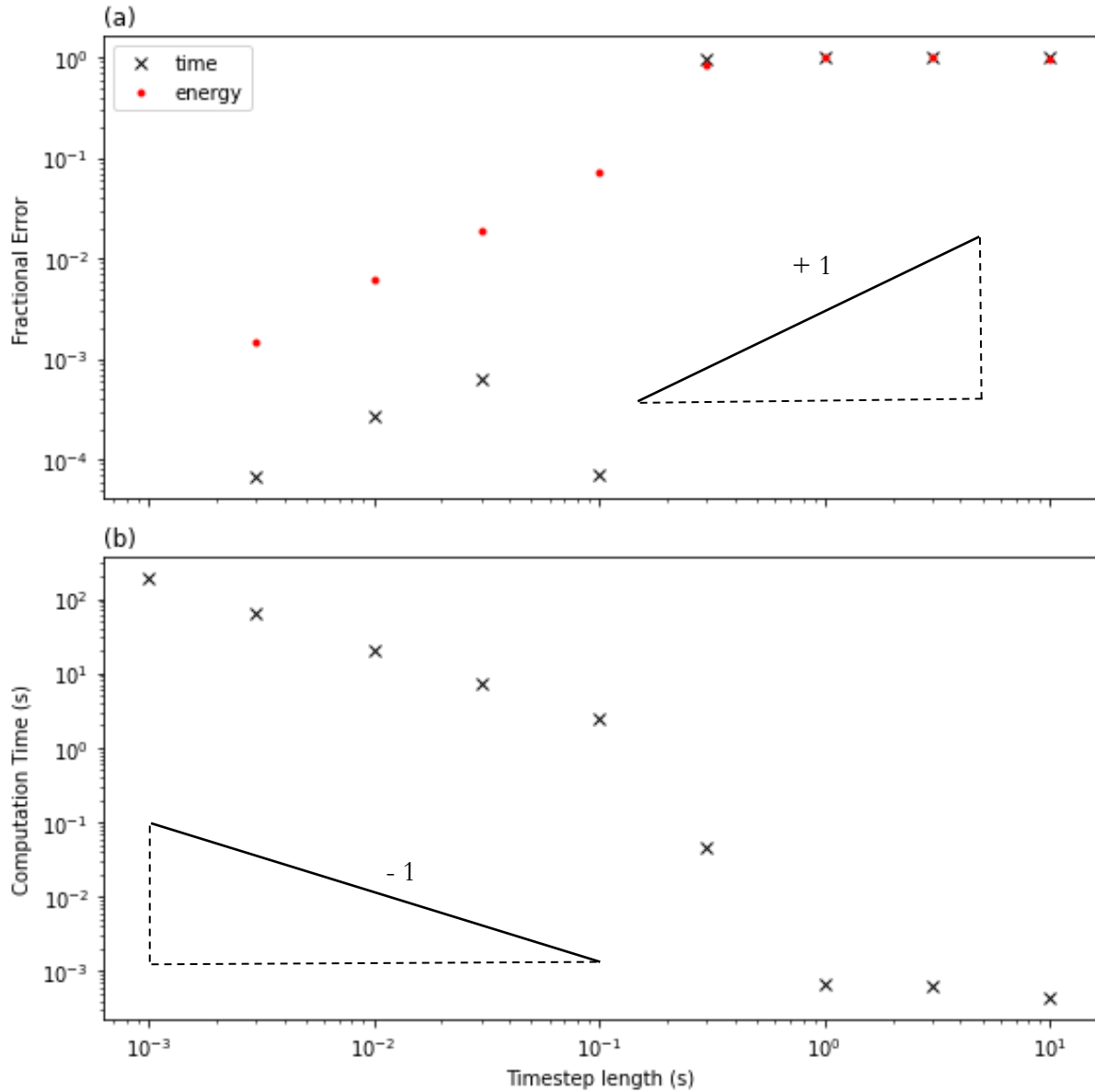


Figure 6.4: Effect of timestep length on (a) the fractional error in cooking time and cumulative power consumption and (b) time taken to run the model. Results for chicken in the COI oven.

6.5: Results

The cooking of pizza and chicken was modelled in three oven configurations; (i) the traditional oven model and the COI oven model both (ii) with and (iii) without the base heater active. The

setpoint of the temperature controllers was 180°C. The power and energy consumption results for this study are shown in Table 6.4. Comparisons with measured energy consumption and cooking time for the traditional oven are given in Table 6.3 and Figure 6.5. The results show reasonable agreement with experiment: the largest percentage error in the parameters of interest was for the cooking time for chicken, which was underpredicted by 17.8%.

The difference can be attributed to the inability of the model to capture the lag time before the heat wave reaches the core of the chicken, as can be seen in Figure 6.5(a). In the experiment the core of chicken remained at its starting temperature for approximately 20 minutes, while the model predicts a roughly linear increase in temperature with time. This was anticipated as the model did not model the spatial variation of temperature within the food. The model also predicted the oven air heating up more quickly than was measured experimentally, which was attributed to some of the thermal mass of the oven being unaccounted for in the model. The imperfections in the oven's control, such as the initial overshoot of the temperature setpoint and the oscillation around the setpoint evident in Figure 6.5(a), were not captured by the model. However, the power consumption of the oven was accurately predicted, as shown in Figure 6.5(b). Another simplification of the model was that it ignored the preheating time of the traditional oven. In the experiment, food was only added to the oven after 5 to 10 minutes, when the setpoint temperature was reached. In the model, food was added to the oven when the oven was powered on. This led to the model underestimating the cooking time in the traditional oven by approximately 5 minutes and also underestimating the power consumption of the traditional oven.

As stated in section 6.1, the aim of the model was not to give quantitatively accurate predictions, but to provide a rough prediction for the efficacy of the COI oven design and suggest which parameters will be most important to optimise in future prototypes. The comparison with experiment shows that the model is sufficiently accurate for this purpose.

Table 6.3: Comparison between the traditional oven model and experimental values.

Food	Value	Units	Experiment Value	Model Prediction	Error (%)
Pizza	Energy	kWhr	0.35	0.39	+12.2
	Consumption				
Chicken	Cooking Time	min	20.0	21.0	+5.0
	Energy	kWhr	1.05	0.91	-13.3
	Consumption				
	Cooking Time	min	90.0	74.0	-17.8

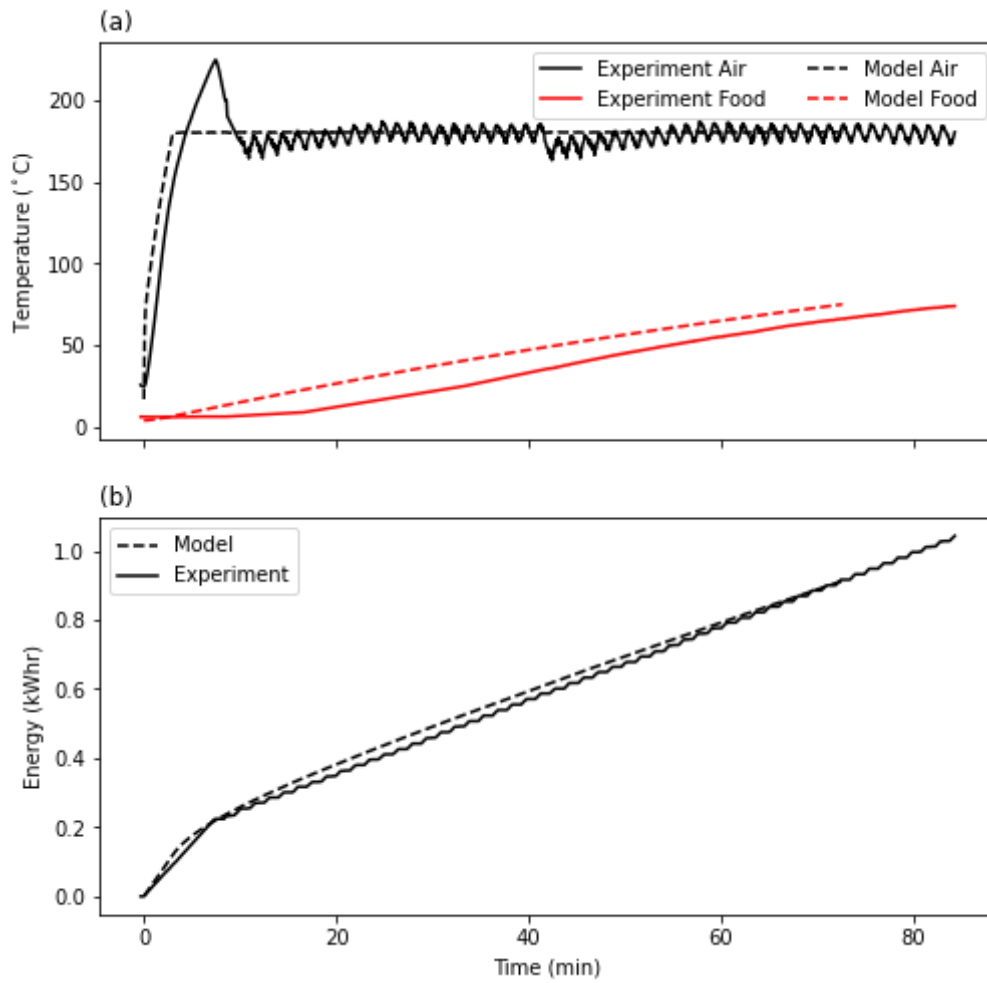


Figure 6.5: Comparison between experiment and the lumped property model for the cooking of chicken. (a) Evolution of the temperature of the air within the oven chamber and the core temperature of the chicken. (b) Energy consumption.

Table 6.4 compares the predicted performance of the traditional oven arrangement and the COI design, both with and without the base heater. The results demonstrate the potential of the COI oven design to reduce energy consumption and cooking time compared to a traditional oven layout for pizza, a food with a low Biot number, and chicken, a food with a relatively high Biot number. Table 6.4 shows that the COI design with a base heater decreased cooking time by more than half for pizza and 48% for chicken, whilst also reducing power consumption considerably. Removing the base heater reduced efficiency. Cooking by conduction is highly efficient, therefore removing the conductive cooking element will reduce the overall efficiency of the system. Removing the base heater also reduces the maximum power of the oven and thus increased the cooking time.

Table 6.4: Summary of model results for three models cooking pizza and chickens. Time and energy savings are calculated compared to the traditional oven. Efficiency is the fraction of the energy supplied by the heaters that is absorbed by the food.

Food	Oven	Time		Energy		Efficiency (%)
		Duration (min)	Saving (%)	Total (kWhr)	Saving (%)	
Pizza	Traditional	21	-	0.393	-	13.3
	COI with base heater	8.4	60.0	0.292	25.7	18
	COI no base heater	12.4	40.9	0.298	24.1	17.7
Chicken	Traditional	74	-	0.91	-	16.7
	COI with base heater	38.4	48.1	0.62	31.9	24.5
	COI no base heater	52.5	29.1	0.81	11	18.7

6.6: Sensitivity Analyses

The second analysis performed using the lumped property model was to investigate the impact of model parameters that had a large uncertainty in their value on energy consumption and cooking time. The aim of this was twofold. First, to assess the validity of the results in Table 6.4 by determining if the simulated performance of the COI oven was solely due to the values of the model parameters used, or if the design outperforms the traditional oven over a range of input parameters. Second, the analysis aimed to assess the impact of these parameters on performance and therefore determine which aspects of the design should be focussed upon in future iterations.

Two analyses were performed for each food type; one investigating parameters relating to convective heat transfer and another considering parameters important to heat transfer between the hot plate and the food. In each analysis three input parameters were varied over a cubic grid and the cooking time and total energy consumption recorded for each case.

To quantify the impact of these parameters on oven performance all the input and output parameters were scaled and normalised using their values in the base model.

$$\langle x \rangle = \frac{x - x_{\text{base}}}{x_{\text{base}}} \quad (6.6)$$

where x is any model parameter, the **base** subscript signifies the base model values, the $< >$ brackets indicate the normalised value.

A linear model using the normalised parameters was then fitted to energy consumption and cooking time:

$$H_{\theta}(< x_{\text{inputs}} >) = \sum_{i=0}^{n_{\text{inputs}}} (\theta_i \times < x_i >) \quad (6.7)$$

where $H_{\theta}(< x >)$ is the fitted energy consumption or cooking time given by the linear model for a given x_{input} or set of normalised input parameters. θ_i is the linear coefficient for a specific input parameter.

The magnitude of the linear coefficients gave a measure of how sensitive the output parameters were to the various input parameters. The coefficients represent the ratio of fractional change in the input parameter to the expected fractional change in the output parameter. For example, a +50% change in input with a coefficient of 0.5 would give a change of +25% in the output parameter.

6.6.1: Convection Sensitivity Analysis

The input parameters considered in the analysis are listed in Table 6.5 alongside the range of values and the number of intervals. The coefficients of the linear model are recorded in Table 6.6.

- i) Heat transfer coefficient: this was chosen as the value was taken from a CFD simulation rather than measured experimentally, with associated uncertainty in its value. In addition, testing higher values gave insight into whether increasing the heat transfer coefficient was important in improving efficiency and cooking time.
- ii) Jet flowrate: this was also taken from the CFD model and was therefore also uncertain.
- iii) Mixing ratio was the ratio of the mass of bulk air within the oven to the mass of air flowing from the jets. This parameter was estimated to be 0.5 in the base model. The

true value of this parameter is unknown. Investigating a large range of values was therefore prudent.

It should be noted that in reality these parameters will be related; increasing either flow rate or mixing ratio will alter the velocity of the air impinging on the food and will therefore alter the heat transfer coefficient. For simplicity, this interaction is not considered in the analysis.

The other parameters inputted into the models were either geometric in origin, such as the areas of the oven walls, or were common between the models, such as food properties.

These parameters were therefore either known more reliably or impact both the COI and traditional oven models similarly.

Table 6.5: Convection sensitivity analysis specification

Object	Variable	Unit	Value in base model	Minimum Value	Maximum Value	Number of steps
Impingement Air	Heat Transfer Coefficient	$\text{Wm}^{-2}\text{K}^{-1}$	35	15	50	8
Jets Air	Flowrate	kg s^{-1}	0.002	0.001	0.003	5
Impingement Air	Mixing Ratio	-	0.5	0	4	8

The linear model fitted to the results from this sensitivity analysis had an adjusted- R^2 of 0.889, indicating the linear model fit the results well. The linear coefficients, θ_i of the model are given in Table 6.6.

The comparison with experimental values for the traditional oven in Table 6.3 showed the lumped property model was able to predict the performance of a traditional oven with reasonable accuracy. The linear coefficients, shown in Table 6.6, are all significantly lower than unity indicating the model of the COI oven was insensitive to changes in the input parameters. Even in the worst case for COI oven, when the heat transfer coefficient was reduced to $15 \text{ Wm}^{-2}\text{K}^{-1}$, the same as in the traditional oven, and less favourable estimates of mixing ratio and flowrate were used, the cooking time and energy consumption were still reduced compared to the traditional design. This is because the design of the COI oven will always have hotter air contacting the food than the oven walls, preferentially heating the food rather than wasting energy heating the oven walls. This analysis therefore gives additional confidence in the model's predictions of the COI design performance.

Table 6.6 shows that heat transfer coefficient had the largest impact on both cooking time and energy consumption of the parameters investigated. This is also evident in Figure 6.6, where scaled cooking time and energy consumption for chicken and pizza are plotted against scaled heat transfer coefficient with the scaled mixing ratio and scaled flowrate shown by the marker size and hue, respectively. The impact of changing heat transfer coefficient over the selected range of values is much larger than for the other parameters. However, the impact of increasing the heat transfer coefficient above the model prediction of $35 \text{ Wm}^{-2}\text{K}^{-1}$ did not greatly reduce energy consumption or cooking time; a 50% increase in heat transfer coefficient gave only a 10% improvement in both output parameters. This indicates that increasing the heat transfer coefficient above the model prediction should not be a priority for future development and ensuring any prototypes achieve $35 \text{ Wm}^{-2}\text{K}^{-1}$ is sufficient.

Table 6.6: Linear model coefficients for the convection sensitivity analysis

Food	<Output Parameter>	<Input Parameter>	Linear Coefficient
Pizza	Energy Consumption	Heat Transfer Coefficient	-0.135
		Flowrate	-0.0106
		Mixing Ratio	0.0075
	Cooking Time	Heat Transfer Coefficient	-0.426
		Flowrate	0.0500
		Mixing Ratio	0.0238
Chicken	Energy Consumption	Heat Transfer Coefficient	-0.106
		Flowrate	-0.00320
		Mixing Ratio	0.00370
	Cooking Time	Heat Transfer Coefficient	-0.292
		Flowrate	0.0177
		Mixing Ratio	0.0100

The linear coefficients were universally higher for pizza cooking compared to chicken cooking. This was expected as the Biot number for pizza is significantly lower than for chicken, meaning that external heat transfer will have a greater effect.

Cooking time and energy consumption are highly correlated, with a Pearson's coefficient >0.98 for all analyses. However, the impact of changing inputs is universally higher for cooking time compared to energy consumption.

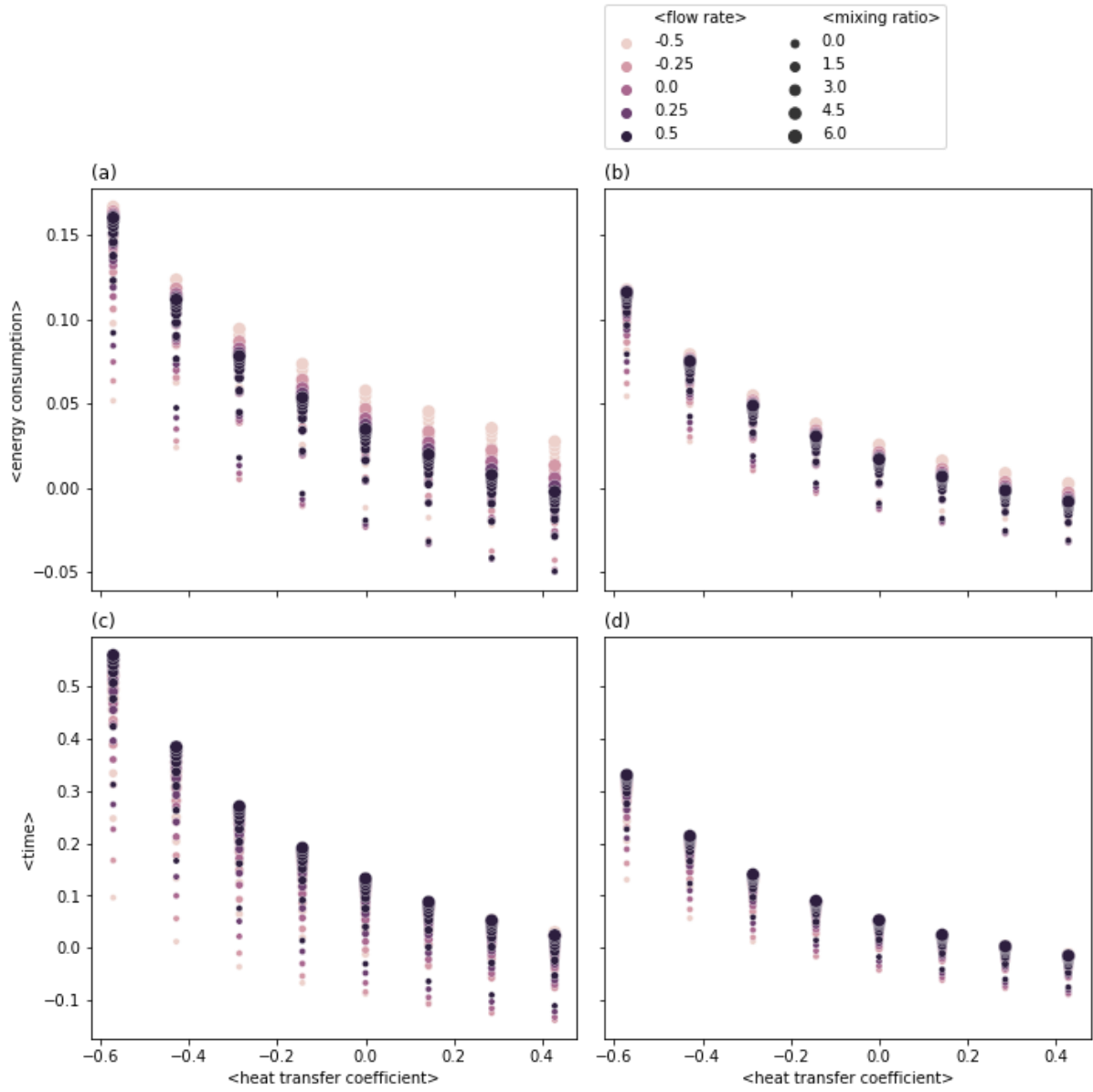


Figure 6.6: Plot of energy consumption (a, b) and cooking time (c, d) against heat transfer coefficient to the food for chicken (b, d) and pizza (a, c). Marker size is proportional to the ratio of bulk oven air to air from the heaters in the impinging air. Marker hue is proportional to flowrate through the jets. All values are normalised against the base model values.

6.6.2: Conduction Sensitivity Analysis

The three parameters varied and their ranges are given in Table 6.7, the linear model coefficients are given in Table 6.8. These parameters were chosen for the following reasons:

- i) The base area is the contact area for heat transfer between the plate and the food. There is a large uncertainty in this value, as food is rarely flat and will not make good or consistent contact with the base plate. The oven must be able to give consistent results despite the inevitable variation in this parameter between batches of the same food type.
- ii) The film resistance is the resistance to heat transfer between the plate. As with the base area this will vary between foods of the same type, depending on, for example, the amount of cooking oil the user applies to the pan.
- iii) The power split is the is the maximum power of the base heater as a fraction of the maximum power of the oven, for example a power split of 0.5 would give a base heater power of 1800 W and an air heater power of 1800 W. This parameter was varied to investigate the optimum value for cooking time, energy consumption and consistency when varying the base area and film resistance.

Table 6.7: Conduction sensitivity analysis specification

Object	Variable	Minimum Value	Maximum Value	Unit	Number of steps
Base Plate	Base Area	0.01	0.035	m ²	10
Base Plate	Film Resistance	0	0.02	m ² KW ⁻¹	10
Base Heater	Power Split	0	0.5	-	5

The linear model fitted to the conduction sensitivity analysis results had an adjusted- R^2 of 0.892, indicating a good fit. The linear coefficients of the model, shown in Table 6.8, are significantly lower than unity, further demonstrating the model's insensitivity to input parameters and its reliability.

The impact of the inputs on cooking time were much greater than their impact on energy consumption, as shown by the linear coefficients in Table 6.8. This is due to the oven design. Heat transferred to the plate by the heater can only transfer to the oven air or the food. Both the

plate and the oven air have a setpoint temperature of 180°C, meaning there will be no temperature gradient to drive energy from the plate to the oven air after the heat-up process is complete. Thus, the majority of energy supplied to the plate must be absorbed by the food and reducing the ability of the food to absorb energy from the plate will similarly reduce the energy delivered to the plate by the base heater, giving the low linear coefficients relating the input parameters to energy consumption seen in Table 6.8. This is also why power split has a greater impact on energy consumption when the base area is increased: it is only when there is a greater ability to transfer energy from the plate to the food that an increased base heater power can be utilised as can be seen in Figure 6.7.

Increasing the power of the base heater and reducing the power of the air heater increased the efficiency and reduced the cooking time, although the effect was small. Increasing the power split also increased the oven's sensitivity to changes in base area and film resistance, as can be seen in Figure 6.7. Due to this the power split used in the base model will be adopted in the prototype oven, allowing the standard 2400 W heating element to be used. Additionally, decreasing the power of the air heaters may reduce the ability of the oven in areas not measured by the oven such as browning of the top surface of the food.

The base area had the largest impact on cooking time and energy consumption for both food types of the three parameters investigated, greater than that of the film resistance. This is expected as the film resistance affects heat transfer to the food in combination with other heat transfer resistances: from the centre of the plate to its surface and from the surface of the food to the core of the food. In comparison, the base area has a directly proportional effect on the overall heat transfer coefficient from the plate to the food.

The impact of the base area and film resistance on cooking time must be considered when creating cooking recipes. These two parameters will vary unpredictably and randomly between foods of the same type. A pizza with a less flat base surface will have reduced contact area than a perfectly flat one. Similarly, the area of chicken contacting the pan could vary considerably depending on its shape and how its placed in the pan. This is of concern for two reasons. Firstly, the oven must be able to cook food with consistent results. Inputting the same recipe must give similar results for the oven to be convenient and easy to use for the consumer. Secondly, some foods such as chicken present a food safety hazard if undercooked, making it important to

understand under what circumstances it could be left undercooked after running a standard recipe, and what may be a sensible safety margin.

Table 6.8 reports a linear coefficient relating cooking time to base area of -0.211. A reduction in the contact area by half would therefore increase the cooking time of a chicken by 10.6% or 4.1 minutes. A safety margin of 5 minutes on the end of the chicken cooking recipe is therefore recommended.

Table 6.8: Linear model coefficients for the conduction sensitivity analysis

Food	<Output Parameter>	<Input Parameter>	Linear Coefficient
Pizza	Energy Consumption	Base Area	-0.0511
		Film Resistance	0.00860
		Power Split	0.0295
	Cooking Time	Base Area	-0.147
		Film Resistance	0.0261
		Power Split	-0.0246
Chicken	Energy Consumption	Base Area	-0.0810
		Film Resistance	0.0071
		Power Split	-0.0104
	Cooking Time	Base Area	-0.211
		Film Resistance	0.0188
		Power Split	-0.0168

6.7: Conclusions

Lumped property models of the COI oven design and a traditional fan oven were developed in Python. The cooking of a pizza and a chicken was modelled for both ovens, with the cooking time and energy consumption recorded. The model was validated by comparison to experimental values and with a sensitivity analysis. Model predictions for energy consumption and cooking time were found to match experimental results reasonably well for the traditional oven geometry, with a maximum error of 18% for chicken cooking time. The model was relatively insensitive to the input parameters.

The model predicted that the COI oven design is capable of greatly reducing energy consumption and cooking times with cooking times reduced by 50% for both food types and energy consumption reduced by 26% and 32% for pizza and chicken, respectively.

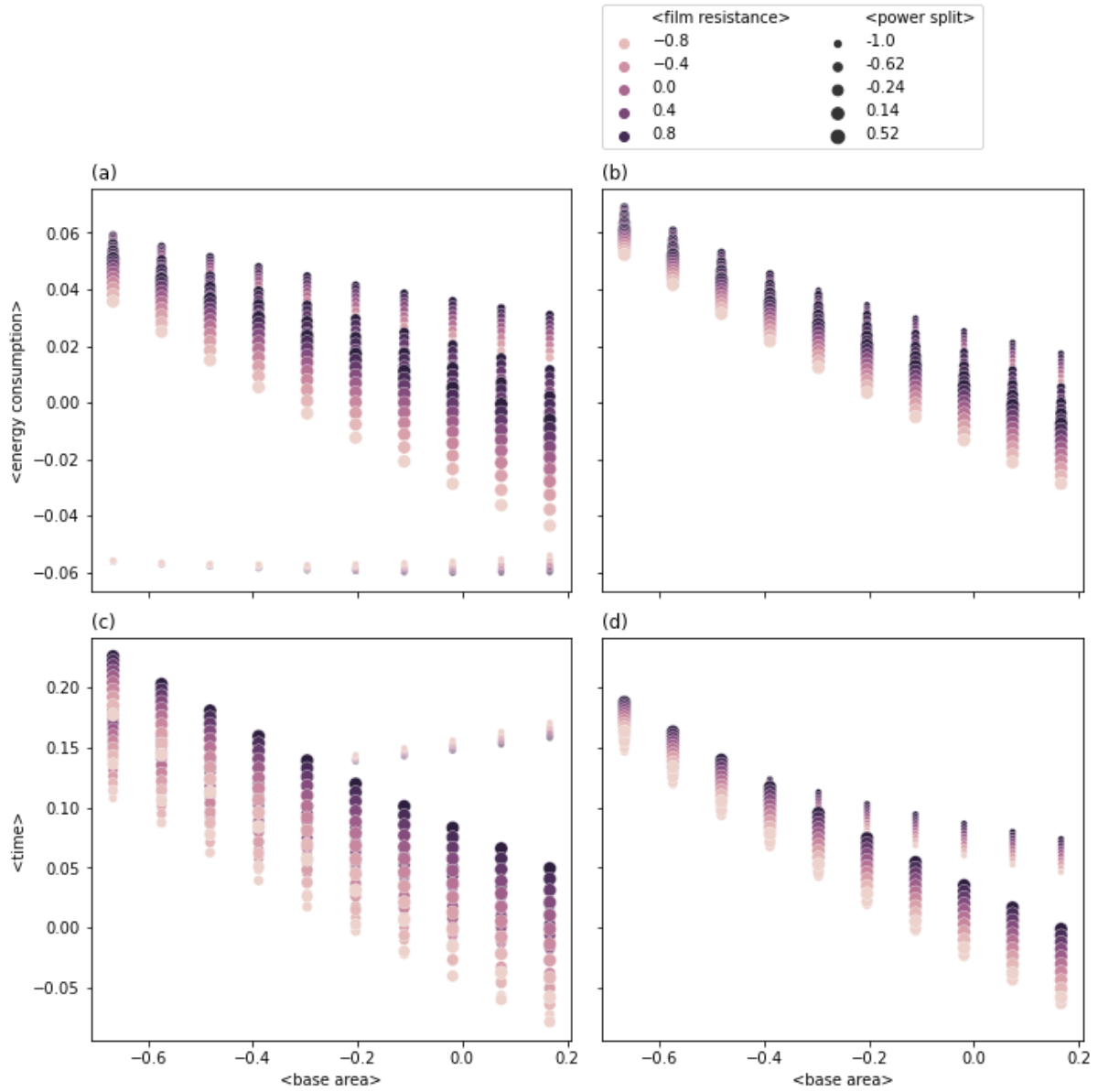


Figure 6.7: Plot of energy consumption (a, b) and cooking time (c, d) against area of pan contacting the food for chicken (b, d) and pizza (a, c). Marker size is proportional to fractional power split between the air and base heater, marker hue is proportional to film resistance to heat transfer between the pan and food. All values are normalised against the base model values.

The sensitivity analysis indicated the heat transfer coefficient from the impinging air to the food was the most influential parameter for both cooking time and energy consumption. Reducing the heat transfer coefficient by 40% increased cooking time by 40%. However, increasing the heat transfer coefficient above the value of $35 \text{ Wm}^{-2}\text{K}^{-1}$ predicted by an initial CFD simulation gave smaller improvements in efficiency and cooking time. An improvement of 40% in heat transfer coefficient gave only a 10% improvement in efficiency. The impact of the contact area between the food and the base plate was also investigated, as this could vary unpredictably for the same food type and lead to inconsistent results. Reducing the contact area of chicken contacting the base plate by 50% resulted in an increase of 4 minutes in the total cooking time, indicating that the oven can give consistent results even if this parameter varies considerably.

7: Computational Fluid Dynamics Simulation

7.1: Software and Computer Specifications

The CFD software used over the course of this project was ANSYS CFX version 18.2 (ANSYS, Cannonsberg, PA, USA). The workflow and associated software packages are shown in Figure 7.1.

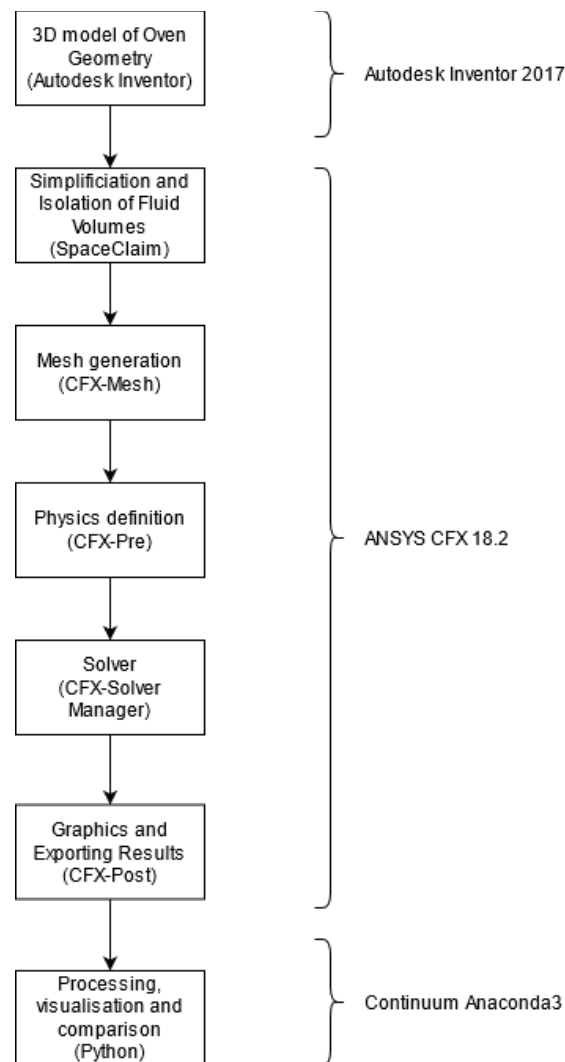


Figure 7.1: Software packages used for the CFD simulations discussed in this work.

Seven software packages were required to create the simulations and analyse their outputs:

- i) Autodesk Inventor 3D CAD (Autodesk, San Rafael, CA, USA) was used to create the 3D models. Geometries were inputted as 2D sketches before being extruded to form the solid parts of the oven. The resultant 3D geometries were exported from Inventor and imported into ANSYS CFX.
- ii) SpaceClaim is a limited 3D CAD package built into ANSYS CFX. It can be used to convert 3D models from other CAD packages into a form usable by the rest of the ANSYS CFX software library. This includes changing the format, isolating the fluid volumes as opposed to the solid volumes, and simplifying the geometry to remove features too small to model.
- iii) CFX-Mesh is used to generate 3D meshes from geometries imported from SpaceClaim. Various algorithms and controls can be selected to generate a suitable mesh.
- iv) CFX-Pre is a physics definition application. It is used to define the boundary conditions, material properties and physical models, such as turbulence and radiation onto meshes imported from CFX-mesh. Solver settings are also inputted.
- v) CFX-Solver manager imports the setup file from CFX-Pre and iteratively solves the required equations either until a set maximum number of iterations is reached or the residual error reaches a set target.
- vi) CFX-Post imports the results file from the solver manager. It can plot graphical features such as contours or streamlines, calculate volume or area averages and integrals or export data from points, lines, planes or volumes in a .csv format readable by other applications.
- vii) Continuum Anaconda3 is a Python 3 distribution designed for scientific and engineering applications. It was used to perform calculations not possible using CFX-Post and to compare simulation results between different cases and with experimental results.

Simulations in this work were run on a custom-made workstation, with an Intel® i7® X990 6 core processor at 3.5 GHz, 24 GB of RAM and 8 TB of storage. The operating system was Windows 10 Enterprise edition. Data processing was performed on a separate workstation with an AMD® Ryzen® 5 2600X 6 core processor at 4.6 GHz, 32 GB of RAM and 2 TB of storage.

7.2: Overview and Objectives of the Model

A CFD simulation of the prototype IB oven was created using ANSYS CFX. The key output was the magnitude and distribution of heat flux impinging on a “food” target. The simulation was validated and its predictions compared to experimental measurements.

The geometry of the system contained a number of regions where small mesh elements were required, such as where the impingement jets entered the cooking chamber and entrained ambient air, the heaters, and close to the food surfaces. The simulation also required a number of different physical models for radiative heat transfer and convective heat transfer. These factors made the prototype IB oven a challenging system to simulate and the number of simplifications and approximate models required reduced the likely accuracy of predictions made using the simulation. Previous studies, discussed in section 3.2.3 and studies specifically in heat transfer achieved accuracies of only $\pm 30\%$ ¹⁵⁹ and in some cases $\pm 50\%$ ¹⁶⁰. The simulation aimed for an accuracy of $\pm 30\%$ in its calculation of heat flux.

7.3: Geometry

The geometry of the metalwork of the oven was created in Inventor before being imported into SpaceClaim. Three conversions took place in SpaceClaim to prepare a suitable geometry for modelling:

- i) The Inventor geometry described the metalwork of the oven, this had to be inverted so that the geometry described the fluid volume.
- ii) The geometry was simplified to remove fine details that were unimportant to the fluid flow, such as fastenings.
- iii) The fluid volume was edited to facilitate easier meshing. This included isolating prism-shaped volumes that could be “swept” to form structured meshes and splitting

¹⁵⁹ M.E. Williamson, ‘Design of a Novel Radiant Burner Using Computational Fluid Dynamics’ (University of Cambridge, 2010); D.-D. Dang et al., ‘CFD Analysis of Turbulent Convective Heat Transfer in a Hydro-Generator Rotor-Stator System’, *Applied Thermal Engineering* 130 (February 2018): 17–28; T. Defraeye, B. Blocken, and J. Carmeliet, ‘CFD Simulation of Heat Transfer at Surfaces of Bluff Bodies in Turbulent Boundary Layers: Evaluation of a Forced-Convective Temperature Wall Function for Mixed Convection’, *Journal of Wind Engineering and Industrial Aerodynamics* 104–106 (May 2012): 439–46.

¹⁶⁰ Verboven, Scheerlinck, Baerdemaeker, and Nicola, ‘Computational Fluid Dynamics Modelling and Validation of the Temperature Distribution in a Forced Convection Oven’.

the geometry in half down the symmetry plane. Bodies of influence were also added. These are volumes that are not meshed or included in the simulation. Instead, they allow mesh controls to be enforced on specific volumes within the geometry.

7.3.1: Geometry Bounds

Figure 7.2 shows the geometry. Three decisions on the bounds of the model were made:

- i) The simulation was bounded by the interior walls of the oven. The steel walls and ceramic wool insulation are not included in the geometry. There are two potential reasons to include the walls in the simulation: (i) To model the transient behaviour of the walls and how the surface temperature changes as the oven heats up. Since the oven was to be modelled at steady state, this was unnecessary. (ii) Modelling the ability of heat to conduct laterally across the walls, parallel to the surface. The walls are made from thin steel sheet with ceramic wool insulation beyond, so this effect is negligible. The heat lost through the walls was modelled by specifying the boundary condition at the inner wall of the oven as a fixed overall heat transfer coefficient to the ambient air.
- ii) The fan motor and impeller were not included in the model: the outlet of the model is the inlet to the eye of the impeller and the inlet to the model is a cylindrical surface surrounding the impeller location. Although it is possible to model the fan impeller using ANSYS CFX it is difficult, time consuming and computationally expensive, requiring a fine mesh in the region of the fan impeller and a small timestep. The aim of the model was not to optimise or investigate the behaviour the fan, therefore the fan was modelled simply as an increase in pressure with a specified mass flow rate.
- iii) It was anticipated that a large number of mesh elements would be required to model the prototype oven, due to fine detail being required in the heater section and impingement jets as well as the requirement for small elements near the wall to model heat transfer accurately. To reduce the element count and computational requirements the symmetry of the geometry was exploited, by modelling the left half of the oven when viewed from the front, with a symmetry plane down the middle.

7.3.2: Geometry Details

Figures 7.3 and 7.4 show the geometry in greater detail. The geometry is split into two parts, one showing the fan outlet, heater sections and impingement jet nozzles, and another showing the cooking chamber.

The heater sections were split into multiple sub-volumes to enable easier meshing, as shown in details A and B in Figure 7.4. The heater sections, shown in red, were able to be swept, while the header sections (green) and the base sections (blue) isolate regions that were unable to be swept and use tetrahedral, unstructured meshing. These regions could not be swept as conformal meshing was used, which forces mesh elements to match where two volumes meet. For example; the circular faces of the jets prevent the heater base sections being swept along their length.

The cooking chamber was a simpler geometry than the heater section and thus was not split into as many sub-volumes. The aim of the subdividing scheme used was to isolate the majority of the volume as a swept region, shown in blue in Figure 7.3. The volume beneath jets could not be swept due to the connection to impingement jets. The base of the oven was similarly challenging due to the semi-circular face intended to simulate food within the oven. An unstructured mesh in this region also allowed the heat flux sensor or a piece of food to be more easily included in the model and allowed additional mesh controls to be specified that would not be available if using a structured mesh. Figure 7.5 shows the bodies of influence added in the volume beneath the impingement jets. The entry of the hot, high velocity and small diameter jets into the cooking chamber created large velocity and temperature gradients that required small mesh elements to resolve. The bodies of influence could be used to enforce local mesh sizing in this region.

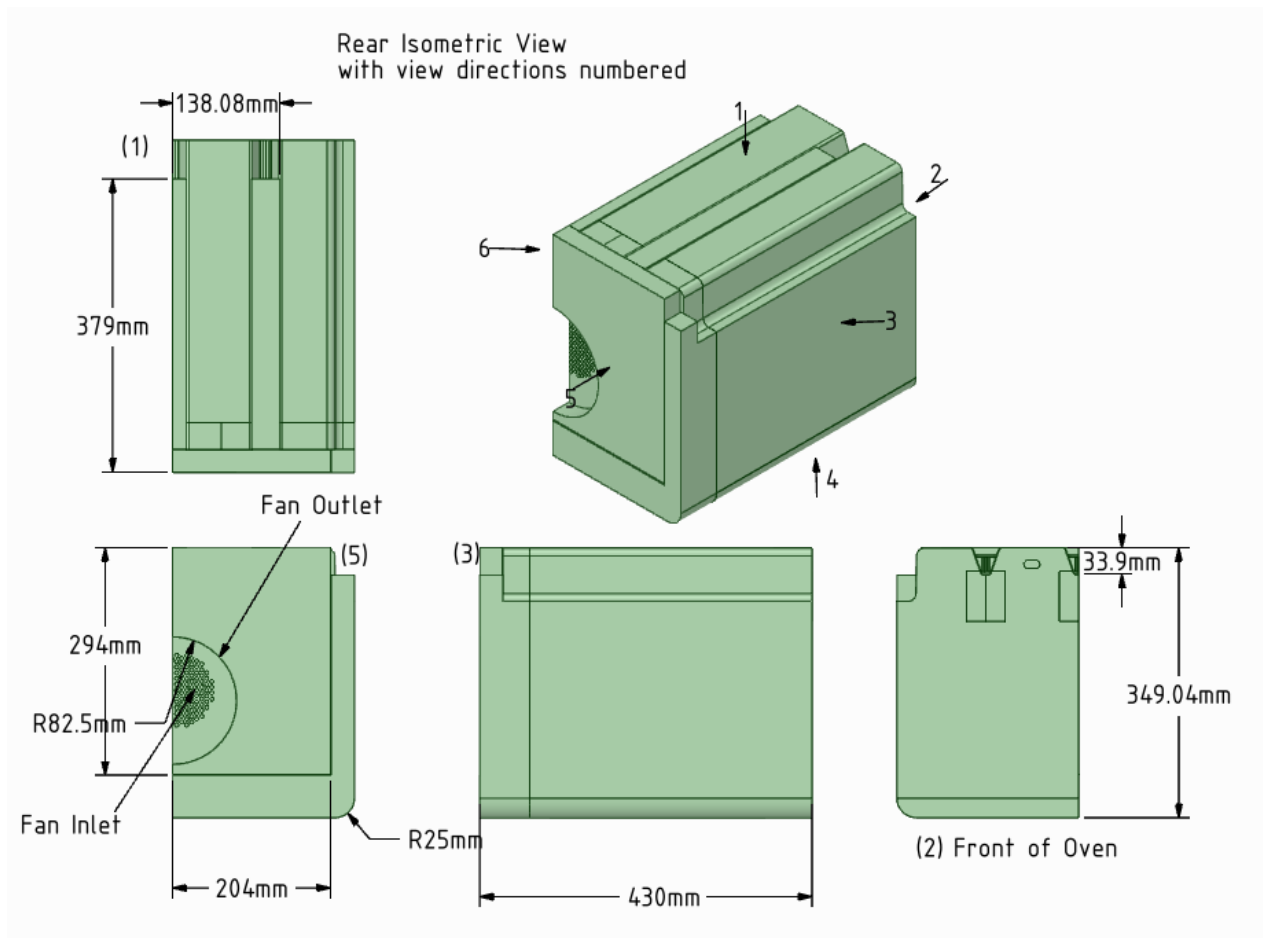


Figure 7.2: Third angle projection showing an overview of the CFD model geometry with key dimensions given. Isometric view gives numbered view angles that are used in subsequent diagrams.

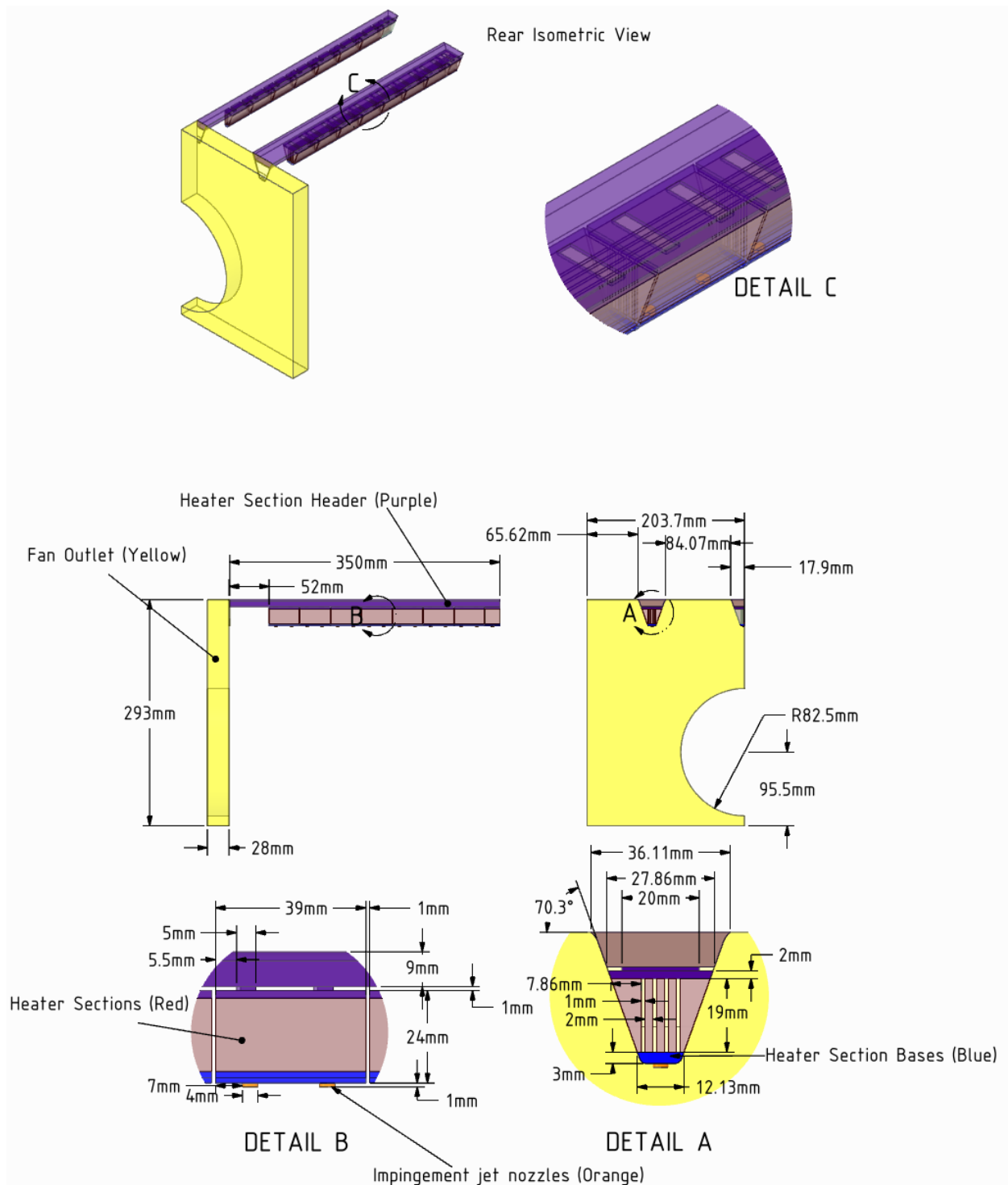


Figure 7.3: Third angle projection of the fluid volume between the fan outlet and the impingement jets, showing detail of the heating section and key dimensions. Different colours indicate where the geometry was split into separate sub-volumes. Detail views show the front and side of an individual heater section.

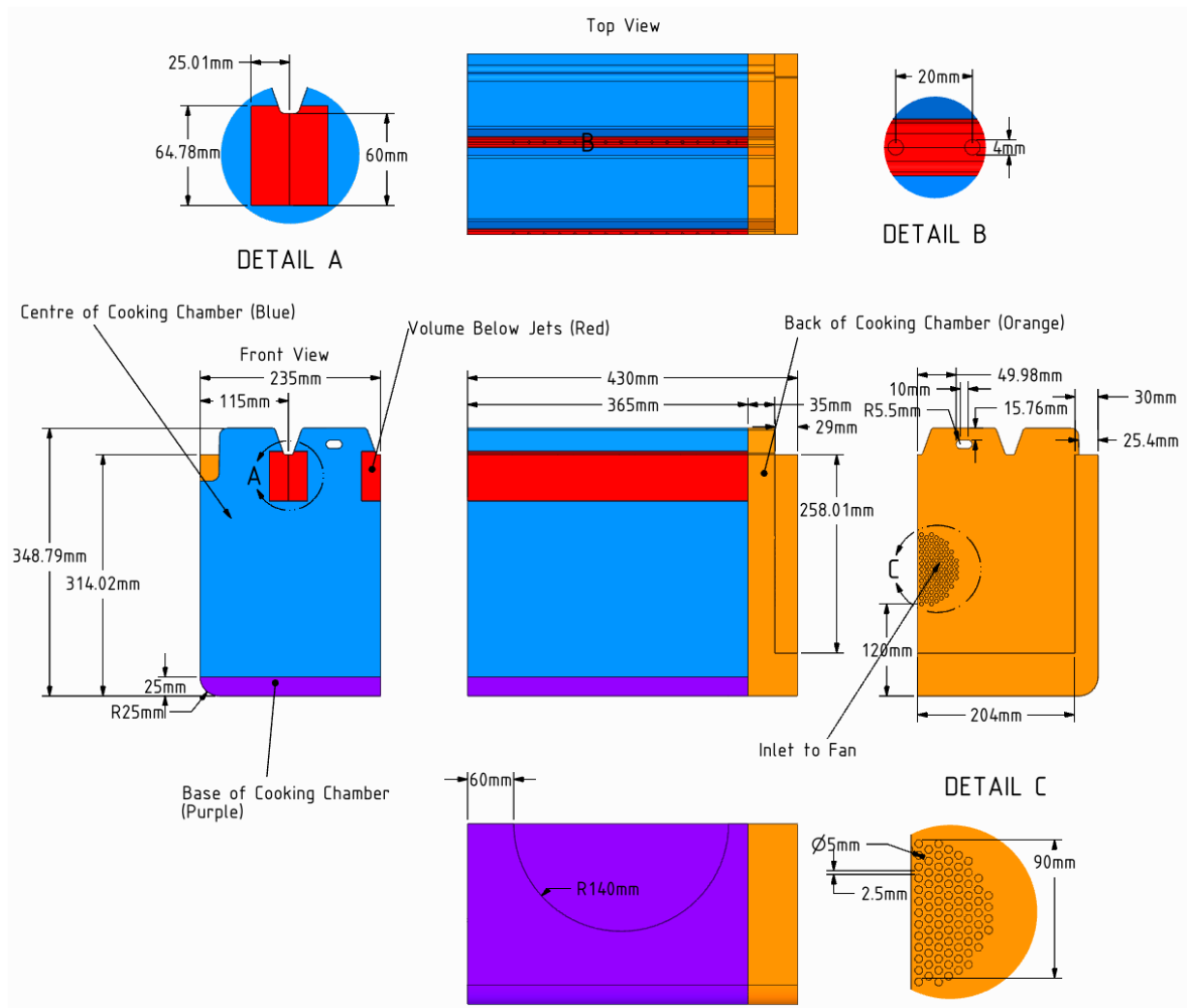


Figure 7.4: Third angle projection of the fluid volume between the impingement jets and fan inlet, showing detail and key dimensions. Different colours indicate where the geometry was split into separate sub-volumes.

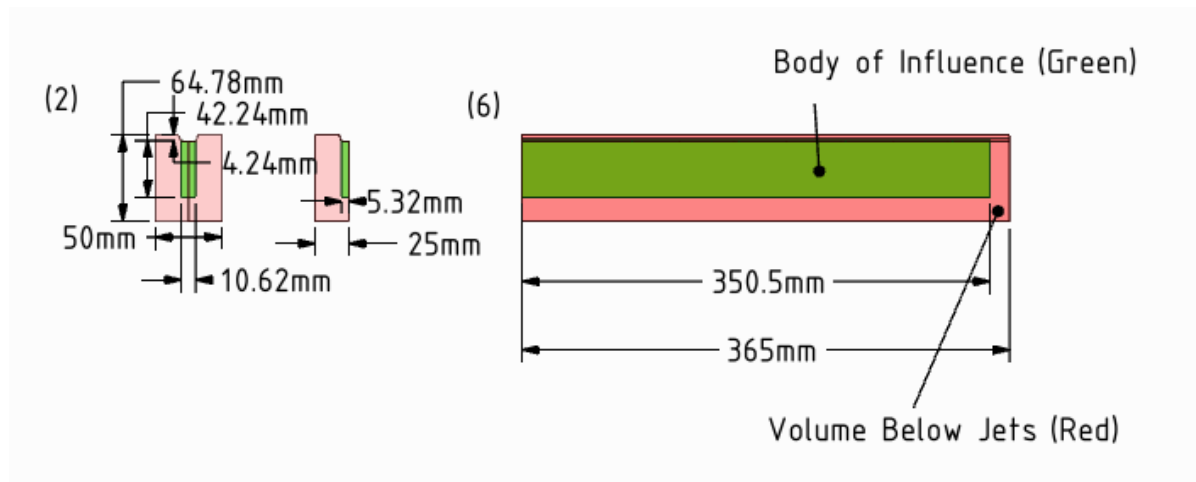


Figure 7.5: Third angle projection of the volume below the jets (shown in red in Figure 7.4), showing dimensions of the bodies of influence.

7.4: Meshing

Details of the final mesh selected are shown in Figures 7.6, 7.7 and 7.8, which show the mesh in the cooking chamber, heater section and the impingement jets, respectively. Details of the mesh selection process are given in section 7.6.3.

The mesh in the cooking chamber had an element size of 6 mm, with a structured mesh in the centre and unstructured tetrahedral meshing for the back and base. An additional face sizing of 1.5 mm was applied to the bottom face of the oven, shown in Figure 7.6(c). An inflation layer was also applied to this face, with a first layer thickness of 0.1 mm, a growth rate of 1.2 and 15 layers. This reduced the value of y^+ in this region to give more reliable predictions of heat flux.

Figure 7.7 shows the mesh in the fan outlet and heaters region. The mesh in the fan outlet and heater header was sized at 6 mm. The structured mesh in the heater section was sized at 0.5 mm and 0.77 mm in the side and centre portions of the heater sections, respectively. These sizing functions were chosen to give 5 mesh elements across each heating section, considered a minimum to capture the velocity profile.

The mesh in the jet nozzles and immediately below them is shown in Figure 7.8. The nozzle had a sizing of 0.3 mm. The volumes where the impingement jets enter the cooking chamber was

within the bodies of influence shown in Figure 7.5 and had an element size of 0.5 mm. A fine mesh was required in this region to capture the large gradients in velocity and temperature there.

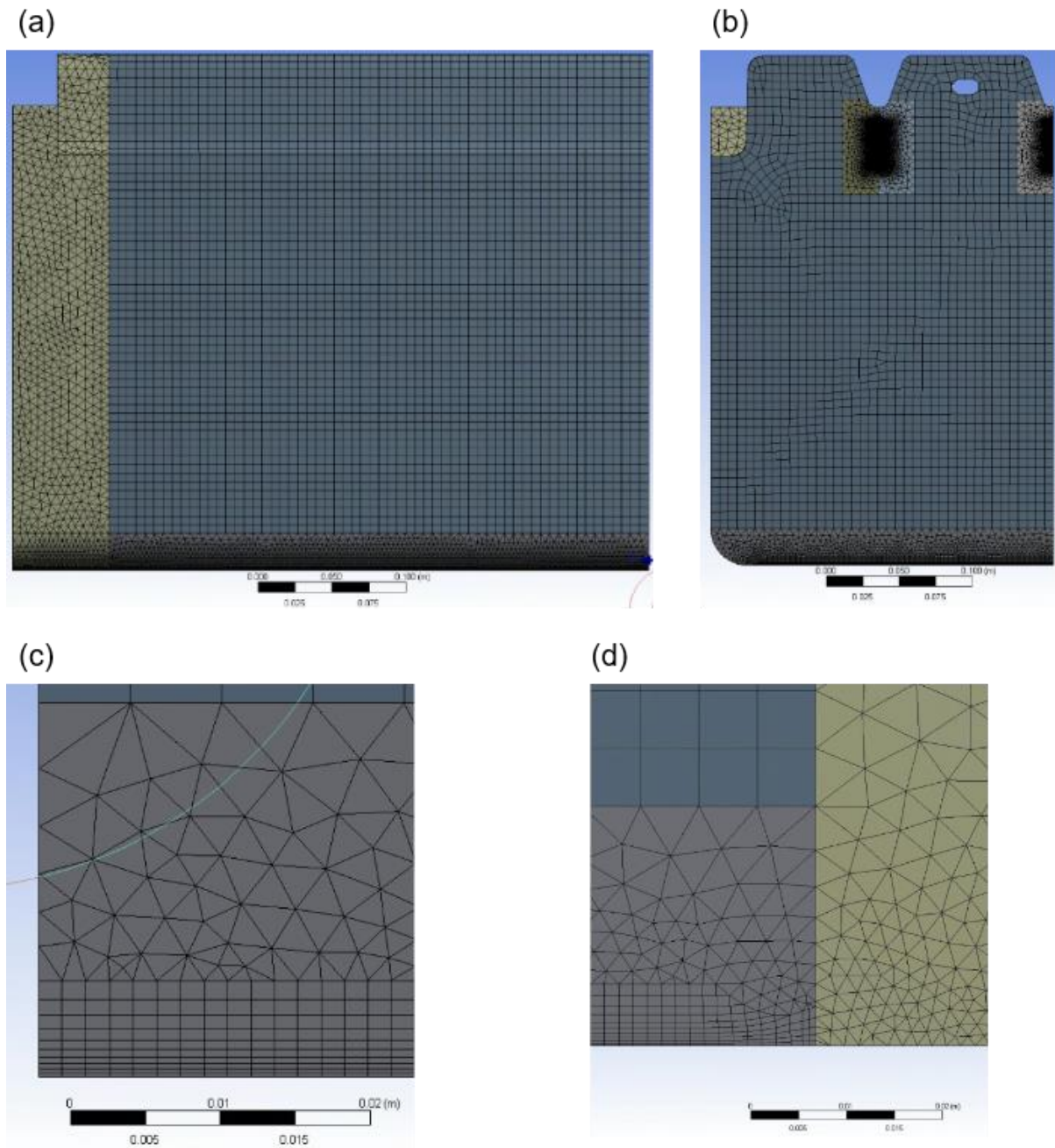


Figure 7.6: Images showing the mesh applied to the cooking chamber. (a) View 3, (b) view 2. (c) Detail of the mesh used for the base of the cooking chamber, showing the inflation layer, view 4. (d) Detail of the mesh at the intersection of the centre of cooking chamber, base of cooking chamber and back of cooking chamber as defined in Figure 7.4, view 6.

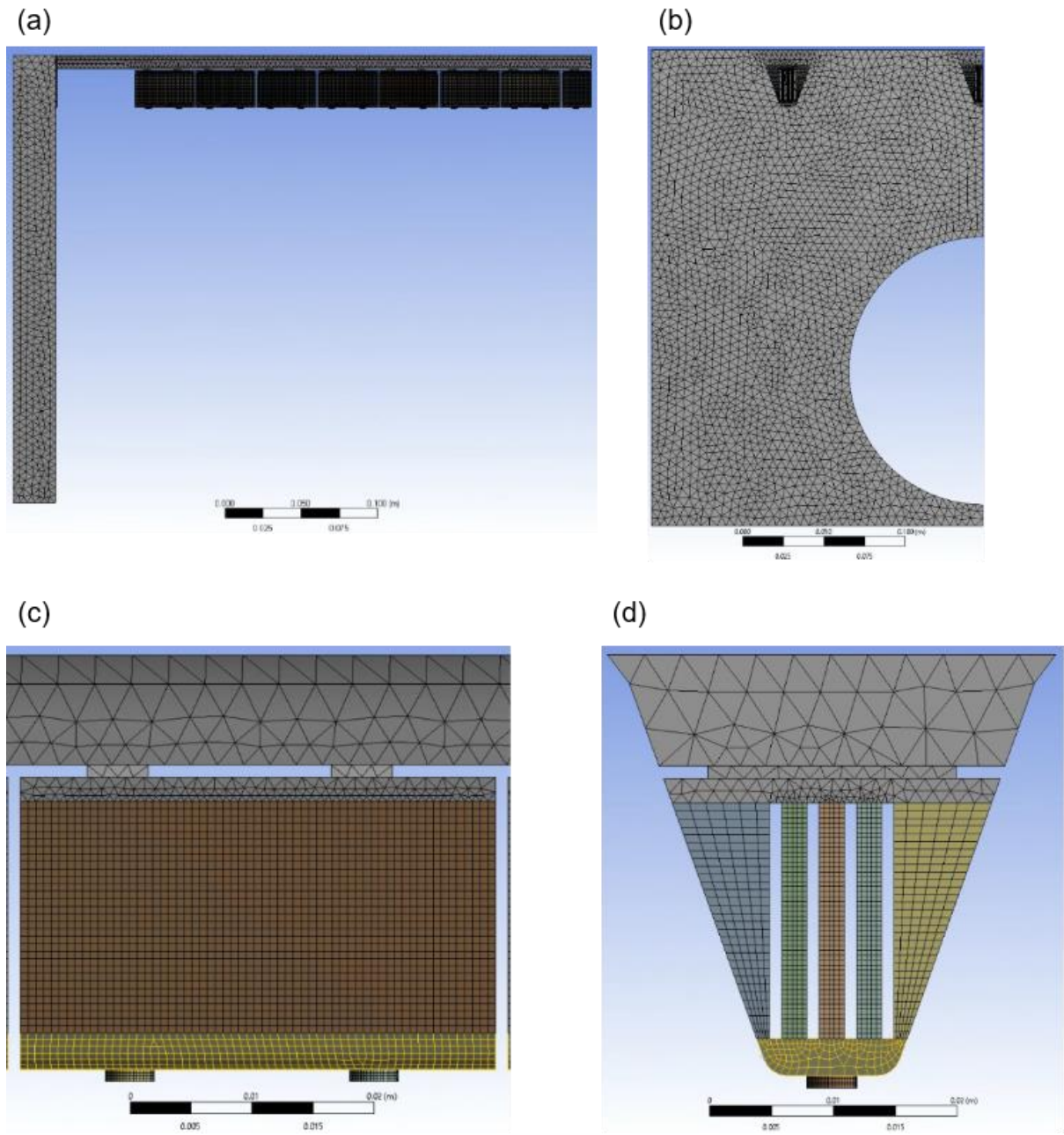


Figure 7.7: Images showing the mesh applied to the fan outlet and heater section. (a) view 3 (b) view 2, (c) detail of the mesh used in the heater section, view 3. (d) Detail of the mesh used in the heater section, view 2.

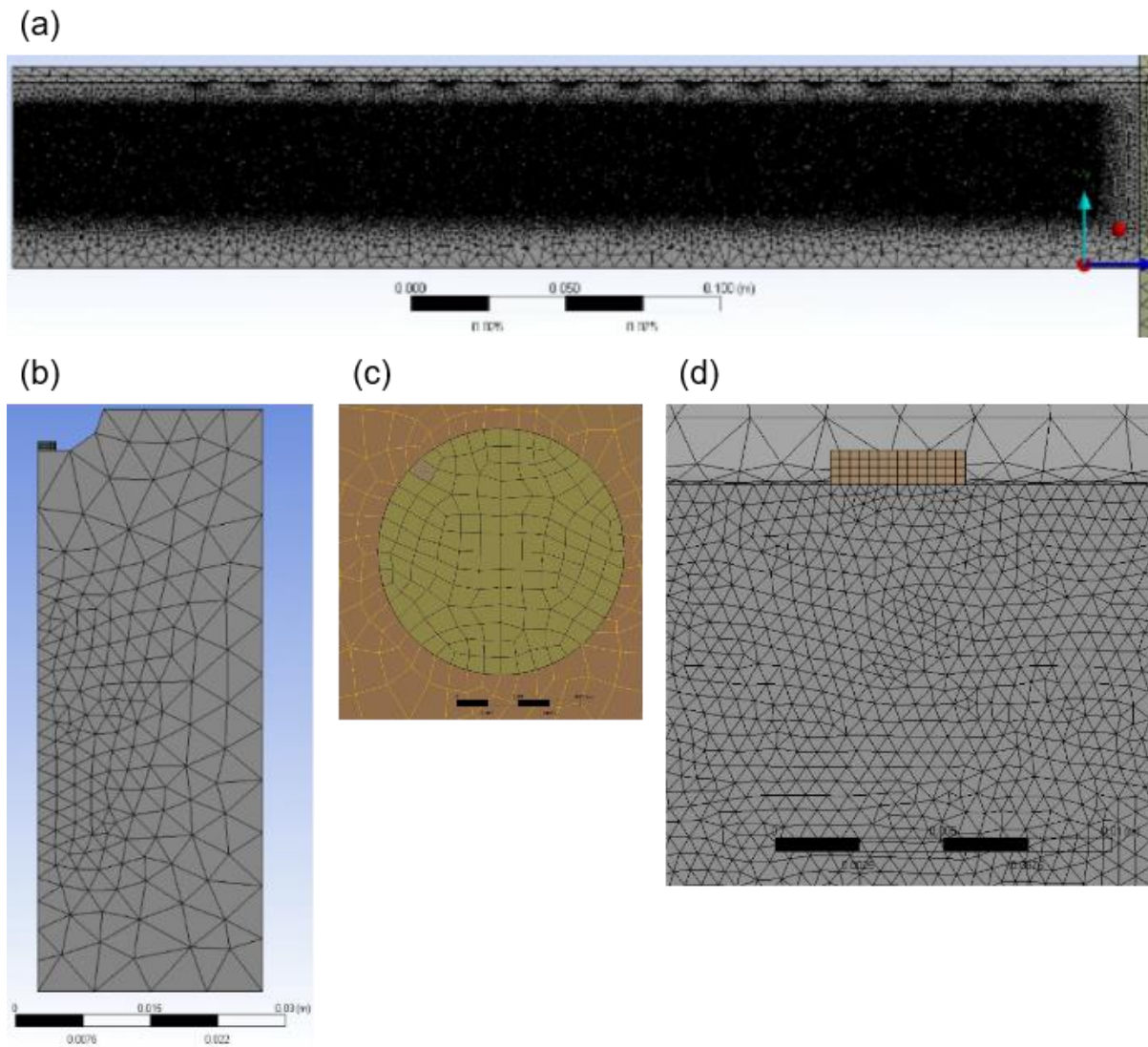


Figure 7.8: Images showing the mesh applied to the jets and volume immediately beneath the jets. (a) View 6, (b) view 2, (c) cross section of a jet nozzle, view 1. (d) Detail of where a jet enters the cooking chamber, view 6.

7.4.1: Mesh Metrics

Table 7.1 gives a number of mesh metrics calculated by CFX-Mesh. The number of nodes is relatively low compared to the number of elements due to the large number of tetrahedral elements in the volume beneath the jets. Figure 7.9 shows a plot of the number of elements and their associated skewness. ANSYS¹⁶¹ rates elements with skewness < 0.5 as “good”, and elements with skewness < 0.75 as “fair”. Figure 7.9 shows that the majority of elements in the mesh are of good quality, with very few poor elements. This is also reflected in the orthogonal

¹⁶¹ . ANSYS Inc., ‘Measures of Mesh Quality’, in *ANSYS CFX, Release 18.2, Help System*, 2021.

quality and element quality metrics, shown in Table 7.1 and graded from 0 to 1, with 1 being the best. The mesh scores over 0.75 for both of these metrics, indicating it is of an acceptable quality.

Table 7.1: Selection of mesh metrics for the final mesh used in the simulation of prototype IB.

Metric	Value
Number of elements, N_{el}	29.4×10^6
Number of nodes	6.4×10^6
Mean element quality	0.84
Mean skewness	0.22
Mean orthogonal quality	0.78

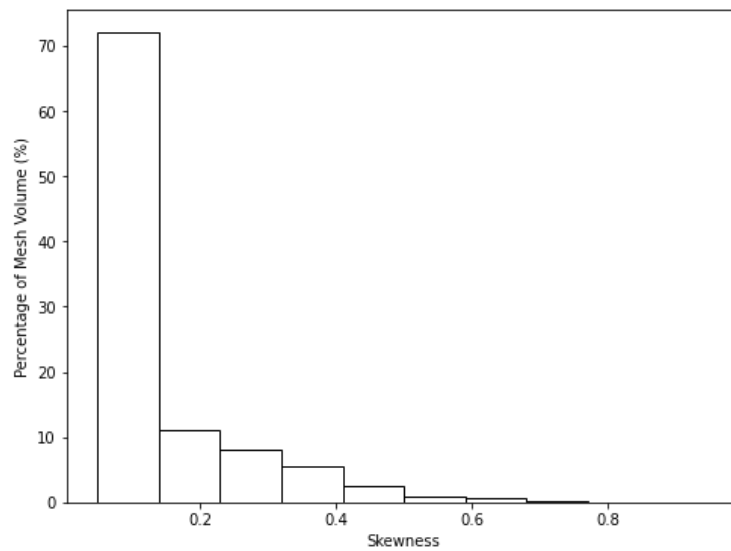


Figure 7.9: Histogram of element skewness, weighted by element volume.

7.5: Physics

7.5.1: Time step

The simulation could not be run in steady state due to inherent instability in the cooking chamber preventing a steady state simulation from converging. A pseudo steady state simulation was therefore used, where the oven was simulated using a transient simulation but with constant boundary conditions. Timestep selection is detailed in section 7.6.4; the final model was run for 60 s, with 0.3 s timesteps. The simulation took approximately 20 s of simulation time to reach a

pseudo-steady state from the specified initial conditions and therefore only data from the final 40 s were used in subsequent analysis.

7.5.2: Turbulence and Radiation Model

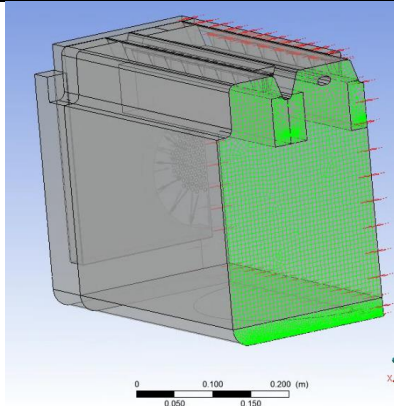
The SST turbulence model was used due to its blend of accuracy and solution speed in heat transfer applications, especially involving impinging jets, as discussed in section 3.2.2. The surface-to-surface form of the discrete-transfer radiation model was selected due to its accuracy in cases with non-participating fluids and reduced computational cost compared to Monte-Carlo methods, as discussed in section 3.2.2.

Mass transport was not considered in the simulation. Buoyancy forces were included in the model as the model contains large temperature differences and therefore large density differences.

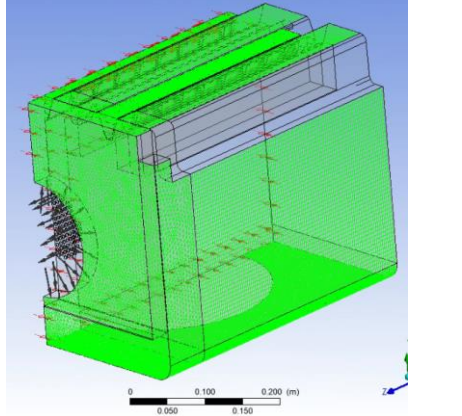
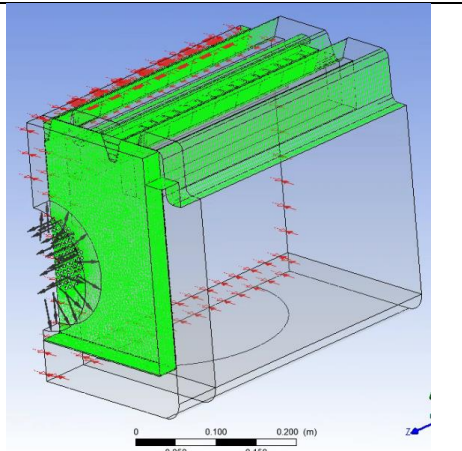
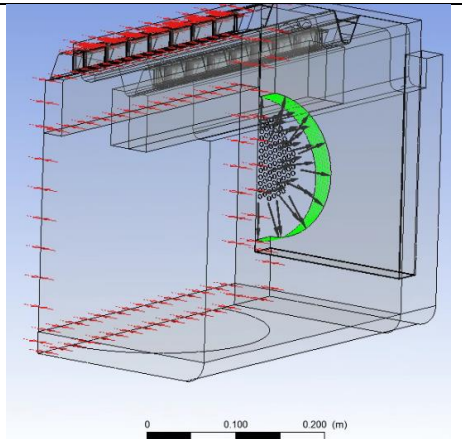
7.5.3: Boundary Conditions

Table 7.2 describes the location and key quantities for the various boundary conditions.

Table 7.2: Summary of boundary conditions and associated quantities.

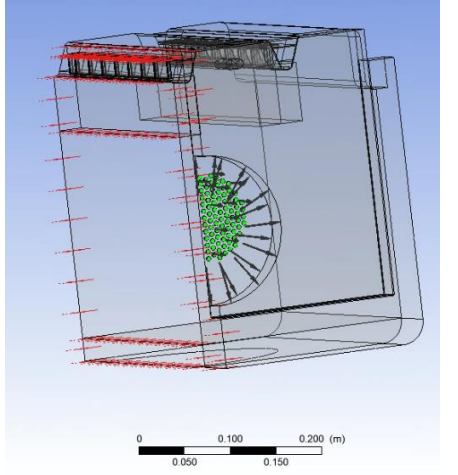
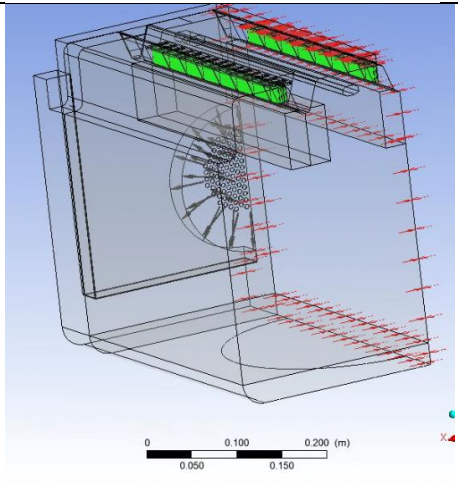
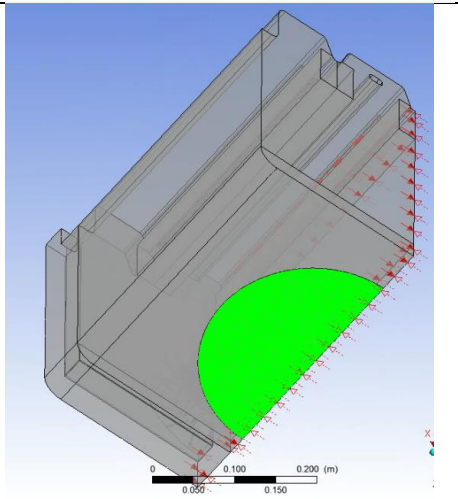
Name (Type)	Description	Key Quantities	Figure (scale bar 0.2 m)
Door (wall)	Portion of the cooking chamber contacting the oven door. The emissivity used is a typical value for glass. The overall heat transfer coefficient, U , to ambient was taken from Aydın ¹⁶²	$\epsilon = 0.6$ $U = 20 \text{ Wm}^{-2}\text{K}^{-1}$ $T_{\text{ambient}} = 300 \text{ K}$	

¹⁶² Aydın, ‘Conjugate Heat Transfer Analysis of Double Pane Windows’.

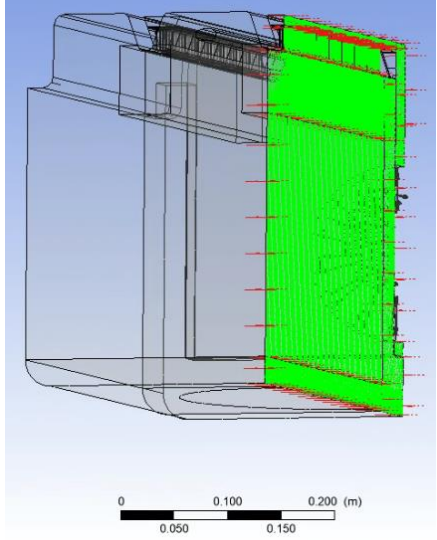
Exterior Walls (wall)	Portion of the oven air contacting walls that directly separate the oven air from the external, ambient air. Overall heat transfer coefficient was calculated assuming 1 cm of ceramic wool. Emissivity was taken from Scarisbrick <i>et al.</i> ¹⁶³	$\epsilon = 0.9$ $U = 4.4 \text{ Wm}^{-2}\text{K}^{-1}$ $T_{\text{ambient}} = 300 \text{ K}$	
Interior Walls (wall)	Interior walls of the oven, separating one air volume from another. These are assumed to be adiabatic. Emissivity is for roughened aluminium due to the sand blasted finish of the plenum assembly ¹⁶⁴ .	$\epsilon = 0.6$	
Inlet (inlet)	Inlet to the model was a surface enclosing the outlet of the fan impeller. The temperature of the inlet was the same as the temperature of the outlet. Derivation of the mass flow rate, \dot{M} is described below.	$\dot{M} = 0.00213 \text{ kgs}^{-1}$	

¹⁶³ Scarisbrick, Newborough, and Probert, 'Improving the Thermal Performances of Domestic Electric Ovens', January 1991.

¹⁶⁴ Fluke Process Instruments, 'Emissivity Values for Metals'.

Outlet (outlet)	<p>Outlet of the model was the grille in the back of the cooking chamber. The eye of the impeller is immediately behind this surface when viewed from the front of the oven. This face provided the reference pressure for the rest of the system, set at 0 Pa gauge</p>	$P_{\text{gauge}} = 0 \text{ Pa}$	
Heater Faces (wall)	<p>The heater design is shown in Figure 4.3. This boundary contains the faces of the mica panels around which the Kanthal wire is wrapped. The individual wires were not modelled, only an average flux from the wall, q_{heater}.</p>	$\epsilon = 1$ $q_{\text{heater}} = 5000 \text{ W m}^{-2}$	
Food (wall)	<p>In the base case, food in the oven was modelled by a 28 cm diameter circular face, approximating a pizza. The surface temperature, T_{surface} was fixed at 100°C with an emissivity of 0.9, that of bread as reported by Hamdami <i>et al.</i>¹⁶⁵</p>	$\epsilon = 0.9$ $T_{\text{surface}} = 100^{\circ}\text{C}$	

¹⁶⁵ N. Hamdami, J.-Y. Monteau, and A. Le Bail, 'Heat and Mass Transfer in Par-Baked Bread during Freezing', *Food Research International* 37, no. 5 (June 2004): 477–88.

Symmetry Plane (symmetry plane)	The symmetry plane at the centre of the oven.	Zero net heat flux Zero net mass flow	
---	---	--	--

Adiabatic Walls

The internal walls, separating the cooking chamber from the heater sections and fan plenum, were adiabatic. This will likely be a good assumption for the wall between the cooking chamber and fan plenum, as these two volumes will have similar temperatures. The heater sections, however, will have significantly higher temperature than the cooking chamber as this is where thermal energy is added to the system. The assumption that the walls of the heater sections are adiabatic is therefore not valid. This assumption will likely increase the convective flux to the food, as no heat is lost from the impingement jets to the walls of the heater, and reduce the radiative flux to the food, as the exterior walls of the heater sections will be cooler in the model than in reality. The simulation was therefore expected to underpredict radiative flux. As radiative flux was anticipated to be a relatively small fraction of the total heat flux into the food the size of this error in comparison to the total flux was expected to be small.

Model Flowrate

The size, number and positions of the nozzles was determined by COI, described in section 2.4.1 and chosen to give a pressure drop of 100 Pa across the nozzles. Although the simulation could have been specified using the pressure drop between the inlet and outlet faces, specifying a mass flowrate gave greater numerical stability and reduced solution time. The mass flowrate specified, \dot{M} was calculated using Bernoulli's equation:

$$\dot{M} = \rho_{\text{air}} N_{\text{nozzle}} A_{\text{nozzle}} C_d \sqrt{\frac{2\Delta P_{\text{nozzle}}}{\rho_{\text{air}}}} \quad (7.1)$$

where N_{nozzle} is the number of nozzles in the model, A_{nozzle} is the area of one nozzle, C_d is the discharge coefficient of the nozzles, ΔP_{nozzle} is the pressure drop across one nozzle and ρ_{air} is the density of air.

The number of nozzles in the complete oven is 45. As the simulation is split down the symmetry plane the simulation N_{nozzle} is 22.5. The pressure drop across the 4 mm diameter nozzles was 100 Pa while the density of air at 200°C is approximately 0.75 kg m⁻³. The discharge coefficient was taken to be 0.65¹⁶⁶, giving $\dot{M} = 0.00225$ kg s⁻¹. This was the flowrate imposed across the Inlet boundary, shown in Table 7.2.

Modelling of the Heater

In prototype IB heat was delivered to the air by resistive kanthal wire, wrapped around mica sheet, shown in Figure 4.3. Applying single phase mains voltage across this wire caused it to heat up and transfer energy to the air passing through the heater. It would be possible to model this by adding the heating wire to the model. However, subdividing faces within the heating section to enable this would further complicate the meshing in this area as the diagonal orientation of the wires would prevent a structured mesh being created. The location and design of the heating wire was not an aim of the model, so for simplicity the heat input was assumed to be homogenous across the heater faces. The area of the heating faces for the simulation of half the oven was 0.067 m² and $q_{\text{heater}} = 5000$ W m⁻². This corresponded to an oven power of 670 W which is similar to the measured power draw of a traditional oven of 750 W when operating at a temperature of 180°C¹⁶⁷.

¹⁶⁶ D.W. Green, 'Flow through Orifices', in *Perry's Chemical Engineers' Handbook*, Eighth (McGraw Hill, 2008), 6–111.

¹⁶⁷ Scarisbrick, Newborough, and Probert, 'Improving the Thermal Performances of Domestic Electric Ovens', January 1991.

7.5.4: Initial Conditions

The initial condition of the model was a uniform air and wall temperature of 180°C and zero velocity. The model required a number of timesteps to evolve from these initial conditions to a quasi-steady state.

7.5.5: Material Properties

The fluid in the model was dry air and was treated as an ideal gas. In cooking trials, the prototype ovens operated with a high concentration of water vapour (>0.5), but this was not included in the model, for simplicity.

7.5.6: Solver Settings

Unless otherwise stated, default solver settings were applied. CFX uses the finite volume method and a pressure-based, implicit solver.

The model was considered converged when the root mean square (RMS) residuals for each time step were $< 10^{-4}$. This is considered reasonable convergence and sufficient for most engineering applications¹⁶⁸. Although tighter convergence was desired, given the complexity of the model geometry and physics it was not achievable. A limit of 20 iterations per timestep was set to prevent the solution from stalling. This limit was only reached for simulation time < 20 s, where the flow profiles within the model were being established and the changes in velocity and temperature between timesteps was large.

A conservation target of 0.01 was set for mass and energy. This forced the solver to continue iterating until the difference between the mass and energy entering and exiting the simulation was less than 1% of the flow into the simulation.

The high-resolution advection scheme and second order implicit backward Euler transient scheme were used for accuracy. The “topology estimate factor” in “memory control” was

¹⁶⁸ . ANSYS Inc., ‘Residual Types and Target Levels’, in *ANSYS CFX, Release 18.2, Help System*, 2021.

increased from its default value of 1.0 to 1.2. This forced the solver to reserve more memory and proved essential to prevent crashes.

The standard transient results file was exported from each iteration, with the additional parameters of “Wall Heat Flux” and “YPlus” (y^+) also saved for each timestep. The results from the solver were saved as individual files for each timestep. Each file contains the fluid properties at every node in the mesh, such as temperature, pressure, the Cartesian velocity components and physical properties.

The model was run in 10 parallel processes, the maximum that could be achieved without using more memory than the workstation possessed.

7.5.7: Data Export

CFX-Post was used to export data for further analysis. The export function in CFX-Post allows the Cartesian coordinates and variables such as temperature, pressure and velocity to be saved in a tabular .csv format. The points can be sampled over a surface or volume with a constant spacing between them, or alternatively exported for every element in the mesh within the selected volume or surface. The former allows data to be exported for large volumes or areas with reduced computational cost and with equal spacing between exported points. The latter gives the maximum resolution available. One limitation of CFX-Post is that it cannot load the results for multiple timesteps simultaneously. Calculation of averages over the quasi-steady state period of the simulation had to be performed separately.

CFX-Post has a scripting function that allows macros to be created to automate repetitive tasks. A python script was created that could output macros as text files in the format required for CFX-Post to read. The macro would sequentially load the results file for every timestep before performing the export of the desired variables across selected surfaces or volumes. This process produced a separate .csv file for each timestep and area or volume selected. For example, exporting data for 4 selections for 60 timesteps would result in 240 export files.

A second python script loaded every exported file and combined them into a single tabular results file in the *feather* format. Each row in the results file contained the data for one point at one timestep. The script also tidied the column names from those generated by CFX-Post,

which contained leading spaces and inconsistent formatting which made indexing difficult. The advantage of the *.feather* format was that it could be read into subsequent python scripts much more quickly than *.csv* files.

7.6: Validation

The 6-step process for validation, described by the NASA validation guide¹⁶⁹, was applied to evaluate the accuracy and reliability of the model and select an appropriate mesh and timestep.

The 6 steps were:

- i) Examine iterative convergence: ensure that the residuals of the model have been reduced to a suitable level, and that parameters of interest are not changing with each iteration and have converged on a final value.
- ii) Examine consistency: ensure that the mass and energy entering and exiting the model are equal.
- iii) Examine spatial or grid convergence: this is to determine the discretisation error of the model. It was performed by running the model and evaluating a parameter of interest with successively finer meshes. Finer meshes reduce the discretisation error at the expense of computational cost. The aim was to determine the point at which further refinement results in a minimal impact on the results.
- iv) Examine temporal convergence: a similar process to examining spatial convergence but with successively smaller timesteps as opposed to finer meshes.
- v) Compare model predictions to experimental results and evaluate the accuracy.
- vi) Examine model uncertainties: the physical models within the CFD code contain uncertainties due to an incomplete understanding of the system. This uncertainty was examined by running a number of simulations with differing physical models and comparing the results. The turbulence model is considered to have the greatest uncertainty in most cases.

These 6 stages are described in greater detail in the subsequent sections.

¹⁶⁹ J.W. Slater, 'Validation Assessment', in *NPARC Alliance CFD Verification and Validation* (NASA, 2021).

7.6.1: Iterative Convergence

As discussed in section 7.5.1, all simulations were converged such that the root mean square (RMS) residuals were less than 10^{-4} . Residuals at early timesteps were higher as larger changes in velocity and temperature occurred between these timesteps due to the initial condition not matching the quasi-steady state. Only data from simulation time, $t_{\text{sim}}, > 20$ s were exported and analysed so potentially non converged results from early time steps did not affect the simulation results.

7.6.2: Consistency

As discussed in section 7.5.7, conservation was enforced by the solver, ensuring consistency in the simulation.

7.6.3: Spatial Convergence

It was hypothesised that the turbulent behaviour preventing the simulation being run in steady state occurred in the cooking chamber and that the sections of the simulation outside the cooking chamber, namely the fan plenum and heater sections, could be modelled successfully in steady state. Splitting the geometry into two volumes, one containing the cooking chamber (volume B) and one containing the fan plenum and heater (volume A) allowed the investigation of spatial convergence to be completed more quickly, by reducing the time required to run a simulation with each mesh.

- i) A steady state model requires fewer total iterations to return a solution. Using a steady state simulation to model volume B was therefore less time consuming than a transient simulation.
- ii) Volume B still required a transient simulation, however volume B contains only approximately 75% the total mesh elements of the system and therefore ran more quickly than a transient simulation of the entire geometry.

The split simulations had the same physics as described in section 7.5 and the same solid boundary conditions. The inlet and outlet boundary conditions were changed to accommodate the dividing of the simulation, this is illustrated in Figure 7.10. In the undivided simulation

(Figure 7.10(b)) the mass flowrate through the simulation was fixed, while the inlet temperature was the mass flow average of the outlet temperature, this data transfer is shown with a red arrow. In the divided simulations (Figure 7.10(a)), the mass flow through the system remained fixed. The inlet temperature to volume A (i) was fixed at 180°C. The conditions at the outlet of the steady state simulation of volume A (ii) were exported and applied as constant inlet conditions to the transient simulation of volume B (iii). The outlet temperature of volume B (iv) was not used to calculate the inlet temperature.

Due to the outlet and inlet temperatures being uncoupled in the divided simulations they were expected to give slightly different results to the undivided simulation. However, for the spatial convergence study the consistency of the results between different meshes was the primary result, not the quantitative results from the simulations. The physics and velocity and temperature fields within the divided simulations were similar to the undivided simulation meaning spatial convergence in one implied spatial convergence in the other.

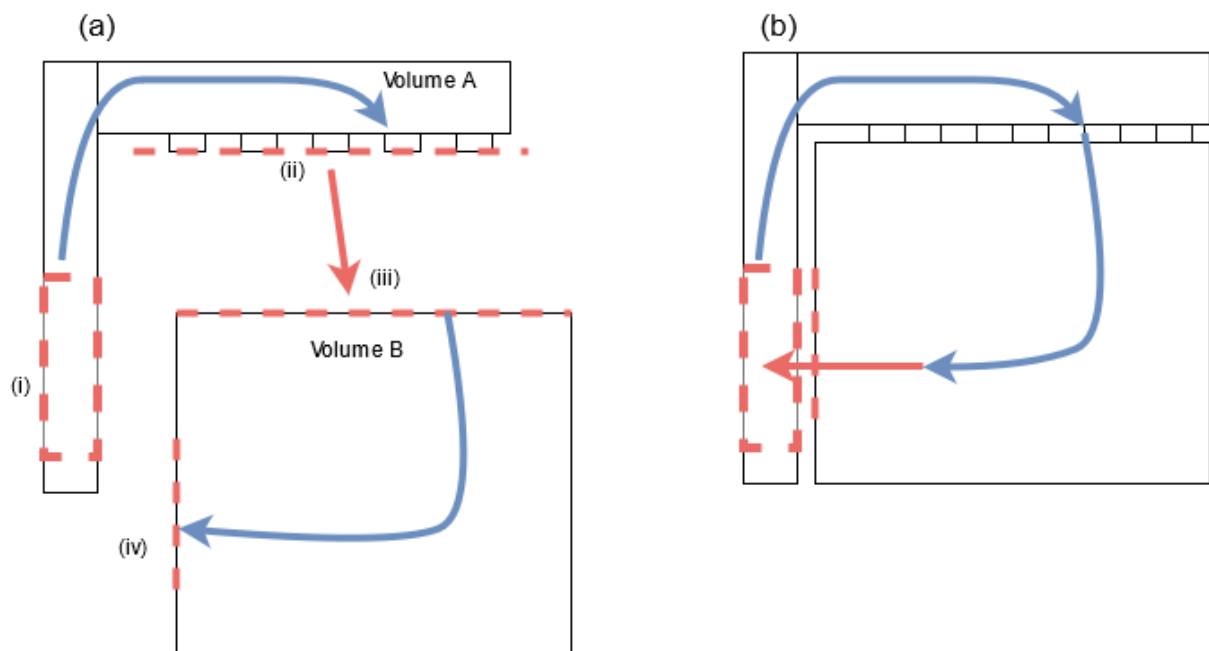


Figure 7.10: Illustration of boundaries of the (a) divided and (b) undivided simulations. Fluid boundaries are shown with a red dashed line, information transfer is shown with a red arrow. Simplified flow of air through the simulation is shown with a blue arrow.

Volume A Spatial Convergence

First the ability to model volume A with a steady state simulation was investigated. The model of volume A was run in steady state and converged to RMS residuals of 10^{-5} . The results from the steady state simulation were compared to the average values from a transient simulation. The average temperature and velocity in each of the jet nozzles was used for the comparison. The average difference in the velocity and temperature was 0.014% and $7.8 \times 10^{-4}\%$, respectively, while the maximum differences were 0.21% and 0.092%, respectively. This demonstrated that a steady state model of volume A was valid and gave similar results to the transient model.

Mesh refinement was performed keeping the normalised element length scale $\langle L_{el} \rangle$ constant for each mesh:

$$\langle L_{el} \rangle = \frac{L_{el}}{L_{el}^{base}} \quad (7.2)$$

where L_{el} is the sizing function length scale as described in section 7.4, and the base superscript indicates the length scale in the base mesh.

The aim of keeping $\langle L_{el} \rangle$ constant was to keep the element shape as similar as possible between meshes.

Figure 7.11 shows the variation in the number of elements as the length scale of the element sizings was decreased. For a constant element shape, the number of elements rises with the inverse of the cube of the element length scale for a 3-dimensional mesh, shown by the solid line in Figure 7.11. The meshes generated by CFX-Mesh closely follow this relationship, indicating that the element shape remained roughly constant.

The primary result from the undivided simulation is the magnitude and distribution of heat flux at the food boundary. The velocity and temperature of the impingement jets entering the cooking chamber is the connection between volume A and these parameters. The average temperature of the air leaving volume A could not vary between meshes as the mass flow and heat added is identical and the conservation of mass and energy is enforced by the solver. The distribution of the mass and energy leaving volume A could vary, however. This was investigated

by calculating the mean air velocity and temperature of the air exiting each of the jets and comparing the results between the 6 meshes.

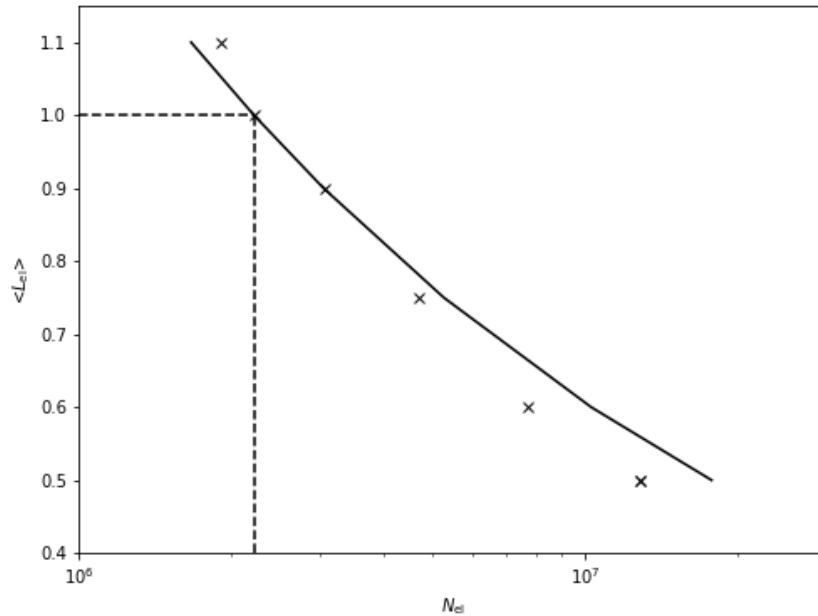


Figure 7.11: Plot of N_{el} against $\langle L_{el} \rangle$ for volume A. Solid line shows the relationship if the element shape is constant. Dotted lines indicate the position of the base mesh, $N_{el} = 2.22 \times 10^6$ and $\langle L_{el} \rangle = 1.0$.

The mean absolute difference between each data set and the results for the finest mesh was calculated and is shown in Figure 7.12. The figure shows that while the average difference to the finest mesh decreases as N_{el} increases, the results for all the meshes are similar with a mean error below 4% for all velocities and below 2.5% for temperatures. This is a small source of error compared to the acceptable accuracy of 30% for the model as a whole.

Figure 7.13 shows all the jet velocity and temperatures used to calculate the means in Figure 7.12. All meshes show broadly the same pattern of alternating faster and hotter jets with slower and cooler ones. This alternating behaviour is due to the bulkheads in the heater sections that separate the rows of jets into pairs.

Differences between meshes occur at the ends of the heaters furthest from the fan and closest to the door. Figures 7.13(c) and (d) show that different meshes have diverging temperature predictions in jets 1-5. The differing predictions do not display a dependence on mesh

refinement, with the most refined (50% element size) and second most refined (60% element size) showing different behaviour. These differences are therefore likely due to unstable flow leading to unsteady results, arising from end effects in the heater header. The different discretisation in the solver, due to varying element sizes and shapes across the various meshes leads to different backpressures from the end of the header and varying flow patterns in this region.

The velocity results, shown in Figure 7.13(a) and (b), are less homogenous, with a greater variation between meshes. As with the temperature predictions, the velocity results diverge in the jets closest to the door. Some meshes, particularly the $N_{el} = 1.91 \times 10^6$ mesh, have higher velocities closer to the fan than the other meshes, but lower towards the door. This is likely due to the calculation of pressure in the heater headers.

As the differences between the meshes are both relatively small and a weak function of mesh refinement, the base mesh ($\langle L_{el} \rangle = 1$) was used in subsequent simulations. The increased computational cost of the more refined meshes was not deemed worthwhile for a change in the output parameter of less than 5%.

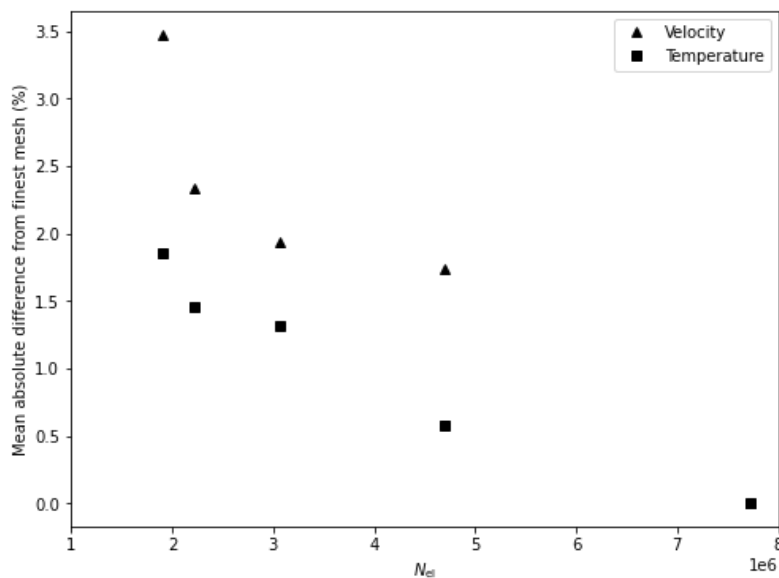


Figure 7.12: Effect of number of mesh elements on difference of solutions from finest mesh ($N_{el} = 7.73 \times 10^6$) for velocity and air temperatures.

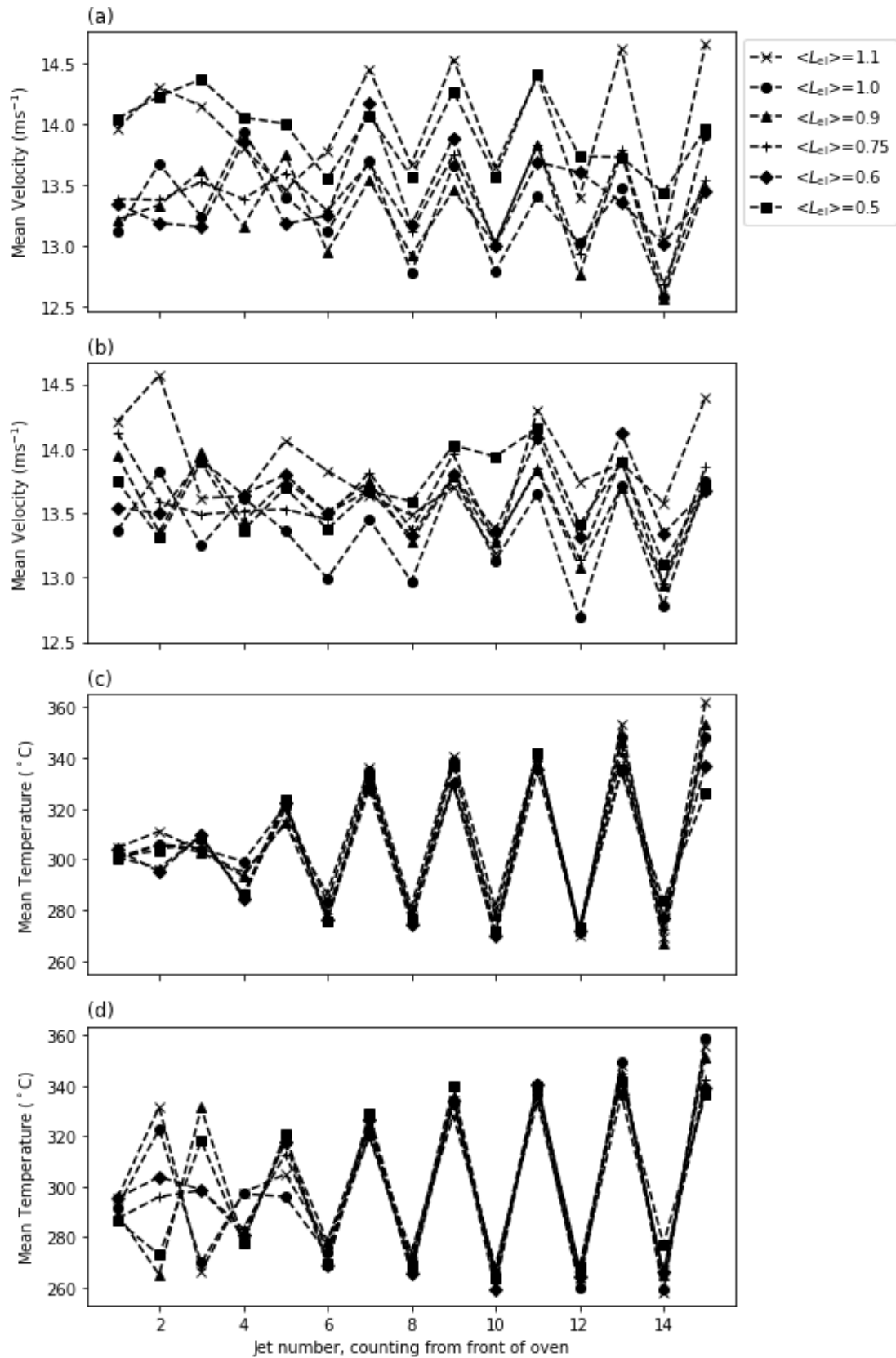


Figure 7.13: Distribution of average jet exit velocity and temperature for the meshes tested for volume A. As seen from view 2; (a) Velocity of central line of jets. (b) Velocity of left side row of jets. (c) Temperature of central line of jets. (d) Temperature of left side row of jets.

Volume B Spatial Convergence

Similar to the analysis of volume A, the inlet and outlet boundaries from volume B could not be coupled to the rest of the simulation. The inlet to volume B was the exported boundary data at the jet exit, the outlet was a constant pressure of 0 Pa.

Mesh refinement was performed in two ways. One was to reduce $\langle L_{el} \rangle$ by a constant factor, keeping the element shape as similar between cases as possible. This was performed without an inflation layer in the base of the oven. The second was changing the size of the elements at the base of the oven. The heat flux into the food is the primary result from the model and the element size at this wall will have a large effect on this value. This investigation was performed on the base, $\langle L_{el} \rangle = 1.0$, mesh by creating an inflation layer on the face of the oven chamber including the food. The thickness of the first layer of the inflation layer was varied.

Figure 7.14 shows the number of elements in each level of mesh refinement. The number of mesh elements closely matches the number of elements if the shape of the elements remains identical, showing the shape of the elements remains similar between the meshes.

Figure 7.15 shows the mean and standard deviation of the predicted heat flux into the food boundary as the size of the elements in the mesh is reduced. Reducing the element size slightly reduces both the mean and deviation of the heat flux into the food. The mean fluxes, plotted in Figure 7.15(a), show the differences to be small with all values within 5% of the finest mesh value. The standard deviation is less consistent between meshes, with a 9.4% difference between the predictions for the $\langle L_{el} \rangle = 0.9$ mesh and the $\langle L_{el} \rangle = 0.75$ mesh.

The results from the inflation layer analysis are shown in Figure 7.16. The mean flux predictions are similar to those from meshes without an inflation layer but the standard deviations of the flux are noticeably lower. This is likely due to the inflation layer enforcing a constant first layer thickness, resulting in a more consistent calculation of heat flux at the wall. Figure 7.17 shows the y^+ (labelled as Yplus) values on the food boundary for meshes with and without an inflation layer and illustrates how setting a constant first element thickness reduces the noise in y^+ at this boundary. Furthermore, the y^+ values are all < 2.5 , which allowed the solver to model the flow behaviour close to the wall and as discussed in section 3.2.2 should give an accurate calculation of heat flux at this boundary. The lowest values of y^+ seen at the centre of the “food” in both

Figures 7.17(a) and (b), labelled as **C**. This is due to this region having the lowest air velocity close to the wall, which by equations 3.9 and 3.11, reduced the value of τ_w and therefore y^+ . The stagnant flow in this region was due to the presence of the symmetry plane in the simulation which only allowed air to flow parallel to it.

The mean flux for all meshes tested was within 5%, well within the allowable tolerance of 30% (section 7.1). Together with the y^+ values on the food surface, this indicated the predictions of heat flux through the base of the oven could be considered accurate and reliable.

The heat flux through the door and side walls of the oven and the y^+ for the $< L_{el} > = 1.0$ and $< L_{el} > = 0.75$ meshes is presented in Table 7.3. Although the mean value for y^+ is relatively low and would indicate the simulation can model the flow close to the wall, this is skewed by the large number of elements on the base of the oven and beneath the impingement jets but bordering the door boundary. Figure 7.18 shows a contour plot of y^+ on the side wall of the oven, illustrating the high y^+ in this region. This indicates that the heat flux calculated in this region will be based on empirical wall functions and is therefore expected to be less reliable than at the base of the oven. Predictions of outputs such as efficiency that require wall heat flux from these boundaries will therefore be less reliable. It was not possible to reduce y^+ in these areas as this would have increased the number of mesh elements such that the simulation could not be run on the available workstation. The aim of the simulation was to predict the magnitude and distribution of heat flux into the food, not to accurately predict efficiency, thus this area of uncertainty was deemed acceptable.

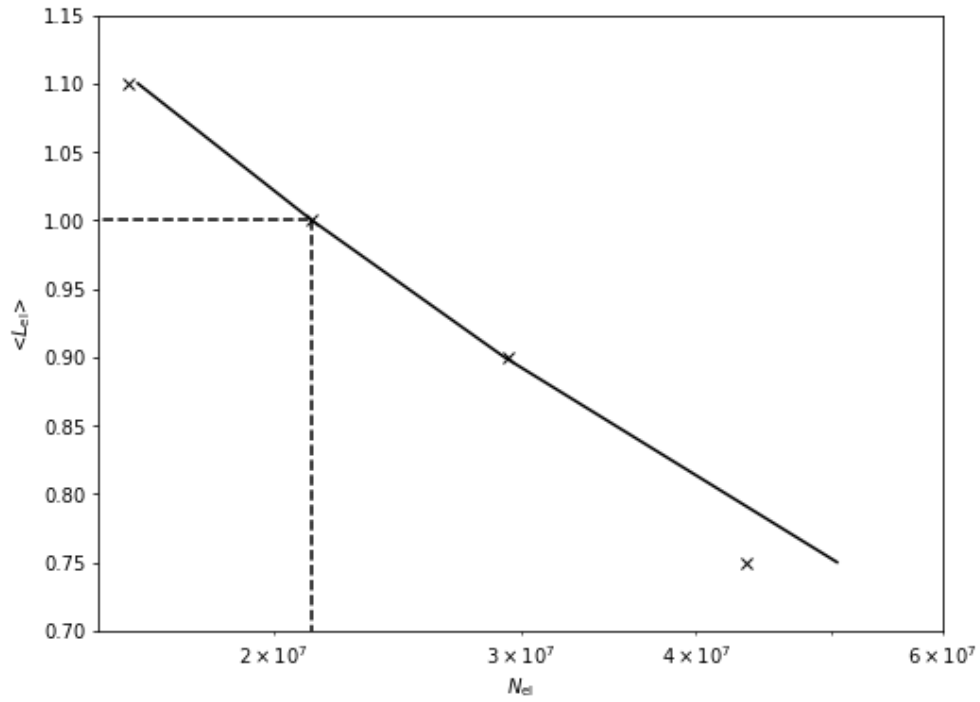


Figure 7.14: Plot of N_{el} against $\langle L_{el} \rangle$ for volume B. Solid line shows the relationship if the element shape is constant. Dotted lines indicate the position of the base mesh, $N_{el} = 2.12 \times 10^7$ and $\langle L_{el} \rangle = 1.0$.

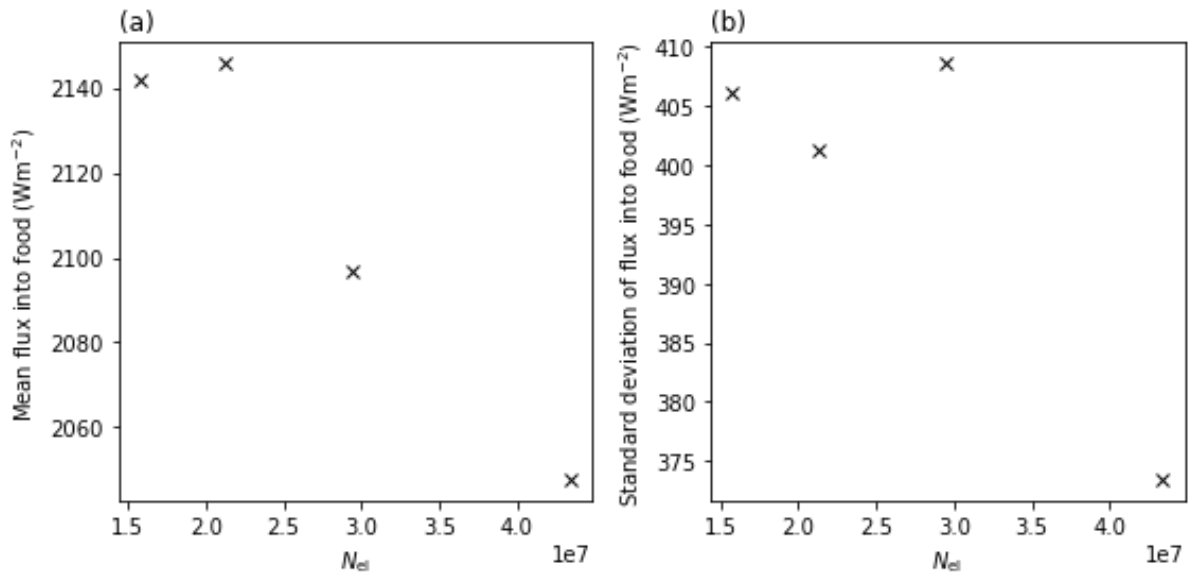


Figure 7.15: Effect of number of elements on (a) predicted mean heat flux into the food, (b) predicted standard deviation of flux into the food.

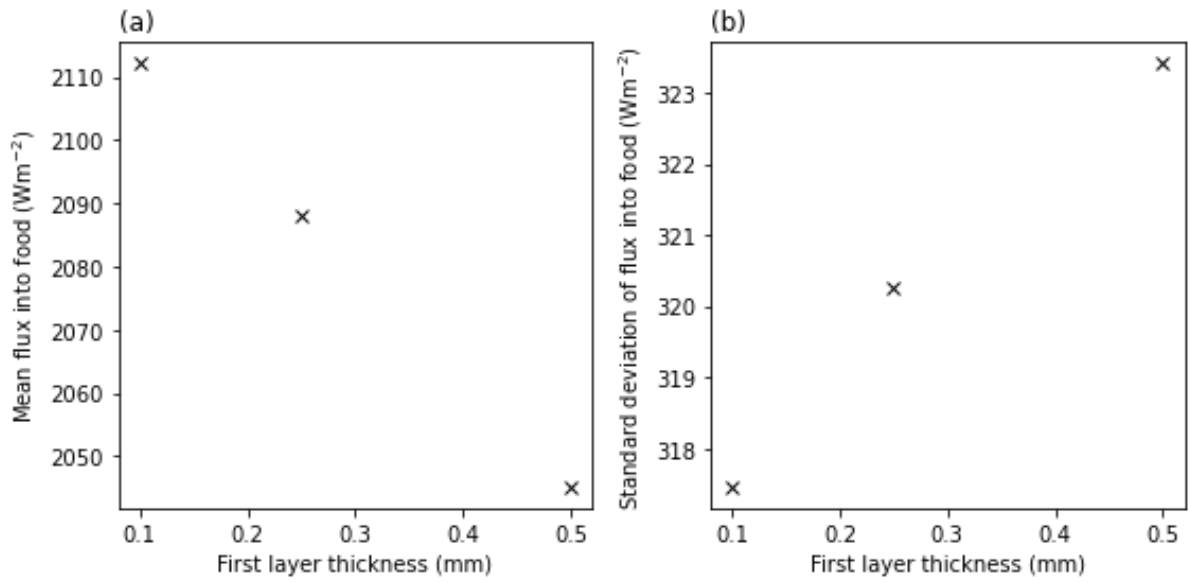


Figure 7.16: Effect of inflation layer element thickness on (a) predicted mean heat flux into the food, (b) predicted standard deviation of flux into the food.

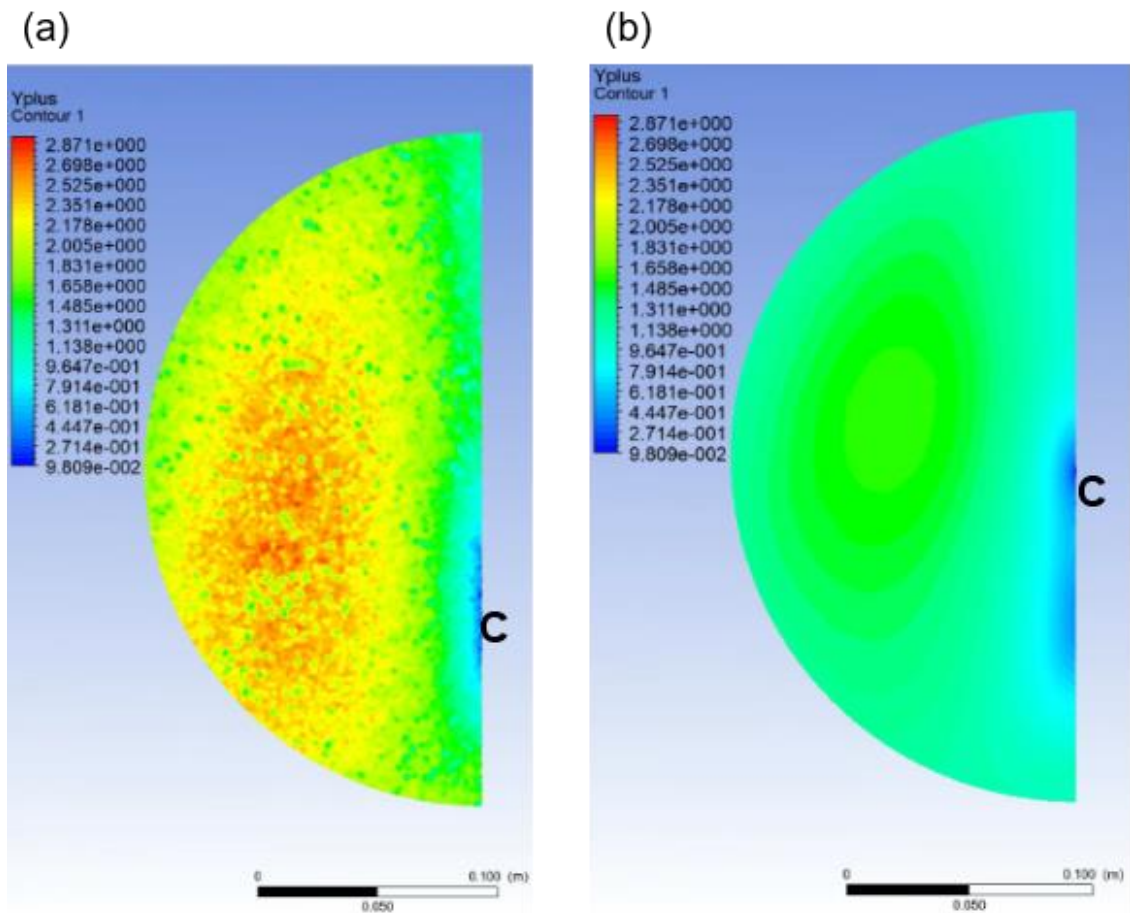


Figure 7.17: Contour plots of y^+ on the food boundary, generated using CFX-Post. (a) without and (b) with an inflation layer. First cell thickness 0.1 mm. View 1.

Table 7.3: Comparison of y^+ and heat wasted from the cooking chamber for the $\langle L_{el} \rangle = 1$ and 0.75 meshes. Heat wasted is the sum of heat lost through walls that are not the food boundary.

Mesh	Mean y^+ on walls and door (-)	Max y^+ on walls and door (-)	Total heat wasted from cooking chamber (W)
$\langle L_{el} \rangle = 1$	1.78	19.0	192
$\langle L_{el} \rangle = 0.75$	1.37	18.7	185

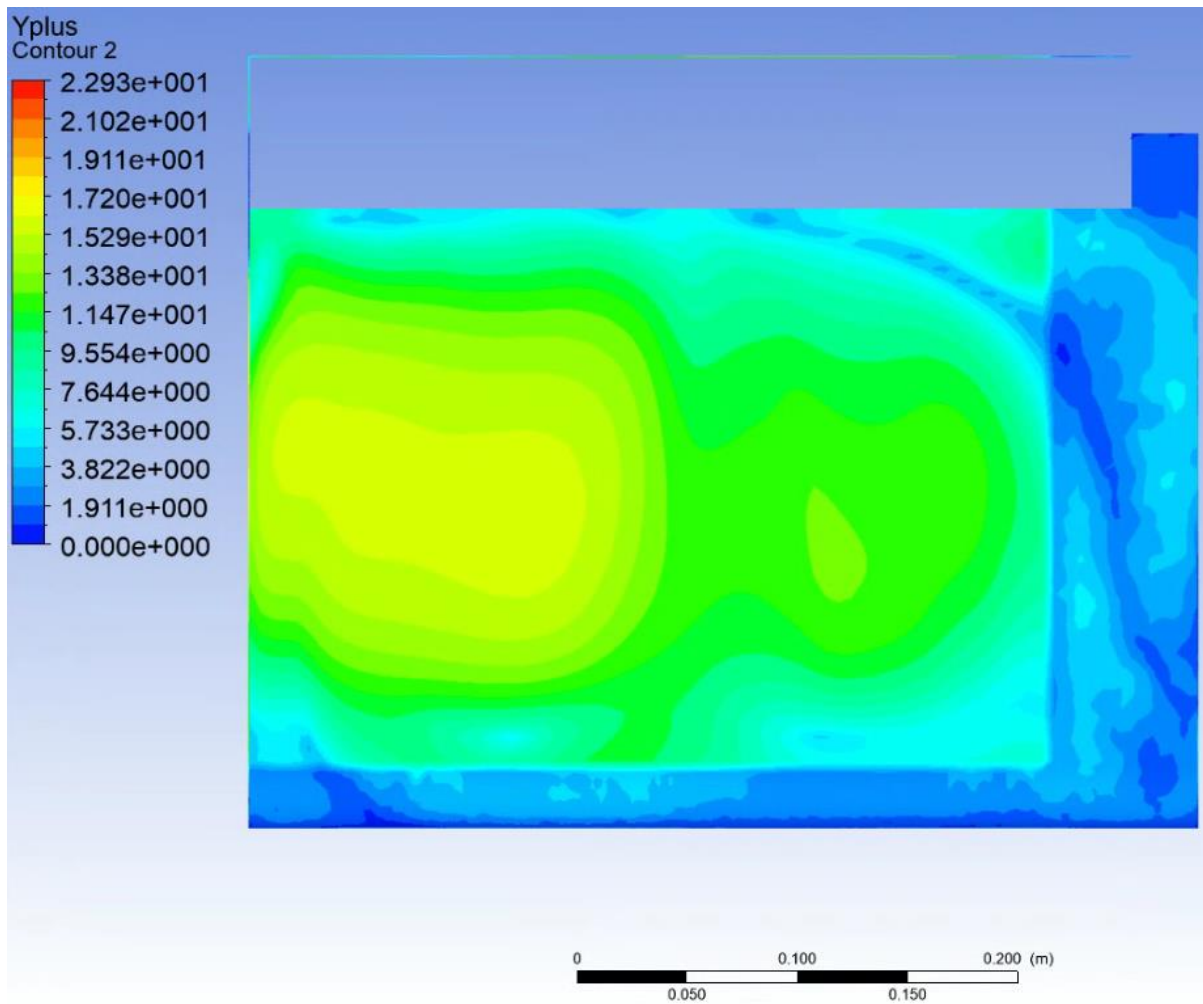


Figure 7.18: Contour plot of y^+ on the side wall of the cooking chamber, view 6.

7.6.4: Temporal Convergence

As discussed in section 7.5.1 the model could not be converged using a steady state simulation. Residuals from the simulation were unacceptably high. The turbulent and chaotic nature of the air flow within the cooking chamber prevented the model from converging to a steady solution.

A transient model was therefore required, and a timestep selected. The model was run for 60 s with timesteps of 0.1, 0.3 and 1 s. The heat flux into the food boundary was exported for every node in the surface mesh. The mean and standard deviation of the heat flux was calculated and the results in Figure 7.19 show that reducing the time step from 1 s to 0.3 s increased the mean heat flux by 10% and reduced the standard deviation by 8%. Further reduction of the timestep to 0.1 s had a smaller effect, mean flux was reduced by 0.5% and standard deviation by 2.7%. A timestep of 0.3 s was selected for subsequent simulations as a timestep of 0.1 s increased computation time with small changes in the simulation results compared to desired accuracy of $\pm 30\%$.

The length of time for which the simulation was run was also investigated. The mean and standard deviation of the flux into the food is plotted against t_{sim} in Figure 7.20. The backwards counting cumulative mean is also plotted: this is the cumulative mean calculated from the 60 s timestep counting backwards to the 1 s timestep. For example, the value of the backwards counting cumulative mean at $t_{\text{sim}} = 30$ s is the mean between $t_{\text{sim}} = 30$ s and $t_{\text{sim}} = 60$ s.

Both the standard deviation and mean of the flux into the food vary over time. There is an initial transient period as the simulation finds the quasi-steady state from the initial condition. This took approximately 20 s. After this point the mean and standard deviations oscillate around the mean value, indicating the quasi-steady state has been reached. The period of these oscillations is approximately 10 s. Between $t_{\text{sim}} = 20$ and 40 s the backwards counting cumulative mean shows little variation, indicating that using results from between 20 and 60 s is sufficient to capture the quasi-steady state.

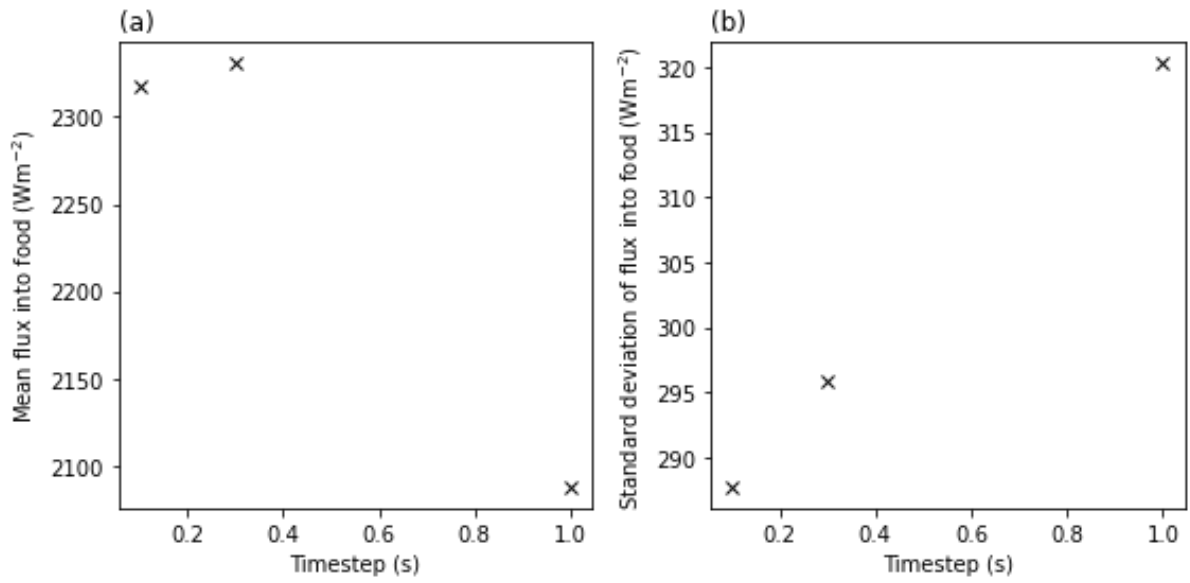


Figure 7.19: Effect of timestep length on (a) predicted mean heat flux into the food, (b) predicted standard deviation of flux into the food.

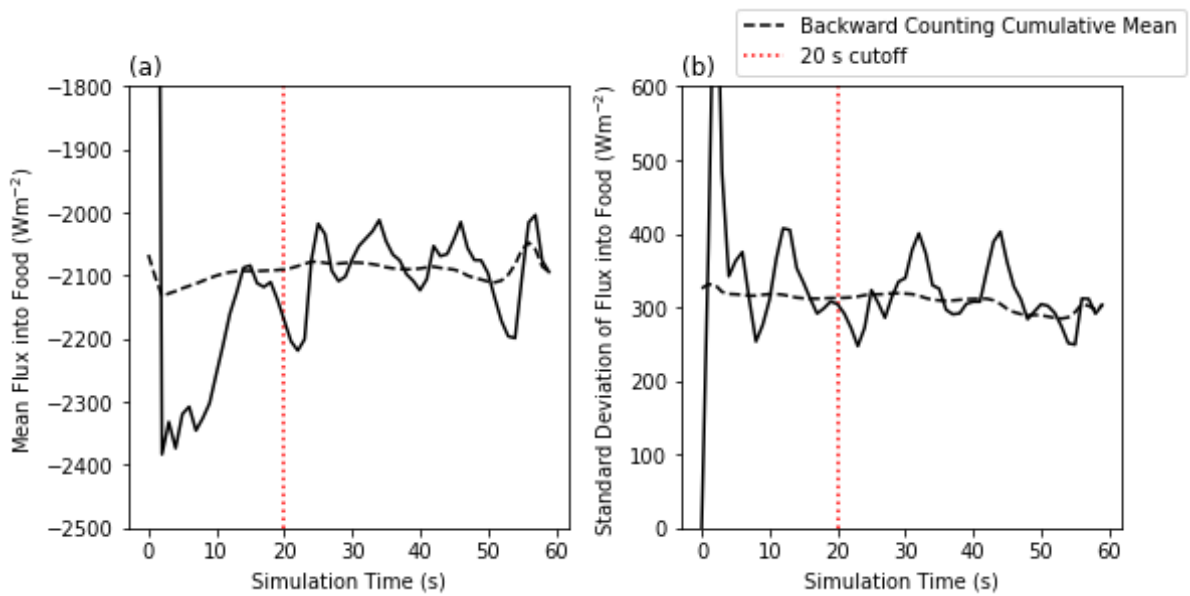


Figure 7.20: Evolution of the heat flux. (a) mean flux, (b) standard deviation of the flux. The backward counting mean of the mean and standard deviation are plotted with a dashed line. The 20 s cut off, before which the results are discarded, is plotted with a red dotted line.

7.6.5: Experimental Comparison

The simulation predictions were compared with two experimental quantities:

- i) The velocity profile beneath the impingement jets, where the high velocity jet entrains ambient air within the cooking chamber.
- ii) The heat transfer coefficient and radiative flux at various positions across the base of the oven.

The prediction of heat flux impinging on the base of the oven was the primary deliverable from the model. Comparing the model prediction of this parameter to experimental data was therefore the most direct way to quantify the accuracy of the model. The velocity profile in this section of the cooking chamber was selected as it is an area with large gradients in temperature and velocity. If the model was able to predict the velocity profiles accurately in this area it would indicate that the turbulence model and mesh were capable of resolving the flow in the rest of the geometry.

Velocity Measurement Comparison

The apparatus and methodology used to experimentally measure velocity within the cooking chamber is described in section 5.3. To generate comparable model results, the model was run isothermally at 20°C with no power supplied to the heaters. Otherwise, the model setup was as described in section 7.5. As with previous simulations, the simulation was run for 60 s and data from the later 40 s were analysed. The data extracted was for every node in a sphere of radius 7.5 cm beneath the central jet closest to the door. The LDA system gave a mean velocity over a 2 x 2 x 2 mm cubic volume. The results from the simulation were processed to give the average values at the same coordinates and volumes as the LDA experiments.

Figure 7.21 shows the coordinate system used for the comparison. The origin of the coordinate system is the centre of the nozzle of the jet. Figure 7.22 shows the downwards velocity profile across the jet at various planes below the nozzle. The velocity v_y is the velocity measured in the y_{jet} direction. Figure 7.23 shows contours of velocity for the experimental results and model prediction on the respective planes.

The simulation gives a generally good prediction of the measured velocity profiles. Two key parameters of the velocity profiles can be compared between the simulation predictions and experimental results. One is the peak velocity and how it changes with distance from the nozzle. The second is how the jet spreads and entrains ambient air from the cooking chamber. This can be seen in how the width and gradient of the velocity profile changes with distance from the nozzle.

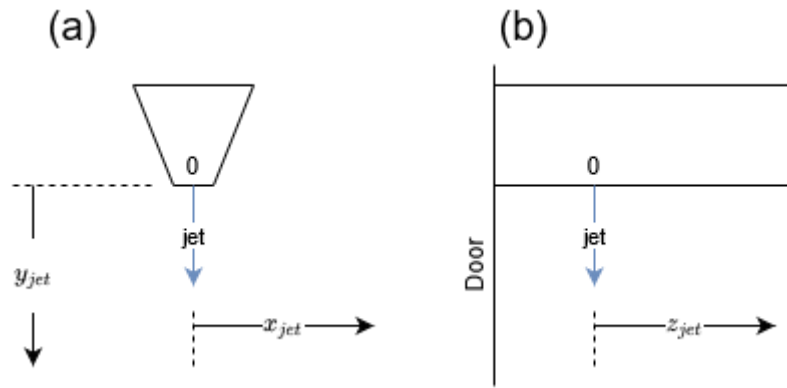


Figure 7.21: Diagram illustrating the coordinate system used for the LDA measurements and comparison to model predictions, third angle projection. (a) view 2, (b) view 6.

The model accurately predicted the peak velocities of the jet, especially at $y_{jet} = 20, 60$ and 80 mm. At $y_{jet} = 40$ mm, the model underpredicted the peak velocity by approximately 20%. The LDA readings at this value of y_{jet} contained more noise than the other planes, reflected by the irregular pattern in Figure 7.23(i)

The simulation also predicted the evolution of the velocity profile accurately. The width and gradient of the predicted profiles match the measured trend. One exception is at $y_{jet} = 80$ mm where the model predicted a more narrow velocity profile than that measured experimentally. This can be seen in the corresponding plots in Figure 7.22. The simulation predicted $v_y \approx 0$ m/s when x_{jet} and $z_{jet} > 15$ mm or < -15 mm. This did not match the experimental values, where $v_y = 2$ m/s when $z_{jet} = -15$ mm.

Overall, the model predictions of velocity in this region were acceptably accurate, especially given the small scale and relatively large velocity gradients in the flow. This indicates the mesh and turbulence model were sufficient to capture the key flow features.

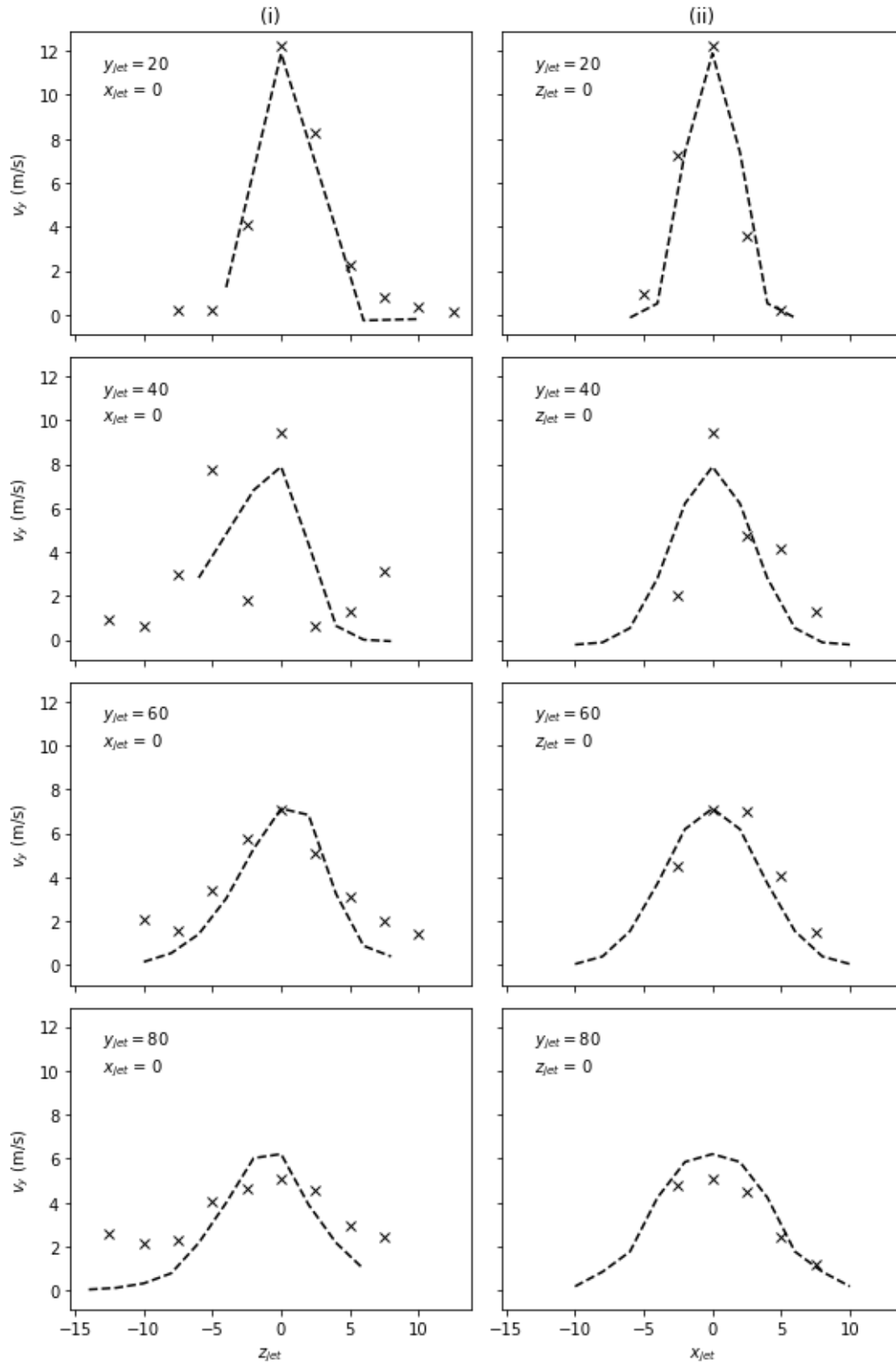


Figure 7.22: Comparison of model predictions, shown by the dotted line, and experimental velocity results, shown by crosses. Column (i) shows the profile across the jet in the z_{jet} direction, column (ii) shows the profile in the x_{jet} direction. All dimensions in mm. Jet nozzle diameter = 4 mm.

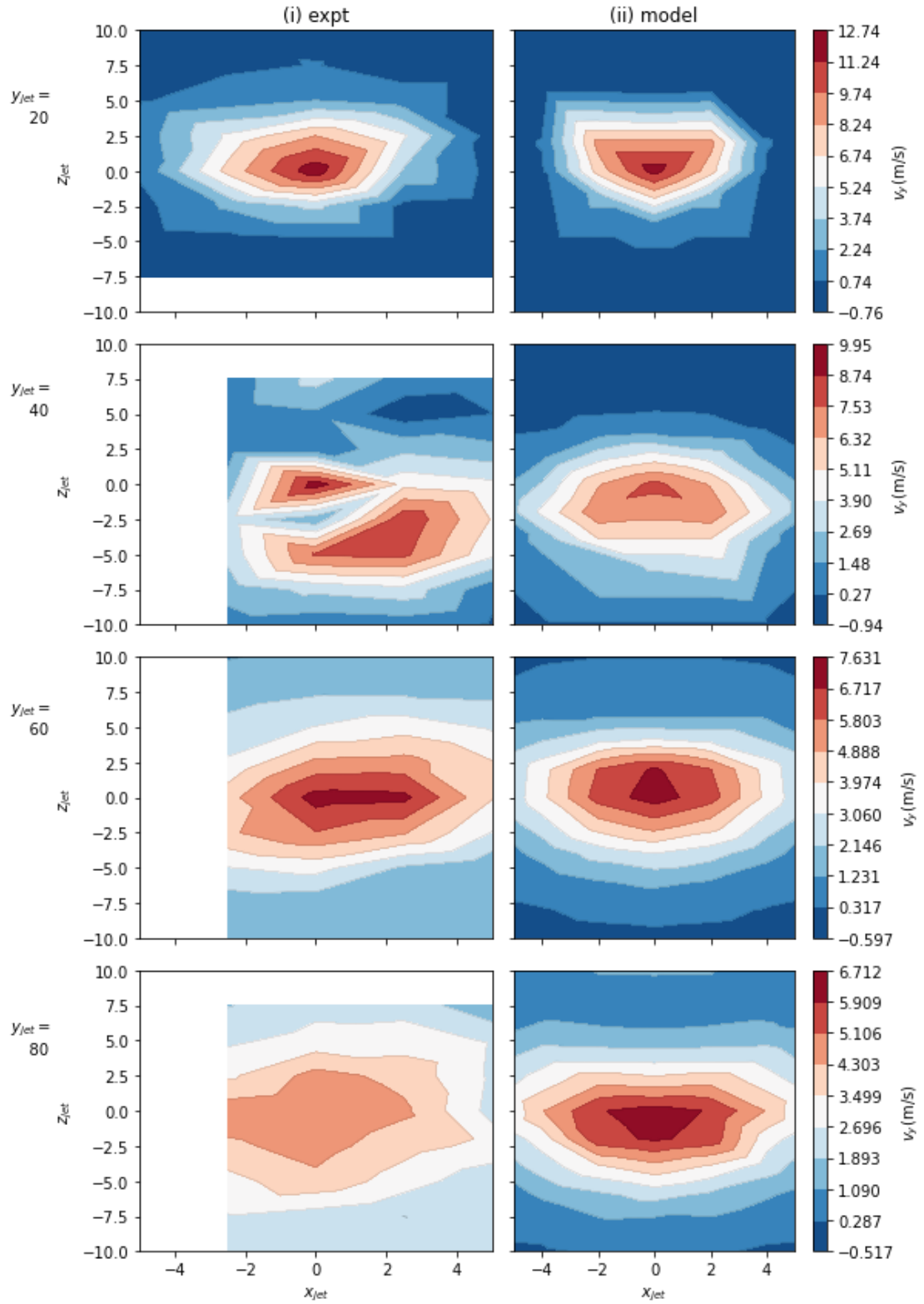


Figure 7.23: Contours of v_y in x_{jet} and z_{jet} at various values of y_{jet} . Column (i) shows experimental values, column (ii) shows model predictions. All dimensions in mm. White gaps are the result of missing data due to problems with the traverse system. Jet nozzle diameter = 4 mm. Note that colorbars vary for different values of y_{jet} .

Heat Fluxes

The heat flux sensor described in section 5.2 was used to measure the convective heat transfer coefficient, h , and the black body temperature, T_{BB} , describing the convective and radiative heat fluxes. The experimental process is described in section 5.2.4. Measurements were taken at 5 positions and the simulation geometry was altered to include the heat flux sensor within the oven. The location of these measurement positions is shown in Figure 7.25. The sensor, in reality, had a depth of 40 mm. In the simulation the sensor took the form of a cuboid, with a top surface of 100×100 mm, and a depth of 20 mm - the thickest the simulated sensor could be while remaining completely enclosed in the unstructured, “base of the cooking chamber” volume, labelled in Figure 7.3. Any thicker would have required remeshing the “centre of the cooking chamber” volume. Therefore, the sensor surface was set 20 mm closer to the impingement nozzles in the experiment than in the model: this was 6 % of the 315 mm separation between the nozzles and the sensor and was considered an acceptable discrepancy.

The mesh was similar to that described in section 7.4. The surface of the base of the oven and the top of the sensor retained the inflation layer shown in Figure 7.24. Due to limitations with the meshing algorithm, the inflation layer could not be enforced consistently across the entire top surface. Figure 7.24 shows how the inflation layer gains additional elements in thickness away from the edge of the sensor. The heat flux measurements at the edge of the sensor may therefore not be reliable and the region 1.5 mm from the edge of the sensor was excluded from subsequent processing and analysis.

The model boundaries, excluding the “food”, were identical to those in section 7.5.3. The top of the sensor was fixed at 80°C, with $\epsilon = 1$. This temperature was used as it was between 25 and 110°C, the temperature of the sensor at the start and end of the tests, respectively. The sides of the sensor were assumed to be adiabatic (see section 5.2.2). The base of the oven was included in the “exterior walls” boundary condition. The power of the heaters was set at $Q_{heater} = 2000 \text{ Wm}^{-2}$, to give a similar air temperature within the cooking chamber to the experiment. The temperature of the return air in the oven was set at 120°C in both the model and experiments, corresponding to a jet temperature of approximately 150°C. This value was chosen as it was at the low end of the temperature range likely to be used for cooking. The lower temperature reduced the flux and allowed the sensor to provide a measurement over a longer time period. All other physics and solver settings were otherwise kept the same.

The jet temperature was not measured due to difficulties in measuring this quantity accurately. The proximity to the heater elements gives a large error in the measurement due to radiative exchange, while the small size of the jets and the large temperature gradients make shielding and locating the thermocouple junction difficult.

The convective and radiative heat fluxes into the top of the sensor were extracted for the final 40 s of each run. The boundary layer temperature for the heat transfer coefficient was taken as a point 20 mm above the sensor surface, matching the position of the boundary layer thermocouple in the experiments.

The mean convective and radiative heat flux was calculated in python for each position. The film heat transfer coefficient, h , could then be calculated:

$$h = \frac{\bar{q}_{\text{conv}}}{T_{\text{boundary}} - 80} \quad (7.2)$$

where \bar{q}_{conv} is the mean convective heat flux into the sensor surface and T_{boundary} is the temperature outside the boundary layer, measured 10 mm above the surface.

The blackbody temperature, T_{BB} , represents a way to measure the radiative heat flux independently of the temperature of the surface of the heat flux sensor, viz.

$$T_{\text{BB}} = \left(\frac{\bar{q}_{\text{rad}}}{\sigma_{\text{SB}}} - (80 + 273)^4 \right)^{\frac{1}{4}} - 273 \quad (7.3)$$

where \bar{q}_{rad} is the mean radiative heat flux into the sensor, as predicted by the simulation, and σ_{SB} is the Stefan-Boltzman constant.

These values could be compared to the values derived from experiment for the 5 sensor positions tested. The experimentally measured values of h and T_{BB} were used to calculate the values of \bar{q} , \bar{q}_{conv} and \bar{q}_{rad} for a sensor temperature of 80°C. These results are shown in Table 7.4 and Figure 7.25. Derivation of the uncertainties in the experimental measurements is described in section 5.2.6.

The simulation predicted convective heat transfer relatively accurately: the simulation prediction of \bar{q}_{conv} is within the sensor's measurement uncertainty for all 4 of the 5 positions, and within the accuracy goal for the simulation of 30% for all of the 5 positions. For a similar exit temperature from the cooking chamber, T_{boundary} is very similar for the model and experiment, within ± 3 K. The heat transfer coefficient, h , was also predicted within the accuracy goal of 30%, with a mean absolute error of 20.3 %. This translates to a mean absolute error of 22.0 % in \bar{q}_{conv} .

Radiative exchange was not predicted accurately by the model. The blackbody temperature of the oven, T_{BB} was underpredicted by 20 - 30 K for all 5 measurement positions, despite the accurate predictions of T_{boundary} . For a sensor temperature of 80°C the mean absolute error in \bar{q}_{rad} was 53.2%, well outside the measurement uncertainty.

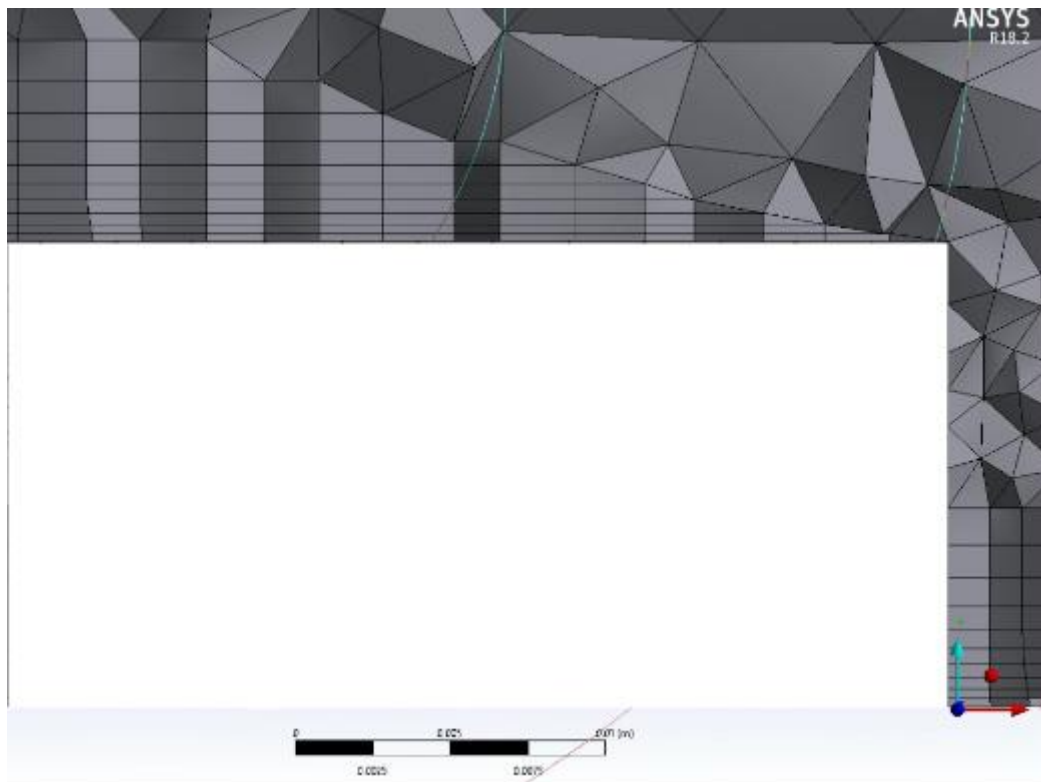


Figure 7.24: Section showing the mesh around the edge of the sensor, view 2.

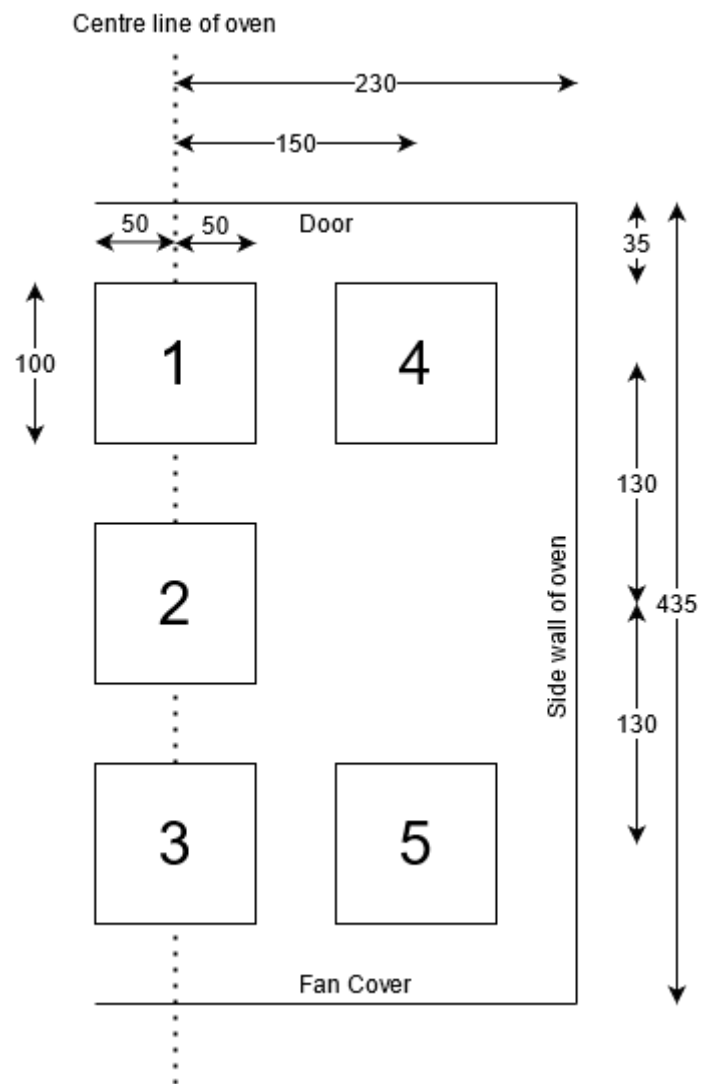


Figure 7.25: Heat flux measurement positions. All dimensions in mm. View 1.

Table 7.4: Experimental results (shown in black, uncertainties in brackets where applicable), simulation predictions (in blue) and percentage error in the simulation predictions (shown in brackets in red) for the 5 positions. Fluxes calculated for a black surface ($\epsilon = 1.0$) at 80°C

Position	$T_{boundary}$ (°C)		h (Wm ⁻² K ⁻¹)		T_{BB} (°C)		\bar{q}_{rad} (W)		\bar{q}_{conv} (W)		\bar{q} (W)	
1	120	121	34.4	25.8	113	98.3	384 (+5, -28%)	197	1390 (+1.4, -27%)	1060	1780 (+0, -20%)	1250
	(-0.83)		(-25)		(-13.0)		(-49)		(-24)		(-30)	
2	122	119	33.3	25.1	120	103	477 (+5, -28%)	249	1400 (+1.7, -28%)	979	1880 (+0, -20%)	1230
	(-2.4)		(-25)		(-14.2)		(-48)		(-30)		(-35)	
3	120	117	29.6	27.1	127	109	569 (+5, -28%)	321	1200 (+2.4-32%)	1000	1770 (+0, -20%)	1323
	(-2.5)		(-8.4)		(-14.2)		(-44)		(-16)		(-25)	
4	117	119	24.7	19.8	122	96.5	505 (+5, -28%)	177	926 (+2.7, -35%)	772	1430 (+0, -20%)	949
	(1.7)		(-20)		(-20.9)		(-65)		(-17)		(-34)	
5	116	117	26.3	20.2	119	105	459 (+5, -28%)	279	973 (2.7, -34%)	747	1430 (+0, -20%)	1030
	(0.86)		(-23)		(-11.7)		(-39)		(-23)		(-28)	

There are three potential contributors to this error in T_{BB} :

- i) The assumption that the heater walls are adiabatic.
- ii) The overall heat transfer coefficient from the inner wall of the cooking chamber to the surroundings may not be accurate. This would mean the predicted temperatures of the inner walls of the cooking chamber are not accurate, therefore making T_{BB} inaccurate.
- iii) The calculation of heat transfer from the air to the interior walls relies on empirical wall functions, which may give inaccurate predictions of flux and therefore wall temperature.

The approximate size of the error due to (i) can be calculated. Figure 7.26 shows a simplified schematic of heat transfer through the heater walls. The film heat transfer coefficient across the heater walls of $27 \text{ Wm}^{-2}\text{K}^{-1}$ assumes 2 mm of aluminium, 1.5 mm of mica and no air gap between them. The temperatures were extracted from the CFD simulation. Equation 6.4 gives the heat flux through the walls of the heaters, $q_{\text{wall}} = 582 \text{ Wm}^{-2}$. This is assuming radiative flux from the outside wall of the heaters is negligible. The total heat flow through the walls of the heater, Q_{wall} is given by:

$$Q_{\text{wall}} = q_{\text{wall}} \times A_{\text{wall}} \quad (7.4)$$

where A_{wall} is the area of the heater walls, $\approx 0.04 \text{ m}^2$.

This gives Q_{wall} as 23 W, compared to Q_{heater} of 140 W, indicating approximately 16% of the heater power conducts through the walls of the heater.

Equation 6.4 can then be used to calculate the temperature of the external wall of the heaters, $T_{\text{wall}} = 158^\circ\text{C}$. The simulation prediction of T_{wall} , neglecting conduction, is 120°C . The radiative flux from the heater wall to the surface of the sensor, $\bar{q}_{\text{rad}}^{\text{wall}}$ is given by:

$$\bar{q}_{\text{rad}}^{\text{wall}} = F_{A \rightarrow B} \epsilon \sigma_{\text{SB}} (T_{\text{wall}}^4 - T_{\text{surface}}^4) \quad (7.5)$$

where $F_{A \rightarrow B}$ is the view factor between the sensor and the external walls of the heater section, $F_{A \rightarrow B} \approx 0.21$. Emissivity for the enamelled interior of the oven ≈ 0.9 .

The difference in $\bar{q}_{\text{rad}}^{\text{wall}}$ when using $T_{\text{wall}} = 158^\circ\text{C}$ and $T_{\text{wall}} = 120^\circ\text{C}$ is 130 Wm^{-2} . Derivation of the film heat transfer coefficients shown in Figure 7.26 and $F_{A \rightarrow B}$ can be found in Appendix B.

It should be noted that this calculation assumes the temperature of the inner walls of the heater remain at 180°C regardless of the flux through the heater walls. In addition, the simulation prediction for the temperature within the heaters will also be dependent on the heater power which is a function of the heat lost through the walls of the oven and is therefore unlikely to be accurate.

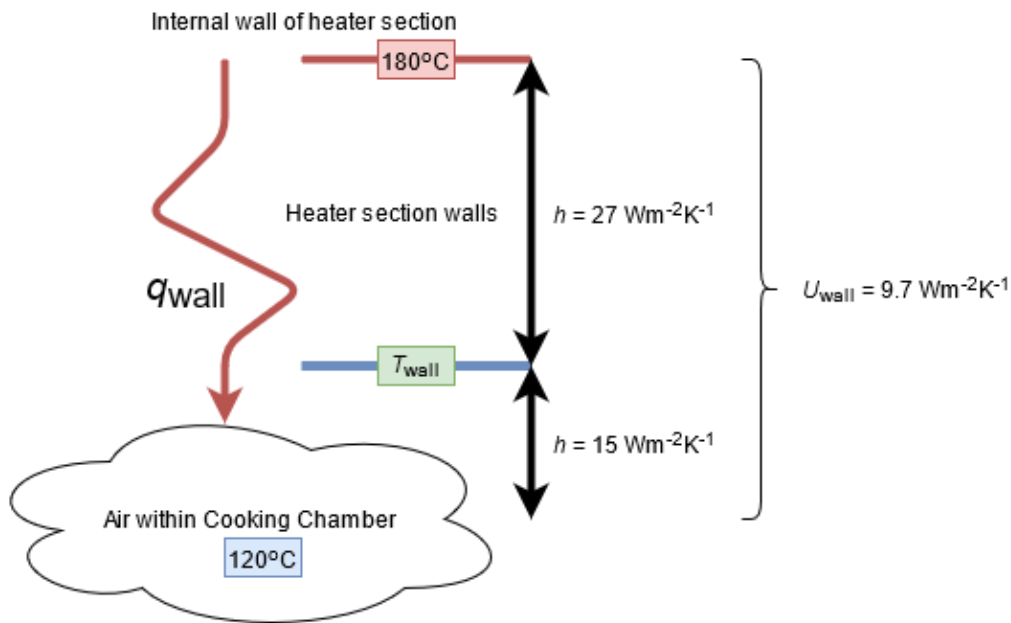


Figure 7.26: Simplified schematic showing heat transfer through the walls of the heater sections.

Factor (ii) can also be approximately quantified. The overall heat transfer coefficient across the ovens walls in the simulation is $4.4 \text{ Wm}^{-2}\text{K}^{-1}$. This gave $T_{\text{BB}} \approx 100^\circ\text{C}$. If the overall heat transfer coefficient across the oven walls is reduced to $3 \text{ Wm}^{-2}\text{K}^{-1}$, this would increase T_{BB} to 110°C for the same heat flux through the walls. Taking the view factor, $F_{A \rightarrow B}$, from the walls to the walls to the sensor as 0.79, \bar{q}_{rad} is increased by 90 W .

Although the calculations are approximate, the error in the predictions of \bar{q}_{rad} in Table 7.4 can be attributed to factors (i) and (ii) as the combined estimated error is 220 W , sufficiently large to describe the observed error.

Combining the radiative and convective fluxes, the mean absolute error in the total flux, \bar{q} was 30.4%, close to the accuracy goal of 30%. None of the simulation predictions were within the sensor measurement uncertainty. Figure 7.27 illustrates that \bar{q}_{conv} was larger than \bar{q}_{rad} and therefore the large errors in \bar{q}_{rad} do not translate directly to large errors in \bar{q} .

Overall, the model predictions lie within the accuracy limits set in section 7.1 of $\pm 30\%$. It should be noted however that the values and errors presented in this section are only for the specific combination of sensor temperature (80°C) and oven setpoint (120°C) used. Reducing the sensor temperature or increasing the oven air temperature would reduce the error and vice versa. Additionally, the emissivity of any food in the oven will be lower than the emissivity of the sensor ($\epsilon = 1$), giving a lower value of \bar{q}_{rad} and a smaller associated error.

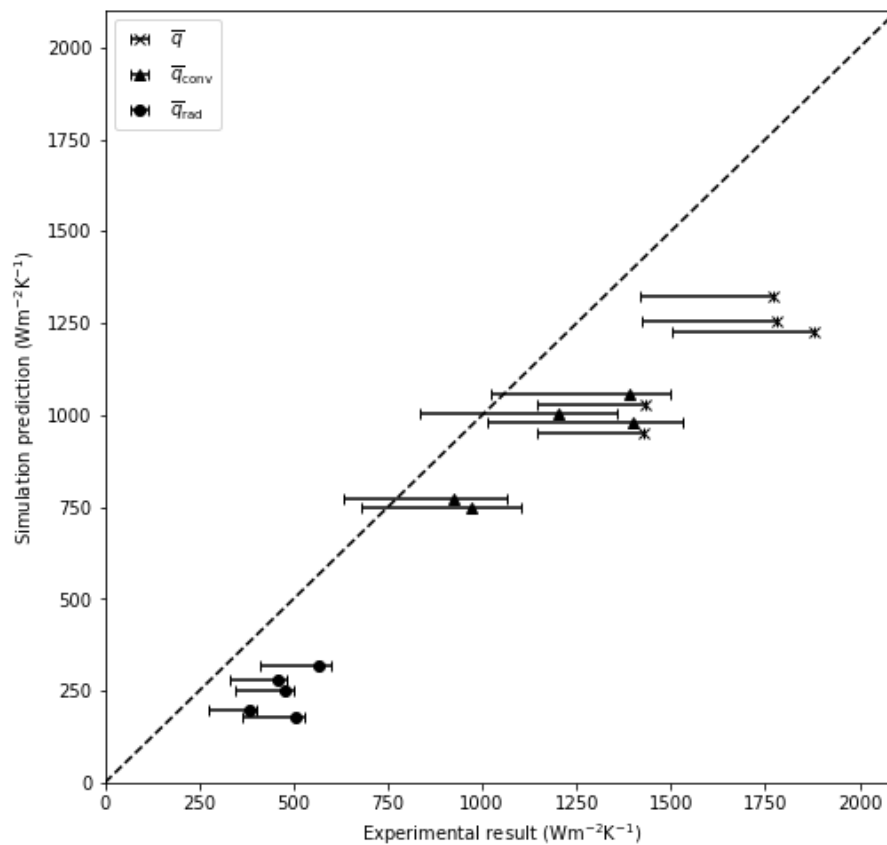


Figure 7.27: Comparison of experiment and simulation predictions for heat flux. Dashed line shows unity. Error bars shown the systematic uncertainty in the measurements, discussed in section 5.2.6.

Conclusions

The heat flux and velocity experimental comparisons showed that the simulation was able to accurately predict parameters relating to convection: air temperature, velocity and film heat transfer coefficient. Predictions of radiative exchange were less accurate, this was attributed to: (i) the simulation neglecting conduction through the heater section walls, (ii) an inaccurate estimate of the overall heat transfer through the oven walls and (iii) a reliance on empirical wall functions to calculate the temperature of the oven walls. Overall, predictions of the primary result from the model, \bar{q} , were close to the accuracy goal of $\pm 30\%$. Predictions from the model can therefore be used in subsequent calculations with some confidence.

7.6.6: Model Uncertainties

Turbulence and radiation models are often sources of uncertainty in CFD simulations. Results from simulations using the $k-\varepsilon$ turbulence model and the Monte-Carlo (MC) radiation model were compared to the results using the SST and discrete transfer models. The Monte-Carlo model was run with 10 million histories, the $k-\varepsilon$ model used the default settings. Other simulation settings were unchanged from the those described in section 7.5. Table 7.5 shows the results of this analysis.

Table 7.5: Comparison of fluxes into the food boundary when changing the turbulence and radiation models.

Turbulence Model	Radiation Model	Convective Flux into the Food (Wm^{-2})		Radiative Flux into the Food (Wm^{-2})		Total Flux into the Food (Wm^{-2})	
		Mean	Standard Deviation	Mean	Standard Deviation	Mean	Standard Deviation
SST	DT	1670	285	392	69.7	2090	320
SST	MC	1680	291	383	94.8	2070	321
$k-\varepsilon$	MC	1230	167	389	95.5	1620	204

Table 7.5 shows that the radiation model had a small effect on the outputs from the simulation. Changing the radiation model to the Monte-Carlo model reduced the radiative flux by 2.3% and total flux by 0.96% compared to the discrete transfer model. This shows that the underprediction of the radiative flux by the model, described in section 7.6.5 is not due to the model choice.

When using the Monte-Carlo model, the standard deviation was increased by 36% and 0.31% for the radiative and overall fluxes, respectively. The increase in standard deviation of the radiative flux was expected, as the randomised starting point and direction of the rays traced by the Monte-Carlo model introduces more variability and noise into the flux calculation compared to other radiation models¹⁷⁰.

Changing the turbulence model from SST to $k-\varepsilon$ had a much larger effect on the flux calculation, reducing the flux by 26.3% and 22.4% for the convective and total fluxes, respectively. This is likely due to the inability of the $k-\varepsilon$ model to simulate flow near walls, and its reliance on empirical wall functions. The simulation generally underpredicted the convective heat flux compared to experiment, and this result shows the $k-\varepsilon$ is likely to underpredict by more and be less accurate in its prediction of heat flux than the SST model¹⁷¹.

7.7: Conclusions

A CFD simulation of the prototype IB oven was created using ANSYS CFX. The goal of the simulation was to predict heat flux into a food target within the cooking chamber. Given the complexity of the simulated geometry an accuracy goal of $\pm 30\%$ was set.

The instability of the flow within the cooking chamber of the oven prevented the simulation from converging to a single steady state solution. Instead, the simulation was run to give a pseudo steady state, in transient mode with constant boundary conditions. A temporal convergence study found that a timestep of 0.3 s was sufficiently low, while the simulation was run for 60 s to capture the entire pseudo steady state and therefore give a meaningful average for the predicted heat flux. A spatial convergence study was also performed and a mesh with 29.4 million elements selected. An inflation layer was added to the base of the oven including the “food” boundary. This was added to keep $y^+ < 2.5$ and increase the accuracy and reliability of heat flux predictions for these boundaries.

To quantify the accuracy of the model predictions, the predictions of heat flux in to a sensor surface at 5 positions around the base of the oven were compared to experimental values. The air velocity at 160 points in the region 20 – 80 mm below one of the impingement jet nozzles

¹⁷⁰ P. Stopford, ‘ANSYS Technical Support’, 2020.

¹⁷¹ Zuckerman and Lior, ‘Jet Impingement Heat Transfer’.

was also measured experimentally and compared to model predictions. The simulation accurately predicted air velocity in this region. In the heat flux comparison, the air temperature at the 5 sensor positions was also accurately predicted by the simulation. This indicated that the simulation was able to accurately simulate the flow of air through the oven. The heat fluxes were less accurately predicted. Heat flux was underpredicted by the simulation, with a mean error of --30%. Convective heat flux was underpredicted by an average of 22% and radiative flux was underpredicted by 53%. The error in the radiative flux was ascribed to the simulation not accounting for conduction through the walls of the heater sections and inaccurate predictions of the temperature of the interior wall of the cooking chamber, due to the use of empirical wall functions to calculate heat flux on these boundaries, and uncertainties in the overall heat transfer coefficient across the oven walls.

The mean absolute error was similar to the accuracy goal, and the reasons for the larger error in the radiative flux were understood. The simulation was therefore used in a subsequent design study.

8: 45 cm Oven Design Study

8.1: Introduction

The CFD simulation described and validated in chapter 7 was used to predict the performance and behaviour of a COI oven adapted to fit in a 45 cm high kitchen unit. The maximum dimensions of an appliance that can fit in this unit are 450 mm in height, 600 mm in width and 550 mm in depth. The typical use of this size unit is for a second, smaller fan oven or for a microwave oven. The cooking chamber had, therefore, to be reduced in height and volume. The motivation for using the COI design in this sized unit were:

- i) The COI design of oven can cook only a single layer of a single type of food while using all three heat transfer modes. Therefore, reducing the volume of the cooking chamber will not reduce the amount of food that can be cooked at a time.
- ii) Reducing the height of the cooking chamber reduces the area of the walls of the cooking chamber. Assuming the overall heat transfer coefficient between the cooking chamber and surroundings remains the same, this will reduce the energy lost through the walls of the oven and increase the thermal efficiency of the oven.
- iii) Reducing the size of the oven will reduce the mass of the oven, reducing the energy wasted heating the walls and insulation of the oven during a cooking cycle and therefore increasing thermal efficiency.
- iv) Reducing the height of the oven will reduce the distance between the impingement nozzles and the food surface. This will increase the velocity of the air impinging on the food and increase the film heat transfer coefficient, h . The lumped property model (chapter 6) predicted an increase in h improved the thermal efficiency and reduced cooking time.

The cost of constructing a physical prototype of a 45cm high design would be significant. Building the heater systems and infra-red lamp assembly within the cooking chamber, as in prototypes I-III, would result in an unacceptably small cooking volume. Similarly, the induction heating system would require re-designing to reduce its vertical footprint. The modifications required to build a 45 cm COI oven would therefore be more complex, expensive and time

consuming than for the 60 cm prototypes. Investigating potential designs *in silico* was therefore prudent.

Four design cases were investigated. Meshing rules, physics and solver settings were the same across all 4 cases.

Case 0: The base case, described in chapter 7 and compared to experimental results from the prototype IB oven.

Case 1: The first design considered for the 45 cm unit, with the geometry kept as similar to case 0 as possible and changing only the height of the cooking chamber.

Case 2: A second design for an oven in a 45 cm unit, with 4 rows of 15 jets. The heater units were identical to Cases 0 and 1.

Case 3: The final design studied. Case 3 was identical to Case 2 but with 3.5 mm diameter impingement nozzles, rather than 4 mm in previous cases.

The geometries for Cases 1, 2 and 3 are described in section 8.2 while the motivation for the different cases and results from the simulations are discussed in section 8.3.

8.2: Simulation Specifications

Only the geometry was varied between the 4 design cases: all meshing controls, physics and solver settings remained the same, as described in chapter 7. Data extraction and processing also remained the same. In Cases 2 and 3, where the area of the heaters was increased, q_{heater} was reduced by 25%, to 3350 W m^{-2} , such that the total heater power remained the same. The air mass flowrate, \dot{M} , was also constant across the 4 cases.

It was anticipated that the temperature within the oven would vary across the 4 cases, as the heat transfer area to the surroundings varied and the film heat transfer coefficients to the walls and food would also change. It was decided to keep heater power constant despite this as varying the power to give constant operating temperature was difficult and time consuming. As the heat flux through the walls and door of the oven was calculated using empirical wall functions, predictions

of oven temperature are not reliable. Metrics of heat flux that are not functions of the oven temperature were therefore used to compare between cases. These were the coefficients of variation for the total and convective heat fluxes, and the overall heat transfer coefficient, U :

$$U = \frac{\bar{q}_{\text{conv}}}{T_{\text{outlet}} - 100} \quad (8.1)$$

where T_{outlet} is the mass flow averaged temperature of air, in °C, flowing through the outlet boundary.

The pressure drop across the system was also anticipated to vary between cases as the flow path was changed, while the mass flow rate, \dot{M} , was held constant. In reality, \dot{M} would be a function of pressure drop and determined by the characteristics of the circulation fan. However, for simplicity and because the fan specifications in reality may change between cases, this was not considered in the analysis.

8.2.1: Case 1

The geometry used for the simulation was similar to that for the 60 cm oven model (section 7.3). An overview of the geometry is shown in Figure 8.1, Figures 8.2 and 8.3 show greater detail of the heater and cooking chamber sections of the model, respectively. The following changes to the geometry were made:

- i) The complete oven was reduced in height by 150 mm. Rearrangement of the assemblies above and below the simulation geometry meant the expected reduction in volume available for the cooking chamber and heater sections was lower. The height of the “centre of the cooking chamber” volume was reduced by 110 mm: the “base of the cooking chamber” volume was moved upwards by 110 mm such that connectivity was maintained. The “fan outlet” volume was also reduced in height by 110 mm.
- ii) The fan impeller had a reduced radius of 60 mm. This was required to fit in the smaller space available.
- iii) The inlet to the fan and outlet from the simulation was altered to resemble the arrangement used in prototypes II and III more closely. Air exited the cooking

chamber through the rectangular face labelled in Figure 8.3. The pathway from this rectangular face to the impeller was not included in the simulation.

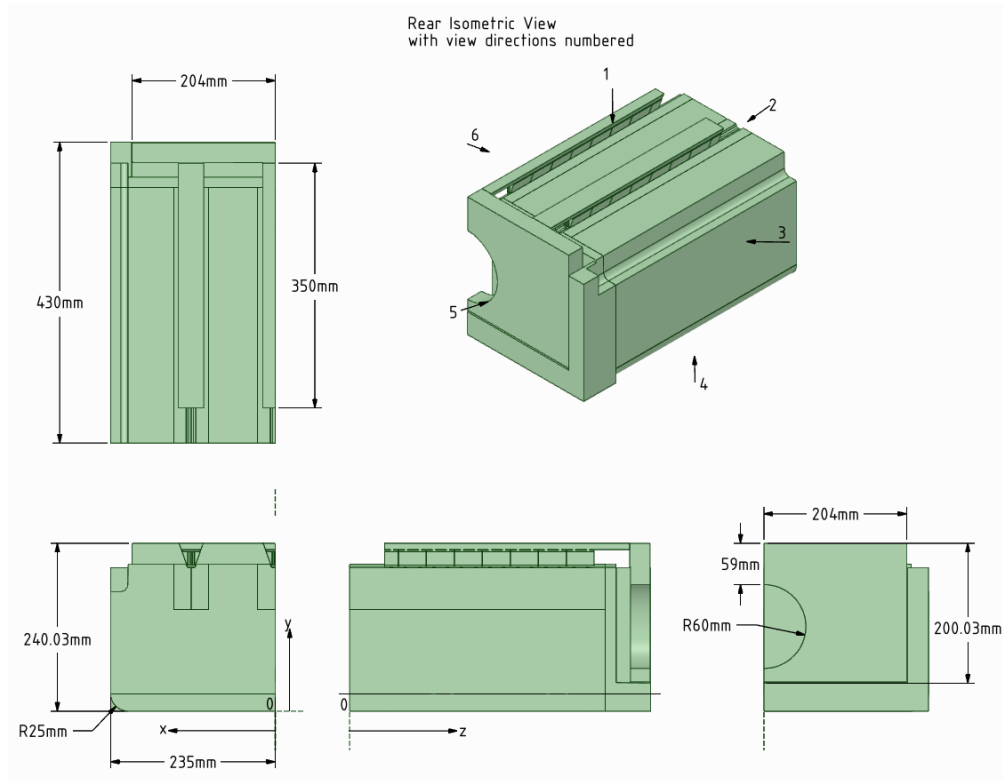


Figure 8.1: Third angle projection showing an overview of the Case 1 simulation geometry with key dimensions given. Isometric view gives numbered view angles that are used in subsequent diagrams. Also shown is the Cartesian coordinate system used in this chapter.

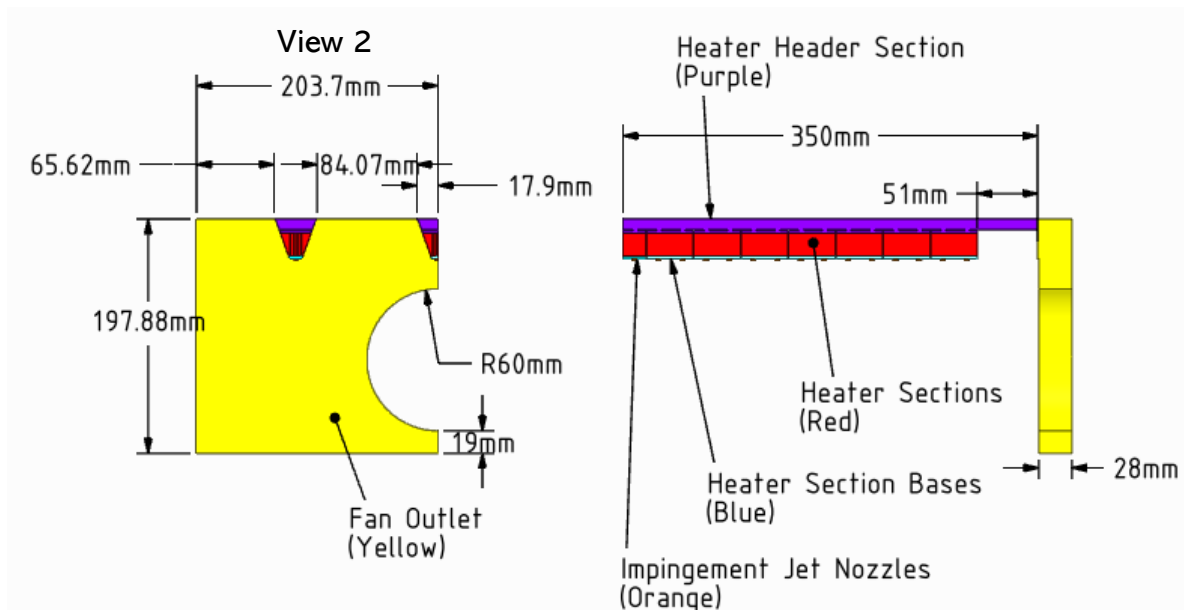


Figure 8.2: Third angle projection of the fluid volume in the Case 1 simulation between the fan outlet and the impingement jets. Detailed views of the heater sections, heater section bases and impingement jet nozzles are shown in Figure 7.3. Different colours indicate where the geometry was split into separate sub-volumes.

8.2.2: Case 2

The geometry was similar to Case 1. The heater section geometry is shown in Figure 8.4 while the cooking chamber geometry is shown in Figure 8.5. As the oven design contained 4 rows of jets, the simulation contained 2 complete rows of jets, rather than a complete row and a row split by the symmetry plane. Apart from being moved in the x direction to give a spacing between the nozzles of approximately 90 mm, the geometry of the heaters and nozzles was identical to previous simulations. The cooking chamber volume was altered to accommodate the additional row of jets. The “volumes beneath the jets” shown in red in Figure 8.4 and the “bodies of influence”, which are not pictured, were moved to lie beneath the new positions of the jet nozzles. The “centre of the cooking chamber”, shown in blue in Figure 8.5, was also altered to accommodate this. The top of this volume was flattened to allow the impingement nozzles to be more easily moved in subsequent simulations if required. As this change in the geometry is above where the jets enter the cooking chamber it was not expected to have a large effect on the flow field within the cooking chamber. All other bodies retained the same dimensions as their counterparts in Case 1.

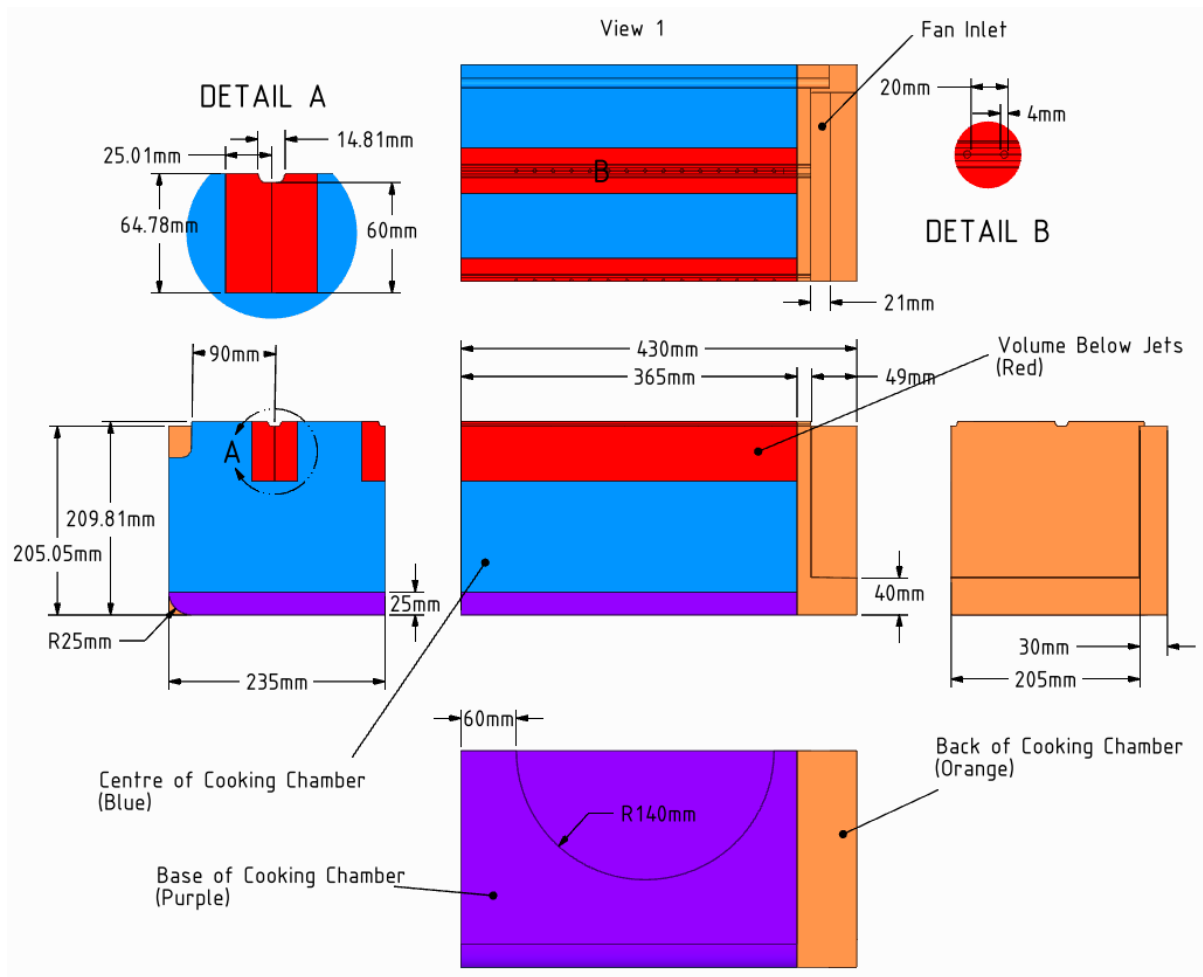


Figure 8.3: Third angle projection of the fluid volume in the Case 1 simulation between the impingement jets and fan inlet, showing detail and key dimensions. Different colours indicate where the geometry was split into separate sub-volumes.

8.2.3: Case 3

The geometry of Case 3 was identical to Case 2 except the diameter of the nozzles was reduced from 4 mm to 3.5 mm. The position of the nozzles remained the same. Mesh and simulation settings also remained identical.

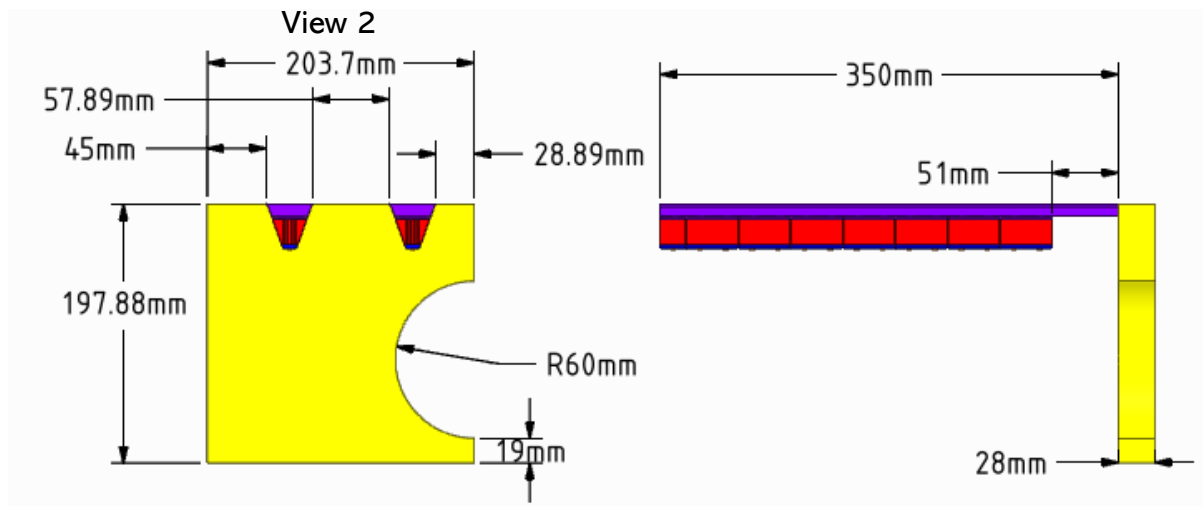


Figure 8.4: Third angle projection of the fluid volume between the fan outlet and the impingement jets in the Case 2 simulation. Detail views of the heater sections, heater section bases and impingement jet nozzles are shown in Figure 7.3. Different colours indicate where the geometry was split into separate sub-volumes, labels for these can be found in Figure 8.2.

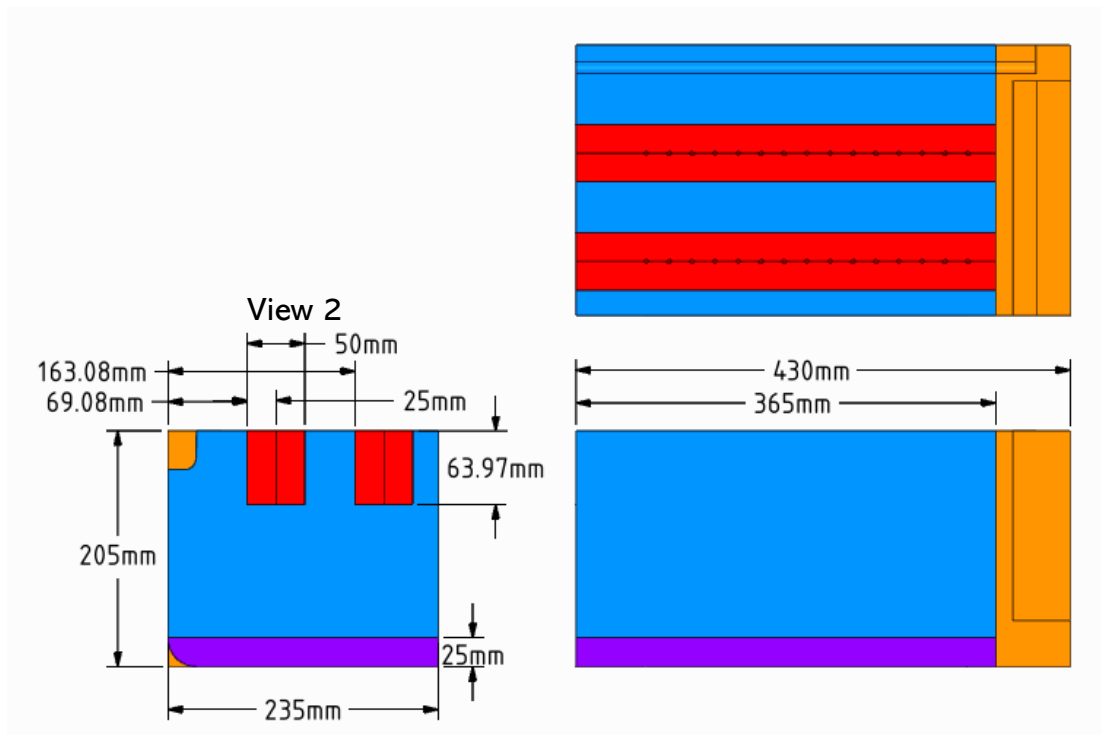


Figure 8.5: Third angle projection of the fluid volume in Case 2 between the impingement jets and fan inlet, showing detail and key dimensions. Different colours indicate where the geometry was split into separate sub-volumes.

8.3: Results and Discussion

A summary of the flux through the food boundary in the four cases is presented in Table 8.1. Contours of the heat flux are displayed in Figure 8.6. Infra-red lamps were not included in the simulations, the radiative fluxes in Table 8.1 are the result of the hot interior walls of the oven radiating heat onto the food boundary.

Table 8.1: Performance indicators for the 4 cases

Quantity	Units	Case 0	Case 1	Case 2	Case 3
Unit height	cm	60	45	45	45
Number of nozzles	-	45	45	60	60
Nozzle diameter	mm	4.0	4.0	4.0	3.5
Mean flux into the food	Wm ⁻²	1830	2330	2300	2330
Standard deviation of flux into the food	Wm ⁻²	350	630	610	600
Coefficient of variation of flux into food	-	0.190	0.272	0.265	0.258
Mean convective flux into the food	Wm ⁻²	1480	1870	1650	1690
Standard deviation of convective flux into the food	Wm ⁻²	330	620	570	590
Coefficient of variation of convective flux into food	-	0.222	0.332	0.345	0.349
Overall heat transfer coefficient	Wm ⁻² K ⁻¹	20.3	19.9	15.9	16.7
Mean radiative flux into the food	Wm ⁻²	350	460	650	640
Mean outlet air temperature	°C	173	194	204	201
Mean inlet pressure	Pa	118	120	68.2	102

As anticipated, the mean heat flux was increased by 26% in Case 1 compared to Case 0, with both convective and radiative flux increasing. Reducing the surface area of the oven increased the predicted outlet air temperature from 173°C to 194°C, although as discussed previously, the exact values of outlet temperature are not considered reliable. The rise in in heat flux was caused by this increased air temperature, as there was a 2% reduction in U compared to Case 0. The similar value of U indicates that the convective flux into the food will be similar between Case 0 and 1 for a given setpoint temperature. The reduced flux through the walls in Case 1 indicates the power required to maintain this setpoint will be lower. The simulation therefore predicted that the Case 1 design would cook food at a similar speed to Case 0 but with a reduced power draw.

The cost of the increased thermal efficiency is a reduction in the evenness of flux into the food, demonstrated by the 80% increase in standard deviation of the flux into the food and the 78%

increase in the coefficient of variation. This is also illustrated in Figure 8.6, which shows a region of high flux towards the right edge of the food surface in Case 1 that is not present in Case 0. This region is below the outer row of jets and was the result of the reduced distance between the food and the jet nozzles.

This unevenness may also be compounded when cooking irregularly shaped food pieces. In the 60 cm oven cooking a chicken with height 100 mm, the top of the chicken is 32% closer to the impingement nozzles than base. In the 45 cm oven the top of chicken would be 49% closer, giving a relatively higher air temperature and velocity, and therefore heat flux compared to parts positioned close to the base of the cooking chamber (e.g. the legs).

The prototype IB oven simulated in the 60 cm simulation cooked food to an acceptable standard (chapter 9). The effect of the predicted reduction in evenness of cooking in Case 1 on cooking is hard to quantify without food trials in a prototype, but it may cause a reduction in food quality by burning some areas before others are completely cooked.

The pressure drop between the fan outlet and inlet was similar in Case 0 and Case 1, this is as expected as the flow through the heaters and nozzles remained the same, and these are the regions with the greatest pressure drop.

Case 2 was an attempt to improve the evenness of cooking by adding an additional row of jets to the oven. It was hypothesised that the additional row of jets would provide more even heat flux for two reasons:

- i) Decreasing the lateral separation between the rows of jets would reduce stagnant zones between the rows of jets.
- ii) Increasing the number of impingement nozzles and flow area reduced the velocity of the air jets, thereby reducing the peak fluxes. The reduced velocity was acceptable in the 45 cm oven due to the reduced distance between the nozzles and the food. If the model predictions showed a significant reduction in flux compared to Case 1, the diameter of the nozzles could be reduced to give the same flow area as in Cases 0 and 1.

Table 8.1 shows that the additional row of jets had a small effect on the evenness of cooking, with the coefficient of variation reduced by only 2.6% in Case 2 compared to Case 1. The predicted total flux remained the same between Case 1 and Case 2, despite U reducing by 20% to $15.9 \text{ Wm}^{-2}\text{K}^{-1}$. This reduction in U was attributed to the increased area of the nozzles reducing the discharge velocity of the jets. The reduced velocity also reduced the heat transfer to the walls and door, increasing the outlet temperature from 194 to 204°C. This increased the temperature difference for convective heat transfer and also increased the temperature of the oven walls and therefore the radiative flux, which increased by 41% from Case 1. This increase in radiative flux does not compensate for the reduction in U , as it will only occur once the oven reaches steady state and the walls are hot, whereas the reduction in U will reduce heat flux into the food over the entire cooking cycle. The pressure drop across the simulation decreased by 43% compared to Case 1 due to the increased flow area through the impingement nozzles and heaters.

Case 2 was an unsatisfactory design, as evenness of cooking was not sufficiently improved from Case 1, while U and therefore thermal efficiency decreased significantly.

The final case investigated was Case 3. This was identical to Case 2 but with the diameter of the impingement jet nozzles reduced from 4 mm to 3.5 mm. This was to give the same flow area from the nozzles as in the 45 jet cases. It was hypothesised this would increase U by increasing the velocity of the impingement jets.

Case 3 improved efficiency and evenness by a small amount compared to Case 2, with the coefficient of variation reduced by 3% and U increased by 5%. Pressure drop also increased by 50% from Case 2, although it was still lower than in Cases 0 and 1. Despite the nozzle area being the same as Cases 0 and 1 there was a larger flow area through the heater section in Case 3 and therefore a lower pressure drop in this region. Despite the improvements, Case 3 was still unsatisfactory for two reasons: (i) the coefficient of variation in the heat flux was still 57% higher than in the 60 cm design indicating uneven cooking. (ii) U was 18% lower than in the 60 cm design, indicating the oven would require higher air temperatures to achieve the same heat flux, increasing heat up time and therefore increasing cooking time and energy consumption. The lower value of U in Cases 2 and 3 compared to Case 1 was ascribed to the position of the outer rows of impingement jets. These were too close to the walls of the oven and were not positioned above the food boundary, meaning the air from them did not directly impinge on the food. In Cases 0 and 1 the jet nozzles were positioned above the food target, giving a higher value of U .

Figure 8.6 illustrates this, for Case 3 there is a region of high heat flux close to the outer edge of the food surface, due to the wider positioning of the jet nozzles.

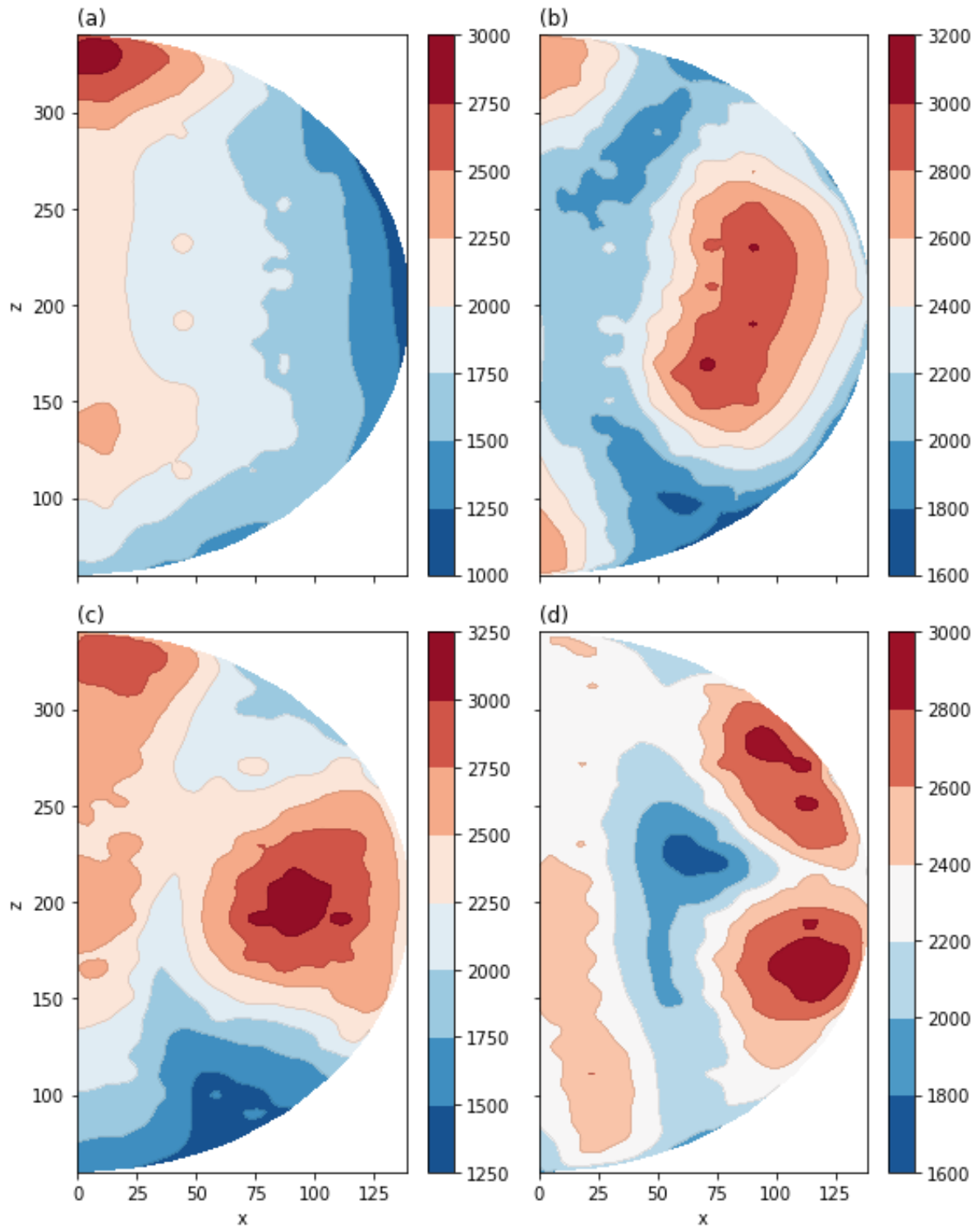


Figure 8.6: Contours of simulation predictions of q ($\text{Wm}^{-2}\text{K}^{-1}$) in x and z , (a) Case 0, (b) Case 1, (c) Case 2, (d) Case 3.

8.3.1: Conclusions

A short design study was performed to investigate the scope of applying the COI design to a 45 cm oven unit. Three design cases were considered; one with a plenum and heater design unchanged from the 60 cm model described in section 7.3, and two cases with 60 impingement jets in 4 rows of 15. One of these cases had 4 mm diameter impingement nozzles, which gave a 33% higher flow area for the impingement jets compared to the 45 nozzles cases. The second had 3.5 mm diameter jets to give the same flow area as the 45 nozzle cases.

The 45 cm cases gave a higher heat fluxes to the food surface for the same air heater power than the 60 cm design, due to the reduced surface area of the oven reducing heat lost to the surroundings and increasing the temperature within the oven. This means the 45 cm ovens were predicted to use less power for a given heat flux into the food. The overall heat transfer coefficient between the oven air and the food was reduced, however, meaning the 45 cm ovens will require a higher set point temperature to achieve the same heat flux. This may increase the time and energy required for shorter cooking events that start from a cold oven.

The evenness of cooking was reduced in all the 45 cm designs. The 60 impingement nozzle cases did increase evenness compared to the 45 nozzle case, but not to the same level as the 60 cm cases. The 60 nozzle cases also reduced U and therefore increased energy consumption and cooking time. This was attributed to the rows of impingement nozzles being too far from the symmetry plane of the oven.

A satisfactory design of a 45 cm oven was not identified from the 3 cases considered here. It is recommended that further cases are considered before a prototype is constructed. There are two avenues of design that could be pursued:

- i) Repositioning the rows of jets in the 60-jet cases so that they are closer to the symmetry plane. This would be relatively simple to model. The disadvantage of this design is that it requires an additional heater section and therefore would be more expensive.
- ii) Modifying the nozzles of the 45-jet design in such a way that the jets are angled away from vertical. Each row of 15 nozzles would be made up from 5 sets of 3. Each set of three would include a vertical nozzle, a nozzle angled 15° to the left and a final

nozzle angled 15° to the right. Figure 8.7(a) shows how this arrangement would lead to a more even distribution of heated air onto the food surface. This design would be more difficult to model and would require removal of the symmetry plane boundary, but would have reduced manufacturing cost compared to the 60-nozzle case, using only three heater modules. Swaging of the nozzles is a simple sheet metal operation that can be achieved with a press.

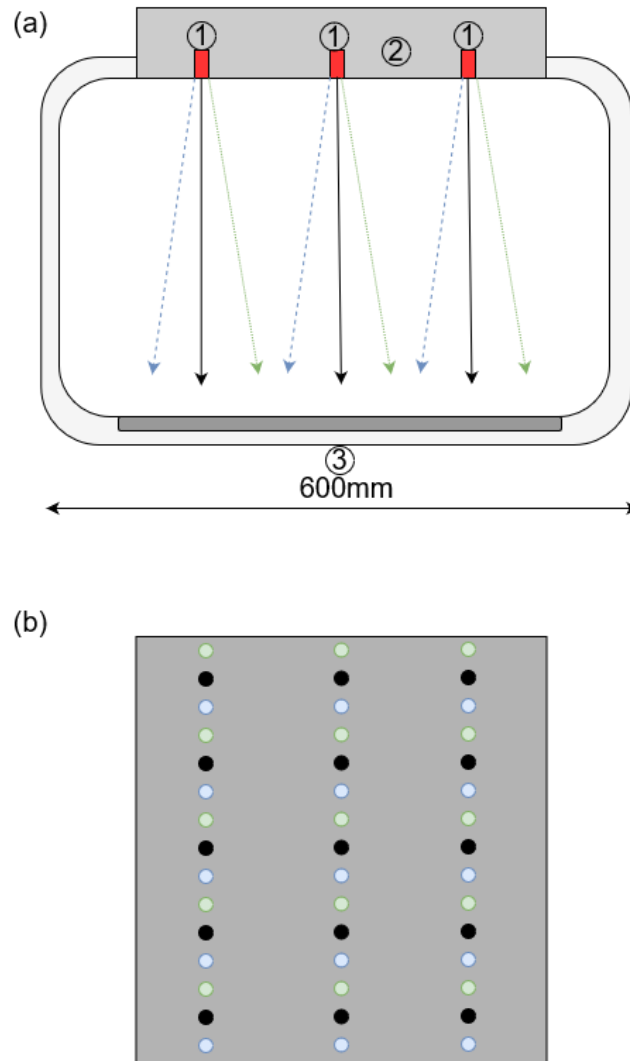


Figure 8.7: Illustration of angled nozzle design. (a) Front view, (b) view of the base of the heater section. 1 – heater units, 2 – heater box, 3 – food. Solid black arrow and circle indicates vertically oriented jet and nozzle. Dotted green and dashed blue lines indicate angled jets and nozzles.

9: Comparative Food Trials

9.1: Introduction

Four food types were cooked in the prototype III oven and a standard domestic fan oven (Model number: BXIM25300XP, Arcelik, Istanbul, TK). Experiments took place at HBE, in Waterbeach, UK. The total power consumption and total cooking time in each oven was recorded and compared. Photographs of the cooked foods were taken to compare the surface colour between ovens and the food piece was weighed before and after to measure moisture loss.

The aim of the trials was to confirm the ability of the COI design to cook food and quantify its ability to save time and energy in comparison to a traditional design while achieving a comparable cooked product. The food science of the cooking processes was not considered and due to the speed of development the optimal cooking parameters for both the COI and traditional design were not necessarily used. Packet instructions were followed when using the traditional oven and some preliminary optimisation of heating modes and sequencing was undertaken with the COI oven.

The four food types considered and their approximate thermal properties are given in Table 9.1. Together these foods span a large range of oven cooked food types. Roast chicken is comparable to other roast meat joints. Ready-made pizza is similar to other low Biot number carbohydrates and ready meals, such as oven chips, veggie burgers or fish cakes. Lasagne is a relatively high Biot number meal, similar to pasta bakes, casseroles, pies and ready meals. The herb bread recipe that was baked is similar to other savoury or sweet loaves.

Table 9.1: Foods cooked in the comparative food trials and their approximate thermal properties, Bi is calculated for $h = 35 \text{ Wm}^{-2}\text{K}^{-1}$, the heat transfer coefficient measured in the centre of the prototype IB oven. The approximate surface area to volume ratio is represented by SA/V .

Food	Mass (g)	C_p (J kg ⁻¹ K ⁻¹)	Thermal Mass (kJ K ⁻¹)	k (Wm ⁻¹ K ⁻¹)	SA/V (m ⁻¹)	Bi
Bread	830	2200	1.83	0.25	25	5.6
Chicken	1320	3570	4.71	0.41	30	2.8
Lasagne	1440	3500	5.04	0.6	40	1.5
Pizza	370	2200	0.814	0.25	200	0.7

9.2: Procedure

9.2.1: Roast Chicken

The 1.3 kg chickens were cooked to a core temperature of 74°C, measured using the datalogger described in section 5.1. This is the USDA recommendation for the temperature of cooked chicken. The traditional oven was preheated to a setpoint of 180°C, after which the chicken was placed on the middle shelf and left until the core temperature reached the target. The oven was run with the circulation fan on. The chicken was cooked in a stainless-steel plated aluminium pan, 2 mm thick and 350 mm in diameter, with a rim 30 mm in height.

The instruction set followed by the COI oven is presented in Table 9.2. The application of high duty cycle infra-red at the start and end of the cooking cycle was required to generate browning and crisping on the top surface of the chicken. The hot plate power was set to the highest power that could be applied without burning the base of the chicken. The chicken was cooked in the same pan used in the traditional oven tests. The chicken and pan were placed on the induction heater before the sequence in Table 9.2 was started.

Table 9.2: COI instruction set used for roast chicken

Step number	Duration (min)	End time (min)	Jet temperature setpoint (°C)	Infra-red duty cycle (%)	Hot plate duty cycle (%)
1	3	3	-	100	100
2	3	6	-	100	60
3	22	28	180	-	50
4	7	35	-	100	50

9.2.2: Bread

The Miele recipe for “Herb Bread” in Table 9.3 was followed. All the ingredients were added to a Kenwood A701 mixer and kneaded with the bread hook attachment for 5 minutes. Sufficient dough was made for two loaves. The dough was divided into two equal masses and shaped into loaves. These were proved at 40°C for 45 minutes, by which time the height of the loaves had doubled. The top of the bread was scored in a criss-cross pattern. The loaves were then baked simultaneously in the traditional and COI ovens. Both loaves were baked on the same type of stainless-steel pan used to roast the chicken. The end point was when the core temperature of the loaf reached 93°C. This was measured using a glass fibre insulated thermocouple and the datalogger described in section 5.1. The thermocouple was inserted into the centre of the bread approximately halfway into the cooking process when the crust had formed, in order that the probe would not hinder the rise of the bread and also to ensure that the probe was close to the centre of the finished loaf. The temperature profile was therefore only captured for the second half of the bake.

The traditional oven was preheated for 10 minutes before the end of the proofing stage so that preheating was complete when the bread was ready to begin baking. The setpoint was 180°C with the fan on. Table 9.4 lists the COI instruction set. The plate power was reduced compared to the roasting of chicken to prevent burning. The infra-red in the first cooking step was intended to increase the “oven bounce”, the infra-red at the end of the cooking cycle was to promote crust formation and browning.

Table 9.3: Ingredients list for the bread recipe, quantities for one loaf.

Ingredient	Amount
Yeast (Allinson’s Instant Dried Yeast)	21 g
Lukewarm water	300 g
Strong White Flour (Allinson’s Very Strong Bread Flour)	500 g
Salt (Tesco Value Table Salt)	1 tsp
Chopped Parsley	1 tbsp
Chopped Dill	1 tbsp
Chopped Chives	1 tbsp

Table 9.4: COI instruction set used for bread baking

Step number	Duration (min)	End Time (min)	Jet Temperature Setpoint (°C)	Infra-Red duty cycle (%)	Hot plate duty cycle (%)
1	3	3	-	100	100
2	17	20	200	-	40
3	5	25	-	100	40
4	5	30	-	-	-

9.2.3: Pizza

Ready-made pizzas from a supermarket (Sainsbury's Basics margherita pizza) were used. The packet instructions were followed to cook the pizzas in the traditional oven, which specified cooking the pizza for 15 minutes in an oven preheated to 190°C with the fan on. Core temperature could not be used due to the slender shape of the pizza: instead, the COI instruction set (Table 9.5) aimed to replicate the surface properties of pizza cooked in the traditional oven, namely the browning and crisping achieved on the top and bottom surfaces of the pizza. It was found that using infra-red heating at the start of the cooking cycle caused the cheese to split rather than melt. The air jets were therefore used to melt the cheese before the infra-red lamps were used to accelerate browning of the cheese and crust. The plate power setting was higher than other foods due to the short cooking time and need to brown and crisp the base.

Table 9.5: COI instruction set used for pizza baking

Step number	Duration (min)	End time (min)	Jet temperature setpoint (°C)	Infra-red duty cycle (%)	Hot plate duty cycle (%)
1	5	5	250	-	100
2	3	8	-	100	60

9.2.4: Lasagne

The ingredients and amounts for the lasagne recipe are given in Table 9.6. The meat sauce and bechamel were mixed until homogenous, after which 200 g of the combined sauce was added to

the base of the cooking utensil and covered with lasagne sheets. The rest of the lasagne was then assembled in the form of 5 repeated layers, each consisting of 200 g of combined sauce, 15 g of grated parmesan and a layer of pasta sheet. The curls of butter were placed on the top of the final layer. The lasagne was cooked in a rectangular steel pan of thickness 1 mm, and dimensions of 200×150×80 mm.

Table 9.6: Lasagne recipe

Ingredient	Amount
Fresh ready-made lasagne sheets (Rana sfogliavelo)	150 g
Ready-made Bechamel sauce (Parmalat Chef)	425 g
Ready made meat sauce (Barilla Ragu alla Bolognese)	800 g
Flaked Parmesan Cheese	75 g
Butter	5 g

The finish point of the cook was when the core temperature of the lasagne reached 70°C. The lasagne in the traditional oven was cooked in an oven preheated to 180°C with the fan on, as specified in the recipe. The instruction set followed by the COI oven is given in Table 9.7. The pan temperature was not recorded for this trial. This was due to the convex base of the cookware being unable to contact the thermocouple pin.

Table 9.7: COI instruction set used for cooking lasagne

Step number	Duration (min)	End time (min)	Jet temperature setpoint (°C)	Infra-red duty cycle (%)	Hot plate duty cycle (%)
1	3	3	250	-	100
2	3	6	250	-	50
3	4	10	-	100	50
4	5	15	-	-	50

9.3: Results and Discussion

Table 9.8 shows the power consumption and cooking times for the four food types as well as the savings in both resources with the COI oven. Temperature and power profiles are plotted in Figures 8.2, 8.4, 8.6 and 8.8 for chicken, bread, pizza and lasagne, respectively. Photographs of

the cooked food pieces are shown in Figures 8.3, 8.5 , 8.7 and 8.9 for chicken, bread, pizza and lasagne respectively.

In the food trials the COI oven was able to reduce the cooking time and power consumption for all 4 food types. The COI oven was more effective at reducing cooking time than power consumption; time was reduced on average by 57.8%, while the average reduction in power consumption was 21.3%. This is expected as cooking requires a set amount of thermal energy to be transferred to the food piece, the saving is achieved by reducing the amount of thermal energy used elsewhere. Figure 9.1 plots time and power saving against the approximate thermal mass and Biot number of the food. The plot shows that substantial time and power savings are possible across the range of thermal masses tested. The cooking of bread gave the lowest power and time savings. This was attributed to its higher Biot number, as foods with larger and smaller thermal masses were able to be cooked more quickly and efficiently. The higher Biot number means that the internal heat transfer within the food limits the rate at which energy can be transferred into the centre of the food, and reduces the effect of the higher heat transfer achieved at the food surface in the COI oven.

Table 9.8: Comparative food trials – food metrics

Food	Mass Loss (g)		Cooking Time (min)			Power Consumption (kWhr)		
	Traditional	COI	Traditional	COI	Saving (%)	Traditional	COI	Saving (%)
Chicken	155	92	84.3	33.0	-61	1.04	0.817	-21
Bread	70	53	44.5	29.8	-33	0.669	0.613	-8.4
Pizza	10	17	24.8	8.1	-67	0.47	0.373	-21
Lasagne	102	128	47.0	14.2	-70	0.758	0.495	-35

Table 9.9 compares the predicted cooking times and the power consumption from the lumped property model (chapter 6) and the results from the food trials. The lumped parameter model accurately predicted the cooking time for the two food types considered, chicken and pizza, but underpredicted the power consumption by approximately 20% in both cases. The model therefore accurately predicted the rate at which thermal energy could be transferred to the food, but underpredicted the energy consumed during the process. The likely source of error is the difference in the oven operation in the model and in the food trial. In the experiments the infra-red lamps were used to increase the surface browning of the food to make it comparable with

the food produced by the traditional oven. In the model, only the air heaters and base heater were used. The infra-red lamps draw a large amount of power, as can be seen in the power profiles in Figures 9.2(f) and 9.6(f). This power is not accounted for in the model and led to an underprediction of power consumption.

Table 9.9: Comparison of lumped property model predictions to experimental results for cooking time and power consumption

Food	Cooking Time (min)			Power Consumption (kWhr)		
	Model Prediction	Experimental Result	Error (%)	Model Prediction	Experimental Result	Error (%)
Chicken	38.4	33	+16	0.62	0.82	-24.1
Pizza	8.40	8.1	+4.0	0.29	0.37	-21.7

The aim of the COI instruction sets shown in Tables 9.2, 9.4, 9.5 and 9.7 was to produce food similar to that cooked in a traditional oven using a standard recipe. Where differences existed, they were to increase food quality rather than vice versa. Figure 9.3 compares the chicken roasted in the COI and traditional ovens. The COI oven was able to generate a larger degree of surface browning than the traditional oven. The degree of browning is noticeably higher on the base of the chicken. The direct heating of the cookware by the induction heater meant a higher amount of thermal energy was supplied to the base of the chicken cooked in the COI oven, giving the greater browning and also contributing to the time and power savings, as conductive heat transfer has a higher heat transfer coefficient than convective. The stainless-steel cookware used had a low emissivity which may have contributed to relatively lower amount of browning on the traditional oven as it reduced the ability of the cookware to absorb thermal radiation from the oven walls.

The COI oven cooked chicken also lost 40% less water than the chicken cooked in the traditional oven, indicating the cooked food may be more moist. A study by Rabeler and Feyissa¹⁷² found that the speed at which chicken meat is cooked had a negligible impact on the

¹⁷² Rabeler and Feyissa, 'Modelling the Transport Phenomena and Texture Changes of Chicken Breast Meat during the Roasting in a Convective Oven'.

final texture, indicating that the faster cooking in the COI oven should not negatively impact metrics such as chewiness and gumminess.

Figure 9.5 shows that the bread loaf cooked in the COI oven had a greater degree of browning on its top surface. Table 9.8 reports that the COI oven baked loaf also lost 24% less mass than the loaf baked in the traditional oven. The rise and crumb structure were similar, as shown in Figure 9.5.

The pizzas are compared in Figure 9.7. The cheese on both pizzas was melted and browned to a similar degree. The base of both pizzas was also browned. The base of the pizza cooked in the COI oven showed more browning and less even browning, with the centre of the pizza more browned than the edges. This is due to the energy to the cookware being supplied to the centre, making this part of the pan hotter than the rest. The crust on the top of the pizza was more browned in the traditional oven. Despite these differences, both pizzas were cooked to an acceptable standard, with crisped bases and melted and browned cheese.

Finally, the top surfaces of the lasagnes are shown in Figure 9.9. The aim of the recipes was to heat the core of the lasagne to 70°C and melt the cheese on the top. The COI oven was able to heat the lasagne to the target temperature very quickly using the base heater. However, this meant that the top surface had less time to cook. Although the cheese was melted, it was significantly less brown than the pieces cooked in the traditional oven. Use of the base heater also led to more of the sauce in the lasagne boiling and a 26% greater mass loss.

It is important to note that the results presented here are functions of the recipes used. There is scope to optimise the COI recipes to reduce energy consumption further. In the trials, food was added to the traditional oven immediately after the preheat was complete whereas a consumer may leave the oven for a longer preheat, which would in turn increase the cooking time and power consumption. In the traditional oven the surface browning could be increased by increasing the air temperature setpoint, at the cost of increased power consumption. It should be noted that the aim of the trials was to prepare comparable food products and compare the power and time and requirements, rather than explore the full range of possible cooking methods and recipes.

One should consider the relative complexity of the recipes and user input required for the two ovens. For the traditional oven two inputs and stages are required, namely the setting of the temperature, waiting for the preheat to end, (the timing of which is flexible,) and adding the food to the oven. In the COI oven there is no need to wait for a preheat. However, the set of instructions to be programmed into the oven is more complex, with three different setpoints required for multiple cooking steps.

Setting the base plate power is a balance: too low a set point and the efficiency gains through using the base heater are not realised and the base of the food will not brown. Too high a setpoint will burn the food. For example, the COI cooked chicken in Figure 9.3 is close to being overcooked on the base. Similarly, too little infra-red will result in insufficient browning while too much may burn the food and the high power draw will reduce the overall efficiency of the oven.

To meet the criteria discussed in section 2.2, the COI oven must be as easy, or easier to use than existing designs. To achieve this the COI oven must reduce the consumer input required to one or two variables. This could be achieved by including a comprehensive set of recipes on the device that can be selected by the consumer and automatically executed by the oven control software. An alternative would be to include a “base” recipe that combined the three heat transfer modes in a way that is acceptable for a large range of food types. In this mode the consumer would only need to select the “base” mode and monitor the food until it is judged to be cooked, similar to the cooking process with a traditional oven.

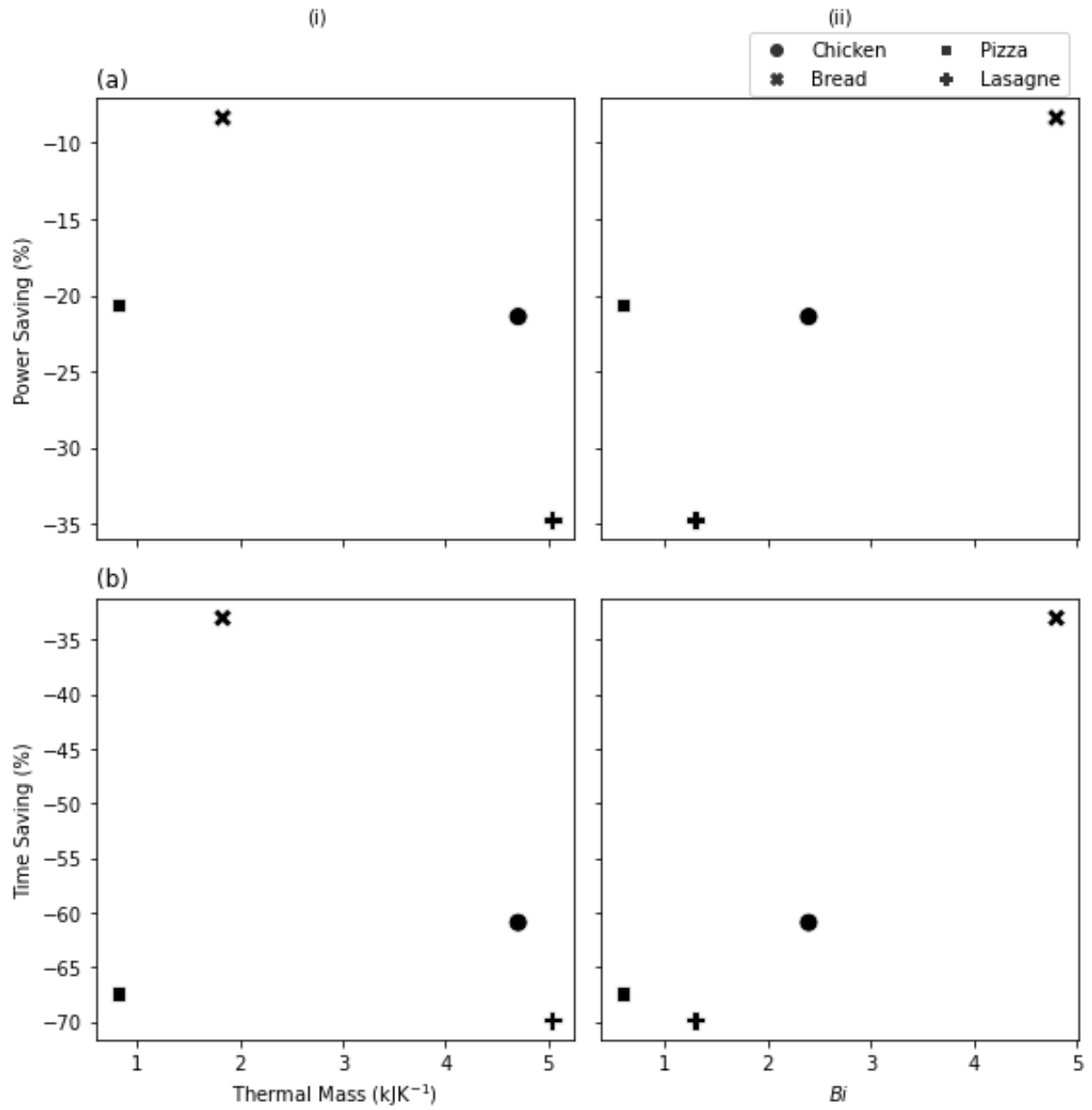


Figure 9.1: Time (a) and power (b) savings in food trails in terms of (i) thermal mass and (ii) Bi . Symbol shape indicates food type.

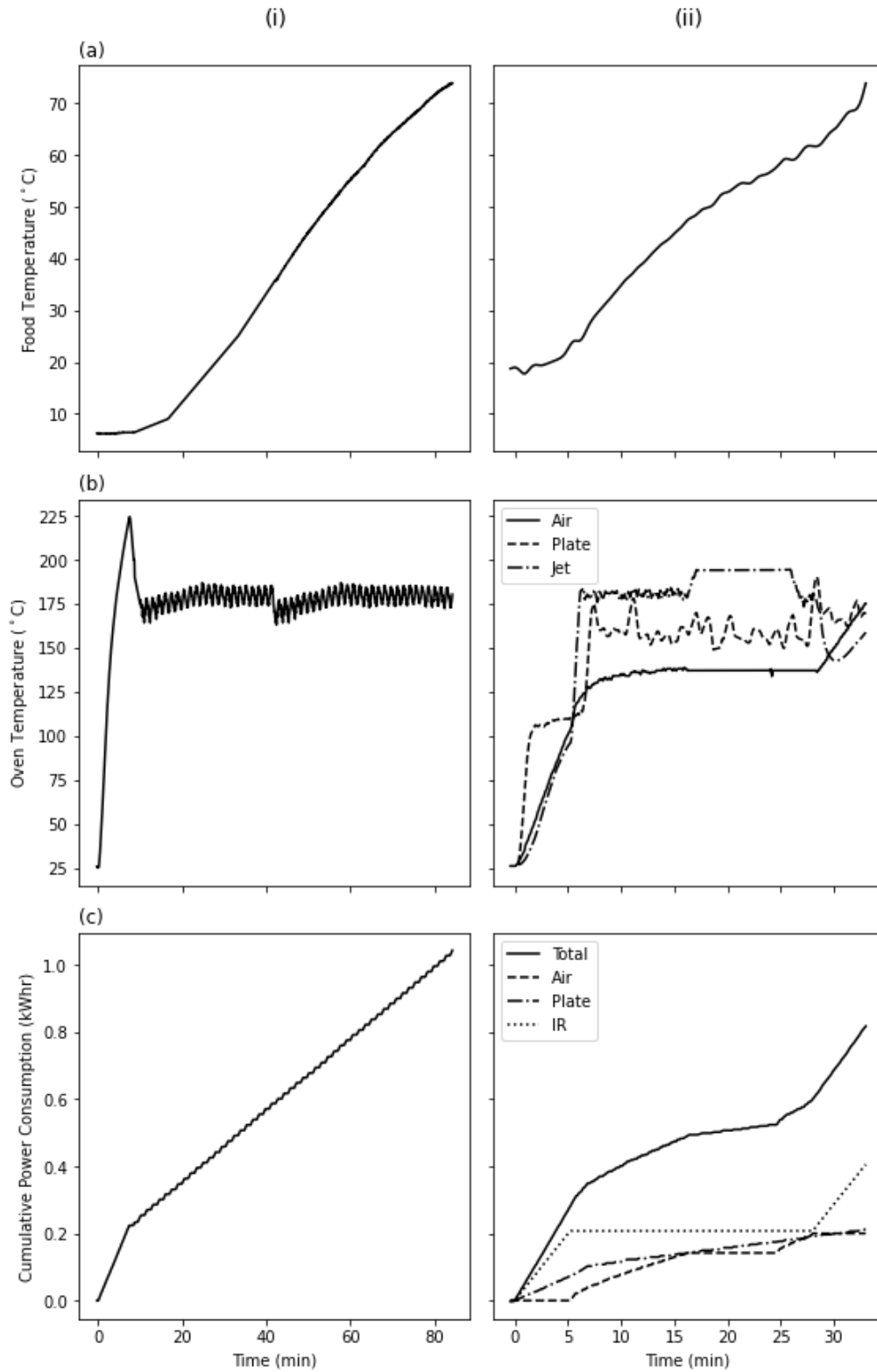


Figure 9.2: Power and temperature profiles for roast chicken food trials. Column (i) shows data for the traditional oven, (ii) shows data for the COI oven. Row (a) food temperature, (b) oven temperatures, (c) power consumption profiles. Note different time scales in columns (i) and (ii).

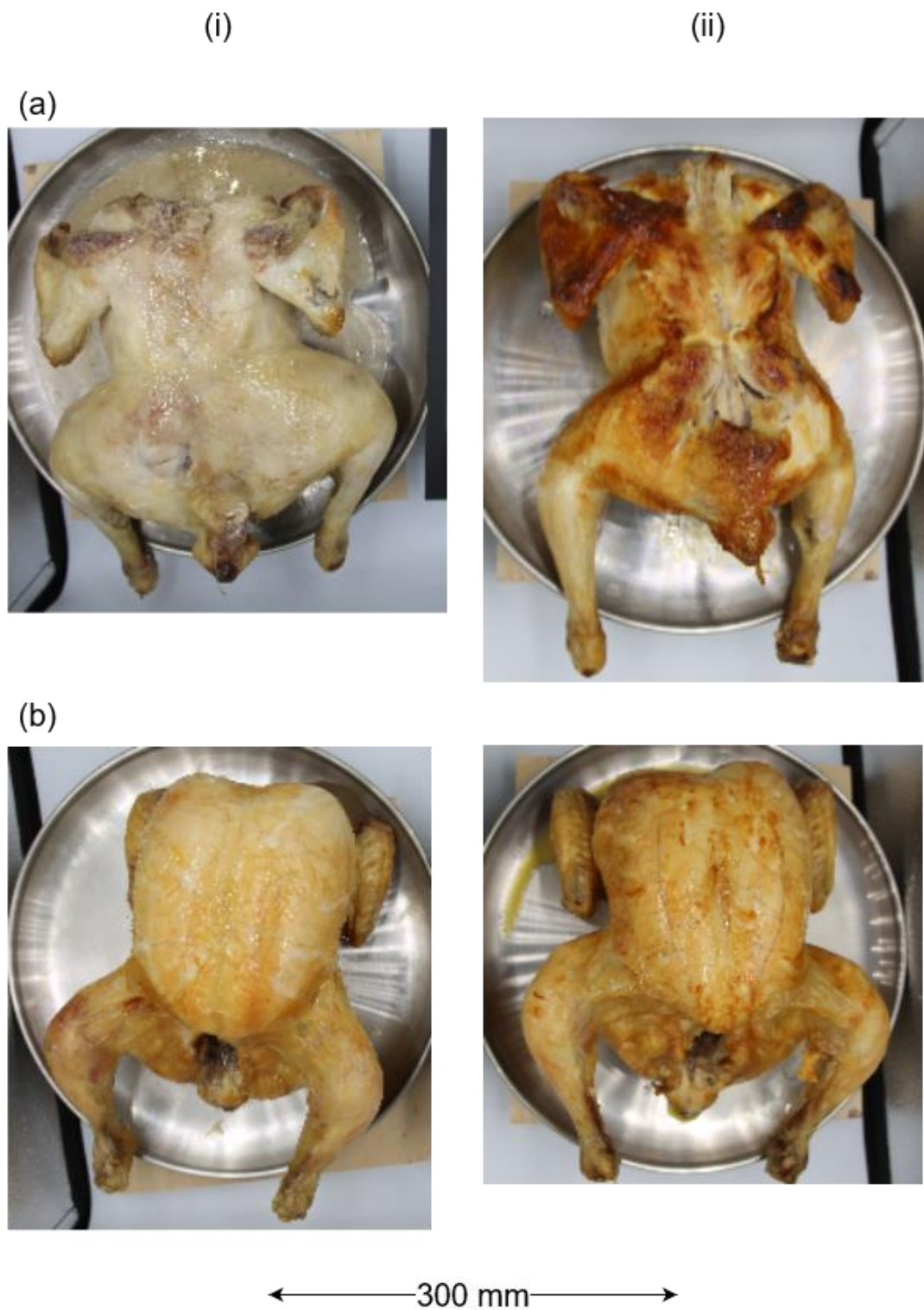


Figure 9.3: Images of roasted chickens. Column (i) shows results from the traditional oven, (ii) shows results from the COI oven. Row (a) bottom of the chicken, (b) top of the chicken.

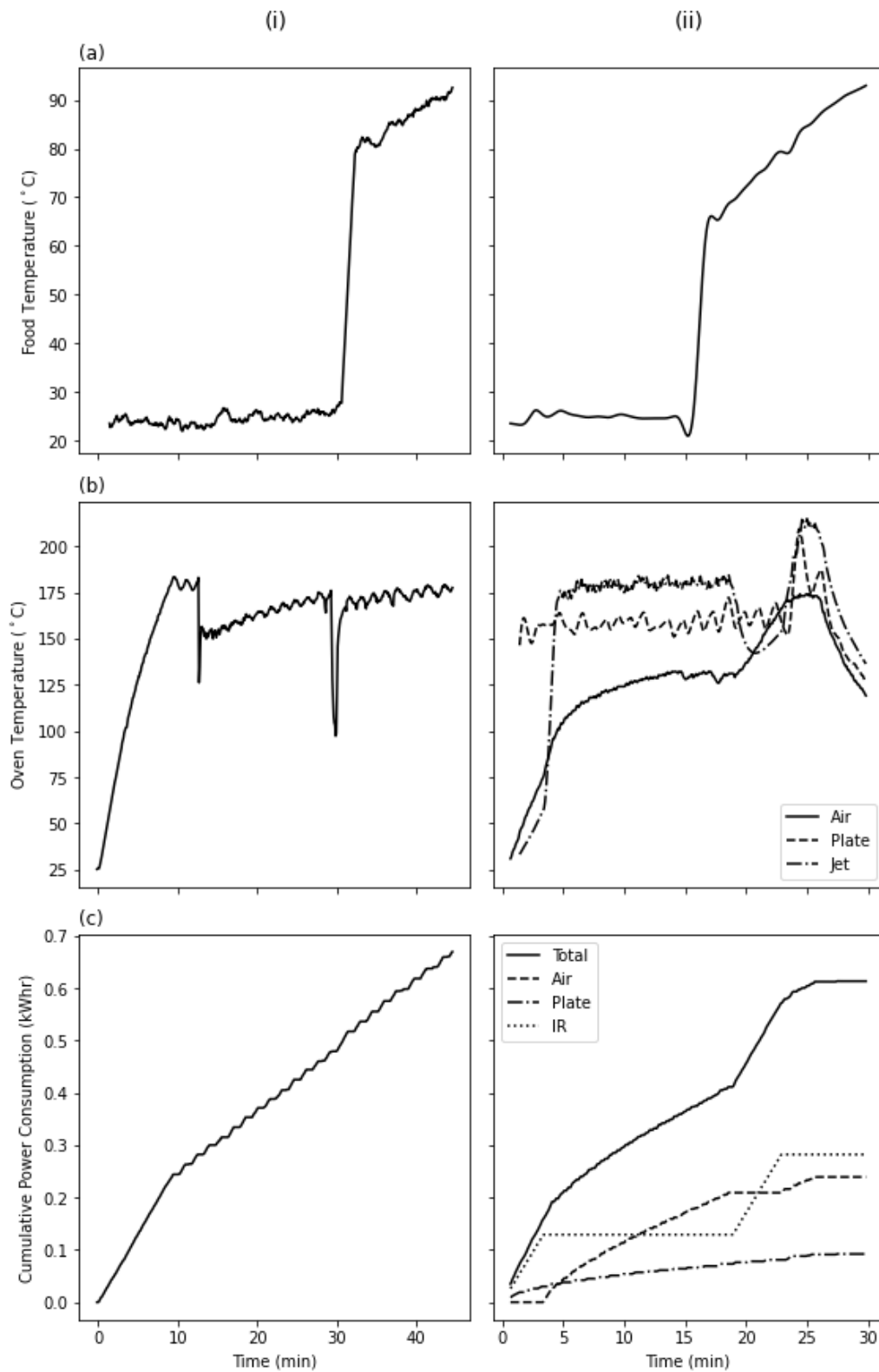


Figure 9.4: Power and temperature profiles for bread food trials. Column (i) shows data for the traditional oven, (ii) shows data for the COI oven. Row (a) food temperature, (b) oven temperatures, (c) power consumption profiles. Note different time scales in columns (i) and (ii).

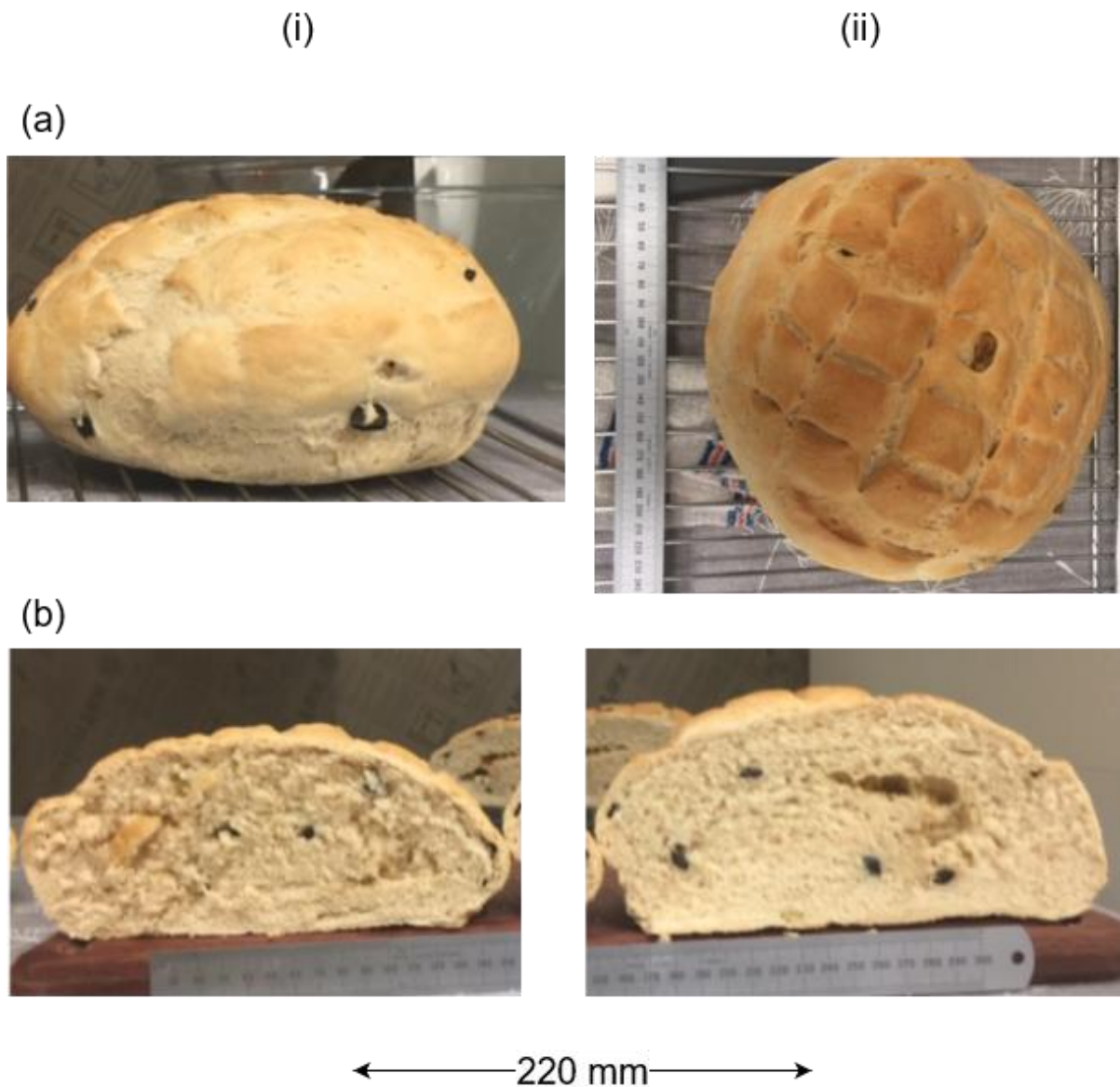


Figure 9.5: Images of baked bread. Column (i) shows results from the traditional oven, (ii) shows results from the COI oven. Row (a) outside of the loaves, (b) internal structure of the loaves, side view.

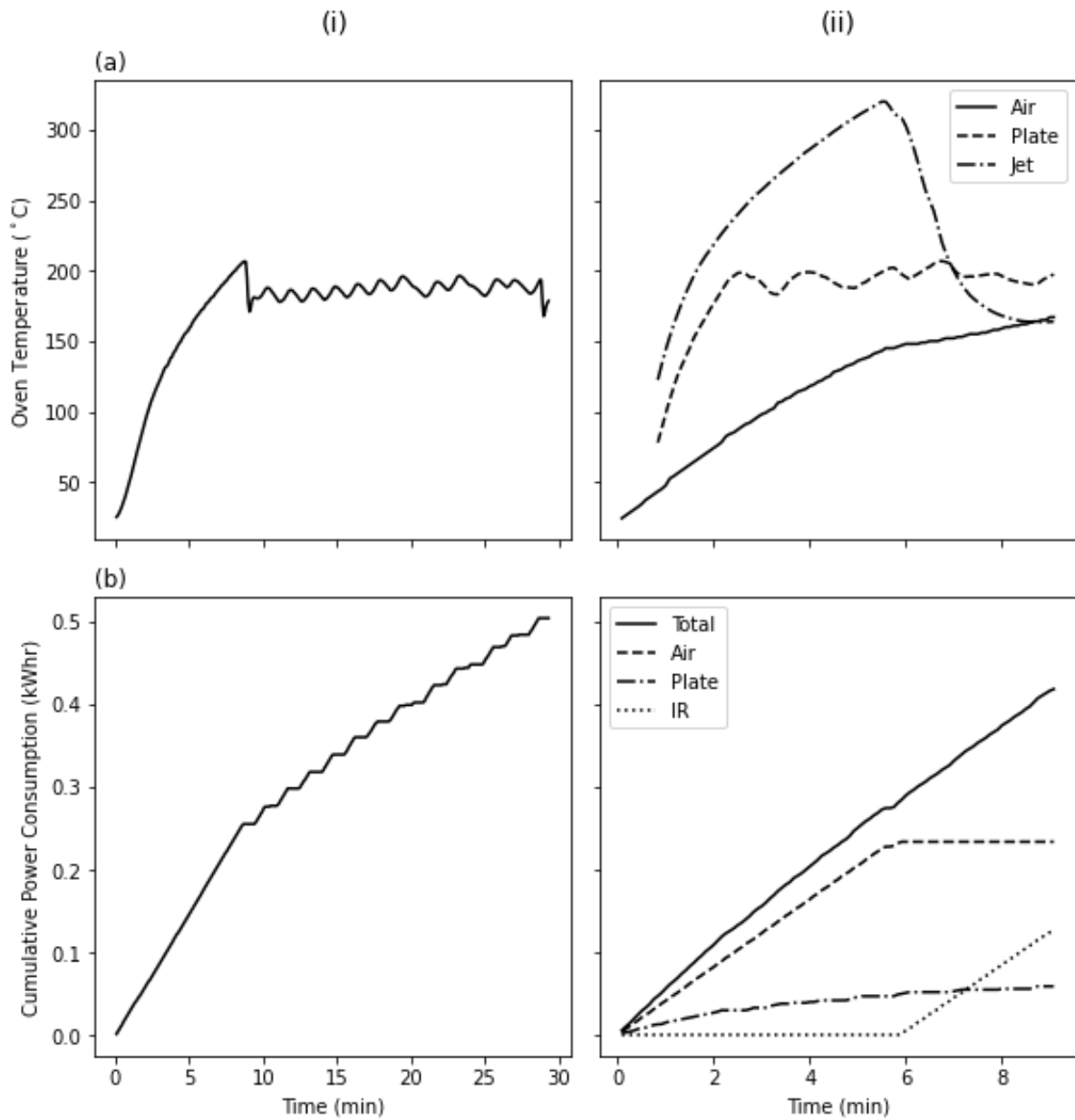


Figure 9.6: Power and temperature profiles for thin pizza food trials. Column (i) shows data for the traditional oven, (ii) shows data for the COI oven. Row (a) oven temperatures, (b) power consumption profiles. Note different time scales in columns (i) and (ii).

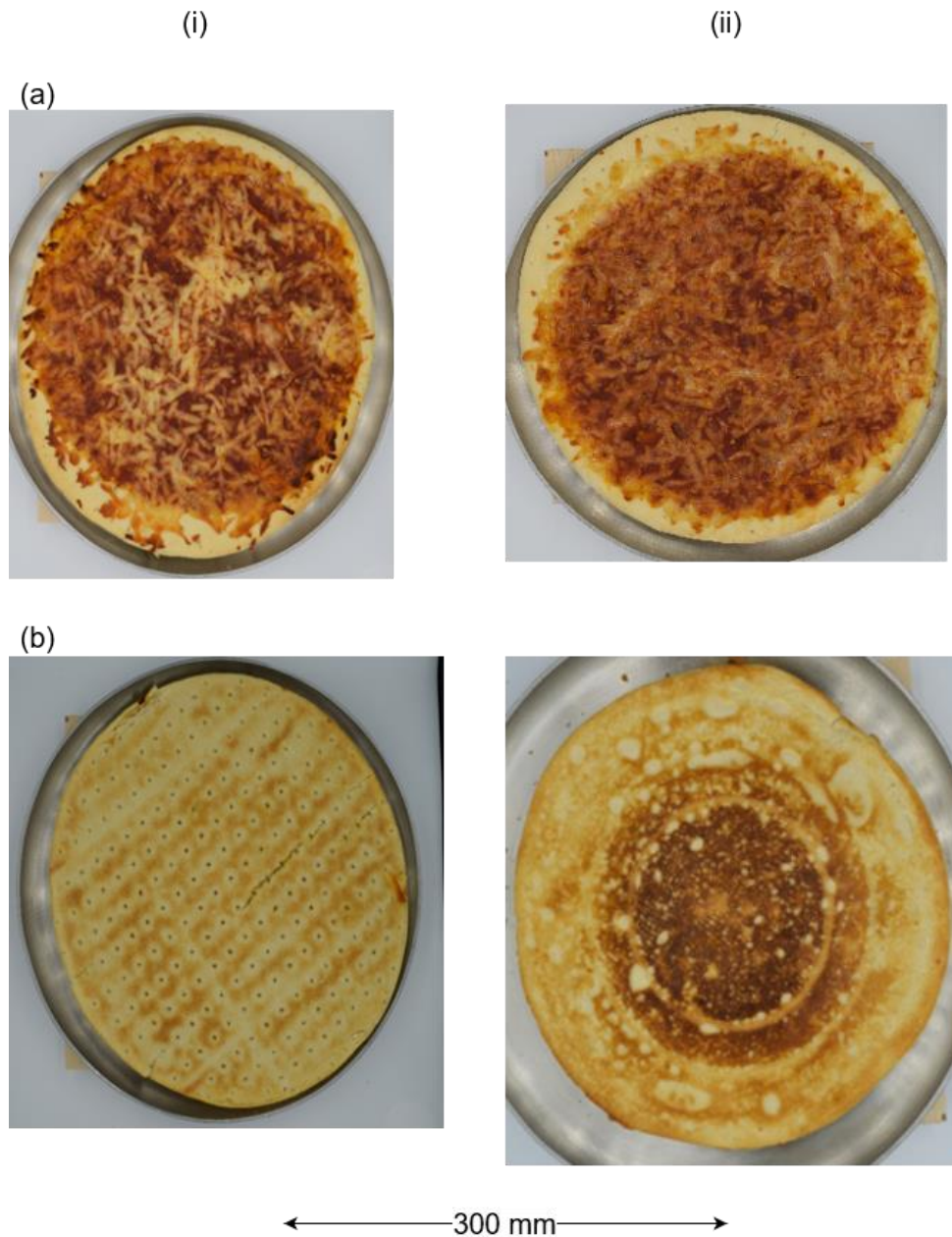


Figure 9.7: Images of cooked pizzas. Column (i) shows results from the traditional oven, (ii) shows results from the COI oven. Row (a) top of the pizza, (b) base of the pizza.

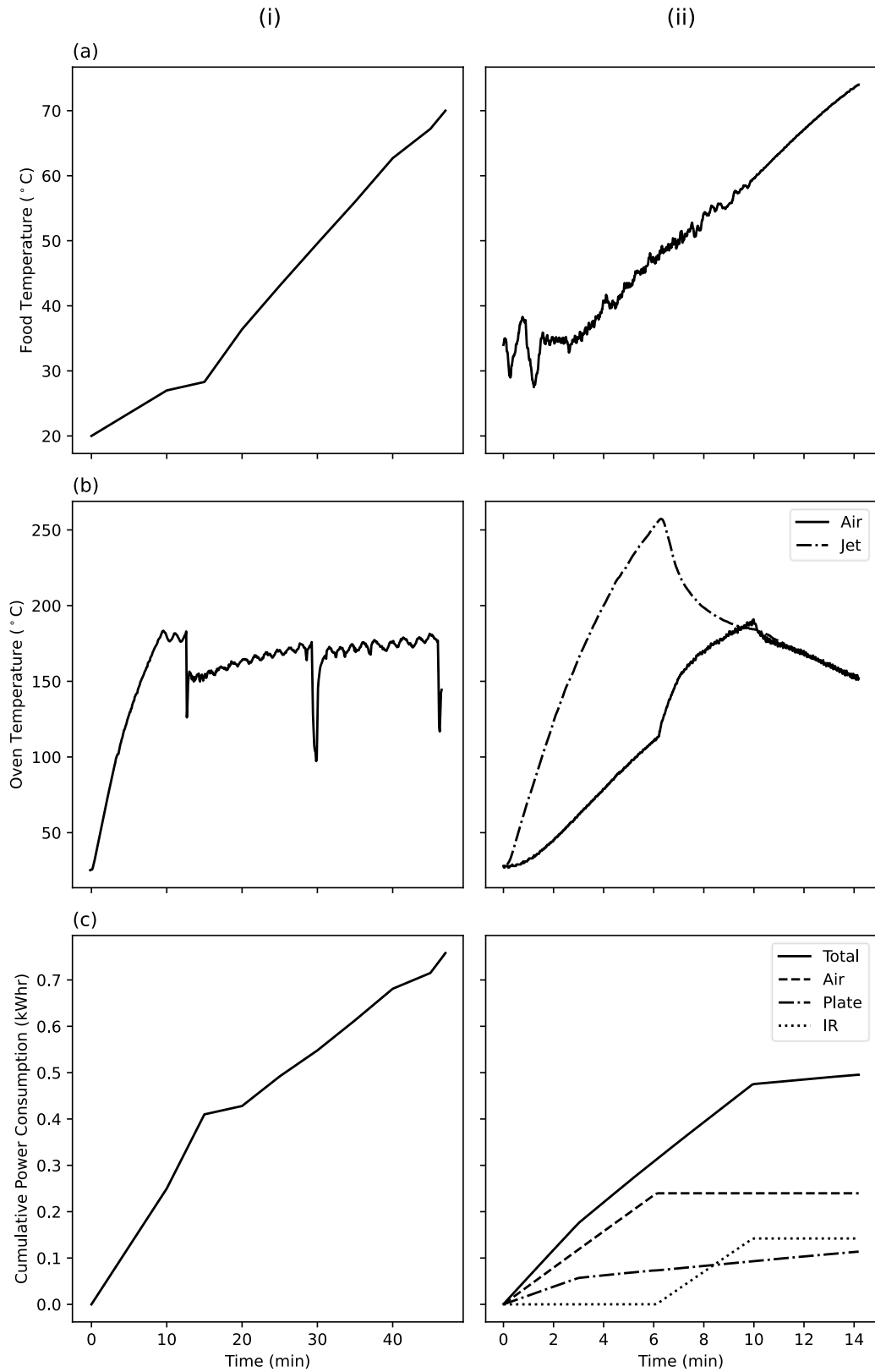


Figure 9.8: Power and temperature data for lasagne food trials. Column (i) shows data for the traditional oven, (ii) shows data for the COI oven. Row (a) Food temperature, (b) oven temperatures, (c) power consumption profiles. Note different time scales in columns (i) and (ii).

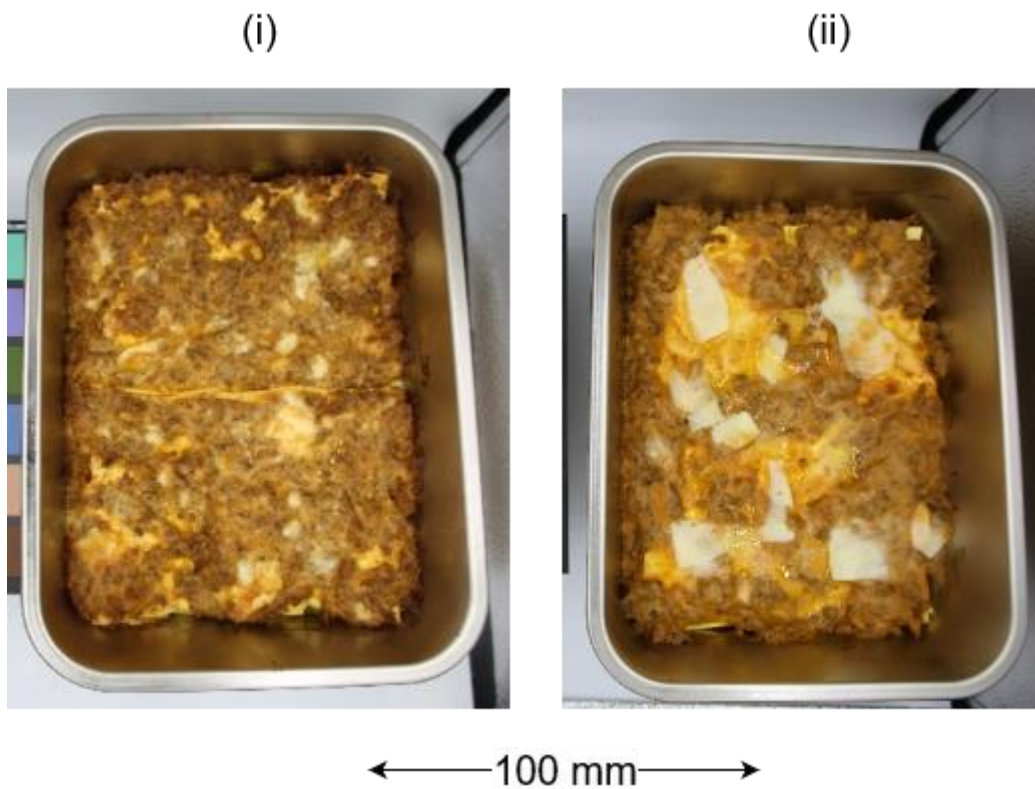


Figure 9.9: Images of the top surfaces of cooked lasagnes. Column (i) shows result from the traditional oven, (ii) shows result from the COI oven.

9.4: Conclusions

Four different foods: pizza, chicken, bread, and lasagne were cooked in a traditional oven and the COI design of oven. These foods covered a wide range of Bi and thermal mass. The COI oven cooked the food more rapidly, to a comparable standard in all cases while using less electrical power. Power and time savings were greater in foods with lower Bi . The lumped property model predicted cooking time and energy consumption reasonably given the simplicity of the model. There were also differences in the operating conditions assumed by the model and used in experiment which will contribute these errors.

Further work needs to be done to investigate more types of food, such as pastries and sweet cakes, as well as blind taste testing and textural measurements of food cooked in the two ovens. This requires investigating and optimising the combination of heat transfer modes for different food types. Further work is also required to increase the ease of use of the COI oven, such as increasing the library of programs for cooking different types of food or a more automated way of generating cooking programs.

10: Conclusions

10.1: Reflection on Project Aims

This work was based around the development of a new design of domestic oven that aimed to reduce energy consumption compared to existing designs. The specific aims were outlined in section 1.2 and are presented here in the same order:

- i) A lumped property model was developed to simulate both the COI and a traditional oven design. The cooking of both chickens and pizzas was simulated. The model was validated by comparing experimentally measured cooking times and energy consumption in the traditional oven to results from the lumped property model. The temperature and energy consumption vs time profiles were captured accurately by the simulation, with errors in the total cooking time and energy consumption between 10 and 20%.

The lumped property simulation of the COI oven showed significant reductions in cooking time and energy consumption, with cooking time reduced by 48% and 60% for chicken and pizza, respectively. Energy consumption was reduced by 32% and 26%, respectively. Further development of the COI design was therefore justified, as the simulation showed the potential to save both energy and time. Time saving was considered to be important as it increased the convenience of using the oven, encouraging uptake and therefore increasing the impact of the design.

A sensitivity analysis was also performed using the lumped property model of the COI design. This showed that the heat transfer coefficient between the oven air and the food was the most important quantity in generating energy and time savings. The sensitivity analysis also showed that COI design was able to save time and energy with less favourable estimates of model parameters

- ii) Three prototypes were constructed over the course of the project. The first prototype required a computer to be connected by USB to control the heaters and was constructed from heavy gauge hand folded and welded aluminium. In

comparison, the third and final prototype was constructed from stamped and pressed metal sheet that was representative of domestic ovens currently in mass production and included a touch screen user interface and recipe system allowing for a simplified and streamlined user experience.

Comparative trials were undertaken, where a range of foods were cooked in this third prototype and a traditional fan oven. These trials confirmed the predictions of the lumped property model, the COI prototype was able to reduce cooking times by between 30 and 70%, and energy consumption by between 8.4 and 35%. This was achievable for foods with a representative range of thermal masses and Bi .

- iii) A CFD simulation of the prototype IB oven was produced and validated using the NASA 6 step process. The simulation accurately predicted air velocity, temperature, and convective heat flux. However, the simulation underpredicted radiative heat flux by an average of 53.2%. This was attributed to the simulation not modelling the conduction of heat through the walls of the heater section and not accurately predicting the temperature of the oven walls. This was due to a combination of an incorrect estimation of the heat transfer coefficient from the interior wall to the ambient, and a reliance upon empirical wall functions to calculate heat flux from the oven air to the interior wall. The mean absolute error in the simulation predictions of heat flux was -30.4%.

The simulation was used to evaluate the possibility of applying the COI design to a 45 cm kitchen unit. This was found to increase the efficiency of the oven. However, the evenness of cooking was greatly reduced. Attempts to alleviate this were made by adding additional impingement jets and reducing the distance between them. These were not successful as the cooking was less uniform than in the 60 cm oven, and power consumption and cooking time were increased compared to the base 45 cm configuration.

10.2: Recommendations for Further Work

10.2.1: CFD Simulation

i) **Include solid ductwork in the model**

As discussed in chapter 7.6.5, neglecting heat transfer through the walls of the heater section and ductwork was the largest source of error in the CFD simulation.

Therefore, including the metal in the ductwork and including conduction physics in the simulation will increase the accuracy of the simulation, making the predictions more reliable. This task would require minor geometry changes to include the ductwork walls, meshing the solid walls and physics definition. A spatial convergence study would also be required.

ii) **Continue the 45 cm design study**

Two recommendations are made in section 8.3.1 to generate an acceptable 45 cm design. One is to adjust the position of the impingement jet nozzles to increase the overall heat transfer coefficient to the food surface, the second is to model swaged and angled impingement jets. The aim of this is to increase the evenness of the heat flux into the food.

The CFD simulation includes only half the volume of the air within the oven, with a symmetry plane boundary placed down the central plane. This prevents angled nozzles from being investigated as angled jets will give non-symmetrical flow within the oven. Removing the symmetry plane would be a simple geometry and meshing operation. However, it would double the elements and nodes in the simulation, doubling the computation time. For this to be practical, a more powerful computer will be required with approximately 64 GB of RAM.

iii) **Inclusion of water vapour in the model**

The simulation assumes the oven is filled with dry air, however, during food trials the gas within the oven chamber was up to 70% water vapour. Water vapour has a higher thermal conductivity and volumetric heat capacity, giving a higher heat flux than dry air. The water vapour will also affect the radiative heat exchange as water vapour will absorb and re-emit infra-red radiation. Inclusion of water vapour in the simulation will require changes only to the physics definition, adding water vapour as a material and defining a mixture model. A grey gas model will also be required to simulate the absorbance and remission of infra-red from the water vapour.

10.2.2: Experimental

i) **Build and test a 45cm oven using the model recommendations**

As discussed in chapter 8, a 45 cm oven unit using the COI design is anticipated to give improved thermal efficiency and reduced cooking times compared to the 60 cm prototypes. Constructing and testing a prototype within a 45 cm unit that applies the findings from the CFD design study is therefore recommended. This would be a time consuming and expensive process however, as an existing 45 cm oven would require extensive modifications to fit the additional COI parts without adversely reducing the cooking volume.

ii) **More complete and rigorous food trials**

The food trials described in chapter 9 demonstrated the ability of the COI design to cook food more quickly and more efficiently than a traditional oven design.

However, only 4 foods were trialled, quantitative measurements of the finished product were not made, and the cooking sequences used were not necessarily optimal. The food trials could be expanded to a wider range of food to further demonstrate the ability of the COI oven to save energy and time, such as sweet cakes, pastries and tarts. Quantitative tests, such as texture measurements and taste tests would establish more concretely any differences in foods cooked in the COI oven compared to a traditional design.

iii) **Improve the ease of use of the oven**

As discussed in chapter 9, a barrier to adoption of the COI oven is that the COI design is more complex to use unless the food being cooked is described by a pre-loaded recipes. Three solutions to this barrier could be pursued: one is to develop a comprehensive list of preloaded recipes such that cooking a food not included in the list is rare. A second is develop a base mode that cycles the three heating modes until the food is cooked, not requiring any other parameters to be set by the user. A third is a system within the oven that allows it to mimic a traditional fan oven, allowing users to use existing recipes for a normal fan oven if desired.

iv) **Allow for recipes commencing in hot oven**

Another limitation of the recipe system is that all recipes begin with the oven cold. In practice consumers will often cook items sequentially, meaning the oven may be hot

when cooking starts. Systems exist that adapt recipes depending on the temperature of the oven, such as that patented by TurboChef®¹⁷³.

v) Characterise and develop the heat recovery system

A heat recovery system, that recovers thermal energy from oven vent gases for use in other chores was included in the prototype III oven. However, this feature was not characterised or developed further. Work is required to determine the fraction of thermal energy that is recovered and to optimise the exchanger area and pressure drop.

vi) Characterise and develop humidity reduction system

Prototype III included a vent from the fan plenum that could be opened to vent gas from the cooking chamber and replace it with dry air from the surroundings, thereby reducing the humidity in the oven. This system requires characterisation and optimisation.

¹⁷³ McKee and Winkelmann, Quick-Cooking Oven.

11: Appendix A

Table 11.1: Solid body properties of the traditional oven model

Body	Material	Volume (m ³)	Thickness (m)
Fan shroud	Steel	6.00×10^{-6}	1.00×10^{-3}
Oven back plate	Steel	1.20×10^{-5}	1.00×10^{-3}
Oven back insulation	Ceramic wool	2.40×10^{-3}	0.02
Oven back outer casing	Steel	1.20×10^{-5}	1.00×10^{-3}
Oven inner wall	Steel	7.20×10^{-4}	1.00×10^{-3}
Oven insulation	Ceramic wool	1.44×10^{-2}	2.00×10^{-2}
Oven outer casing	Steel	7.20×10^{-4}	1.00×10^{-3}
Oven door	"Door"	6.00×10^{-3}	3.00×10^{-2}
Food	Variable	Variable	Variable

Table 11.2: Gaseous body properties of the traditional oven model

Body	Volume (m ³)	Heat Transfer Coefficient (Wm ⁻² K ⁻¹)
Fan air	2.00×10^{-4}	25
Oven air	5.00×10^{-2}	15

Table 11.3: Mass exchanger properties of the traditional oven model

Name	Body 1	Body 2	Flowrate (kg s ⁻¹)
Mass 1	Fan air	Oven air	0.002
Mass 2	Oven air	Fan air	0.002

Table 11.4: Heat exchanger properties of the traditional oven model

Name	Body 1	Body 2	Area (m ²)
Heat 1	Fan air	Oven back plate	0.06
Heat 2	Fan air	Fan shroud	0.06
Heat 3	Oven back plate	Oven back insulation	0.2
Heat 4	Oven back insulation	Oven back outer casing	0.2
Heat 5	Oven air	Oven back plate	0.14
Heat 6	Oven air	Fan shroud	0.06
Heat 7	Oven air	Oven inner wall	0.72
Heat 8	Oven air	Oven door	0.2
Heat 9	Oven air	Food	Variable
Heat 10	Oven inner wall	Oven insulation	0.72
Heat 11	Oven insulation	Oven outer casing	0.72
Heat 12	Oven outer casing	Surroundings	0.72
Heat 13	Oven door	Surroundings	0.2
Heat 14	Oven back outer casing	Surroundings	0.2

Table 11.5: Controllers used in the traditional oven model

Controller	Measured Body Temperature	Temperature Setpoint (°C)	Power (W)	Body power supplied to
Air temperature	Oven air	180	2400	Fan air

Table 11.6: Solid body properties of the COI oven model

Body	Material	Volume (m ³)	Thickness (m)
Heater ductwork	Steel	6.00×10^{-6}	1.00×10^{-3}
Fan shroud	Steel	6.00×10^{-6}	1.00×10^{-3}
Oven back plate	Steel	1.20×10^{-5}	1.00×10^{-3}
Oven back insulation	Ceramic wool	2.40×10^{-3}	2.00×10^{-2}
Oven back outer casing	Steel	1.20×10^{-5}	1.00×10^{-3}
Oven inner wall	Steel	7.20×10^{-4}	1.00×10^{-3}
Oven insulation	Ceramic wool	1.44×10^{-2}	2.00×10^{-2}
Oven outer casing	Steel	7.20×10^{-4}	1.00×10^{-3}
Oven door	“Door”	6.00×10^{-3}	3.00×10^{-2}
Hot plate	Aluminium	6.30×10^{-4}	2.00×10^{-3}
Food	Variable	Variable	Variable

Table 11.7: Gaseous body properties of the COI oven model

Body	Volume (m ³)	Film Heat Transfer Coefficient (Wm ⁻² K ⁻¹)
Heater air	2.00×10 ⁻⁴	35
Impingement air	2.00×10 ⁻⁴	35
Oven air	5.00×10 ⁻²	15
Fan air	2.00×10 ⁻⁴	35

Table 11.8: Mass exchanger properties of the COI oven model

Name	Body 1	Body 2	Flowrate (kg s ⁻¹)
Mass 1	Heater air	Impingement air	0.002
Mass 2	Oven air	Impingement air	0.002 × <i>mixing ratio</i>
Mass 3	Impingement air	Oven air	0.002×(<i>mixing ratio</i> +1)
Mass 4	Oven air	Fan air	0.002
Mass 5	Fan air	Heater air	0.002

Table 11.9: Heat exchanger properties of the COI oven model

Name	Body 1	Body 2	Area (m ²)
Heat 1	Fan air	Oven back plate	0.06
Heat 2	Fan air	Fan shroud	0.06
Heat 3	Oven air	Oven back plate	0.14
Heat 4	Heater air	Heater ductwork	0.06
Heat 5	Heater ductwork	Oven air	0.06
Heat 6	Oven back plate	Oven back insulation	0.2
Heat 7	Oven back insulation	Oven back outer casing	0.2
Heat 8	Oven air	Oven inner wall	0.66
Heat 9	Oven air	Oven door	0.2
Heat 10	Oven inner wall	Oven insulation	0.72
Heat 11	Oven insulation	Oven outer casing	0.72
Heat 12	Heater air	Oven inner wall	0.06
Heat 13	Impingement air	Food	Variable
Heat 14	Heater plate	Food	Variable
Heat 15	Heater plate	Oven air	0.13-(Heat 14 area)
Heat 16	Oven back outer casing	Surroundings	0.2
Heat 17	Oven door	Surroundings	0.2
Heat 18	Oven outer casing	Surroundings	0.72

Table 11.10: Controllers used in the COI oven model

Controller	Measured Body Temperature	Temperature Setpoint (°C)	Power (W)	Body which power was supplied to:
Air temperature	Oven air	180	2400	Heater air
Plate temperature	Hot plate	180	1200	Hot plate

12: Appendix B

Film heat transfer from heater walls to oven air is taken as $15 \text{ Wm}^{-2}\text{K}^{-1}$, as measured by Carson *et al.*¹⁷⁴

Film heat transfer coefficient through the heater walls was found by calculating the overall heater transfer coefficient through 1.5 mm of mica and 2 mm of aluminium:

$$\left(\frac{0.015}{0.4} + \frac{0.02}{205} \right)^{-1} = 27 \quad (12.1)$$

The view factor of the heater section external walls from the sensor, $F_{A \rightarrow B}$ was calculated by projecting the roof of the oven onto a horizontal plane and calculating the fraction of the projected plane taken up by external wall of the heater section:

$$F_{A \rightarrow B} = \frac{\text{Projected heater wall area}}{\text{Projected cooking chamber roof area}} = \frac{0.017 \times 0.3 \times 3}{0.35 \times 0.2} = 0.21 \quad (12.2)$$

¹⁷⁴ Carson, Willix, and North, ‘Measurements of Heat Transfer Coefficients within Convection Ovens’, 1 February 2006.

